

©Copyright 2006

Stuart Lee Jackson

Density Characteristics of a Sheared-Flow Z-Pinch

Stuart Lee Jackson

A dissertation submitted in partial fulfillment
of the requirements for the degree of

Doctor of Philosophy

University of Washington

2006

Program Authorized to Offer Degree: Aeronautics & Astronautics

University of Washington
Graduate School

This is to certify that I have examined this copy of a doctoral dissertation by

Stuart Lee Jackson

and have found that it is complete and satisfactory in all respects,
and that any and all revisions required by the final
examining committee have been made.

Chair of the Supervisory Committee:

Uri Shumlak

Reading Committee:

Thomas R. Jarboe

Brian A. Nelson

Uri Shumlak

Date: _____

In presenting this dissertation in partial fulfillment of the requirements for the doctoral degree at the University of Washington, I agree that the Library shall make its copies freely available for inspection. I further agree that extensive copying of this dissertation is allowable only for scholarly purposes, consistent with "fair use" as prescribed in the U.S. Copyright Law. Requests for copying or reproduction of this dissertation may be referred to Proquest Information and Learning, 300 North Zeeb Road, Ann Arbor, MI 48106-1346, 1-800-521-0600, to whom the author has granted "the right to reproduce and sell (a) copies of the manuscript in microform and/or (b) printed copies of the manuscript made from microform."

Signature_____

Date_____

University of Washington

Abstract

Density Characteristics of a Sheared-Flow Z-Pinch

Stuart Lee Jackson

Chair of the Supervisory Committee:
Associate Professor Uri Shumlak
Aeronautics & Astronautics

The ZaP Flow Z-Pinch experiment investigates the effects of sheared flow on gross plasma stability. The sheared-flow Z-pinches produced are characterized by a quiescent period, during which the Z-pinch exhibits low magnetic mode activity, high electron density on axis, and other characteristics of stability. Measurements made with a holographic interferometer are inverted using an Abel inversion and combined with measurements from a multi-chord He-Ne interferometer to track the time evolution of the radial electron density profile. A Z-pinch with a radius of 1 cm and an electron number density profile peaked at approximately 10^{17} cm^{-3} is observed during the quiescent period. The electron density drops as the quiescent period ends. These results are in agreement with the time evolution of the density profile from MACH2 simulations. The density profile is used to estimate temperature and magnetic field profiles for the Z-pinch. Experimental parameters such as capacitor bank energy and neutral gas injection are adjusted to investigate their influence on the density and behavior of the Z-pinch. Results of these investigations show that lower capacitor bank energy and injection of more neutral gas into the experiment lead to a longer quiescent period.

TABLE OF CONTENTS

List of Figures	iii
List of Tables	ix
Glossary	x
Chapter 1: Introduction	1
1.1 The ZaP Flow Z-Pinch	2
1.2 Motivation for Density Profile Measurement	4
1.3 Previous Measurements of Density Profiles in Z-Pinches and Similar Plasma Configurations	8
1.4 Kadomtsev Profile	9
Chapter 2: Experimental Diagnostics and Results	12
2.1 Magnetic Probes	12
2.2 He-Ne Interferometer	21
2.3 Holographic Interferometer	45
2.4 Fast-Framing Camera	62
Chapter 3: Equilibrium Profile Calculation	69
3.1 Constant Current Density	70
3.2 Current Density Proportional to Number Density	72
3.3 Limited Perpendicular Thermal Conduction with Uniform Heating	74
3.4 Constant Temperature	82
3.5 Time Evolution of Equilibrium Profiles	85
3.6 Comparison with Kadomtsev Pressure Profile	86
Chapter 4: Simulation of Density Profile Evolution	88
4.1 Simulation Geometry	88
4.2 Boundary Conditions	88
4.3 Current Characteristics	90

4.4	Initial Conditions	92
4.5	Simulation Results	92
4.6	Time Evolution of Equilibrium Profile	107
Chapter 5:	Influence of Experimental Parameters	114
Chapter 6:	Discussion and Conclusions	121
Chapter 7:	Future Work	126
Chapter 8:	Summary	128
Bibliography		129
Appendix A:	Holographic Interferometry User's Guide	133
A.1	Safety	133
A.2	Optical Configuration of the Holographic Interferometer	134
A.3	Loading the Film	144
A.4	Making the Holographic Interferogram	145
A.5	Developing the Holographic Interferogram	147
A.6	Reconstructing the Holographic Interferogram	148
A.7	Density Determination and Data Storage	149
Appendix B:	Input File for MACH2 ZaP Simulation	152
Appendix C:	IDL Procedure <i>dense_fin.pro</i>	165
Appendix D:	IDL Procedure <i>analyze_interferogram.pro</i>	182
Appendix E:	IDL Procedure <i>invert_interferogram.pro</i>	204
Appendix F:	Matlab Functions for Temperature Profile Calculation	232
F.1	Constant Current Density	232
F.2	Current Density Proportional to Number Density	237
F.3	Limited Perpendicular Thermal Conduction with Uniform Heating	242
F.4	Constant Temperature	256

LIST OF FIGURES

Figure Number	Page
1.1 $m = 0$ “sausage” and $m = 1$ “kink” instabilities in a Z-pinch	2
1.2 ZaP Flow Z-Pinch experimental apparatus	3
1.3 Cartoons showing the formation of a ZaP Flow Z-Pinch.	5
1.4 Plasma current and normalized $m=1$ mode at axial location $z = 0$, with the quiescent period indicated.	6
1.5 Photos of Z-pinch emission showing a quiescent Z-pinch plasma during the quiescent period.	6
1.6 Normalized Kadomtsev pressure profile.	10
2.1 Photographs of probes used to measure magnetic fields in the experiment. . .	13
2.2 Azimuthal magnetic fields measured by the eight probes of the azimuthal array located at $z = 0$ and $\theta = 0^\circ, 45^\circ, 90^\circ, 135^\circ, 180^\circ, 225^\circ, 270^\circ$, and 315° . .	14
2.3 Average magnetic fields measured by the azimuthal magnetic probe arrays in the assembly region.	16
2.4 Magnitudes of the normalized $m = 1$ mode measured by the azimuthal magnetic probe arrays in the assembly region.	16
2.5 Normalized $m = 1$ mode at $z = 0$ and total plasma current, with the quiescent period indicated.	17
2.6 Azimuthal magnetic fields measured at various axial locations in the acceleration region during a 6 kV and a 9 kV plasma pulse.	18
2.7 Current distribution in the acceleration region.	19
2.8 The current distribution in the acceleration region can be determined using the magnetic fields measured by the axial array of magnetic probes embedded in the outer electrode.	20
2.9 He-Ne interferometer optical configuration.	21
2.10 Drawing of the ZaP Flow Z-Pinch Experiment showing the axial locations of the interferometer chords used to make measurements in the acceleration region.	22
2.11 Block diagram of the interferometer electronics on a panel in the screen room and in a shielded box in the laboratory.	23
2.12 Electrical schematic of the interferometer photodiode amplifier circuit. . . .	25

2.13	Electrical schematic of the interferometer photodiode amplifier's power and bypassing circuit.	26
2.14	Block diagram of mixer-splitter operation.	27
2.15	Mixer-splitter input and output signals over a short time interval, with the 40-MHz reference signal frequency apparent in the waveforms of all four signals.	30
2.16	Mixer-splitter input and output signals over a longer time interval, with the influence of the phase shift visible.	31
2.17	Mixer-splitter output signals before and after the 10 MHz low-pass filter.	33
2.18	Lissajous curves that result when the sine and cosine components of the phase are plotted against one another.	34
2.19	Determination of the chord-integrated electron density during a plasma pulse.	36
2.20	Chord-integrated electron number density measured at $z = 0$ and two impact parameters, along with normalized $m = 1$ mode and total plasma current for a 6 kV hydrogen plasma pulse.	38
2.21	Chord-integrated electron number density measured at $z = 0$ and two impact parameters, along with normalized $m = 1$ mode and total plasma current for a 9 kV hydrogen plasma pulse.	39
2.22	The length of the quiescent period decreases with increasing capacitor bank voltage.	40
2.23	Chord-integrated electron number density measured at $z = 61$ cm and two impact parameters, along with normalized $m = 1$ mode at $z = 0$ and total plasma current for a 6 kV hydrogen plasma pulse.	41
2.24	Chord-integrated electron number density measured at $z = 61$ cm and two impact parameters, along with normalized $m = 1$ mode at $z = 0$ and total plasma current for a 9 kV hydrogen plasma pulse.	42
2.25	The end of the quiescent period is correlated with the exhaustion of plasma in the accelerator.	43
2.26	Chord-integrated electron density in the acceleration region during a 9 kV hydrogen plasma pulse.	44
2.27	Normalized $m = 1$ mode, plasma current, and chord-integrated electron number density for the helium Z-pinch used to study the density profile during arrival (Fig. 2.40)	46
2.28	Normalized $m = 1$ mode, plasma current, and chord-integrated electron number density for the helium Z-pinch used to study the density profile during early formation (Fig. 2.40)	47
2.29	Normalized $m = 1$ mode, plasma current, and chord-integrated electron number density for the helium Z-pinch used to study the density profile during late formation (Fig. 2.40)	48

2.30 Normalized $m = 1$ mode, plasma current, and chord-integrated electron number density for the helium Z-pinch used to study the density profile during the middle of the quiescent period (Fig. 2.41)	49
2.31 Normalized $m = 1$ mode, plasma current, and chord-integrated electron number density for the helium Z-pinch used to study the density profile during the late quiescent period (Fig. 2.41)	50
2.32 Normalized $m = 1$ mode, plasma current, and chord-integrated electron number density for the helium Z-pinch used to study the density profile after the quiescent period (Fig. 2.41)	51
2.33 Optical arrangement of the single-pass holographic interferometer	52
2.34 Holographic interferograms made before and after the laser was refurbished . .	55
2.35 Holographic interferograms made with and without plasma present	55
2.36 Graphical depiction of each coefficient A_{ki} as half the path length through a cylindrical shell of plasma at a given impact parameter	57
2.37 Chord-integrated electron density and radial electron density profile for a hydrogen Z-pinch	60
2.38 Holographic interferograms made using the single-pass holographic interferometer	61
2.39 Radial electron density profiles for hydrogen, 50% methane/50% hydrogen, and helium Z-pinches	61
2.40 Radial electron density profiles for helium Z-pinches during formation of the Z-pinch	63
2.41 Radial electron density profiles for helium Z-pinches during and after the quiescent period	64
2.42 Streak photo of the Z-pinch	65
2.43 Photos of Z-pinch emission showing the arrival of the current sheet	66
2.44 Plasma current and normalized $m=1$ mode associated with the images capturing the arrival of the current sheet	66
2.45 Photos of Z-pinch emission showing the development of a possible kink instability near the end of the quiescent period	67
2.46 Plasma current and normalized $m=1$ mode associated with the images showing the development of a possible kink instability near the end of the quiescent period	67
2.47 Photos of Z-pinch emission showing the development of a possible sausage instability near the end of the quiescent period	68
2.48 Plasma current and normalized $m=1$ mode associated with the images showing the development of a possible sausage instability near the end of the quiescent period	68

3.1	Z-pinch equilibrium profiles obtained for a hydrogen Z-pinch with the assumption that the current density is constant.	71
3.2	Z-pinch equilibrium profiles obtained for a hydrogen Z-pinch with the assumption that the current density is proportional to the number density.	73
3.3	Z-pinch equilibrium profiles obtained for a hydrogen Z-pinch obtained using the thermal conduction model.	81
3.4	Z-pinch equilibrium profiles obtained for a hydrogen Z-pinch obtained using the constant temperature model.	84
3.5	Magnetic field profiles for helium Z-pinches during the middle of the quiescent period and near the end of the quiescent period.	86
3.6	Comparison between the Kadomtsev pressure profile and the normalized pressure profiles obtained from the experiment.	87
4.1	Geometry used for the MACH2 simulation	89
4.2	Current and voltage across the insulator between the inner and outer electrodes for the simulation and for a plasma pulse	91
4.3	Contour plots at $10 \mu\text{s}$ for the simulation with an initial mass density of $4.72 \times 10^{-4} \text{ kg/m}^3$ and a capacitor bank voltage of 9 kV.	93
4.4	Contour plots at $16 \mu\text{s}$ for the simulation with an initial mass density of $4.72 \times 10^{-4} \text{ kg/m}^3$ and a capacitor bank voltage of 9 kV.	94
4.5	Contour plots at $20 \mu\text{s}$ for the simulation with an initial mass density of $4.72 \times 10^{-4} \text{ kg/m}^3$ and a capacitor bank voltage of 9 kV.	95
4.6	Contour plots at $30 \mu\text{s}$ for the simulation with an initial mass density of $4.72 \times 10^{-4} \text{ kg/m}^3$ and a capacitor bank voltage of 9 kV.	96
4.7	Contour plots at $37 \mu\text{s}$ for the simulation with an initial mass density of $4.72 \times 10^{-4} \text{ kg/m}^3$ and a capacitor bank voltage of 9 kV.	97
4.8	Contour plots at $42 \mu\text{s}$ for the simulation with an initial mass density of $4.72 \times 10^{-4} \text{ kg/m}^3$ and a capacitor bank voltage of 9 kV.	98
4.9	Contour plots at $46 \mu\text{s}$ for the simulation with an initial mass density of $4.72 \times 10^{-4} \text{ kg/m}^3$ and a capacitor bank voltage of 9 kV.	99
4.10	Contour plots at $57 \mu\text{s}$ for the simulation with an initial mass density of $4.72 \times 10^{-4} \text{ kg/m}^3$ and a capacitor bank voltage of 9 kV.	100
4.11	Contour plots at $60 \mu\text{s}$ for the simulation with an initial mass density of $4.72 \times 10^{-4} \text{ kg/m}^3$ and a capacitor bank voltage of 9 kV.	101
4.12	Contour plots at $80 \mu\text{s}$ for the simulation with an initial mass density of $4.72 \times 10^{-4} \text{ kg/m}^3$ and a capacitor bank voltage of 9 kV.	102
4.13	Chord-integrated number density at various axial locations from the simulation with an initial mass density of $4.72 \times 10^{-4} \text{ kg/m}^3$ and a capacitor bank voltage of 9 kV.	105

4.14	Chord-integrated number density at various axial locations from the simulation with an initial mass density of 4.72×10^{-4} kg/m ³ and a capacitor bank voltage of 6 kV.	106
4.15	Azimuthal magnetic fields at various axial locations in the acceleration region for the 9 kV and 6 kV simulations.	108
4.16	Current distribution in the acceleration region for the 9 kV and 6 kV simulations.	109
4.17	Number density profile evolution from the simulation at 16, 30, and 37 μ s, corresponding to arrival and formation of the Z-pinch.	110
4.18	Number density evolution from the simulation at 42, 57, and 60 μ s, corresponding to during the dense Z-pinch, late dense Z-pinch , and after the dense Z-pinch.	111
4.19	Magnetic field profile evolution from the simulation at 42, 57, and 60 μ s, corresponding to during the dense Z-pinch, late dense Z-pinch , and after the dense Z-pinch.	112
4.20	Temperature profile evolution from the simulation at 42, 57, and 60 μ s, corresponding to during the dense Z-pinch, late dense Z-pinch , and after the dense Z-pinch.	113
5.1	Mass injected into the experiment for the gas line pressures used in the experimental investigation of accelerator exhaustion.	115
5.2	Quiescent period length at capacitor bank voltages from 5 to 9 kV for the gas line pressures used in the experimental investigation of accelerator exhaustion.	117
5.3	Quiescent period length and dense Z-pinch period length while decreasing gas line pressure with a capacitor bank voltage of 7 kV.	118
5.4	The effects of wall conditioning are evident when the gas pressure is increased, rather than decreased, between sets of pulses.	119
5.5	The time-averaged chord-integrated density during the quiescent period does not show a clear trend with changing capacitor bank voltage.	120
A.1	Optical configuration of the single-pass holographic interferometer with the lengths of each section of the scene and reference beam paths indicated.	135
A.2	Photograph of the optical configuration of the single-pass holographic interferometer with the scene and reference beam paths indicated.	136
A.3	Optical configuration of the double-pass holographic interferometer with the lengths of each section of the scene and reference beam paths indicated.	138
A.4	Photograph of the optical configuration of the double-pass holographic interferometer with the scene and reference beam paths indicated.	139
A.5	Optical configuration used to reconstruct holographic interferograms.	148

A.6	Photograph of the optical configuration used to reconstruct holographic interferograms.	149
A.7	Reconstructed images that result when the reconstruction laser beam is diffracted by the holographic film.	150

LIST OF TABLES

Table Number	Page
1.1 ZaP Flow Z-Pinch typical operating parameters	7
A.1 Darkroom processing of holographic film	147

GLOSSARY

ABEL INVERSION: a mathematical technique used to obtain profile information from chord-integrated measurements of an axisymmetric, cylindrical object.

ACCELERATION REGION: the annulus between the inner and outer electrodes where gas is ionized and accelerated by the Lorenz force towards the assembly region.

ASSEMBLY REGION: the cylindrical volume inside the outer electrode from the inner electrode nose cone to the outer electrode end wall. The Z-pinch is formed along the axis of the assembly region.

ELECTRON NUMBER DENSITY: the number of electrons per unit volume present at a given location in the plasma.

HE-NE INTERFEROMETER: a device that uses a helium-neon (He-Ne) laser to measure chord-integrated electron number density along one or more chords through a plasma.

HOLOGRAPHIC INTERFEROMETER: a device that uses holographic techniques to produce a two-dimensional map of the chord-integrated electron number density in a plasma. This chord-integrated density is then used to determine the radial electron number density profile.

$m = 0$ “SAUSAGE” INSTABILITY: one of two prominent classical MHD instabilities that affect the Z-pinch. The “sausage” instability is an azimuthally symmetric density perturbation that quickly grows and destroys the Z-pinch.

m = 1 “KINK” INSTABILITY: one of two prominent classical MHD instabilities that affect the Z-pinch. The “kink” instability is an azimuthally asymmetric density perturbation that quickly grows and destroys the Z-pinch.

MAGNETOHYDRODYNAMICS (MHD): a highly idealized and simplified model often used to predict the macroscopic behavior of plasma configurations.

NORMALIZED *m* = 1 MODE: a Fourier component of the magnetic field measured by an azimuthal array of eight magnetic field probes embedded in the outer electrode around the Z-pinch, normalized by the average magnetic field measured by the probes. The period of this normalized mode spans all eight probes. When multiplied by the diameter of the outer electrode, its magnitude corresponds to twice the displacement of the Z-pinch from the axis of the experiment.

QUIESCENT PERIOD: the period of time after the arrival of the plasma at the azimuthal magnetic probe array where the magnitude of the normalized *m* = 1 mode of the Z-pinch is below 0.2.

SHEARED-FLOW STABILIZATION: the theory that a Z-pinch or another inherently unstable plasma configuration can be stabilized by a gradient in the plasma flow. In the case of a Z-pinch, a radial gradient in the axial velocity of $dv_z/dr > 0.1kV_A$ has been shown numerically to stabilize the Z-pinch against the *m* = 1 “kink” instability.

Z-PINCH: a plasma column with a current flowing through it in the axial (z) direction.

ZAP FLOW Z-PINCH: a basic plasma physics experiment designed to investigate the effects of sheared flow on gross plasma stability. The experiment consists of a coaxial assembly region attached to a cylindrical assembly region where a sheared-flow Z-pinch is formed. The Z-pinches produced exhibit characteristics of stability for over one thousand theoretical instability growth times.

ACKNOWLEDGMENTS

The author wishes to express sincere appreciation to Uri Shumlak, Brian Nelson, Ray Golingo, Ed Crawford, Ted Shreve, Jim Pasko, and the rest of the ZaP Team for their assistance, encouragement, support, and many thoughtful discussions regarding this investigation.

Chapter 1

INTRODUCTION

One of the earliest and most basic magnetic confinement concepts studied by fusion scientists is the Z-pinch. A Z-pinch is a column of plasma with an axial current flowing through it that creates an azimuthal magnetic field. The magnetic pressure from the azimuthal field confines and compresses the column, creating a hot, dense plasma. Typically, a Z-pinch is made by connecting a wire of tungsten or frozen deuterium between two electrodes. When a large potential is applied across the electrodes, the wire vaporizes and then ionizes, forming the Z-pinch.

Unfortunately, a *static* Z-pinch formed in this manner is susceptible to two types of magnetohydrodynamic (MHD) instabilities. The $m = 0$ “sausage” mode occurs when the plasma column begins to become thinner at any point along its length. Magnetic pressure builds at this point, causing the column to become thinner still, until finally it breaks and the plasma current is disrupted. The $m = 1$ “kink” instability occurs when the plasma column begins to kink or bend. Magnetic pressure builds inside the bend, pushing it farther out until the column is broken and the current is lost. Figures 1.1(a)–1.1(b) show the $m = 0$ “sausage” and $m = 1$ “kink” instabilities in a Z-pinch. These MHD instabilities usually destroy the Z-pinch within tens of nanoseconds, limiting its usefulness as a fusion reactor [11]. Z-pinches are commonly used in experiments where the production of a large amount of x-ray radiation is desired [17].

Several methods have been proposed to reduce the destructive effects of MHD instabilities on the Z-pinch [23, 26, 35]. One such method is sheared-flow stabilization. Numerical linear stability analysis shows that a linear velocity shear of $v_z/a > 0.1kV_A$ inhibits the growth of the $m = 1$ mode [37]. Similar behavior has been shown through simulation for the $m = 0$ mode [39]. This result is supported by sheared-flow stabilization experiments

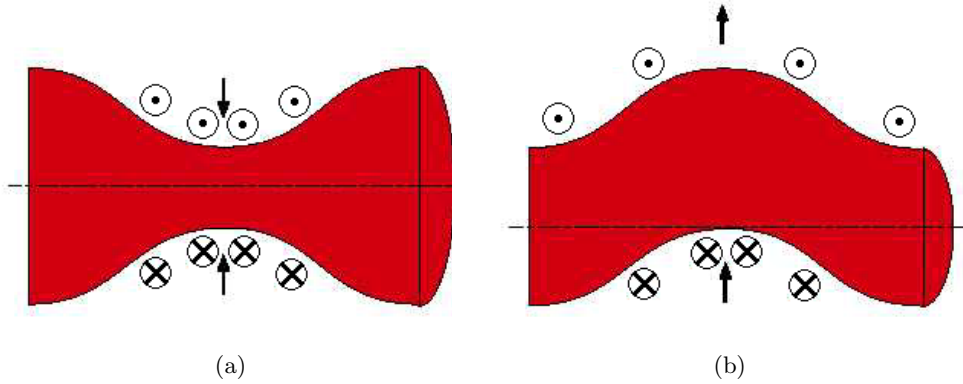


Figure 1.1: $m = 0$ “sausage” and $m = 1$ “kink” instabilities in a Z-pinch. (a) $m = 0$ “sausage” mode. (b) $m = 1$ “kink” mode.

conducted on the ZaP Flow Z-Pinch. These experiments have produced Z-pinch plasmas that exhibit characteristics of stability for over 1000 times the theoretical instability growth time [38].

1.1 The ZaP Flow Z-Pinch

The ZaP Flow Z-Pinch experiment at the University of Washington is a plasma physics experiment designed to investigate the behavior of a sheared-flow Z-pinch. The origins of the experiment can be traced to sheared-flow stabilization theory and the Marshall gun experiments of the 1950s and 1960s [37, 27].

The experimental apparatus, shown in Fig. 1.2, is composed of two coaxial, cylindrical electrodes enclosed in a vacuum chamber [12]. The outer electrode is a 200 cm long, 20 cm inner diameter hollow copper cylinder with a copper end wall. This outer electrode end wall has a 2 cm diameter hole in it to allow plasma to escape on the downstream side of the Z-pinch. The inner electrode is a 100 cm long, 10 cm outer diameter hollow copper cylinder that ends 100 cm before the outer electrode. A nose cone is attached to the end of the inner electrode, extending its length slightly beyond 100 cm. The area between the electrodes before the inner electrode ends is called the “acceleration region.” The space from the tip of the inner electrode nose cone to the outer electrode end wall is referred to as the “assembly region.”

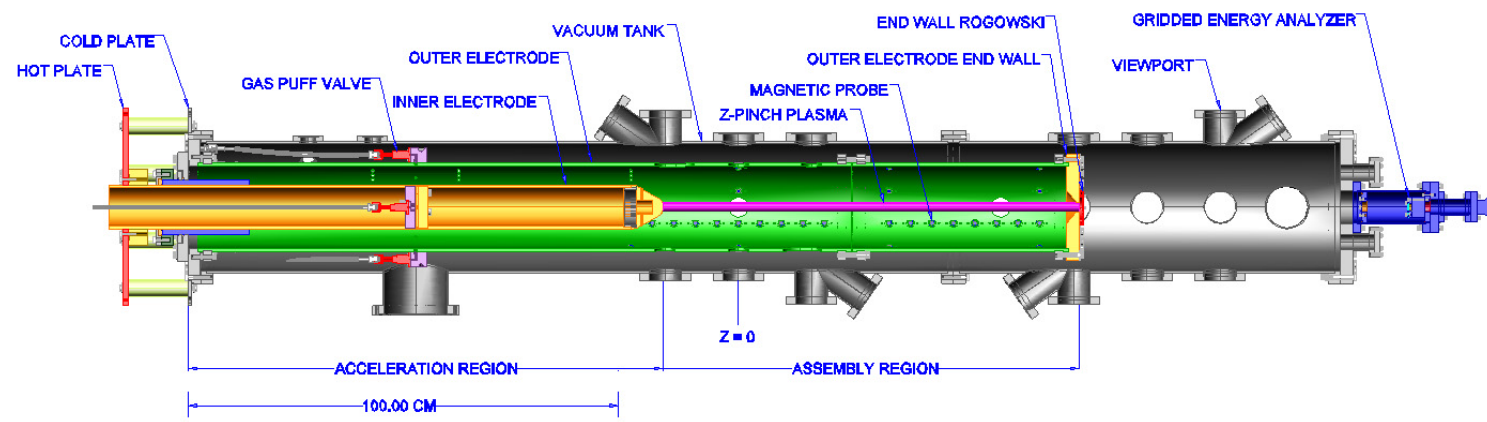


Figure 1.2: ZaP Flow Z-Pinch experimental apparatus.

Hydrogen gas is puffed into the acceleration region between the two electrodes at a point about halfway down the length of the inner electrode. A potential difference of 5 to 9 kV is applied across the two electrodes, causing the gas to ionize. Current is carried between the two electrodes by the plasma, causing a magnetic field to form behind the plasma. The radial current and the azimuthal magnetic field interact to create a Lorentz force that accelerates the plasma axially down the electrodes towards the assembly region.

One end of the forming Z-pinch attaches at the tip of the inner electrode as the other end moves down the outer electrode and attaches to the end wall. The Lorentz force is now directed radially inward towards the center of the plasma, confining and compressing the Z-pinch. This formation process results in a flowing Z-pinch with axial velocities of $10 \text{ cm}/\mu\text{s}$ [38]. Figures 1.3(a)–1.3(d) are cartoons showing ZaP Flow Z-Pinch formation. Formation of the flowing Z-pinch is followed by a $10\text{--}40 \mu\text{s}$ -long quiescent period, characterized by low magnetic mode activity. Figure 1.4 is a plot of the plasma current and the normalized $m=1$ mode at the axial location labeled as $z = 0$ in Fig. 1.2. The quiescent period, defined as where the magnitude of the normalized $m=1$ mode is less than 0.2, begins at $20 \mu\text{s}$ and ends at $40 \mu\text{s}$ for the plasma pulse shown. Photos of plasma emission also indicate the existence of a quiescent Z-pinch plasma during this time. Figures 1.5(a)–1.5(h) is a series of images taken at axial location $z = 0$ along the Z-pinch at the times indicated during the plasma pulse of Fig. 1.4. These images show a quiescent Z-pinch plasma during the quiescent period. Table 1.1 lists typical operating parameters for the ZaP Flow Z-Pinch.

1.2 Motivation for Density Profile Measurement

The purpose of this dissertation is to describe the density characteristics of a sheared-flow Z-pinch. Both the radial and axial profiles will be investigated, as well as their behavior over time and under different experimental conditions. This information, when combined with temperature measurements, can be used to determine the equilibrium profile of the sheared-flow Z-pinch. This equilibrium profile can then be compared with theoretical predictions and with the conditions required for a fusion reactor based on a sheared-flow Z-pinch. The density measurements also give insight into the instabilities that affect the Z-pinch, since the sausage and kink instabilities manifest themselves as density perturbations.

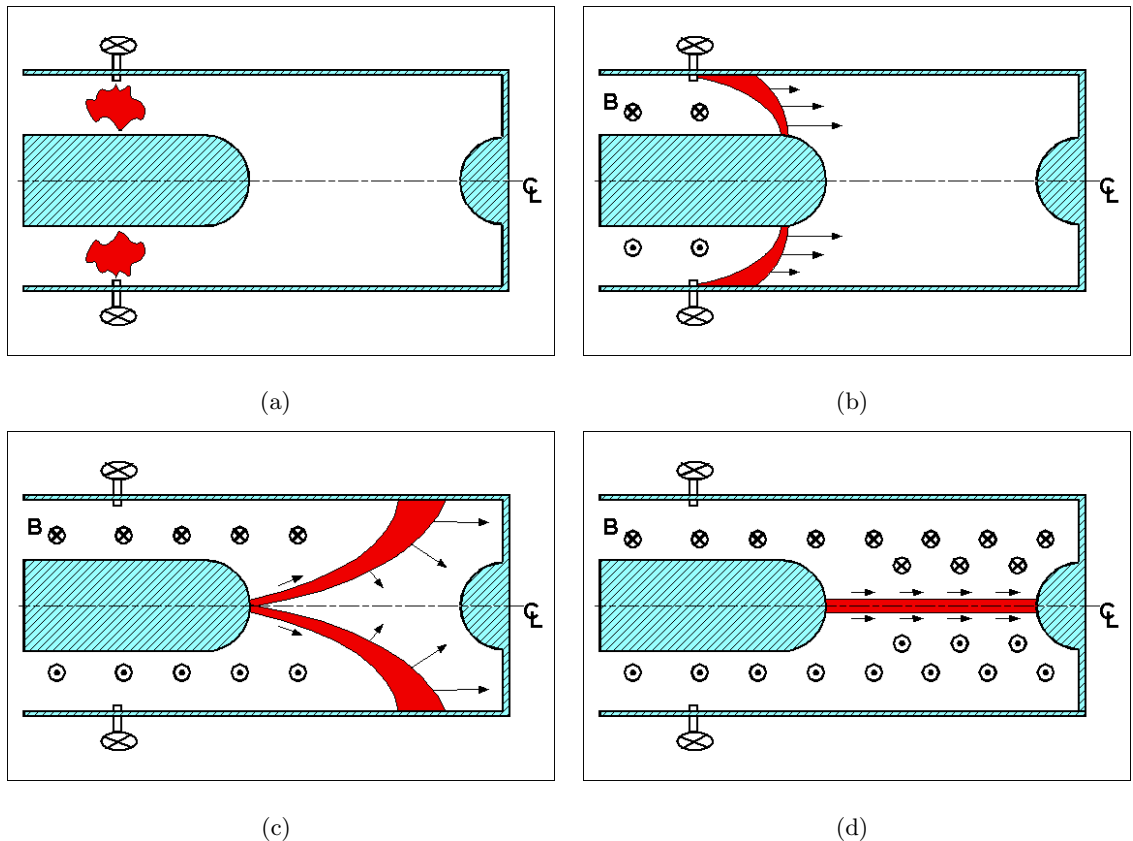


Figure 1.3: Cartoons showing the formation of a ZaP Flow Z-Pinch. (a) Hydrogen gas is puffed between the inner and outer electrodes. (b) The gas is ionized and accelerated by Lorentz forces. (c) Current flows between the two electrodes as the Z-pinch begins to form. (d) Flowing Z-pinch is formed.

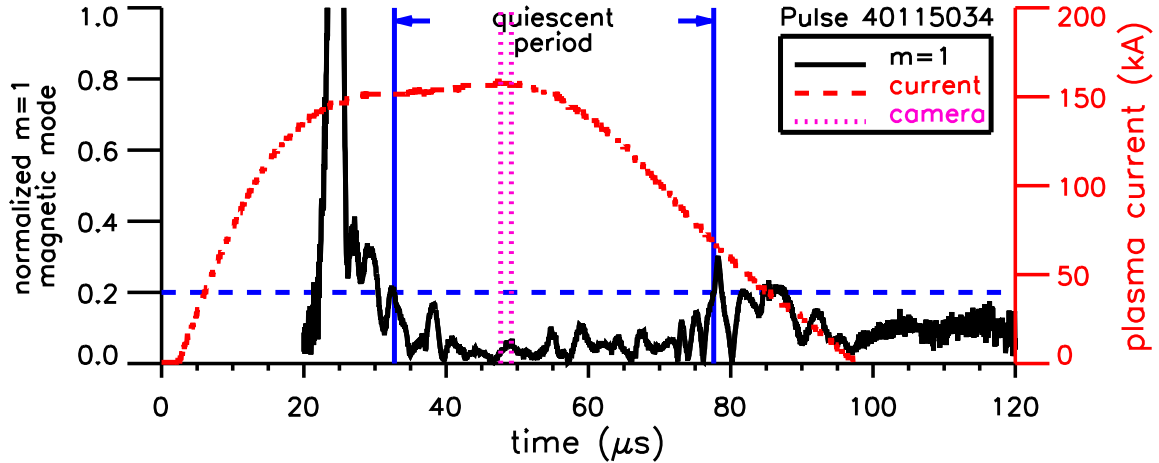


Figure 1.4: Plasma current and normalized $m=1$ mode at axial location $z = 0$, with the quiescent period indicated. Also shown as vertical lines are the times at which the first and last of eight images shown in Figs. 1.5(a)–1.5(h) were made (Pulse 40115034).

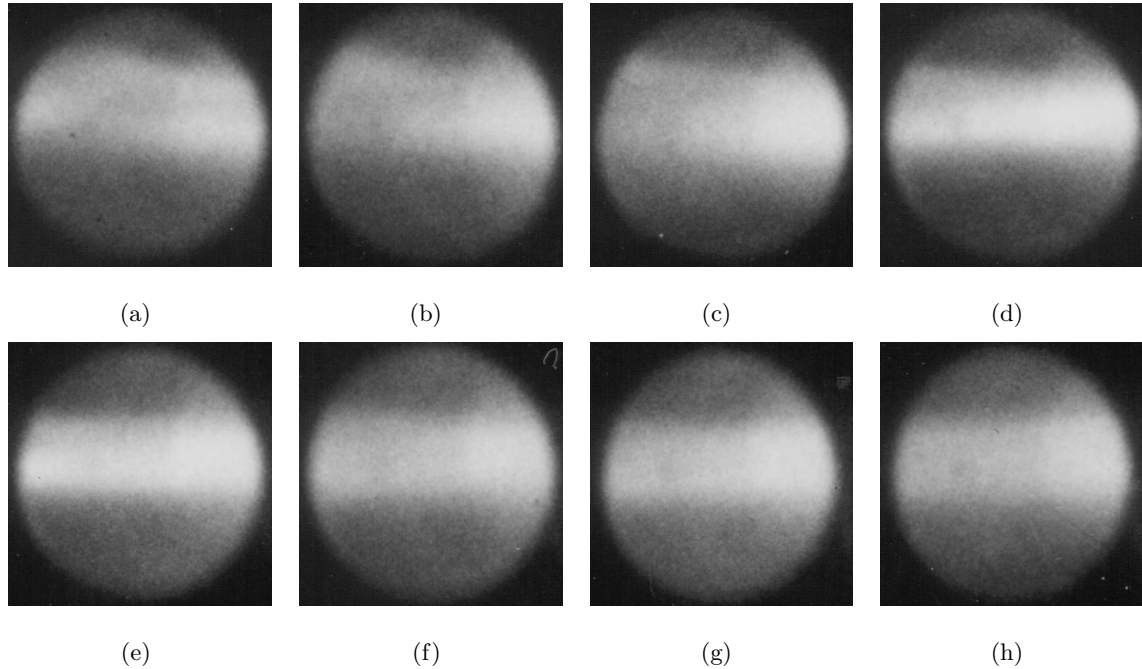


Figure 1.5: Photos of Z-pinch emission showing a quiescent Z-pinch plasma during the quiescent period. The photos represent unfiltered visible light emitted by the plasma and are made approximately 200 ns apart through the vacuum tank viewport and 2 in diameter hole in the outer electrode at $z = 0$ (Pulse 40115034). (a) 47.7 μ s. (b) 47.9 μ s. (c) 48.1 μ s. (d) 48.3 μ s. (e) 48.6 μ s. (f) 48.8 μ s. (g) 49.0 μ s. (h) 49.2 μ s.

Table 1.1: ZaP Flow Z-Pinch typical operating parameters.

parameter	symbol	value
ion velocity	v_{ion}	5–10 cm/μs
Alfvén speed	v_A	15 cm/μs
quiescent period length	τ_q	10–40 μs
total temperature	$T_e + T_i$	150–200 eV
electron number density	n_e	10^{16} – 10^{17} cm ^{−3}
edge magnetic field	B_{edge}	1–2 T
Z-pinch radius	a	1 cm
Z-pinch length	L	100 cm
peak current	$I_{p \ max}$	150–280 kA
peak power	$\mathcal{P}_{p \ max}$	0.2–1 GW
capacitor charge voltage	V_{mb}	5–9 kV

It is important to note that the density profile that can be measured using interferometric techniques is the electron number density profile. The assumption made many times in this document is that the shape of the electron number density profile is similar to the shape of the ion number density profile. This assumption is made because charge separation is not significant in a Z-pinch. It is possible that the electron and ion number densities are equal in a hydrogen Z-pinch, because ionization of hydrogen produces equal numbers of positive ions and electrons. For Z-pinches produced with helium, however, the electron number density is likely to be up to twice the ion number density, and for a 50 % hydrogen/50 % methane mixture, it may be between one and two times the ion number density. Impurity ions in the plasma may further raise the ratio between the electron and ion number densities.

1.3 Previous Measurements of Density Profiles in Z-Pinches and Similar Plasma Configurations

Density profiles have been investigated in previous Z-pinch and plasma focus experiments. Shiloh et al., used shadowgraphy and Abel inversion of holographic interferograms to study the density profile of an imploding argon gas puff Z-pinch [36]. They obtained density profiles that showed an initially hollow density distribution collapsing on axis over roughly 30 ns, sweeping up plasma as it imploded to form a high-density, peaked density profile with a radius of 0.1 cm and a peak electron density of 10^{19} cm^{-3} . Following the collapse, the Z-pinch stagnated on axis and its overall radial contraction stopped. $m = 0$ sausage density perturbations developed along the Z-pinch, and bursts of X-rays were emitted from the more constricted sections of the Z-pinch as it was disrupted by the instabilities.

Holographic interferometry was used by Bailey et al., to study gas puff Z-pinches of pure deuterium and deuterium-argon mixtures [4]. They found that the addition of a small amount of argon resulted in a higher density Z-pinch with a longer lifetime. They also determined that the initial gas density determined whether the Z-pinch pinched to a minimum radius at or before the current maximum, resulting in a high-density or low-density Z-pinch, respectively.

Qi et al., studied the density of a dense plasma focus and several imploding argon gas puff Z-pinch experiments using shearing interferometry [31, 32]. Shearing interferometry was better suited to the high-density plasmas studied than holographic interferometry because of the large fringe shifts produced. A contour plot of electron density versus radial and axial coordinates during implosion was obtained for Z-pinches on the Hawk pulsed-power generator. This contour showed a hollow radial profile 75 ns before the X-ray emission that occurred after the Z-pinch stagnated on axis. A radial electron density profile was also obtained on the higher-current Double Eagle pulsed power generator. A hollow profile was observed 75 ns before X-ray emission, with a peak near the axis that may have been an artifact magnified by the Abel inversion. Subsequent interferograms of both the Hawk and the Double Eagle Z-pinches show further implosion of the plasma consistent with the density profile evolution of Ref. [36].

A three-frame holographic interferometer was employed by Zou et al., to make interferograms of a single neon gas puff Z-pinch implosion at three separate times [42]. This process was repeated on subsequent plasma pulses to track the time evolution of the Z-pinch. Abel inversion was used to obtain radial velocity profiles at different axial locations for a single interferogram, so that a contour plot of electron density versus radial and axial coordinates was constructed. The contour obtained 363 ns before the final stagnation of the Z-pinch shows a hollow density profile with a radius of approximately 1.8 cm and a peak electron density of $3 \times 10^{18} \text{ cm}^{-3}$. Subsequent interferograms show further implosion consistent with Ref. [36].

The previous density investigations discussed here focused on imploding gas puff Z-pinch. The dynamic behavior of these Z-pinch is similar to the behavior expected of the sheared-flow Z-pinch produced by ZaP during the Z-pinch's initial assembly. Although the equilibrium is the same, it is not clear what aspects of the imploding Z-pinch density profiles and time evolution will carry over to the density of the sheared-flow Z-pinch during the quiescent period. Because of its less dynamic nature, it is likely that the density profile will conform to a theoretical steady-state equilibrium such as that proposed by Kadomtsev [23].

1.4 *Kadomtsev Profile*

The two-dimensional Z-pinch equilibrium with flow is

$$\frac{\rho u_\theta^2}{r} = \frac{\partial p}{\partial r} + \frac{B_\theta^2}{\mu_0 r} + \frac{B_\theta}{\mu_0} \frac{\partial B_\theta}{\partial r}, \quad (1.1)$$

where ρ is the mass density, u_θ is the azimuthal velocity, p is the pressure, B_θ is the magnetic field, which in a Z-pinch is purely azimuthal, r is the coordinate in the radial direction, and $\mu_0 = 4\pi \times 10^{-7} \text{ H/m}$ is the permeability of free space. It can be seen from Eq. 1.1 that the Z-pinch equilibrium does not depend on the axial (z) component of the velocity [3].

In addition, according to classical MHD theory, a Z-pinch whose pressure profile does not fall off too rapidly with increasing radius will be stable to the $m = 0$ “sausage” mode shown in Fig. 1.1(a). The limit on how quickly the pressure can drop with increasing radius

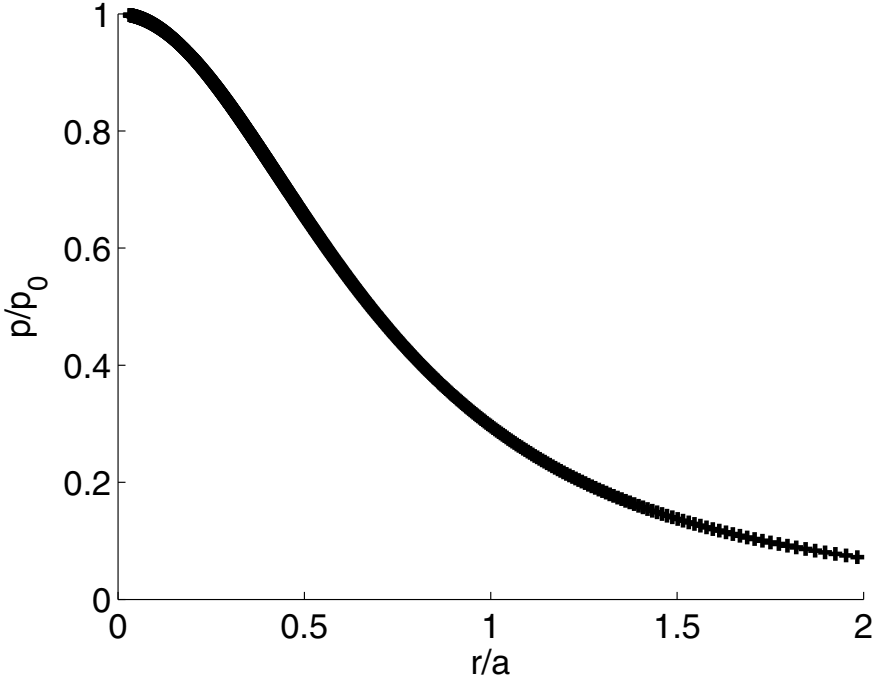


Figure 1.6: Normalized Kadomtsev pressure profile.

is given by the Kadomtsev pressure profile,

$$p = p_0 \left(\frac{\beta}{0.8 + \beta} \right)^{5/2} \quad (1.2)$$

$$r = a \frac{(0.8 + \beta)^{1/4}}{\beta^{3/4}}, \quad (1.3)$$

where p_0 is the pressure at $r = 0$, a is the characteristic radius of the Z-pinch, and $\beta = 2\mu_0 p/B^2$ is the local ratio of plasma pressure to magnetic pressure.

Fig. 1.6 shows the pressure profile that results when Eqs. 1.2–1.3 are evaluated over the range $\beta = \{0.4, 1000\}$. A Kadomtsev pressure profile was assumed for the linear stability analysis of Ref. [37] that showed that the $m = 1$ mode could be stabilized by the appropriate velocity shear. Therefore it is reasonable that it be used as a basis for comparison with a pressure profile derived from the measured density profile of a sheared-flow Z-pinch.

For this comparison, a pressure profile will be obtained from the measured density profile

using the ideal gas law. In this case, the ideal gas law is

$$p = (1 + 1/Z)nkT, \quad (1.4)$$

where $n = n_e = Zn_i$ is the electron density, Z is the effective ionization state and the ratio of electrons to ions, $k = 1.38 \times 10^{-23}$ J/K is Boltzmann's constant, and $T = T_e = T_i$ is the electron or ion temperature, which are assumed to be equal, in degrees Kelvin. The temperature profile is obtained from the density profile using one of several Z-pinch equilibrium models described in Chapter 3. This temperature is used along with the measured density to evaluate Eq. 1.4 and obtain the pressure profile.

Chapter 2

EXPERIMENTAL DIAGNOSTICS AND RESULTS

A suite of experimental diagnostics is used to characterize the behavior of the sheared-flow Z-pinches produced by the ZaP Flow Z-pinch. Axial and azimuthal magnetic probe arrays are used to measure magnetic fields in the experiment. Two interferometers—a holographic interferometer and a multichord helium-neon (He-Ne) interferometer—are used to measure the electron number density of plasmas produced. A fast-framing camera capable of making both framed and streak images is used to record the plasma emission. The operation of each of these experimental diagnostics is described in the following sections, as well as the experimental results obtained.

2.1 Magnetic Probes

The probes used to measure magnetic fields in the ZaP experiment are made by winding thin (AWG 32) copper wire ten times about a Kel-F form [12, 6]. The copper wire is insulated by an enamel coating and wound in such a way that the lead at the end of the winding ends up in the same place as the lead at the beginning. These leads are twisted to prevent stray magnetic flux between them from causing erroneous readings. The wound probe form is mounted inside a hat-shaped piece of stainless steel, with the top of the hat open except for a piece of 0.003-inch-thick tantalum foil. The foil is stretched over the top of the hat towards its brim and held on by a copper washer. The entire assembly is embedded in the outer electrode, with the tantalum-covered top of the hat-shaped piece facing the plasma. The probes are arranged in three azimuthal arrays of eight probes at $z = 0$, $z = 35$, and $z = 70$ cm and one axial array running the length of the outer electrode. The probes in the axial array are spaced nominally 5 cm apart, but their spacing is wider far upstream near the insulator in the acceleration region. There is also a six-probe azimuthal array at $z = -25$ cm. The arrangement of the magnetic probes is visible in Fig. 1.2. Each of the

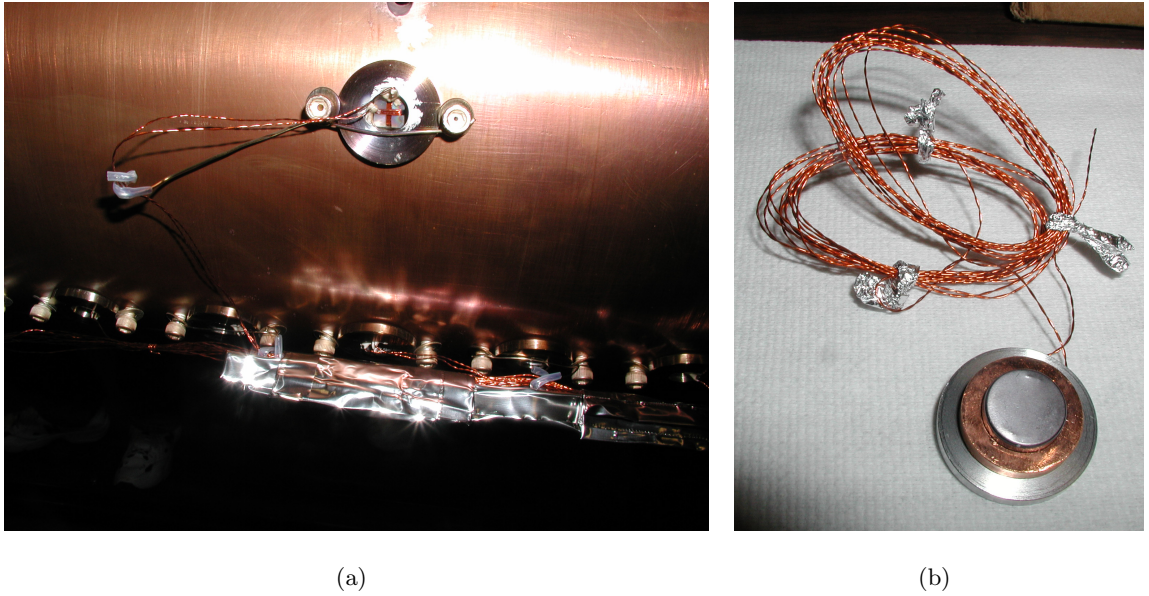


Figure 2.1: Photographs of probes used to measure magnetic fields in the experiment. (a) View of the back sides of several magnetic probes from outside the outer electrode. (b) Plasma-facing side of a magnetic probe before installation.

probes has a winding that is oriented to detect magnetic fields in the azimuthal direction. The probes of the azimuthal arrays have a second winding capable of detecting fields in the axial direction. Figure 2.1(a) is a photograph taken from outside the outer electrode showing the back sides of several magnetic probes. The Kel-F form and two copper windings of an azimuthal array probe are visible in the center of the photograph. Several axial array probes are visible in the bottom part of the picture. Figure 2.1(b) shows the plasma-facing side of a magnetic probe before installation. The stainless steel hat and copper washer are visible, as well as the tantalum foil that protects the Kel-F form and copper windings from the plasma. The probe shown has two windings—one to measure azimuthal fields and one to measure axial fields. The twisted-pair leads for the two windings are coiled and secured temporarily with aluminum foil in the photograph.

Each magnetic probe measures the change in magnetic flux as a voltage across the copper windings. This voltage is transmitted to an integrating circuit in the ZaP experiment screen room and recorded by a digitizer module mounted in a CAMAC (Computer Automated

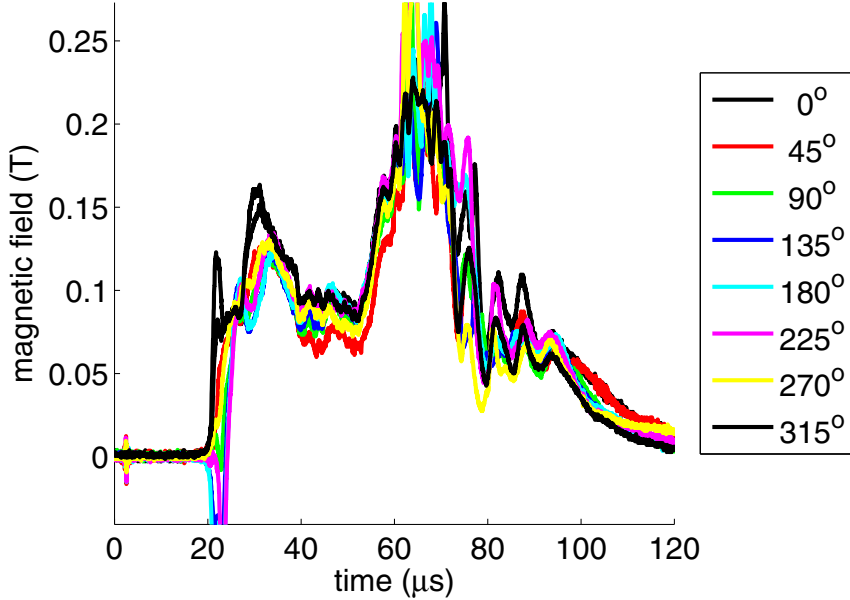


Figure 2.2: Azimuthal magnetic fields measured by the eight probes of the azimuthal array located at $z = 0$ and $\theta = 0^\circ, 45^\circ, 90^\circ, 135^\circ, 180^\circ, 225^\circ, 270^\circ$, and 315° (Pulse 30924047).

Measurement And Control) crate. Calibration factors for each probe are determined ahead of time by passing a known current through a copper rod temporarily mounted on the axis of the experiment. These calibration factors are used to obtain the magnetic field from the integrated and digitized voltage.

Figure 2.2 shows the azimuthal magnetic fields measured by the eight probes of the azimuthal array at $z = 0$ for a hydrogen plasma pulse with an initial capacitor bank voltage of 6 kV. The fields measured by the azimuthal array can be used to describe the motion and deformation of the Z-pinch in terms of its various mode components. The field measured by each probe of the azimuthal array can be expressed in terms of its Fourier components,

$$B(\theta) = C_0 + [C_1 \cos \theta + S_1 \sin \theta] + [C_2 \cos(2\theta) + S_2 \sin(2\theta)] \quad (2.1)$$

$$+ [C_3 \cos(3\theta) + S_3 \sin(3\theta)] \\ = \sum_{m=0}^3 [C_m \cos(m\theta) + S_m \sin(m\theta)], \quad (2.2)$$

where $B_m = (C_m^2 + S_m^2)^{1/2}$ is the magnitude of the m th Fourier mode component and θ is the azimuthal location of the probe. The $m = 0$ magnitude does not depend on the azimuthal angle and only the single coefficient $B_0 = C_0$ is necessary to describe it. Theta is measured as a positive angle counter-clockwise about the z-axis from the azimuthal location of the axial magnetic probe array. A matrix method described in Ref. [12] is used to determine the various Fourier mode components. $2m + 1$ probes are necessary to measure the m th mode component, so eight probes are capable of resolving $m = 0, 1, 2$, and 3 modes. The $m = 0$ component in this case is just the average magnetic field measured by the eight probes. The $m = 1$ component represents an asymmetric displacement of the Z-pinch from the axis. The $m = 2$ and $m = 3$ components represent, respectively, a more oval or triangular cross-section, rather than circular. When the $m = 1$ Fourier mode component is normalized by the $m = 0$ component, or average magnetic field, it is proportional to the displacement of the Z-pinch from the axis of the electrode,

$$\frac{B_{m=1}}{B_{m=0}} = \frac{2\Delta r}{r_{wall}}, \quad (2.3)$$

where Δr is the displacement of the Z-pinch and $r_{wall} = 0.0963$ cm is the radius of the outer electrode.

Figure 2.3 shows the average magnetic fields, or $m = 0$ components, measured by the azimuthal magnetic probe arrays located at $z = 0$, $z = 35$, and $z = 70$ cm. Figure 2.4 shows the magnitude of the $m = 1$ mode, normalized by the average magnetic field, or $m = 0$ component. The normalized $m = 1$ mode at all three locations shows a period of reduced mode activity following the arrival of the current sheet. The quiescent period of the Z-pinch is defined as the period of time after the current sheet arrival where the magnitude of the normalized $m = 1$ mode is less than 0.2. This corresponds to a displacement of the Z-pinch from the axis of less than 1 cm, approximately the radius of the Z-pinch. Figure 2.5 shows the normalized $m = 1$ mode at $z = 0$ and the total plasma current, with the quiescent period indicated. A horizontal dashed line at 0.2 is plotted for reference.

Figs. 2.6(a) and 2.6(b) show the azimuthal magnetic fields measured by the magnetic probes in the acceleration region during a 6 kV and a 9 kV plasma pulse. The measured fields rise sharply near the gas injection plane at $z = -75$ cm. The behavior of the two

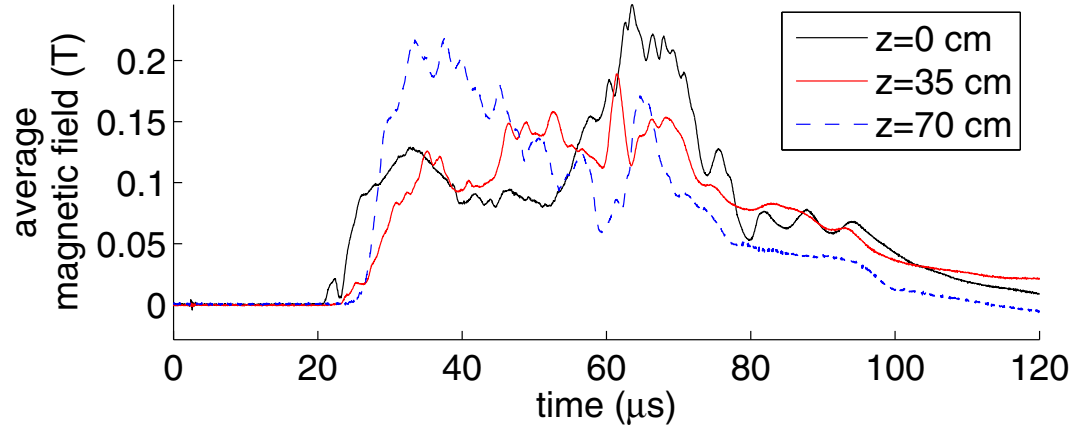


Figure 2.3: Average magnetic fields measured by the azimuthal magnetic probe arrays in the assembly region at $z = 0$, $z = 35$ cm, and $z = 70$ cm (Pulse 30924047).

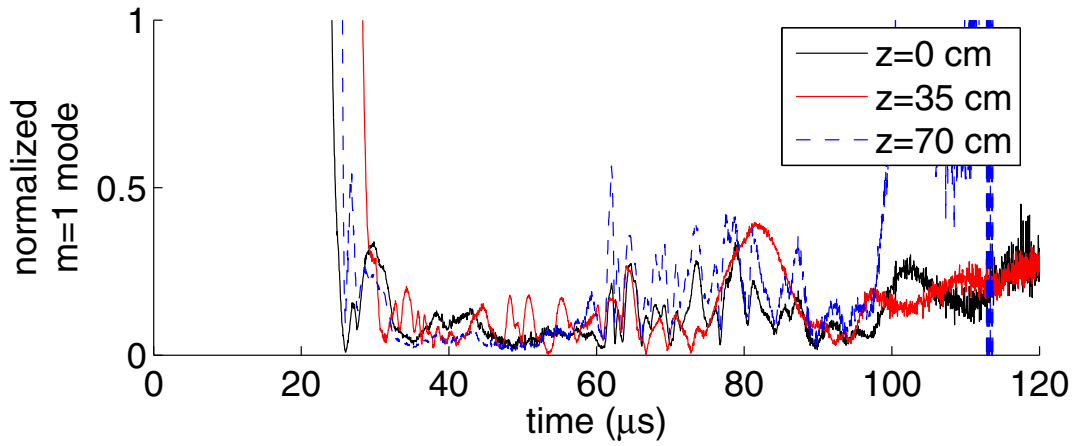


Figure 2.4: Magnitudes of the normalized $m = 1$ mode measured by the azimuthal magnetic probe arrays in the assembly region at $z = 0$, $z = 35$ cm, and $z = 70$ cm (Pulse 30924047).

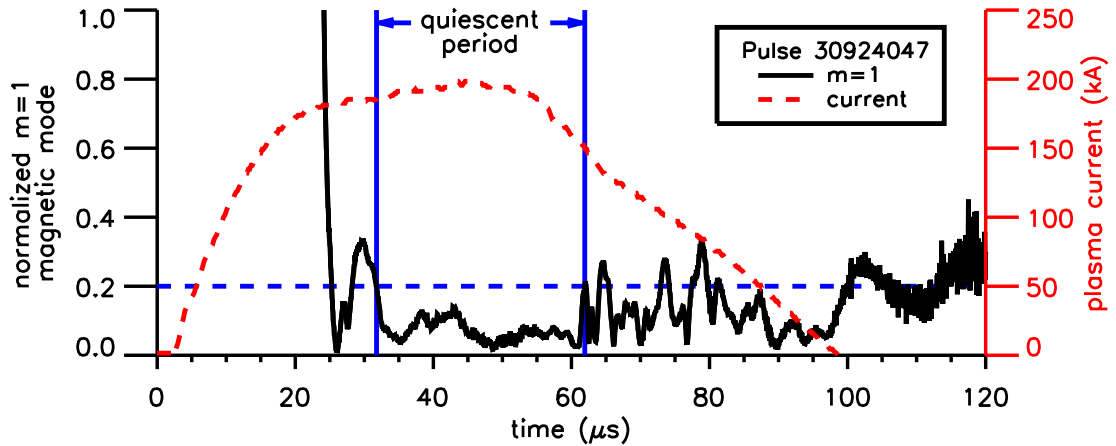


Figure 2.5: Normalized $m = 1$ mode at $z = 0$ and total plasma current, with the quiescent period indicated. A horizontal dashed line at 0.2 is plotted for reference (Pulse 30924047).

sets of fields overall is similar. More insight into processes in the acceleration region can be gained from the contour plots of the current distribution over time shown in Figs. 2.7(a) and 2.7(b). In the figures, the current measured by each magnetic probe is normalized by the total current. The result shows what percentage of the total current passes a given magnetic probe along the outer electrode and then attaches downstream through the plasma to return along the inner electrode and produce the magnetic field at the probe, as shown in Fig. 2.8. The locations of the 90, 80, 70, 60, and 50 % lines are plotted as contours versus time, showing the dynamics of the current distribution in the acceleration region. Most of the current flows initially near the gas injection plane, but is quickly swept out of the acceleration region in the current sheet. As the quiescent period begins, current spreads back into the accelerator and remains there until it is swept out again at the end of the quiescent period. During the quiescent period, half of the total current through the plasma flows in the acceleration region. The current distribution also undergoes oscillations that are more dramatic for a 9 kV plasma pulse than for a 6 kV pulse.

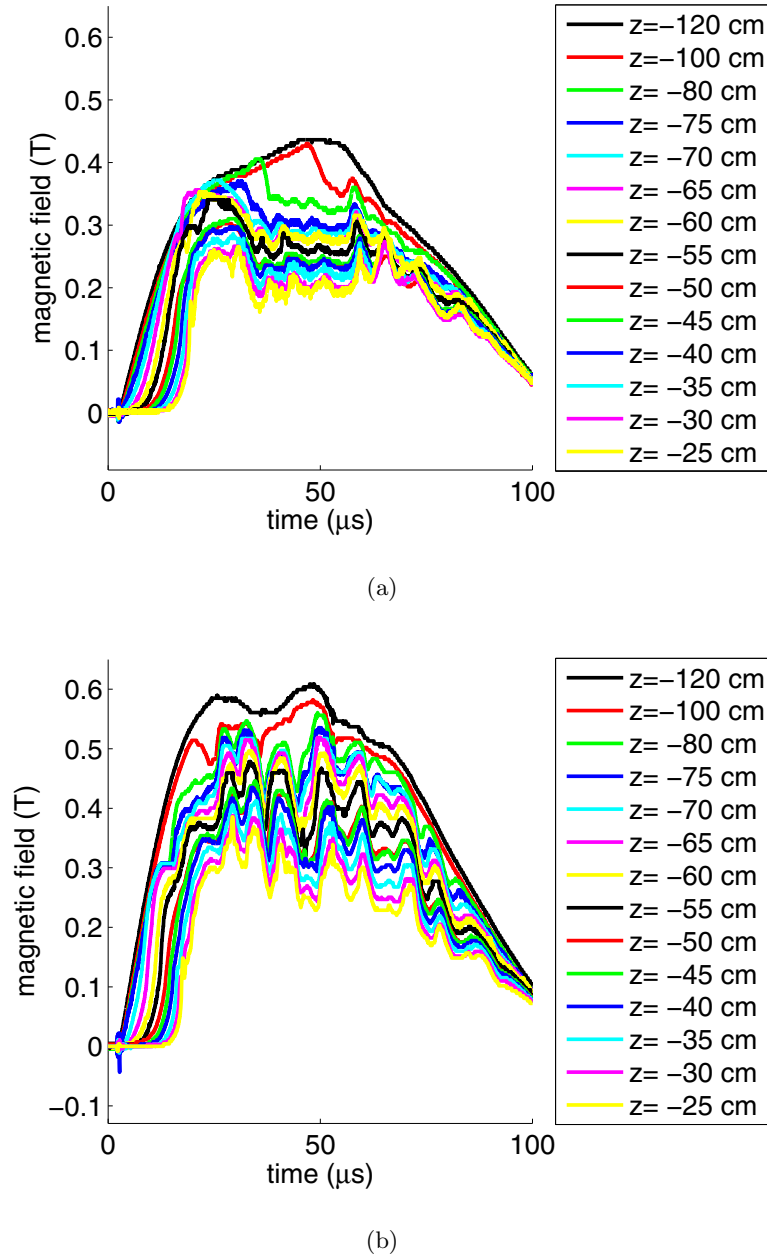


Figure 2.6: Azimuthal magnetic fields measured at various axial locations in the acceleration region during a 6 kV and a 9 kV plasma pulse. (a) Magnetic fields at $z = -120$ cm, $z = -100$ cm, etc. during a 6 kV plasma pulse (Pulse 30924047). (b) Magnetic fields at $z = -120$ cm, $z = -100$ cm, etc. during a 9 kV plasma pulse (Pulse 40914027).

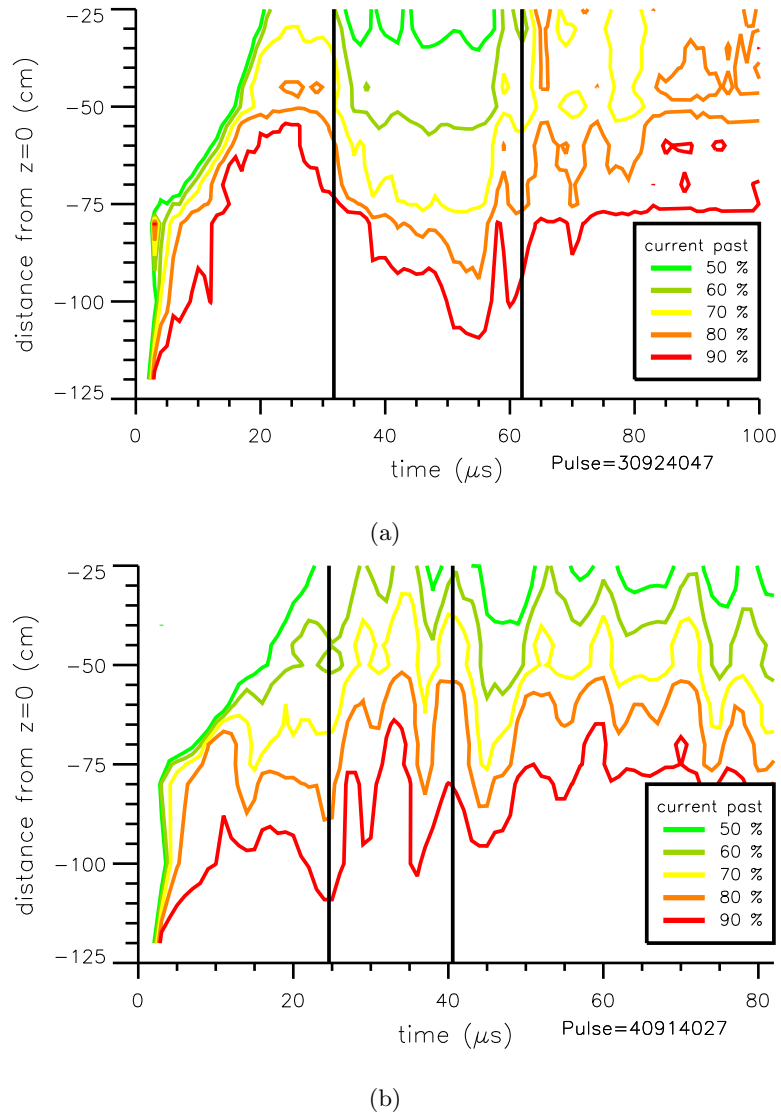


Figure 2.7: Current distribution in the acceleration region, expressed as percentage of total current passing an axial location along the outer electrode, attaching downstream through the plasma to the inner electrode, and returning through the inner electrode. (a) Current distribution during a 6 kV plasma pulse (Pulse 30924047). (b) Current distribution during a 9 kV plasma pulse (Pulse 40914027). The quiescent period is between the two dark vertical lines.

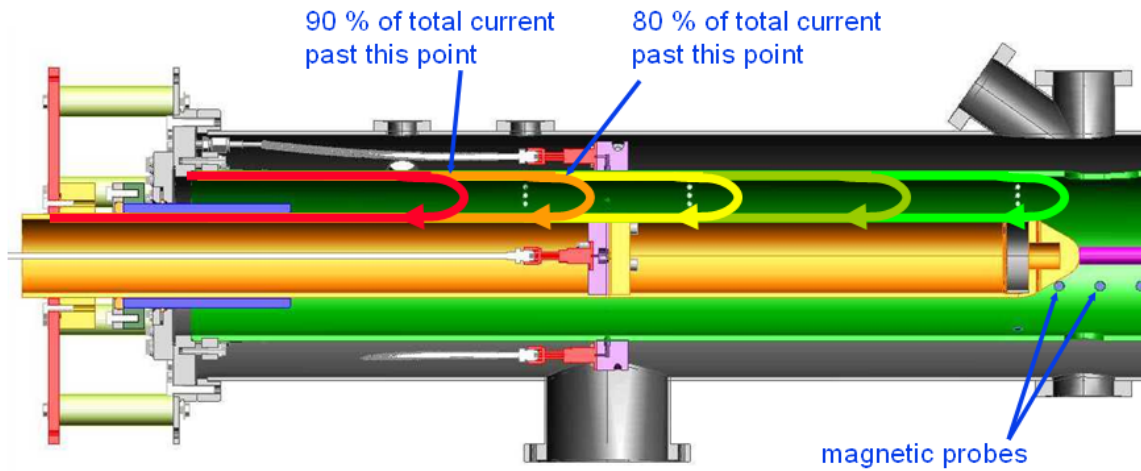


Figure 2.8: The current distribution in the acceleration region can be determined using the magnetic fields measured by the axial array of magnetic probes embedded in the outer electrode. The magnetic field at each probe is used to determine the current past that probe, which is then normalized by the current past the probe located at $z = -120$ cm. The result at each probe is the percentage of the total current that passes a given magnetic probe along the outer electrode and then attaches downstream through the plasma to return along the inner electrode and produce the magnetic field at the probe. The locations of the 90, 80, 70, 60, and 50 % lines are plotted as contours versus time in Figs. 4.16(a)–2.7(b).

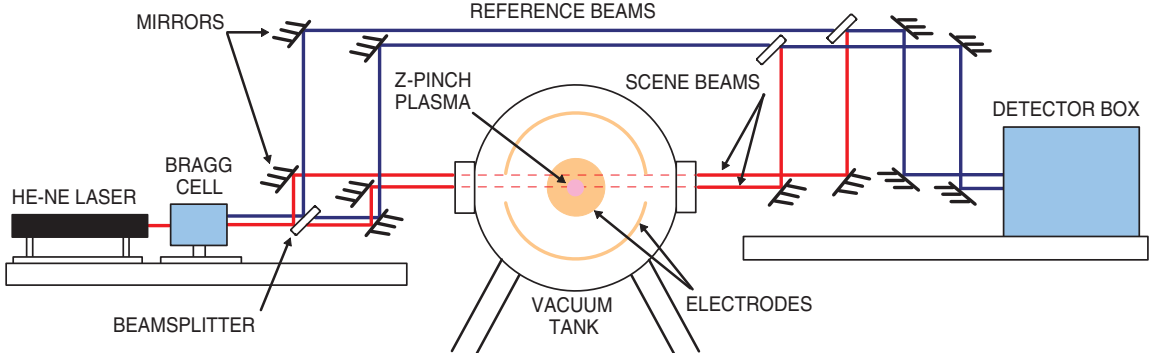


Figure 2.9: He-Ne interferometer optical configuration. The He-Ne laser beam is split by the Bragg cell into scene and reference beams, and 40 MHz is added to the frequency of the reference beam. The scene and reference beams are then split into up to four separate chords (only two are shown). The scene beam for each chord passes through the experiment, while the reference beam does not. The two beams interfere at the detector, allowing the chord integrated electron density along each chord to be obtained from the relative phase shifts of the scene and reference beams.

2.2 He-Ne Interferometer

The He-Ne Interferometer is a multichord, heterodyne, quadrature, Mach-Zehnder interferometer [7, 21]. Parts of the system were inherited from the High Beta-Q Machine at the University of Washington, in Seattle [34]. It is used to make time-dependent, chord-integrated electron density measurements and records density information along two chords at different axial locations or impact parameters.

2.2.1 He-Ne Interferometer Operation

The He-Ne interferometer optical configuration is shown in Fig. 2.9. An approximately 10 mW He-Ne laser with wavelength 632.8 nm is used with the multichord He-Ne interferometer. The He-Ne laser beam is split by a Bragg cell into scene and reference beams, and 40 MHz is added to the frequency of the reference beam. The scene and reference beams are then split into up to four separate chords. The scene beam for each chord passes through the experiment, while the reference beam does not. The two beams interfere at the detector, allowing the chord integrated electron density along each chord to be obtained

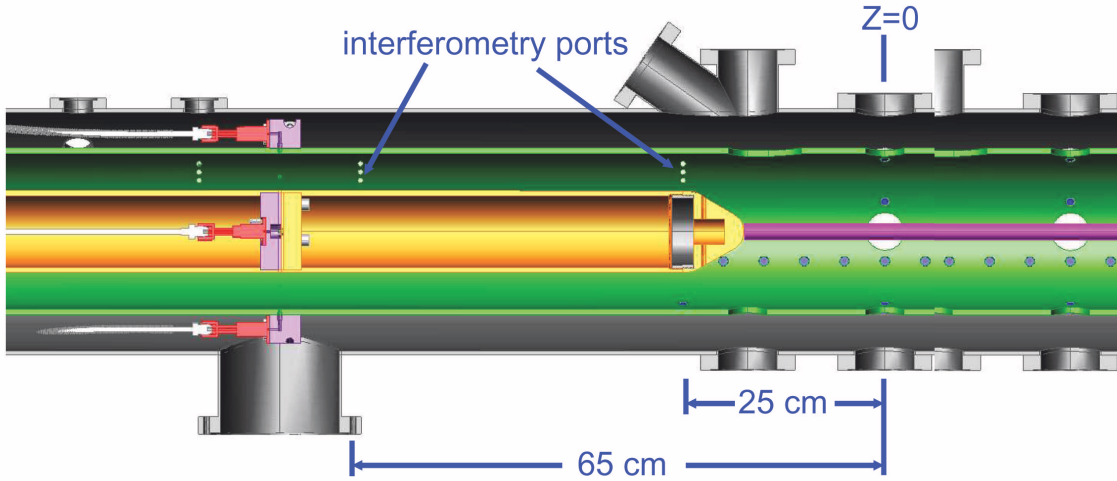


Figure 2.10: Drawing of the ZaP Flow Z-Pinch Experiment showing the axial locations of the interferometer chords used to make measurements in the acceleration region. The interferometer chord located at $z = -25$ cm measures the density near the exit from the acceleration region. The chord located at $z = -65$ cm measures the density just downstream of the gas injection plane.

from the relative phase shifts of the scene and reference beams. The He-Ne interferometer can be positioned with two or more chords at the same axial location and different impact parameters to measure profile information in the assembly region, as in Fig. 2.9. It can also be set up with chords at different axial locations to make measurements in the acceleration region, as shown in Fig. 2.10

The He-Ne interferometer electronics are used to power the Bragg cell, detect and amplify the amplitude of the laser light resulting from the interference of the scene and reference beams, and determine the sine and cosine of the phase shift between the beams due to the plasma. Figure 2.11 is block diagram of the interferometer electronics on a panel in the ZaP experiment's screen room and in a shielded box in the laboratory. A function generator is used in the screen room to generate a sine wave with a frequency of 40 MHz. This reference signal is then amplified and split. Half of the signal is attenuated and used to power the Bragg cell, adding 40 MHz to the frequency of the reference beam. As described later, the other half of the signal is used as a reference signal in measuring the sine and cosine of the

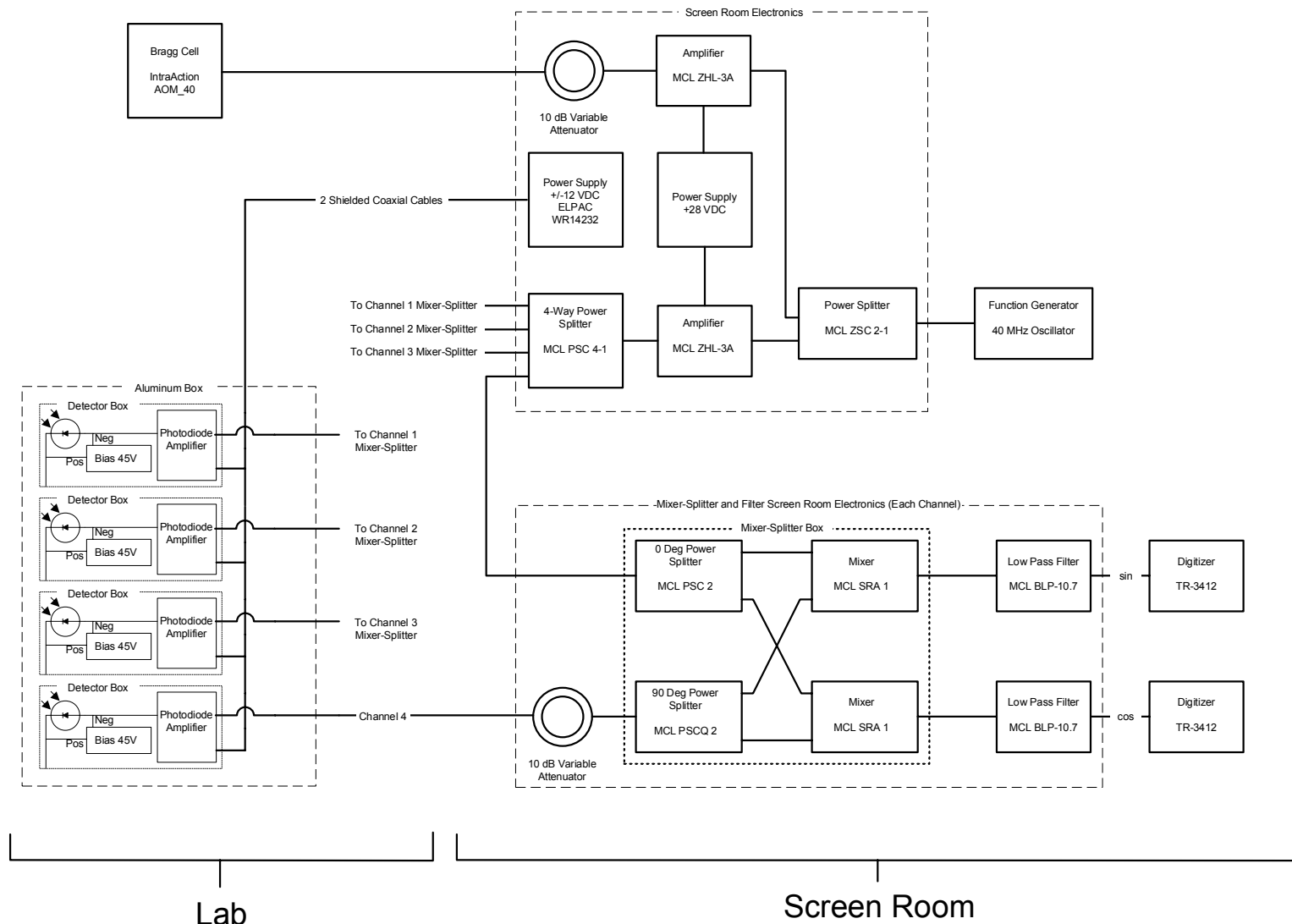


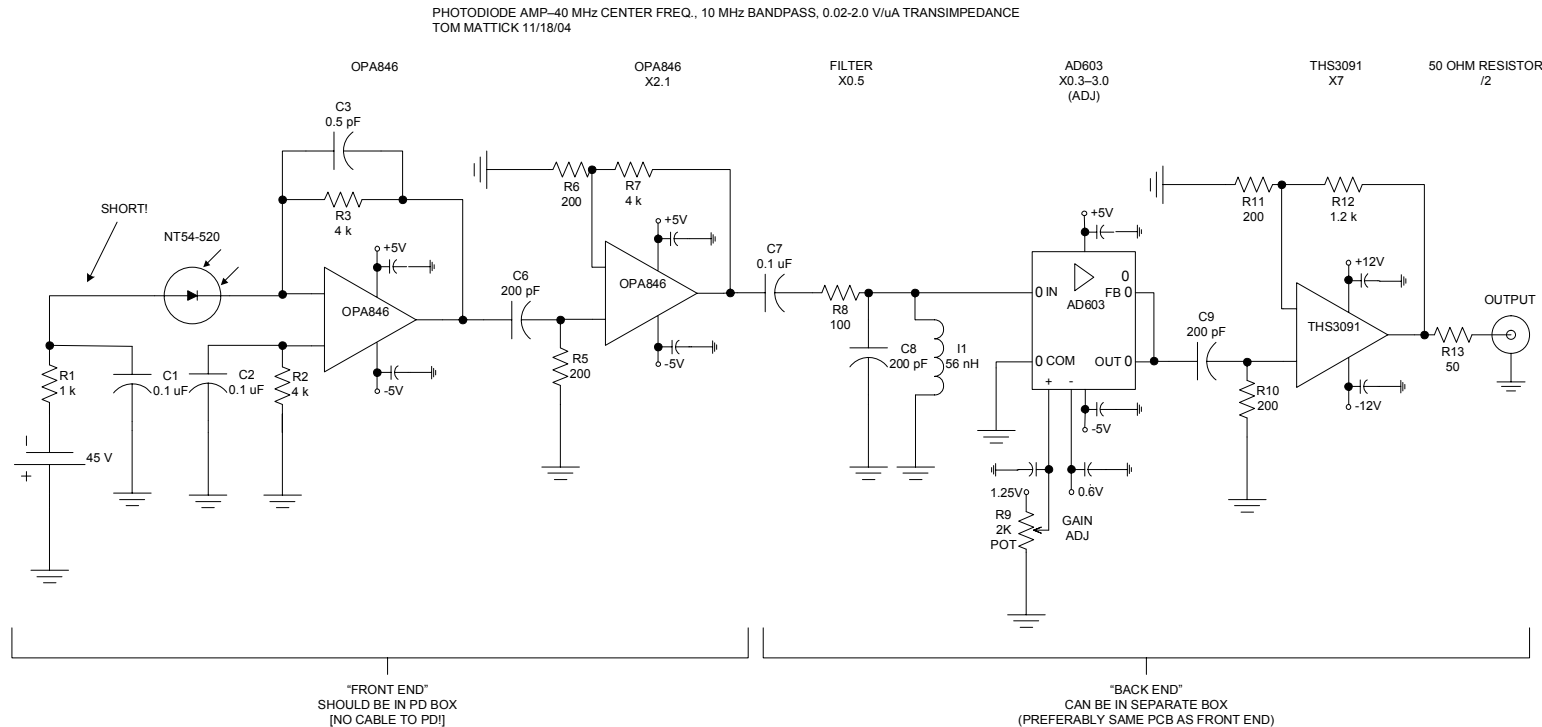
Figure 2.11: Block diagram of the interferometer electronics on a panel in the screen room and in a shielded box in the laboratory.

phase shift.

The vibration of ultrasonic waves in the Bragg cell separates the He-Ne laser beam into zeroth and first order components. The zeroth order beam is likely to be the brighter of the two, so it is used as the scene beam, which may be attenuated on its way through the plasma and the vacuum tank viewports. The Bragg cell vibration adds 40 MHz to the frequency of the first order beam, which becomes the reference beam. The two beams are then split into the separate chords of the interferometer, and the scene and reference beams of each chord are steered together again at a photodiode detector box within the shielded box in the lab.

As shown in Fig. 2.11, the shielded box in the lab contains four photodiode detector boxes for the four chords of He-Ne interferometry. Each detector box contains a photodiode, biasing electronics, and a transimpedance amplifier. Electrical schematics of the photodiode amplifier circuit and its power and bypassing circuit are shown in Figs. 2.12 and 2.13. The photodiode and biasing electronics are also included in the amplifier circuit schematic. The transimpedance amplifier is used to amplify the signal resulting from the interference of the scene and reference beams. The amplifier circuit is designed for low-noise operation with a 35 to 45 MHz bandpass and a gain that is adjustable from 0.02 to 2 V/ μ A at 40 MHz. The amplified signal is then carried by a coaxial cable to the screen room. The cables from all four channels are run together with two power cables inside a copper braid for shielding to a cable tray and then to the screen room.

The amplified signal from the lab is attenuated in the screen room, reducing the influence of electrical noise picked up on its way from the lab. As shown in Fig. 2.14, a 90-degree splitter is used to divide the detector signal into two components. The phase of one component is shifted 90 degrees. The 40 MHz reference signal from the lab is split, but not shifted, by a zero degree splitter and mixed with the two detector signal components. This produces a two signals, one of which is the cosine of the phase shift between the scene and reference beams, and the other of which is the sine of the phase shift between the scene and reference beams. In addition to the sine and cosine components of the phase shift, these two signals also have higher frequency components. Low-pass filters are used to filter out these high-frequency components, leaving the sine and cosine of the phase shift to be recorded by two channels of a Data Design Corporation TR3412 digitizer. An Interactive



GAIN: ADJUSTABLE FROM 0.02-2 V/uA @ 40 MHz
BANDPASS: 3 dB POINTS AT 35 MHz, 45 MHz
NOISE: OUTPUT NOISE VOLTAGE (BROADBAND): 0.05 Vrms (0.25 Vp-p) at full gain [Vn proportional to gain]
OUTPUT: CAN DRIVE UP TO ~5 V INTO 50 OHM LOAD (10 V PEAK-TO-PEAK)
NOTES: USE LIBERAL GROUND PLANE.
BYPASS CAPS ON AMP POWER LEADS SHOULD BE VERY CLOSE TO PINS.
FOLLOW AMP DATA SHEETS FOR RECOMMENDED BYPASS.
FRONT END CAN USE OPA2846 [DUALOPA846].
THIS WILL EASILY FIT ON A 2"X1" PCB. [ALL PARTS ARE SURFACE MOUNT.]

Figure 2.12: Electrical schematic of the interferometer photodiode amplifier circuit. (Design courtesy of Professor Tom Mattick, University of Washington.)

POWER AND BYPASSING FOR PHOTODIODE AMP
TOM MATTICK 11/18/04

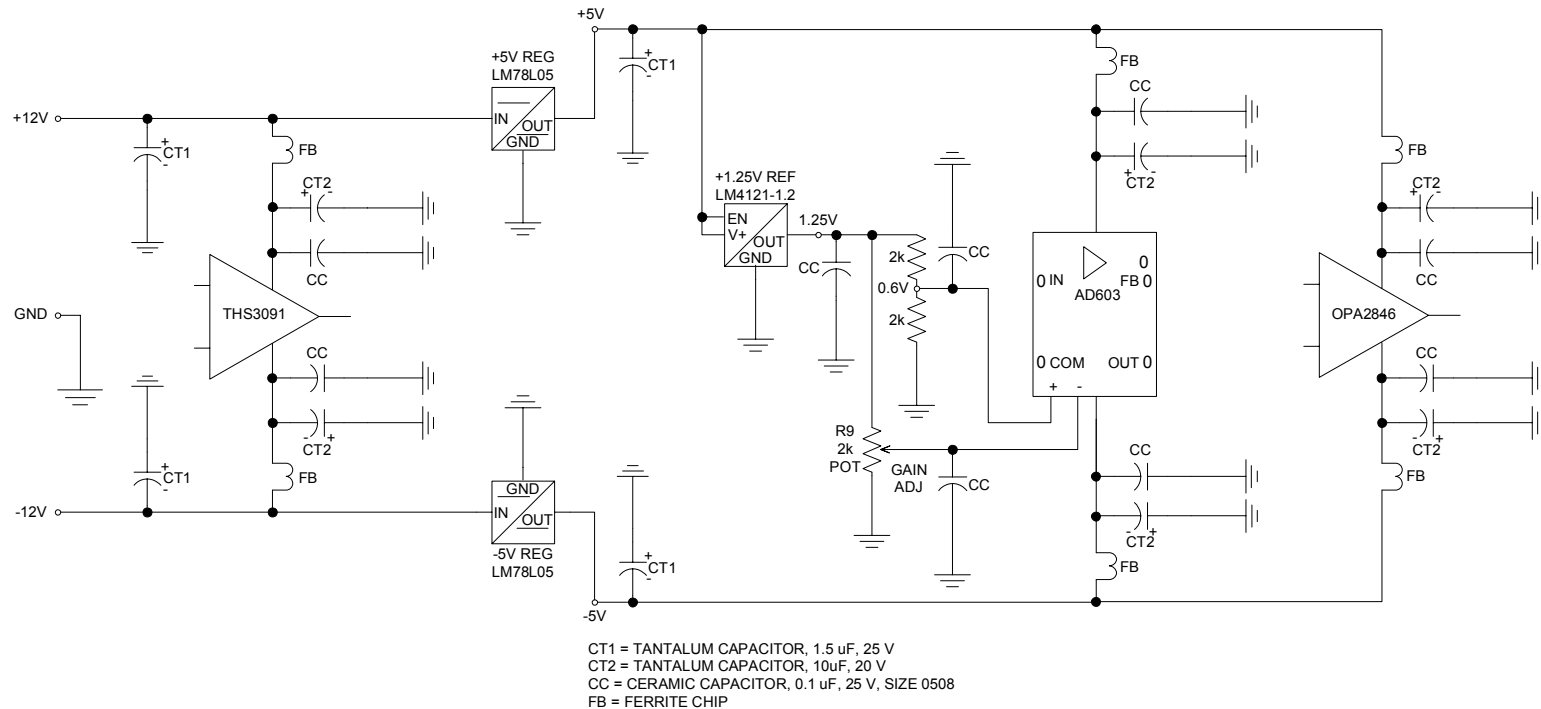


Figure 2.13: Electrical schematic of the interferometer photodiode amplifier's power and bypassing circuit. (Design courtesy of Professor Tom Mattick, University of Washington.)

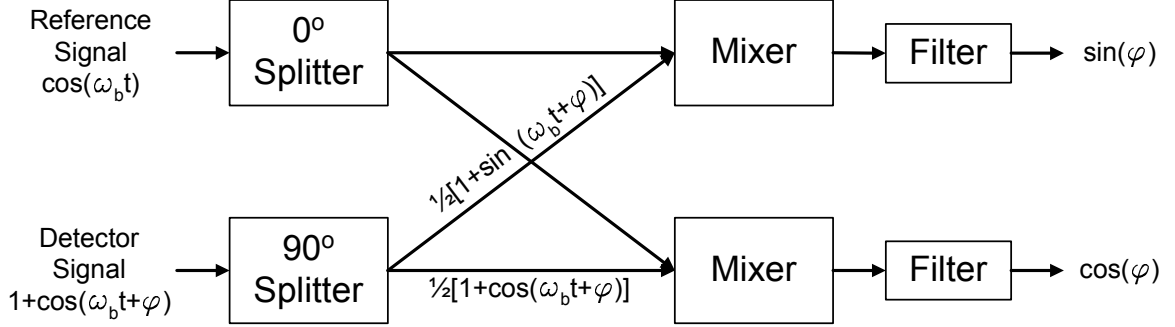


Figure 2.14: Block diagram of mixer-splitter operation. The amplified and attenuated detector signal from the lab is split by a 90° splitter, and each component is mixed with the 40 MHz reference signal. The products are then filtered to remove high-frequency components and isolate the sine and cosine of the phase shift.

Data Language (IDL) procedure *dense_fin.pro*, included in Appendix C, is used to determine the phase shift and the chord-integrated electron number density from the recorded sine and cosine components.

Mathematically, the operation of the He-Ne interferometer is as follows. The scene and reference beam electric fields at the detector are described by

$$u_s = U_s e^{i[\omega_0 t + \Delta\phi(t)]} \quad (2.4)$$

$$u_r = U_r e^{i(\omega_0 + \omega_b)t}, \quad (2.5)$$

where ω_0 is the laser light frequency, ω_b is the reference frequency applied by the Bragg cell ($2\pi \times 40$ MHz), and $\Delta\phi(t)$ is the time-dependent phase shift caused by the electron density of the plasma. The real parts of these fields are given by

$$u_s = U_s \cos [\omega_0 t + \Delta\phi(t)] \quad (2.6)$$

$$u_r = U_r \cos [(\omega_0 + \omega_b)t]. \quad (2.7)$$

The intensity of the two beams when combined at the detector is the square of the sum of

the two fields,

$$I = (u_s + u_r)^2 \quad (2.8)$$

$$\begin{aligned} &= U_s^2 \cos^2 [\omega_0 t + \Delta\phi(t)] \\ &\quad + U_r^2 \cos^2 [(\omega_0 + \omega_b) t] \\ &\quad + 2U_s U_r \cos [\omega_0 t + \Delta\phi(t)] \cos [(\omega_0 + \omega_b) t]. \end{aligned} \quad (2.9)$$

The identity

$$2 \cos \alpha \cos \beta = \cos(\alpha - \beta) + \cos(\alpha + \beta) \quad (2.10)$$

can be used to rearrange the intensity, which becomes

$$I = (u_s + u_r)^2 \quad (2.11)$$

$$\begin{aligned} &= U_s^2 \cos^2 [\omega_0 t + \Delta\phi(t)] \\ &\quad + U_r^2 \cos^2 [(\omega_0 + \omega_b) t] \\ &\quad + U_s U_r \{ \cos [\omega_b t + \Delta\phi(t)] + \cos [(2\omega_0 + \omega_b) t + \Delta\phi(t)] \}. \end{aligned} \quad (2.12)$$

All terms in the previous equation that contain the laser frequency ω_0 are too high-frequency to be correctly measured by the detector and are instead detected as their time-averaged intensities. Terms involving the square of the cosine are time-averaged to one-half their amplitudes, while other, unsquared cosine terms are time-averaged to zero,

$$\cos^2 \alpha \rightarrow \frac{1}{2} \quad (2.13)$$

$$\cos \alpha \rightarrow 0. \quad (2.14)$$

This leaves

$$I = \frac{1}{2} (U_s^2 + U_r^2) + U_s U_r \cos [\omega_b t + \Delta\phi(t)], \quad (2.15)$$

which is the intensity measured by the detector—a sinusoidal function at the reference frequency, ω_b , with a time-dependent phase shift, $\Delta\phi(t)$, due to the plasma electron density. This signal is amplified and sent through the shielded cable to the screen room electronics.

In the screen room, the amplified signal from the detector box is attenuated and then split by a 90° splitter into two components, $\pi/2$ radians out of phase, to eliminate what

would otherwise cause a sign ambiguity as the phase passes through $\pm\pi$ radians,

$$A_c = \frac{1}{4} (U_s^2 + U_r^2) + \frac{1}{2} U_s U_r \cos [\omega_b + \Delta\phi(t)] \quad (2.16)$$

$$A_s = \frac{1}{4} (U_s^2 + U_r^2) + \frac{1}{2} U_s U_r \cos [\omega_b + \Delta\phi(t) - \pi/2] \quad (2.17)$$

$$= \frac{1}{4} (U_s^2 + U_r^2) + \frac{1}{2} U_s U_r \sin [\omega_b + \Delta\phi(t)], \quad (2.18)$$

where the constant scale factors associated with amplifying and attenuating the signal have been neglected. The 40-MHz reference signal that also went to the Bragg cell is amplified and then split by a 0° splitter into two components, each described by

$$A_b = \frac{1}{2} U_b \cos (\omega_b t). \quad (2.19)$$

A mixer is used to multiply each part of the split reference signal by one of the detector signal components. Figures 2.15(a)–2.15(d) show the splitter input signals—the reference signal and the detector signal—and the resulting mixer outputs. The 40 MHz reference signal frequency is visible in all of the signals. Figures 2.16(a)–2.16(d) show the splitter inputs and mixer outputs recorded over a longer time interval. The lower-frequency influence of the phase shift is visible in the silhouettes of the detector signal and mixer outputs. The signals shown were not obtained during a plasma pulse, so the phase shift in this case is due to vibration of the interferometer optics, instead of the plasma electron density. This vibration occurs over a time interval (4 ms) that is much longer than the plasma pulse (100 μ s). It is accounted for in the IDL procedure used to obtain the chord-integrated density by subtracting a high-order polynomial baseline from the measured phase shift. For the present discussion of interferometer operation, however, it serves as a substitute for the phase shift

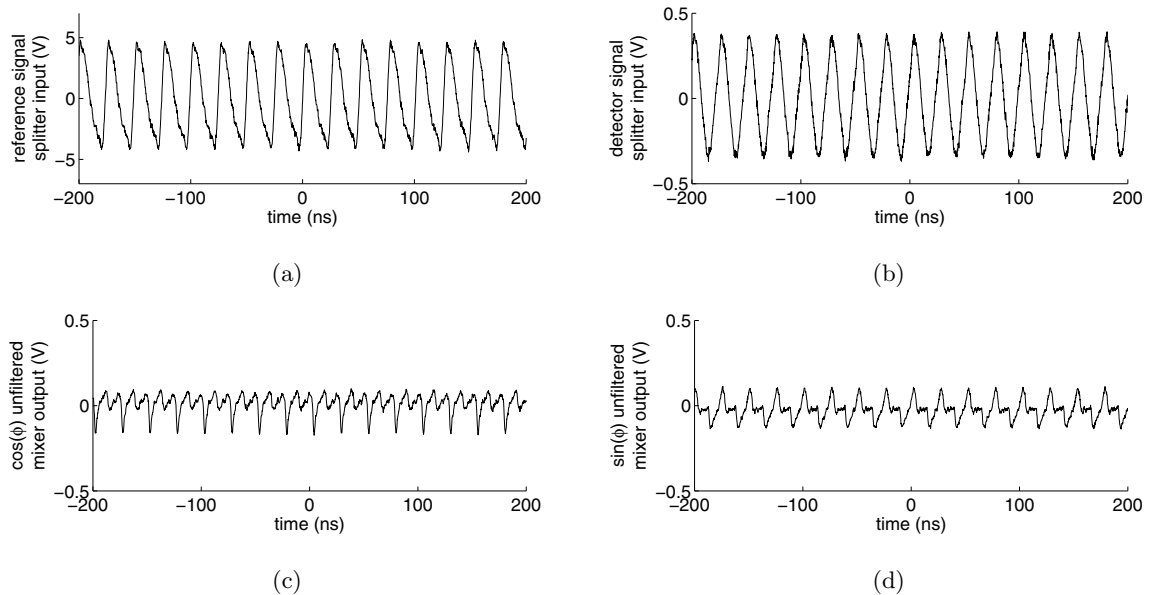


Figure 2.15: Mixer-splitter input and output signals over a short time interval, with the 40-MHz reference signal frequency apparent in the waveforms of all four signals. (a) 40-MHz reference signal splitter input. (b) Detector signal splitter input. (c) Unfiltered cosine component of the phase shift mixer output. (d) Unfiltered sine component of the phase mixer output.

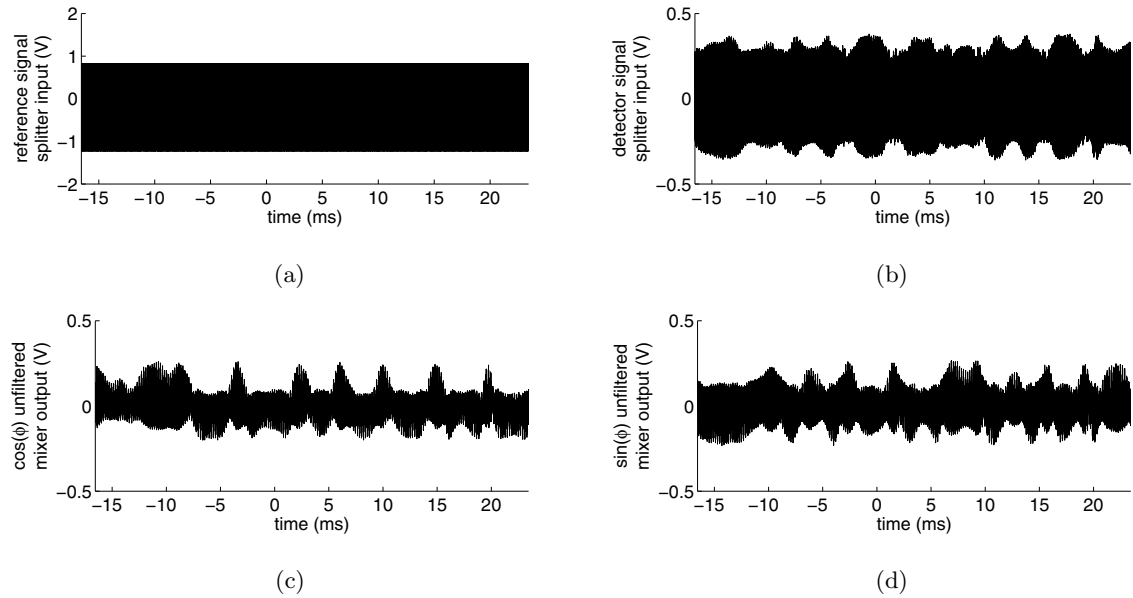


Figure 2.16: Mixer-splitter input and output signals over a longer time interval, with the influence of the phase shift visible in the silhouettes of some signals. (a) 40 MHz reference signal splitter input. (b) Detector signal splitter input. (c) Unfiltered cosine component of the phase shift mixer output. (d) Unfiltered sine component of the phase mixer output.

caused by the plasma density. The products of the mixers are

$$A_{\cos \Delta\phi} = A_c A_b \quad (2.20)$$

$$= \left\{ \frac{1}{4} (U_s^2 + U_r^2) + \frac{1}{2} U_s U_r \cos [\omega_b + \Delta\phi(t)] \right\} \left\{ \frac{1}{2} U_b \cos (\omega_b t) \right\} \quad (2.21)$$

$$= \frac{1}{8} (U_s^2 + U_r^2) U_b \cos (\omega_b t) + \frac{1}{4} U_s U_r U_b \cos [\omega_b t + \Delta\phi(t)] \cos (\omega_b t) \quad (2.22)$$

$$A_{\sin \Delta\phi} = A_s A_b \quad (2.23)$$

$$= \left\{ \frac{1}{4} (U_s^2 + U_r^2) + \frac{1}{2} U_s U_r \sin [\omega_b + \Delta\phi(t)] \right\} \left\{ \frac{1}{2} U_b \cos (\omega_b t) \right\} \quad (2.24)$$

$$= \frac{1}{8} (U_s^2 + U_r^2) U_b \cos (\omega_b t) + \frac{1}{4} U_s U_r U_b \sin [\omega_b t + \Delta\phi(t)] \cos (\omega_b t). \quad (2.25)$$

These can be rewritten using the trigonometric identity described above and the trigonometric identity

$$2 \sin \alpha \cos \beta = \sin (\alpha + \beta) + \sin (\alpha - \beta) \quad (2.26)$$

to contain terms that depend solely on the phase,

$$A_{\cos \Delta\phi} = \frac{1}{8} (U_s^2 + U_r^2) U_b \cos (\omega_b t) \quad (2.27)$$

$$+ \frac{1}{8} U_s U_r U_b \{ \cos [\Delta\phi(t)] + \cos [2\omega_b t + \Delta\phi(t)] \} \quad (2.28)$$

$$A_{\sin \Delta\phi} = \frac{1}{8} (U_s^2 + U_r^2) U_b \cos (\omega_b t) \quad (2.29)$$

$$+ \frac{1}{8} U_s U_r U_b \{ \sin [\Delta\phi(t)] + \cos [2\omega_b t + \Delta\phi(t)] \}. \quad (2.30)$$

Both mixer signals are filtered by 10 MHz low pass filters to remove the components at one and two times the 40 MHz reference signal frequency. The time-averaged value of these components is zero, leaving two signals that depend only on the sine and cosine of the phase,

$$A_{\cos \Delta\phi} = \frac{1}{8} U_s U_r U_b \cos [\Delta\phi(t)] \quad (2.31)$$

$$A_{\sin \Delta\phi} = \frac{1}{8} U_s U_r U_b \sin [\Delta\phi(t)]. \quad (2.32)$$

Elimination of the extraneous high-frequency components and isolation of the sine and cosine components of the phase shift by the low pass filters is evident in the unfiltered and filtered

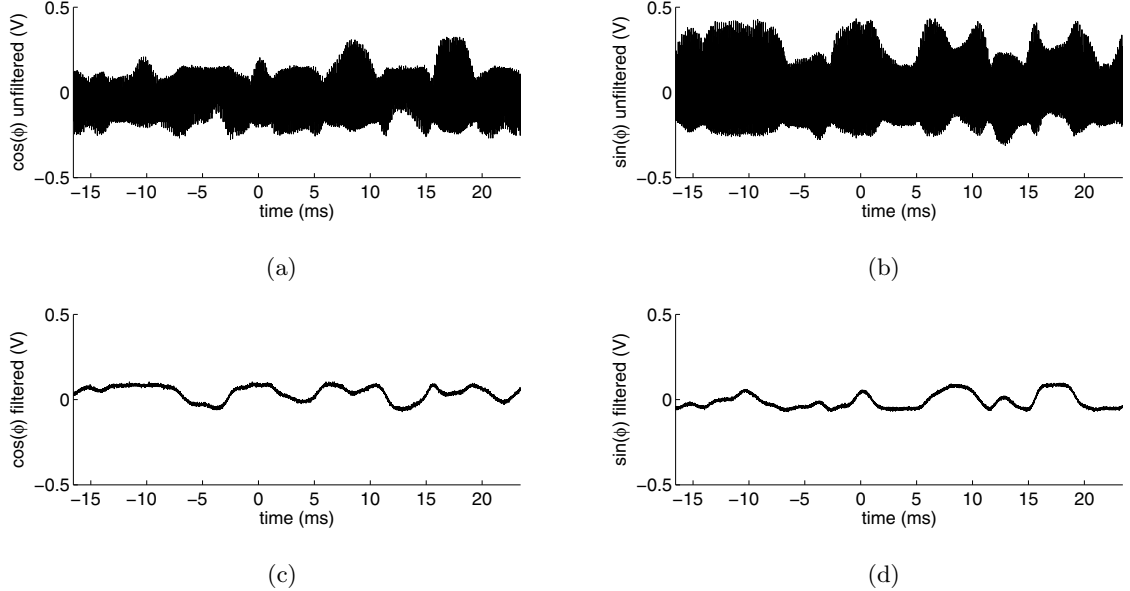


Figure 2.17: Mixer-splitter output signals before and after the 10 MHz low-pass filter. (a) Unfiltered mixer output signal containing high-frequency components in addition to a low-frequency term that depends on the cosine of the phase shift. (b) Unfiltered mixer output signal containing high-frequency components in addition to a low-frequency term that depends on the sine of the phase shift. (c) Mixer output signal after the high-frequency components have been removed by the low-pass filter, leaving the cosine of the phase shift. (d) Mixer output signal after the high-frequency components have been removed by the low-pass filter, leaving the sine of the phase shift.

mixer outputs shown in Figures 2.17(a)–2.17(d). The sine and cosine components can be plotted as a circular Lissajous curve that is useful when aligning the interferometer and running the experiment. In polar coordinates, the radius of the Lissajous curve corresponds to the amplitude of the filtered signals, and the angle of each Lissajous point is the relative phase shift measured by the interferometer. The radius remains relatively constant as the angle varies with the phase shift over time. A typical Lissajous curve is plotted in Fig. 2.18(a). When the adjustable detector gain is too high, artifacts in the filtered mixer outputs are often visible in the shape of the Lissajous, which can become diamond-shaped or have a variable radius. Figure 2.18(b) is an example of a Lissajous indicating that the detector gain is too high.

After the filters, the sine and cosine components of the phase shift are digitized, and the

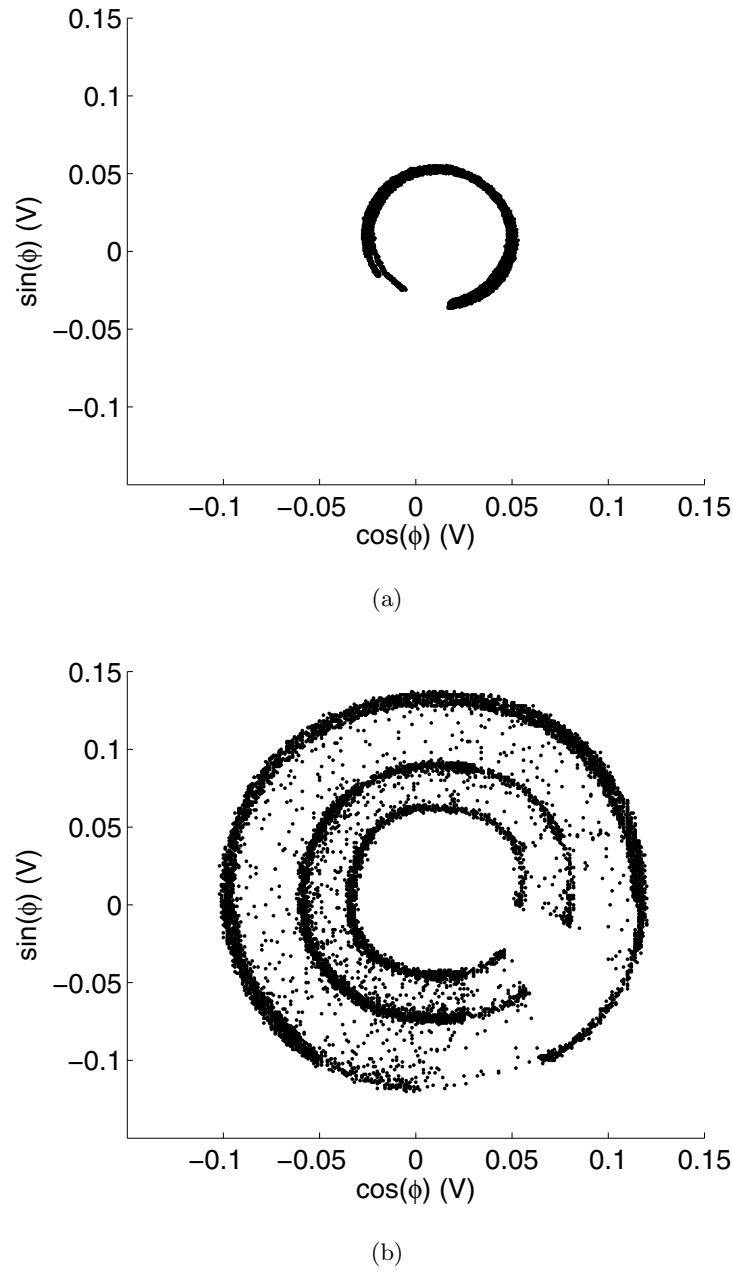


Figure 2.18: Lissajous curves that result when the sine and cosine components of the phase are plotted against one another. (a) Typical Lissajous curve. (b) Distorted Lissajous curve indicating that the detector gain is set too high.

phase shift is found in the IDL procedure mentioned above by taking the arctangent of the quotient of the two signals,

$$\Delta\phi(t) = \arctan\left(\frac{A_{\sin\phi}}{A_{\cos\phi}}\right) \quad (2.33)$$

$$= \frac{\frac{1}{8}U_sU_rU_b \sin[\Delta\phi(t)]}{\frac{1}{8}U_sU_rU_b \cos[\Delta\phi(t)]}. \quad (2.34)$$

Figure 2.19(a) shows the sine and cosine components of the phase shift, digitized during an actual plasma pulse. In finding the phase shift, the IDL procedure must also adjust the offsets of the sine and cosine signals and correct any fringe jumps. It can also be set to apply a minus sign to the sine component of the phase shift if the 40 MHz reference signal is connected to the 90° splitter instead of the detector signal. This phase shift (in radians) is then converted to the chord-integrated density using the result of Eq. 4.2 in Ref. [28],

$$\int n_e(t) dl(t) = 5.61 \times 10^{20} \Delta\phi(t) \text{ [m}^{-2}\text]}, \quad (2.35)$$

which assumes the plasma density is small compared to the cutoff density, $n_e \ll n_c$, an appropriate assumption in this case [18]. The cutoff density is given by

$$n_c \equiv \left(\frac{2\pi c}{\lambda}\right)^2 \frac{m_e \epsilon_0}{e^2}, \quad (2.36)$$

where c is the speed of light, λ is the laser wavelength, m_e is the electron mass, ϵ_0 is the permittivity of free space, and e is the elementary charge. Figure 2.19(b) is the chord-integrated electron density obtained during a plasma pulse using the sine and cosine signals of Fig. 2.19(a).

2.2.2 He-Ne Interferometer Results

The multichord He-Ne interferometer was used to record the time evolution of the chord-integrated electron number density in the experiment at various axial locations and impact parameters. During the quiescent period, a highly pinched plasma is observed at or near the axis of the experiment, and lower density is observed off-axis, as shown in Figs. 2.20(a) and 2.20(b) for a 6 kV hydrogen plasma pulse. In this case, two chords of interferometry were used, both located at axial location $z = 0$ cm, but at different impact parameters. One

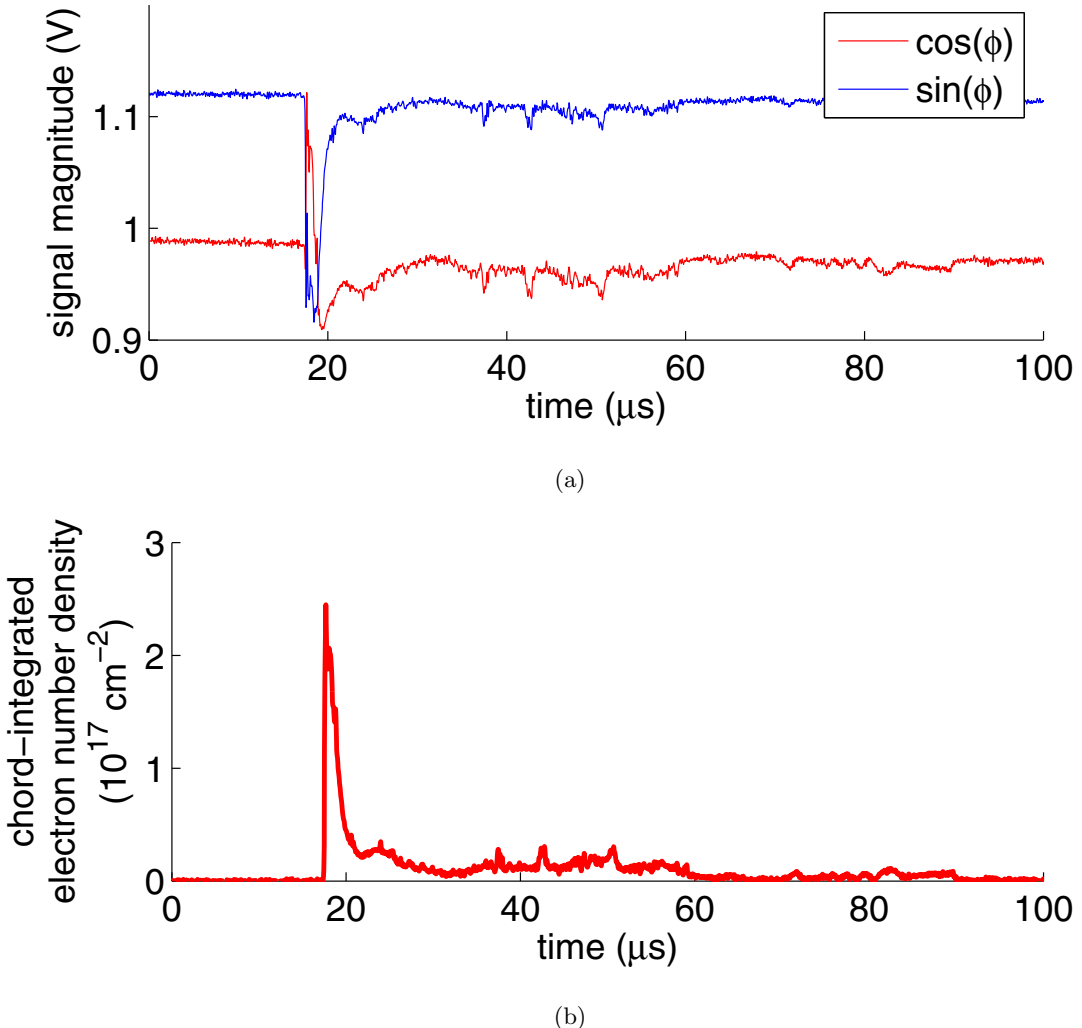


Figure 2.19: Determination of the chord-integrated electron density during a plasma pulse. (a) Digitized cosine and sine of the phase shift. (b) Chord-integrated electron density obtained by applying the IDL procedure *dense_fin.pro* to the digitized sine and cosine of the phase shift (Pulse 30924047).

chord passes through the center of the cylindrical assembly region containing the Z-pinch, at impact parameter $y = 0$ cm. The second is located slightly off-axis, at impact parameter $y = 2.5$ cm. The arrival of the plasma at $z = 0$ cm is indicated by the high electron number density along both chords beginning at $23 \mu\text{s}$. The presence of a dense Z-pinch is indicated by the drop in the off-axis density measured at $y = 2.5$ cm and the concurrent rise in the density measured by the on-axis chord at $y = 0$ cm that occurs near the beginning of the quiescent period. This density difference persists throughout the quiescent period, indicating the presence of a dense Z-pinch at or near the axis of the experiment during the quiescent period.

Figures 2.21(a) and 2.21(b) show the normalized $m = 1$ mode, total plasma current, and chord-integrated density along two chords at $z = 0$ and $y = 0$ and 2.0 cm. The density is high along both chords as the plasma arrives, as in the 6 kV case. With the higher capacitor bank voltage, however, the separation between the two chords is not as well-correlated with the beginning and end of the quiescent period.

Figure 2.22 shows the correlation between the quiescent period and the period of time during which a dense Z-pinch is observed on the axis of the experiment. In this case, the dense Z-pinch period begins when the chord-integrated density measured by the on-axis interferometer chord is twice that measured by the off-axis chord. It ends when the density along both chords drops. Because the chord-integrated density along the two chords is nearly uniform during the arrival of the current sheet and formation of the Z-pinch (see Fig. 2.20(b)), the dense Z-pinch period begins well after the arrival of the current sheet. The lengths of the quiescent period and the dense Z-pinch period decrease with increasing capacitor bank voltage. Both are so short at 9 kV that they are difficult to reliably determine.

Interferometer chords positioned at $z = 61$ cm and impact parameters $y = 0$ and $y = 2.1$ cm show the time evolution of the density profile farther downstream in the assembly region, near the outer electrode end wall. Figures 2.23(a) and 2.23(b) show the normalized $m = 1$ mode at $z = 0$, total plasma current, and chord-integrated electron density measured along two chords at $z = 61$ cm during a 6 kV hydrogen plasma pulse. The quiescent period measured by the $z = 0$ azimuthal magnetic probe array is indicated in both figures.

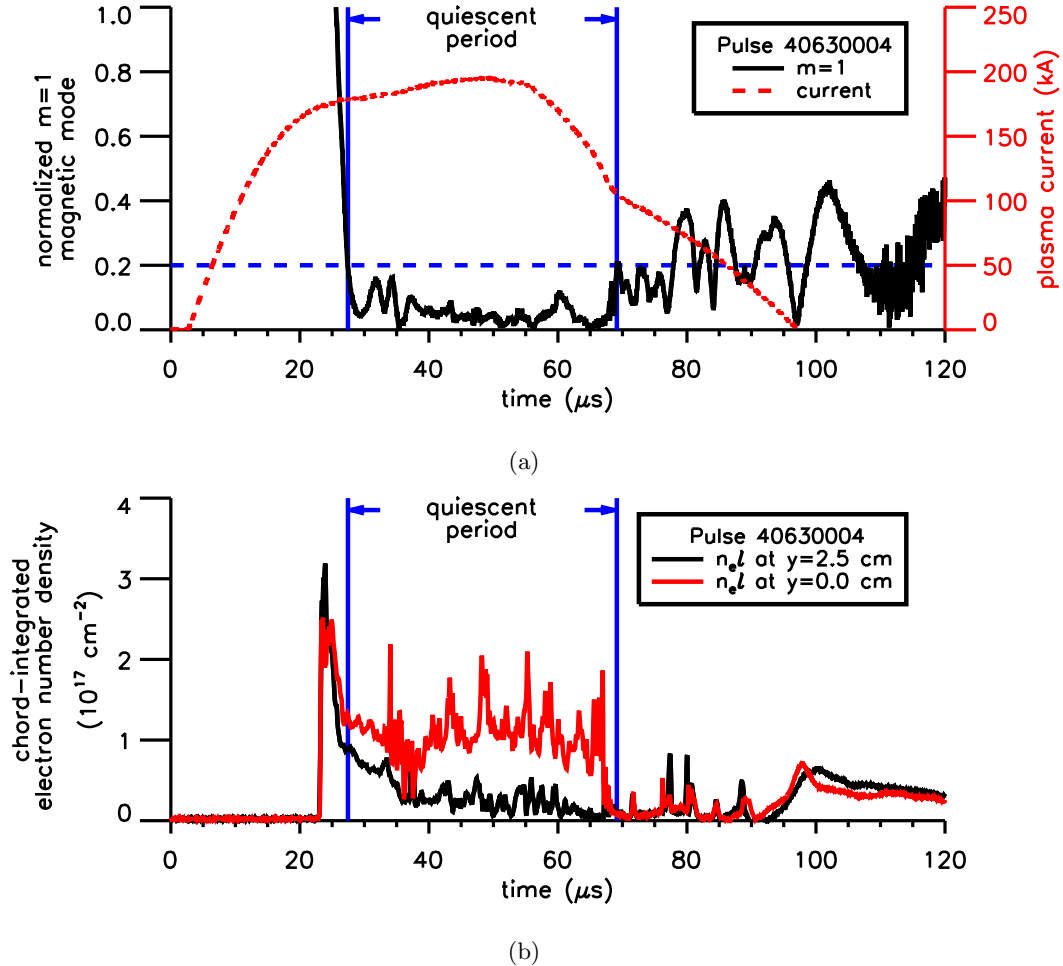


Figure 2.20: (a) Normalized $m = 1$ mode at $z = 0$ and total plasma current for a 6 kV ZaP plasma pulse with hydrogen as the working gas. Magnetic mode activity is low during the quiescent period, which extends from 27 μ s to 68 μ s. (b) Chord-integrated electron number density measured at $z = 0$ and two impact parameters. One chord passes through the center of the cylindrical assembly region containing the Z-pinch. The other is located 2.5 cm above the center of the assembly region. Both chords are perpendicular to the axis of the assembly region. The difference between the measurements at the two locations indicates the presence of a highly pinched plasma at or near the axis of the experiment during the quiescent period (Pulse 40630004).

The chord-integrated density along both chords is high from the time the plasma arrives at $z = 61$ cm to well after the end of the quiescent period at $z = 0$ cm. Similar behavior is observed for the 9 kV hydrogen plasma pulse in Figs. 2.24(a) and 2.24(b).

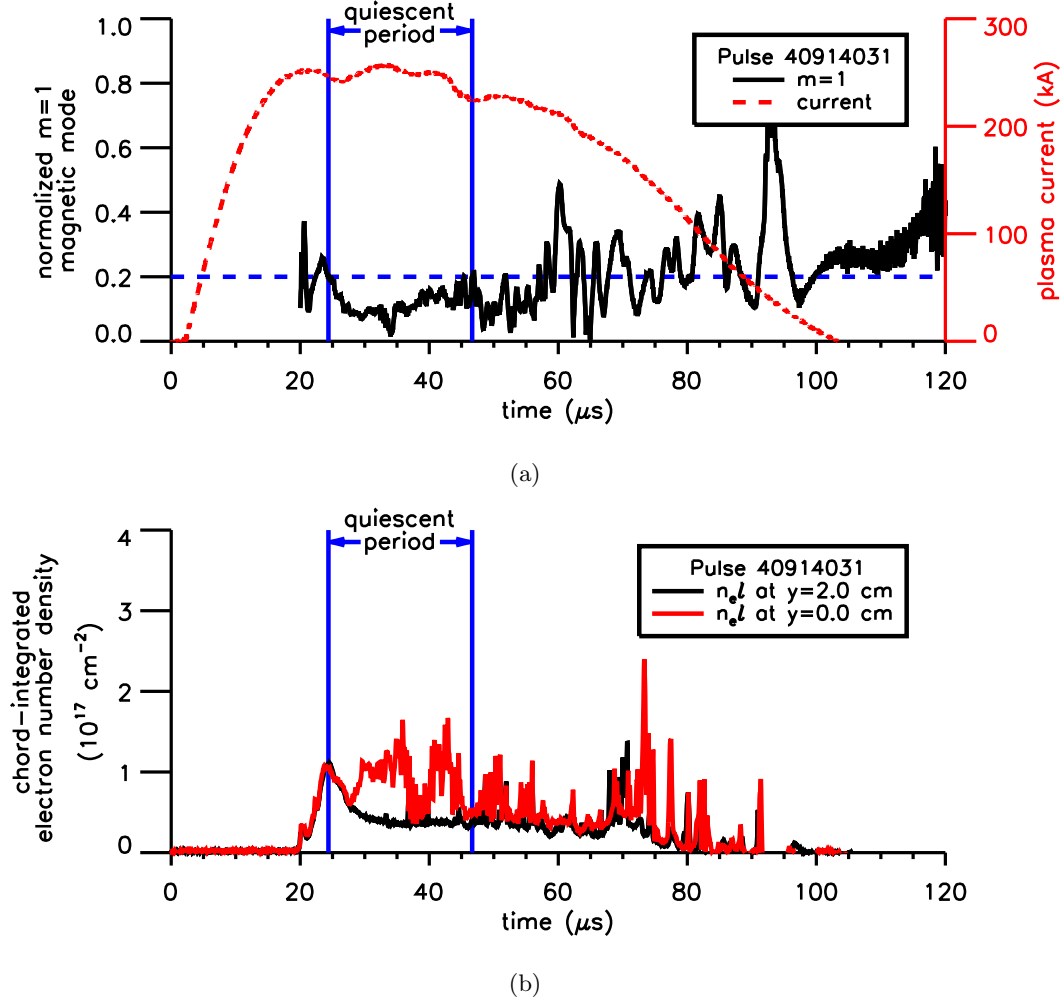


Figure 2.21: (a) Normalized $m = 1$ mode at $z = 0$ and total plasma current for a 9 kV hydrogen plasma pulse. (b) Chord-integrated electron number density measured at $z = 0$ and $y = 0$ and 2.0 cm (Pulse 40914031).

Interferometer measurements also show the acceleration of plasma along the electrodes in the acceleration region towards the assembly region during formation of the Z-pinch. Fig. 2.25(a) shows the normalized $m = 1$ mode and plasma current for the plasma pulse whose chord-integrated electron number density is shown in Fig. 2.25(b). As shown in Fig. 2.10, one interferometer chord measures the density near the exit from the acceleration region, while the other is located just downstream of the gas injection plane. Figures 2.26(a)

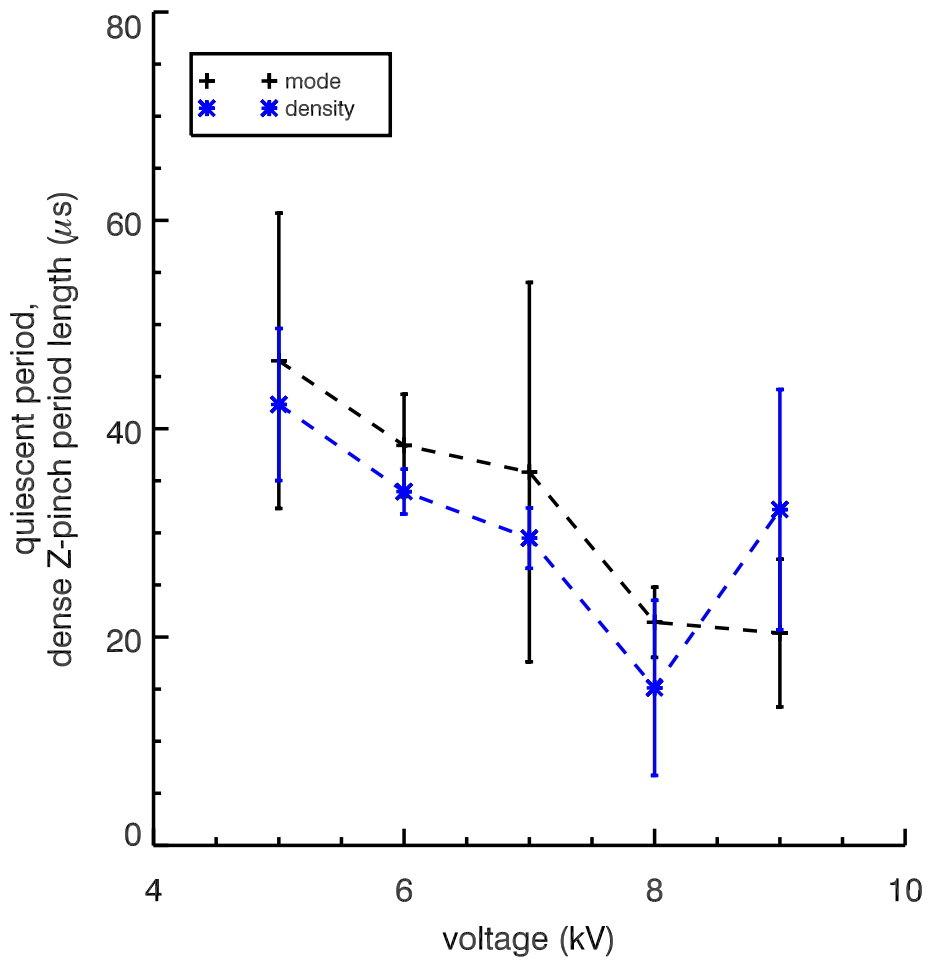


Figure 2.22: The length of the quiescent period decreases with increasing capacitor bank voltage. The quiescent period is highly correlated with the time period during which a dense Z-pinch is observed on the axis of the experiment.

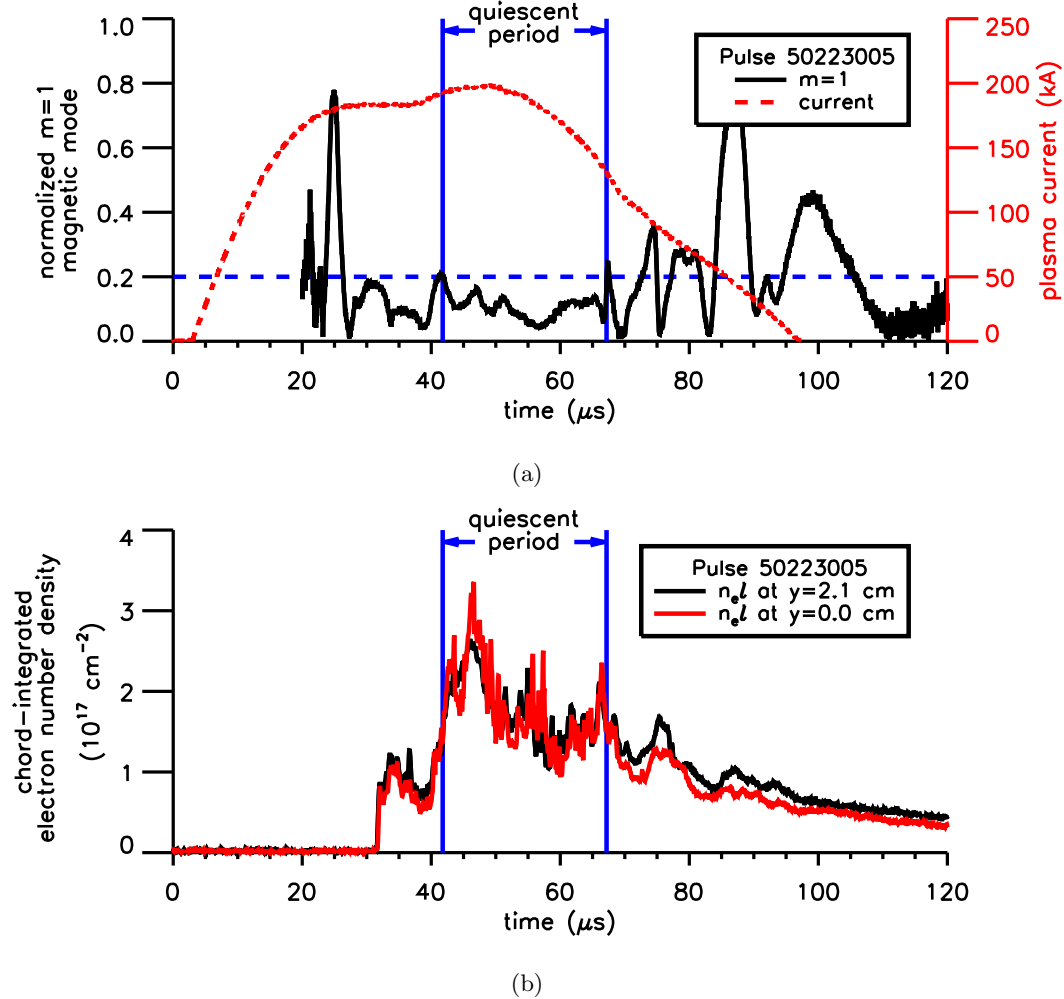


Figure 2.23: (a) Normalized $m = 1$ mode at $z = 0 \text{ cm}$ and total plasma current for a 6 kV hydrogen plasma pulse. (b) Chord-integrated electron number density measured at $z = 61 \text{ cm}$ and two impact parameters. One chord passes through the center of the cylindrical assembly region containing the Z-pinch. The other is located 2.1 cm above the center of the assembly region. Both chords are perpendicular to the axis of the assembly region. The chord-integrated density along both chords is high from the time the plasma arrives at $z = 61 \text{ cm}$ to well after the end of the quiescent period at $z = 0$ (Pulse 50223005).

and 2.26(b) show similar measurements made during a 9 kV hydrogen plasma pulse.

Just prior to a plasma pulse, hydrogen gas is injected by nine gas valves located at the gas injection plane. One valve injects gas through eight channels in the inner electrode, and the other eight valves inject gas through holes in the outer electrode. When the voltage is

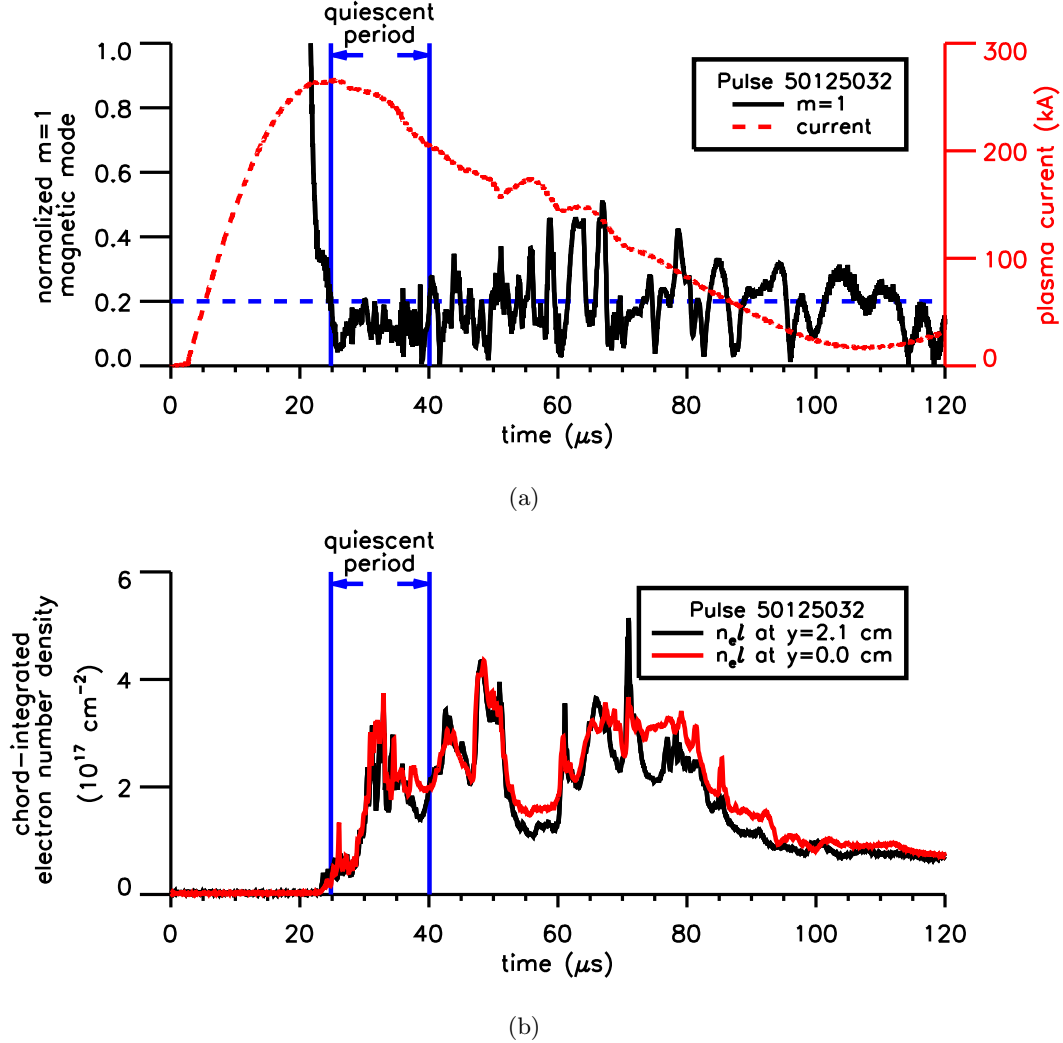


Figure 2.24: (a) Normalized $m = 1$ mode at $z = 0$ cm and total plasma current for a 9 kV hydrogen plasma pulse. (b) Chord-integrated electron number density measured at $z = 61$ cm and $y = 0$ and 2.1 cm (Pulse 50125032).

applied to the electrodes, this gas is ionized, forming a plasma that is accelerated along the electrodes by the Lorentz force, towards the assembly region [13]. The sharp rise in density measured by both chords occurs as the current sheet passes first the chord closer to the gas injection plane and then the chord at the exit of the accelerator. Both interferometer chords show the continued presence of plasma in the accelerator throughout the quiescent period, indicating that gas is being ionized and accelerated from the acceleration region

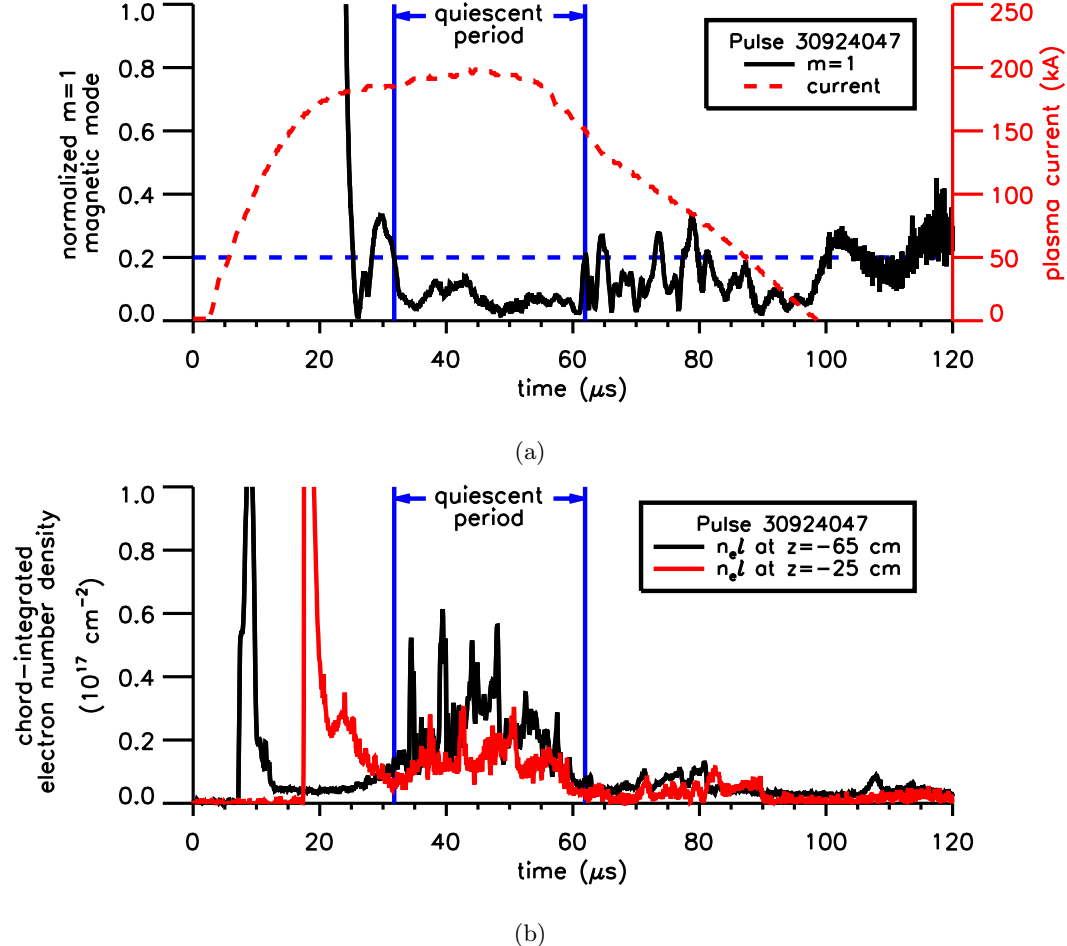


Figure 2.25: (a) Normalized $m = 1$ mode and total plasma current for a 6 kV hydrogen plasma pulse. (b) Chord-integrated electron number density measured at two axial locations. The interferometer chord located at $z = -25 \text{ cm}$ measures the density near the exit from the acceleration region. The chord located at $z = -65 \text{ cm}$ measures the density just downstream of the gas injection plane. The difference in arrival times of the plasma at the two axial locations indicates acceleration of plasma along the electrodes in the acceleration region towards the assembly region. The end of the quiescent period is correlated with the exhaustion of plasma in the accelerator (Pulse 30924047).

into the assembly region, maintaining the flow in the Z-pinch. Depletion of plasma in the acceleration region corresponds to the onset of large mode fluctuations and the end of the quiescent period.

The helium-neon interferometer was positioned at axial location $z = 0$ and impact pa-

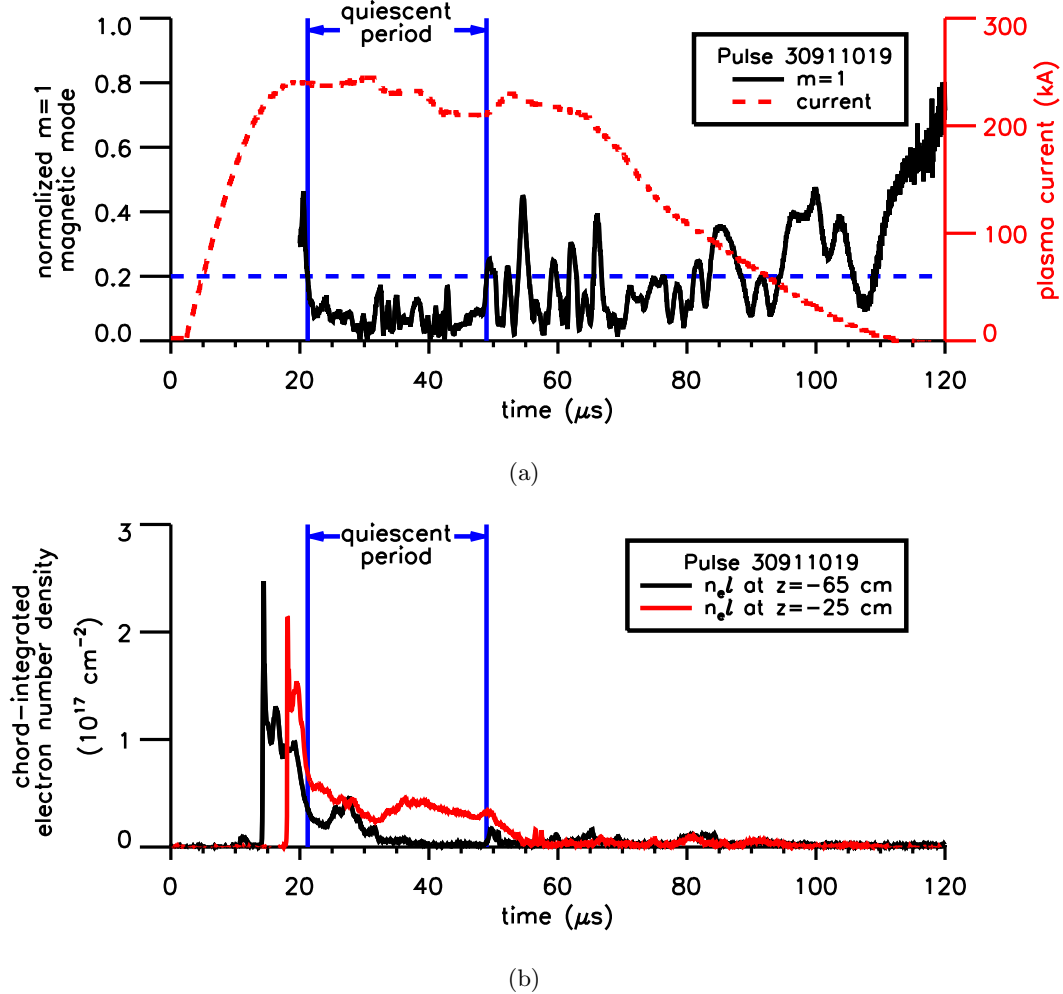


Figure 2.26: (a) Normalized $m = 1$ mode and total plasma current for a 9 kV hydrogen plasma pulse. (b) Chord-integrated electron number density measured at $z = -25 \text{ cm}$ and $z = -65 \text{ cm}$ (Pulse 30911019).

rameters $y = 0$ and $y = -1.5 \text{ cm}$ during a density profile investigation conducted with the holographic interferometer positioned at the same axial location. To avoid the holographic interferometer optics, the beams of the He-Ne interferometer were aligned to pass through the vacuum tank at a slight diagonal in the horizontal (x - z) plane. The time evolution of the chord-integrated electron number density at the midplane of a 50 cm-long helium Z-pinch was studied with the He-Ne interferometer during the investigation. A capacitor bank voltage of 9 kV was used for the pulses. The two-chord He-Ne interferometer measure-

ments shown in Figs. 2.27(b), 2.28(b), and 2.29(b) correspond to holographic interferometer measurements made during arrival and formation of the Z-pinch. The corresponding normalized $m = 1$ mode, total plasma current, and holography laser monitor are plotted in Figs. 2.27(a), 2.28(a), and 2.29(a) for each pulse. The holography laser monitor in the figures shows when each interferogram was made. The chord-integrated electron density is approximately the same at $y = 0$ cm and $y = -1.5$ cm during arrival and late formation, when the interferograms of Pulses 30205010 and 30205018 were made. It is higher at $y = 0$ cm during early formation, corresponding to the peaked profile obtained from the interferogram of Pulse 30205014.

Figures 2.30(a)–2.32(b) show the normalized $m = 1$ mode, plasma current, holography laser monitor, and chord-integrated electron number density from the two-chord He-Ne interferometer for helium plasma pulses used to study the density profile during and after the quiescent period. The chord-integrated electron density measured at $y = 0$ cm is much higher than that measured at $y = -1.5$ cm during the middle of the quiescent period, when the interferogram of Pulse 30204007 was made. Later in the quiescent period, when the interferogram of Pulse 30204019 was made, the value of the chord-integrated density at $y = 0$ drops, leading to a less-peaked density profile. The interferogram of Pulse 30204021 was made after the quiescent period, when the chord-integrated density at both $y = 0$ cm and $y = -1.5$ cm is low. The decrease in the peak of the density profile late in the quiescent period is typically sharper for helium than for hydrogen or hydrogen/methane.

2.3 Holographic Interferometer

The holographic interferometer uses the expanded beam of a pulsed ruby laser to make a single-time measurement of the electron number density, in the form of a holographic interferogram [19]. It produces a two-dimensional map of the chord-integrated electron density, as opposed to a single-point measurement. An Abel inversion is used to determine the radial electron density profile based on the chord-integrated electron density. Holographic interferograms are made at different times on successive plasma pulses to study the time evolution of the density profile.

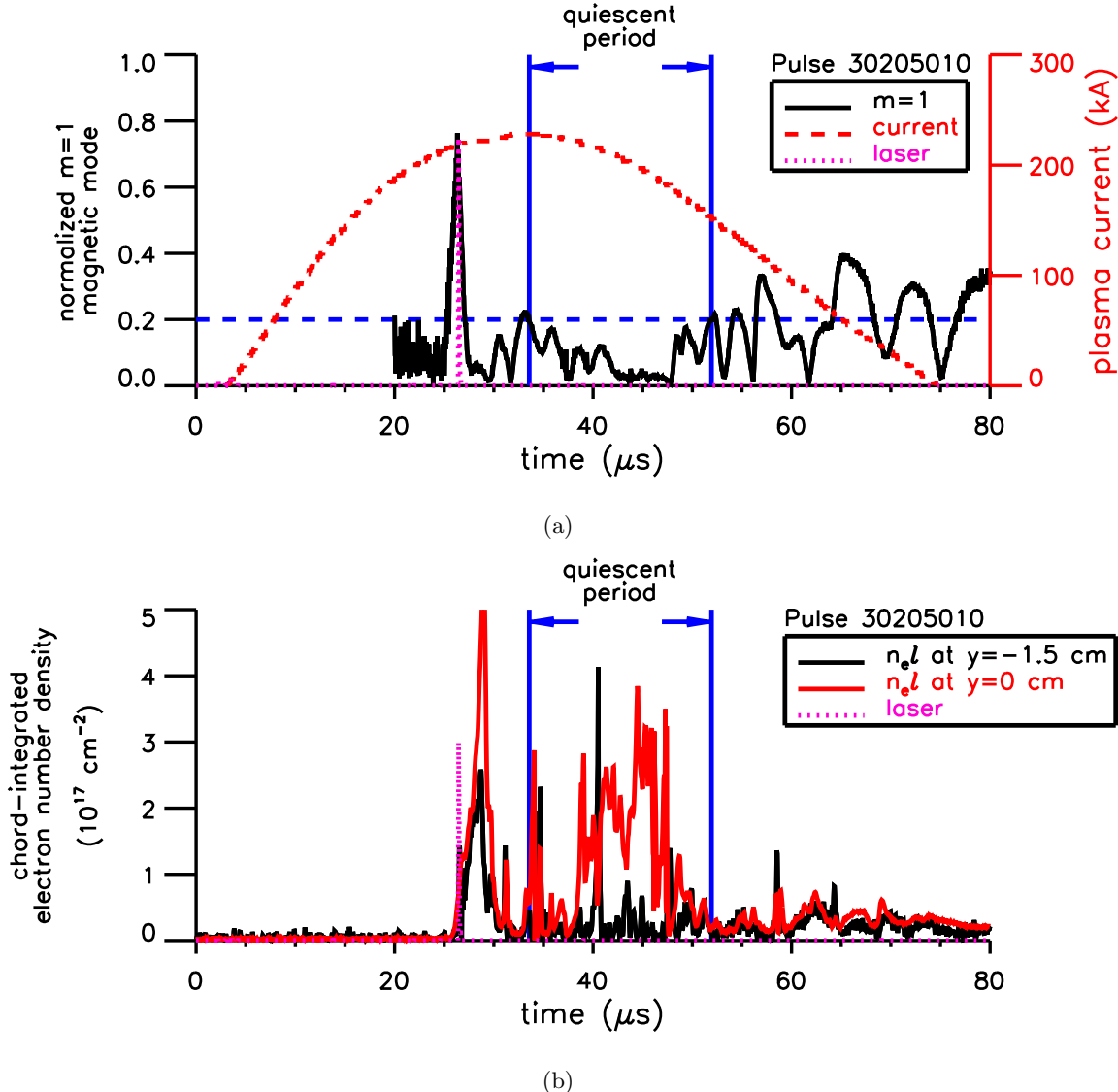


Figure 2.27: Normalized $m = 1$ mode, plasma current, and chord-integrated electron number density for the helium Z-pinch used to study the density profile during arrival (Fig. 2.40). The holography laser monitor shows when the interferogram was made (Pulse 30205010). (a) Normalized $m = 1$ mode and plasma current. (b) Chord-integrated electron number density.

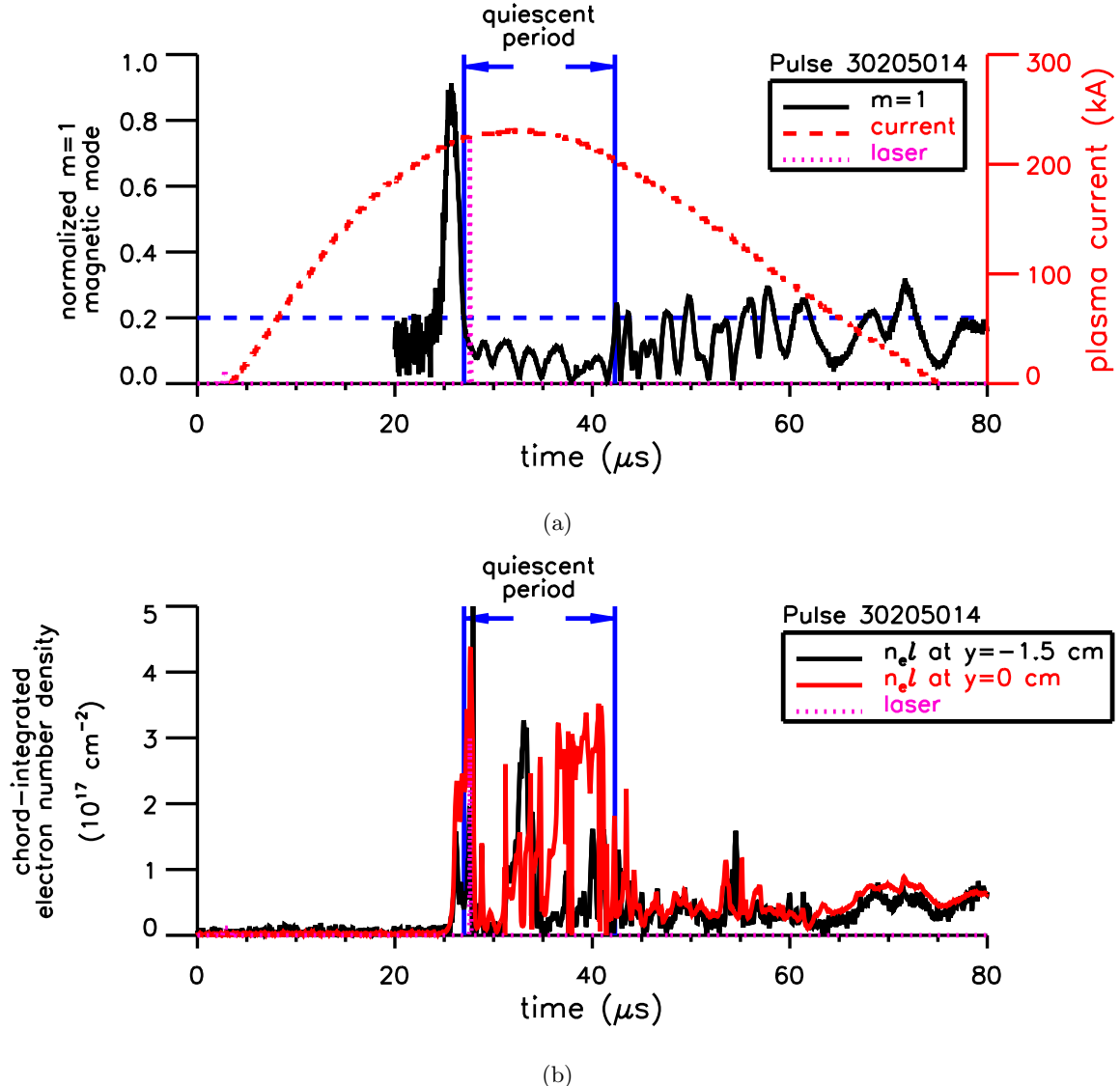


Figure 2.28: Normalized $m = 1$ mode, plasma current, and chord-integrated electron number density for the helium Z-pinch used to study the density profile during early formation (Fig. 2.40). The holography laser monitor shows when the interferogram was made (Pulse 30205014). (a) Normalized $m = 1$ mode and plasma current. (b) Chord-integrated electron number density.

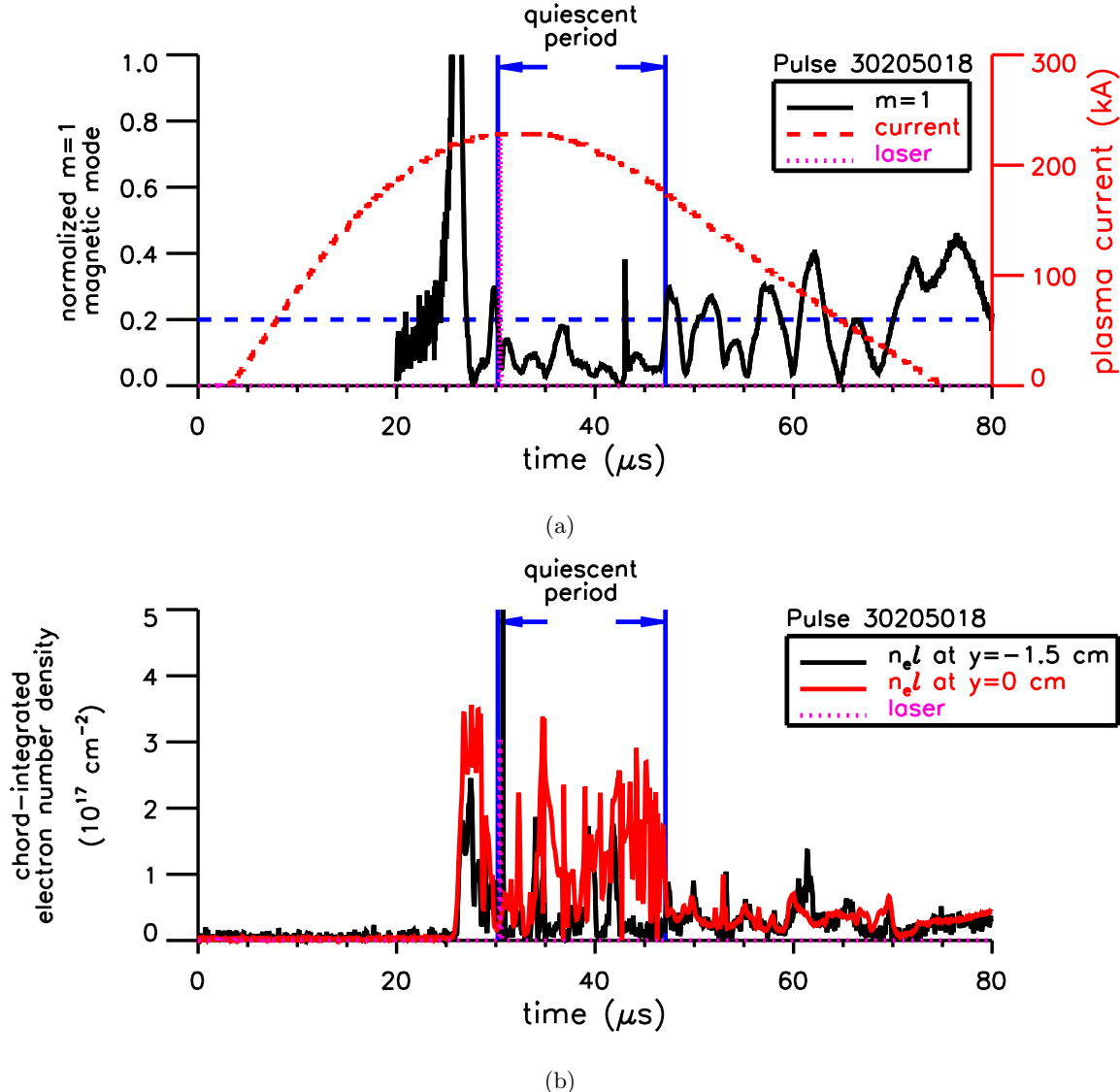


Figure 2.29: Normalized $m = 1$ mode, plasma current, and chord-integrated electron number density for the helium Z-pinch used to study the density profile during late formation (Fig. 2.40). The holography laser monitor shows when the interferogram was made (Pulse 30205018). (a) Normalized $m = 1$ mode and plasma current. (b) Chord-integrated electron number density.

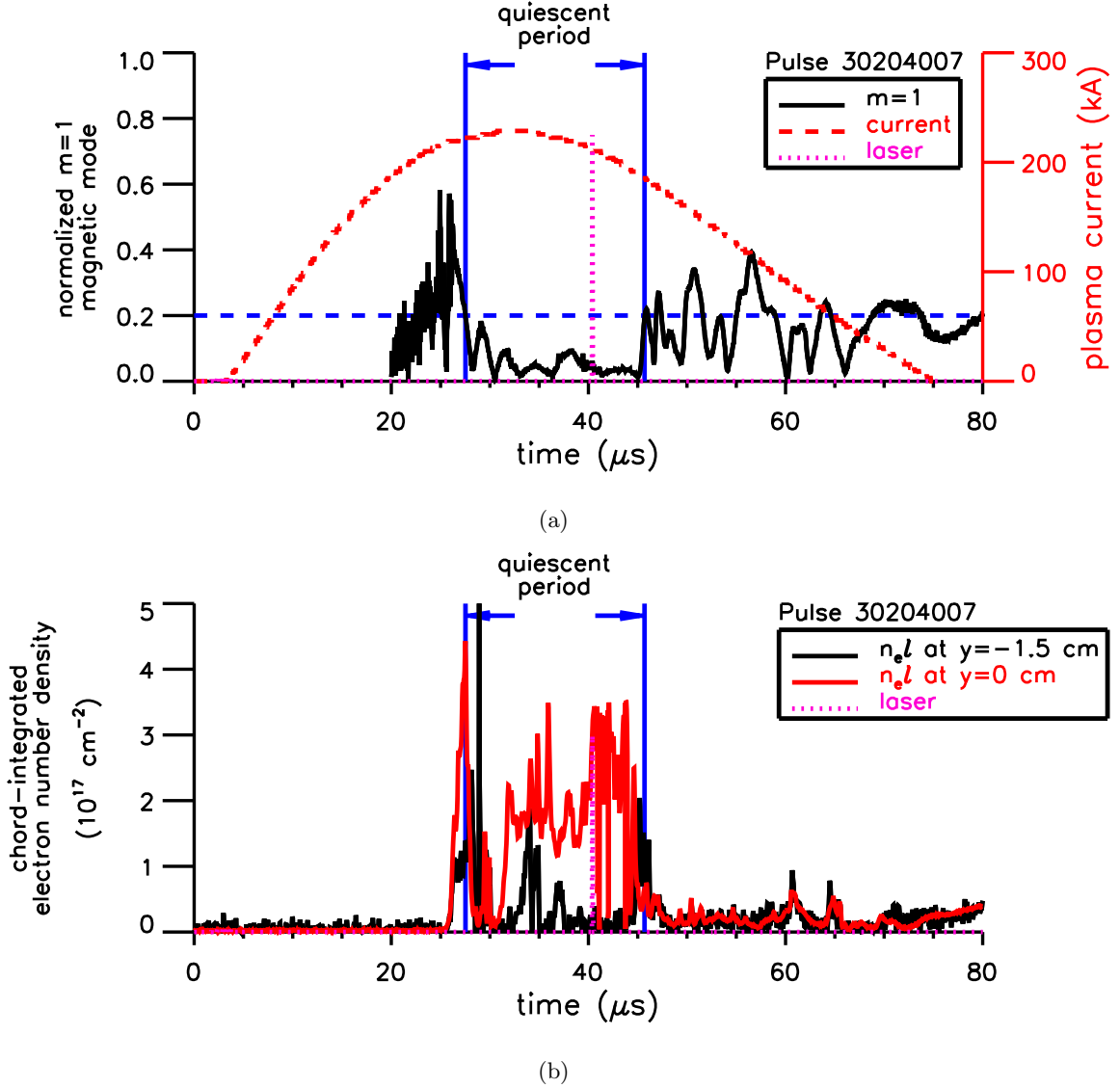


Figure 2.30: Normalized $m = 1$ mode, plasma current, and chord-integrated electron number density for the helium Z-pinch used to study the density profile during the middle of the quiescent period (Fig. 2.41). The holography laser monitor shows when the interferogram was made (Pulse 302040007). (a) Normalized $m = 1$ mode and plasma current. (b) Chord-integrated electron number density.

2.3.1 Holographic Interferometer Operation

The holographic interferometer used to measure the time evolution of the density profile of the flowing Z-pinch was a single-pass system whose optical arrangement is pictured in

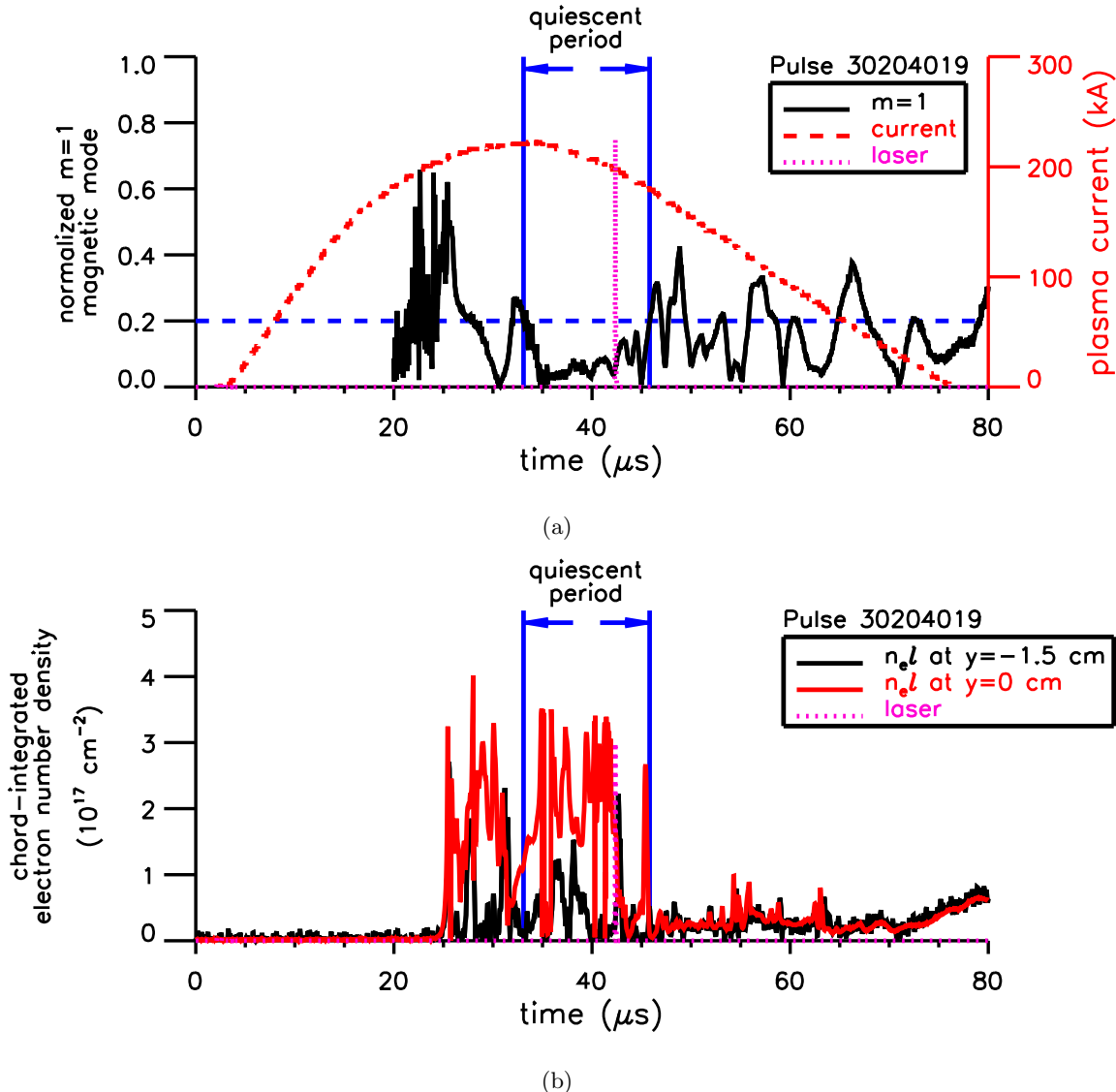


Figure 2.31: Normalized $m = 1$ mode, plasma current, and chord-integrated electron number density for the helium Z-pinch used to study the density profile during the late quiescent period (Fig. 2.41). The holography laser monitor shows when the interferogram was made (Pulse 30204019). (a) Normalized $m = 1$ mode and plasma current. (b) Chord-integrated electron number density.

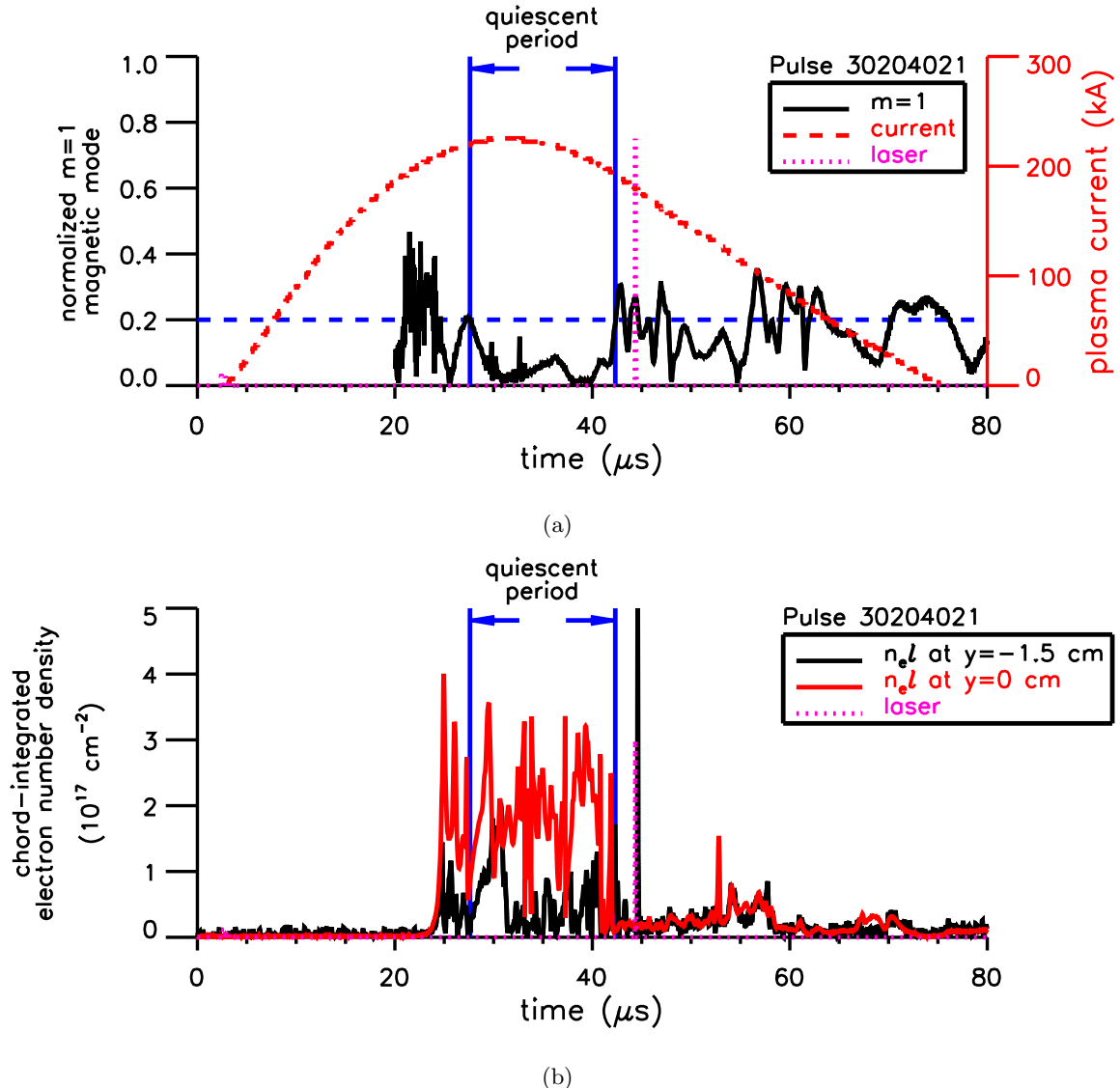


Figure 2.32: Normalized $m = 1$ mode, plasma current, and chord-integrated electron number density for the helium Z-pinch used to study the density profile after the quiescent period (Fig. 2.41). The holography laser monitor shows when the interferogram was made (Pulse 30204021). (a) Normalized $m = 1$ mode and plasma current. (b) Chord-integrated electron number density.

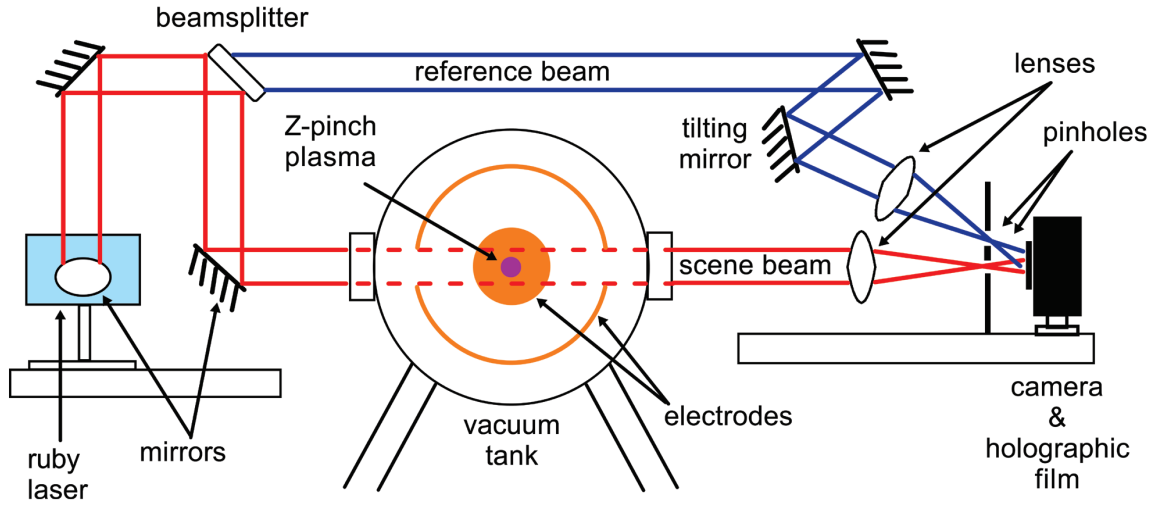


Figure 2.33: Optical arrangement of the single-pass holographic interferometer.

Fig. 2.33. The expanded beam of a pulsed ruby laser is split by a beamsplitter into two beams: a scene beam and a reference beam. The scene beam passes through the plasma and hits the holographic film. The reference beam does not pass through the plasma and hits the holographic film at an angle with respect to the scene beam (roughly 15 degrees). The phase of the scene beam is changed through interaction with the plasma electrons as it passes through the Z-pinch. This phase difference is recorded in the interference pattern produced by the two beams at the holographic film.

Phase differences in the two beams may also be caused by windows and other imperfections in the optical setup, so two holograms are made at the same spot on the film. The first hologram is made by the method described above, except prior to the plasma pulse, with no plasma present in the vacuum chamber. This hologram records the phase difference due to windows and imperfections. The second hologram is made during the plasma pulse. It records the phase difference due to windows and imperfections, as well as the electrons in the Z-pinch. When these two holograms are reconstructed using a beam to mimic the original reference beam, the resulting interference pattern will be the result of the phase difference due to the plasma electrons alone. This method of double-exposure holographic interferometry creates a two-dimensional record of the chord-integrated electron number

density in the plasma.

To aid in interpretation of the interferogram, a mirror in the reference beam is tilted slightly between the two holographic exposures by passing a current through a wire attached to the mirror mount, causing the wire to heat and lengthen. This introduces reference fringes into the interferogram, an effect similar to the heterodyning technique used with the He-Ne interferometer described earlier. The spatial frequency of the fringes results from the slight difference in the angle between the scene and reference beams in the two exposures. It is analogous to the temporal 40 MHz reference frequency added to the He-Ne interferometer reference beam by the Bragg cell.

In addition to the beamsplitter and mirrors used to steer the scene and reference beams onto the film, a lens is used to image the scene beam's pass through the Z-pinch onto the film. This lens serves three purposes. First, imaging the location of the plasma onto the film helps to reduce the refractive effects of dirty windows, improving the quality of the hologram [22]. Second, it allows an iris to be placed in front of the film to reduce the amount of light from the plasma that hits the film. Third, the image is demagnified on the film, increasing the energy density of the laser light to a level that will adequately expose the film. A lens is included in the beam path of the reference beam for the second and third reasons as well.

Reflections from the window must be prevented from reflecting into the laser cavity or from interfering with the scene and reference beams at the holographic film. For this reason, the mirror used to reflect the scene beam through the plasma is positioned slightly downstream (towards the outer electrode end wall) of the $z = 0$ viewport. As a result, the scene beam passes through the glass of the $z = 0$ viewports at a slight angle and the stray reflection from the laser-side window hits the mirror mount.

A Korad K-1 pulsed ruby laser with a KQS2 Pockels cell is used to make the holographic interferograms on 35 mm Slavich PFG-01 holographic film. After both holographic exposures are made for each interferogram on the film, it is developed for ten minutes in Kodak Developer D-19, put into Kodak X-Ray Indicator Stop Bath for ten seconds, and fixed using Kodak Rapid Fixer for five minutes, all in the dark in a developing tank. The rest of the processing steps can then be done in light. The film is rinsed for five minutes,

bleached in a diluted potassium dichromate solution to improve the diffraction efficiency of the holograms, and rinsed for ten minutes.

Once processed, the hologram is reconstructed using a He-Ne laser to mimic the original ruby laser reference beam. This reconstruction beam is diffracted by the interferogram as it passes through the film at the same angle as the original reference beam. The resulting interference pattern, the reconstructed holographic interferogram, is photographed using Polaroid film and scanned into a computer at a resolution of 300 pixels per inch.

A significant degradation in the quality of the interferograms occurred in moving from the single-pass holographic interferometer to a double-pass setup used later. A great deal of time and effort was spent to determine the source of this degradation, including removing vacuum tank windows, changing mirrors and beamsplitters, adjusting beam path lengths, switching power supplies, repairing the ground connection to the Pockels cell, cleaning the polarizer stack in the Pockels cell, and refining the output beam from the laser by adjusting the power supply settings, the iris size and location, and the optical alignment of the components in the laser cavity. None of these efforts had a significant impact on the quality of the interferograms. The quality was finally improved, however, after the laser cavity was disassembled and cleaned. Several corroded bolts and a flashlamp connector were replaced, and the electrical connections to the flashlamp were tightened. Some evidence of arcing was discovered inside the housing. At the same time, the deionization and particle filters in the laser cooling lines were replaced, and an unreliable connection between the power supply and the high voltage output to the laser head was replaced. This high voltage connector showed signs of arcing. Examples of holographic interferograms made before and after the laser was refurbished are shown in Figs. 2.34(a)–2.34(b). Both interferograms are baseline interferograms made with no plasma present and should be composed of straight, vertical reference fringes.

Figs. 2.35(a)–2.35(b) show examples of interferograms made with and without plasma present during the second holographic exposure. (Plasma was not present during the first exposure of either interferogram.) The presence of the plasma causes a measurable fringe shift in the interferogram of Fig. 2.35(b). This fringe shift can be normalized by the distance between neighboring bright or dark fringes and expressed as the fringe order. The maximum

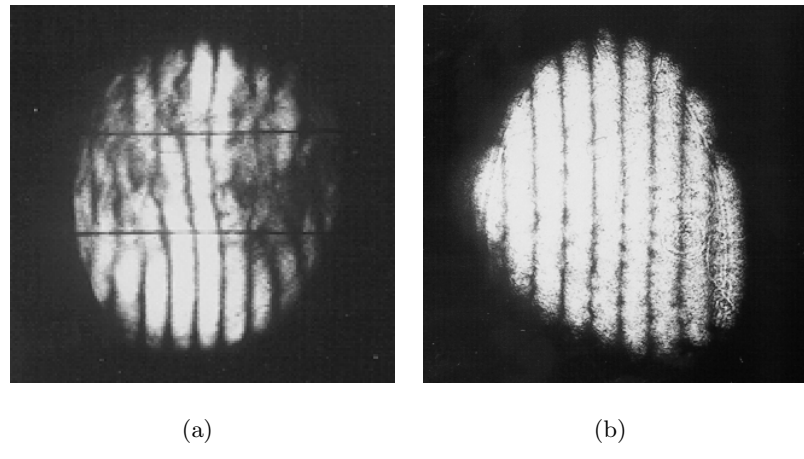


Figure 2.34: Holographic interferograms made before and after the laser was refurbished. Both interferograms were made with no plasma present and should be composed of straight, vertical reference fringes. (a) Low quality holographic interferogram made before the laser was refurbished. (b) Higher-quality interferogram made after the laser was refurbished. Placement of the beamsplitter was not optimized for the optical configuration used, so a portion of the interferogram is cut off by the beamsplitter.

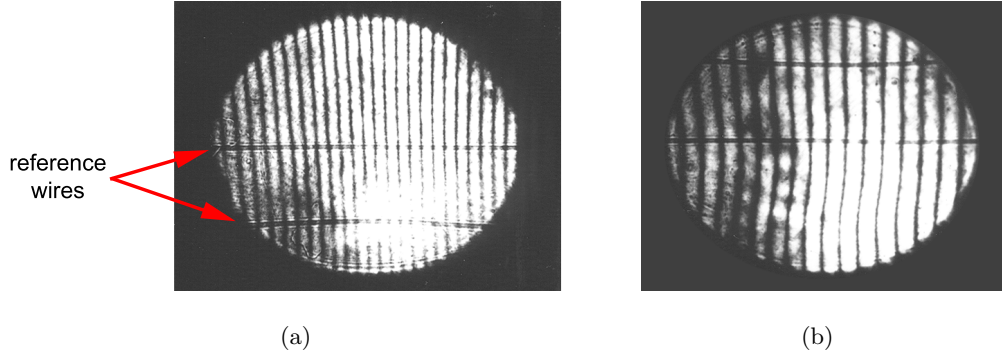


Figure 2.35: Holographic interferograms made with and without plasma present. (a) No plasma. (b) Hydrogen Z-pinch plasma (Pulse 20910027). Reference wires attached to the vacuum tank are visible in both interferograms. The reference wires were attached 0.5 cm above and below the center of the vacuum tank window for both interferograms, but the vertical position of the scene beam was lower when the interferogram of the Z-pinch was made.

fringe shift in Fig. 2.35(b) is approximately one-half fringe width, or a fringe order of one-half. The fringe order is proportional to the phase shift in the laser light as it passed through the plasma and also proportional to the chord-integrated electron number density according to the equation

$$f = \frac{\Delta\phi}{2\pi} = \frac{1}{2\lambda n_c} \int n_e dl, \quad (2.37)$$

where f is the fringe order, $\Delta\phi$ is the phase shift, n_e is the electron density, λ is the ruby laser wavelength, and n_c is the plasma cutoff density, described by Eq. 2.36. This relationship is used in the IDL procedure *invert_interferogram.pro*, contained in Appendix E, to calculate the chord-integrated electron number density based on the fringe shift in the interferogram. The fringe shift is measured by the IDL procedure *analyze_interferogram.pro*, contained in Appendix D. Once the fringe shift and the chord-integrated density have been determined, a discrete Abel inversion is used to obtain the radial density profile from the chord-integrated density. This inversion is also performed by the IDL procedure *invert_interferogram.pro*. Reference [19] contains a more detailed explanation of this process.

The plasma is assumed to be radially symmetric, so that the chord-integrated number density at a given impact parameter is given by the Abel transform equation,

$$N_e(y) = 2 \int_y^\infty \frac{n_e(r)}{(y^2 - r^2)^{1/2}} r dr, \quad (2.38)$$

where N_e is the chord-integrated electron number density, n_e is the electron number density, y is the impact parameter of the chord and r is the distance of a point on the chord from the center of the Z-pinch [40]. The “2” in front of the integral in this expression is a “4” when the double-pass system is used instead of the single-pass system. If the plasma is modeled as I concentric, cylindrical shells, the integral can be discretized and inverted to arrive at the discrete Abel inversion formula,

$$n_{ei} = \frac{1}{A_{ii}} \left(\frac{1}{2} N_{ei} - \sum_{k=i+1}^{I-1} n_{ek} A_{ki} \right). \quad (2.39)$$

where n_{ei} is the number density across shell i and N_{ei} is the chord-integrated number density at the impact parameter corresponding to shell i . As shown in Fig. 2.36, the coefficients A_{ki} are half the path lengths through each cylindrical shell at each impact parameter,

$$A_{ki} = (r_{k+1}^2 - r_i^2)^{1/2} - (r_k^2 - r_i^2)^{1/2}. \quad (2.40)$$

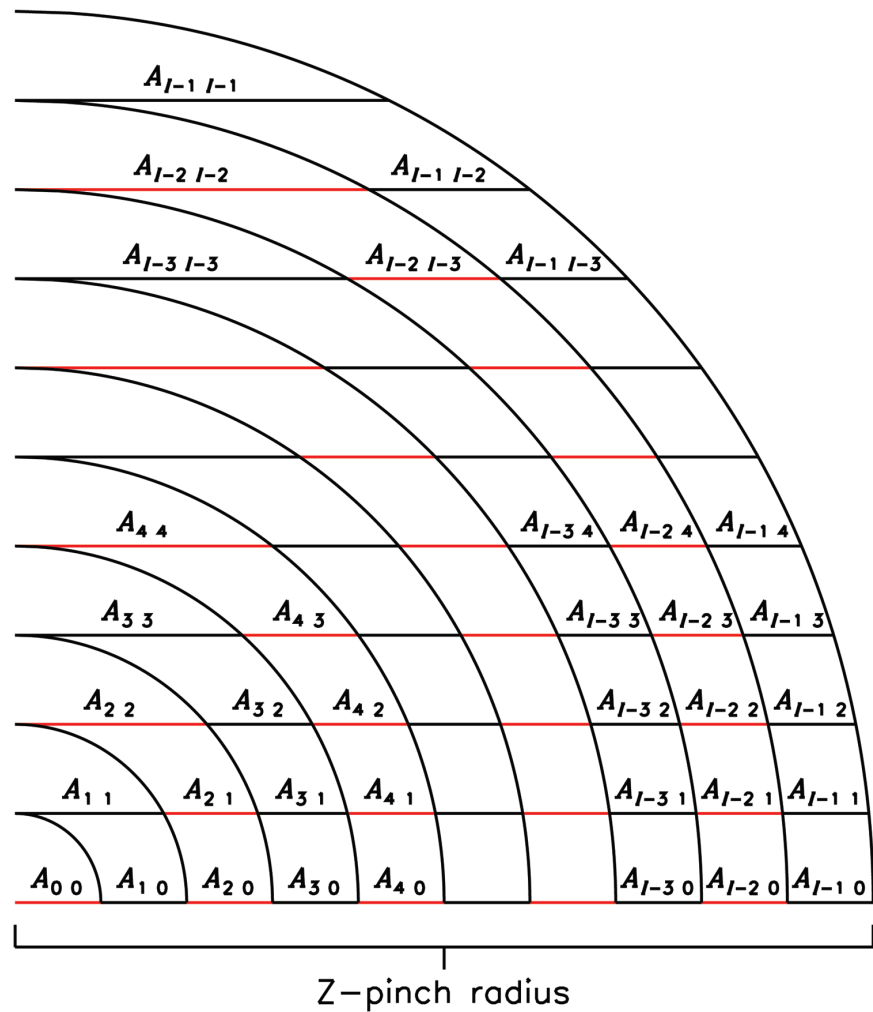


Figure 2.36: Graphical depiction of each coefficient A_{ki} as half the path length through a cylindrical shell of plasma at a given impact parameter.

The shell widths are usually uniform, but can vary to account for points missed during fringe localization.

In effect, using the Abel inversion method is equivalent to the following process. The electron density of the outermost shell (shell I) is calculated by dividing the chord-integrated density at the first chord by the path length through the shell at that impact parameter. The electron density of the second outermost shell (shell $I - 1$) is calculated in a similar manner using the chord-integrated density at the second chord, except there are two shells involved. The contribution of the outermost shell can be calculated, since the electron density and the path length through the outermost shell are known. This contribution is then subtracted from the chord-integrated density to yield the chord-integrated density due to the second outermost shell alone. This value is divided by the path length through the second outermost shell to yield the electron density of that shell. This process is repeated, working inward, until the innermost shell is reached and the electron density at every shell has been determined. Each interferogram contains enough information to produce two radial density profiles by this method; one is based on the lower part of the interferogram, and the other is based on the upper part.

The location of the center of the shell model affects the results of the inversion method. For this reason, the Abel inversion method is run several times, with the shell model centered about a different point each time. The two radial density profiles that result at each center are compared using the square root of the sum of the squares of the differences in the average slopes of the electron densities in their ten innermost shells,

$$\Delta = \left\{ \sum_{i=0}^9 \left[\left(\frac{n_{ei+1} - n_{ei}}{r_{ei+1} - r_{ei}} \right)_U - \left(\frac{n_{ei+1} - n_{ei}}{r_{ei+1} - r_{ei}} \right)_L \right]^2 \right\}^{1/2}, \quad (2.41)$$

where the subscripts U and L denote quantities calculated from the upper and lower portions of the interferogram, respectively. The center where this quantity is smallest yields the most symmetric shell model, and the resulting radial density profiles indicate the radial electron density profile of the Z-pinch. Minimizing Δ is essentially the same as setting the second derivative of the electron density equal to zero across the axis ($d^2n_e/dr^2 = 0$). This leads to two density profiles that are symmetric about an axis located at a local maximum or minimum in the density.

Figures 2.37(a)–2.37(b) show the chord-integrated electron number density and radial electron number density profile obtained from the bright fringe just to the left of the center-most bright fringe in the holographic interferogram of Fig. 2.35(b). The error bars shown for the chord-integrated density result primarily from smoothing data stored as pixels in the interferogram. The error bars for the radial profile result when the errors in the chord-integrated density are passed through the inversion method. They are particularly large near $r = 0$ because the effect of smoothing the chord-integrated density is large near its peak, tending to reduce the magnitude of the radial profile near the axis of the Z-pinch.

A single-pass optical setup was used to investigate the electron density profiles of 50 cm-long Z-pinches composed of hydrogen, a 50% methane/50% hydrogen mixture, and helium. Examples of 50% methane/50% hydrogen and helium Z-pinch interferograms are shown in Figs. 2.38(a)–2.38(b). The fringe shift due to the plasma electron density in these interferograms can be compared to that of the hydrogen Z-pinch interferogram of Fig. 2.35(b). As shown in Fig. 2.39, a Z-pinch formed with helium has a higher density than a methane/hydrogen or pure hydrogen Z-pinch. This leads to a maximum fringe order of about one fringe for a helium Z-pinch and a higher signal-to-noise ratio in the chord-integrated density. As a result, features of the chord-integrated density and the radial electron density profile are more discernible. For that reason, the investigation of the time evolution of the electron number density profile of a helium Z-pinch was performed with the single-pass holographic interferometer.

2.3.2 Holographic Interferometer Results

The holographic interferometer was used on successive helium plasma pulses to investigate the time evolution of the radial electron density profile of 50 cm-long helium Z-pinches on the ZaP experiment, rather than the 100 cm-long Z-pinches made using the experimental configuration shown in Fig. 1.2. A capacitor bank voltage of 9 kV was used on the pulses, with a single ignitron connected to four 170 μ F capacitors in parallel. A higher capacitor bank voltage decreases the length of the quiescent period but generally increases the temperature and density in the Z-pinch. For that reason, the highest capacitor bank voltage

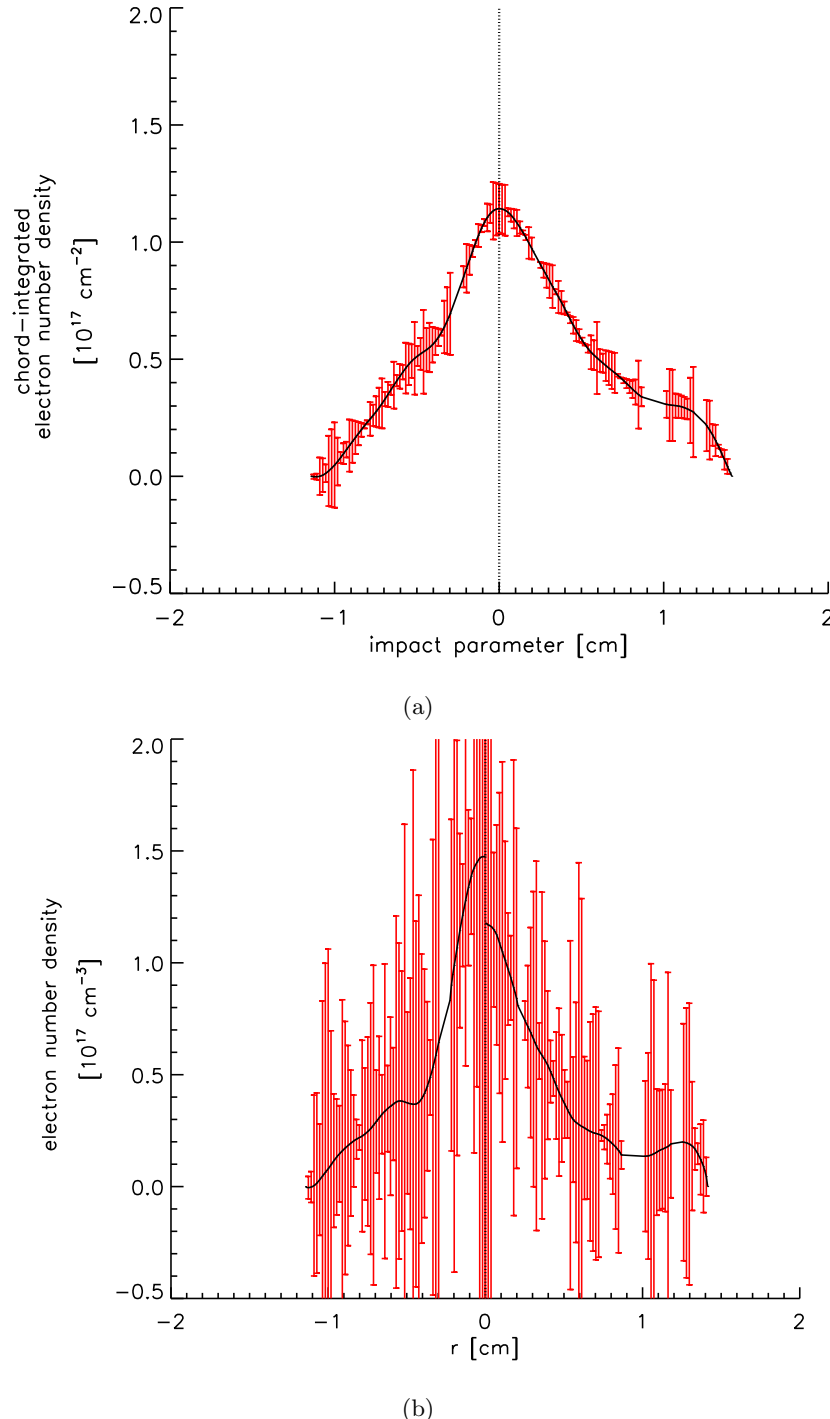


Figure 2.37: Chord-integrated electron density and radial electron density profile for a hydrogen Z-pinch, obtained from the holographic interferogram of Fig. 2.35(b). (a) Chord-integrated density determined from the shift of a fringe in the interferogram. (b) Radial electron density profile that results from Abel inversion of the chord-integrated density.

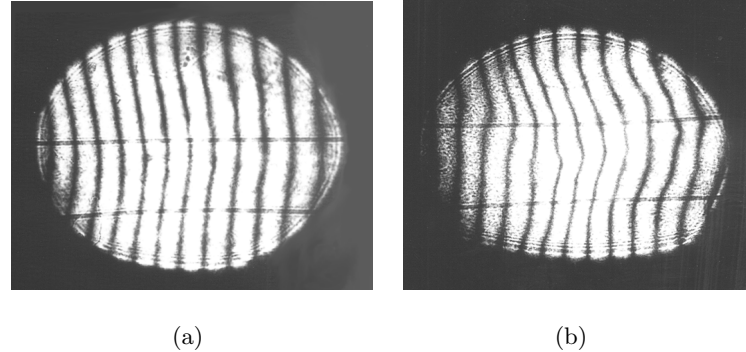


Figure 2.38: Holographic interferograms made using the single-pass holographic interferometer. (a) 50% methane/50% hydrogen Z-pinch (Pulse 21029011). (b) Helium Z-pinch (Pulse 30204007).

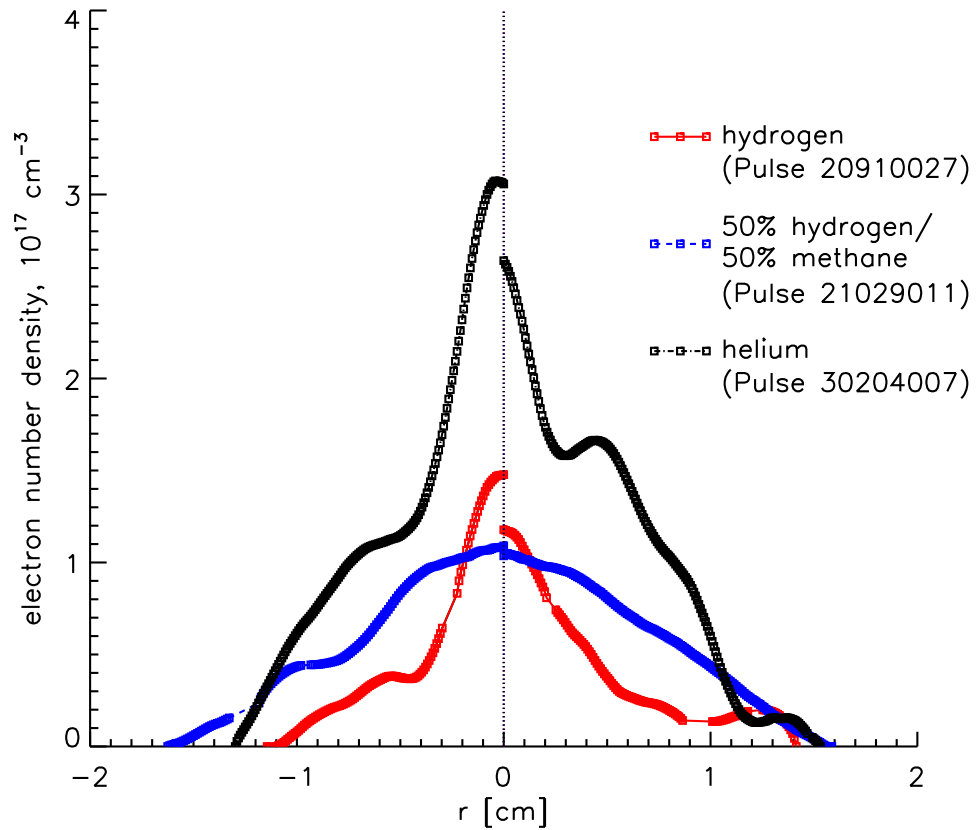


Figure 2.39: Radial electron density profiles for hydrogen, 50% methane/50% hydrogen, and helium Z-pinches (Pulses 20910027, 21029011 and 30204007).

typically used when operating the experiment was used for the time survey. Several interferograms were made before, during, and after the quiescent period, on separate plasma pulses. Figure 2.40 shows density profiles during formation of the Z-pinch near the beginning of the quiescent period. These profiles were obtained during the plasma pulses whose He-Ne interferometer measurements and normalized $m = 1$ mode is shown in Figs. 2.27(a)–2.29(b). The peak in the holography laser monitor shown in the figures indicates when each interferogram was made. To within the resolution and view of the holographic interferometer, the density profile is initially flat or zero as the plasma arrives at the axial location where the holographic measurements were made (Pulse 30205010). The density profile becomes more peaked during the early part of the Z-pinch's formation (Pulse 30205014). During the latter part of the formation process, the density profile becomes relatively flat or zero, indicating that either the electron density is below the resolution of the holographic interferometer or its edges are out of view (Pulse 30205018).

Figure 2.41 shows density profiles during and after the quiescent period of the Z-pinch. These profiles were obtained during the plasma pulses whose He-Ne interferometer measurements and normalized $m = 1$ mode is shown in Figs. 2.30(a)–2.32(b). The peak in the holography laser monitor shown in the figures indicates when each interferogram was made. A peaked profile was observed during the middle of the quiescent period (Pulse 30204007). The density profile becomes less peaked late in the quiescent period (Pulse 30204019) and flattens following the quiescent period (Pulse 30204021).

2.4 Fast-Framing Camera

The time evolution of the Z-pinch emission has been captured by an Imacon fast-framing camera capable of taking either streak photos or individual frames 200 ns apart. Figure 2.42 shows a streak photo of a 5 kV hydrogen Z-pinch at $z = 0$ made through a 25 micron slit at a scan rate of 1000 ns/mm. The vertical position of the Z-pinch, calculated from the magnetic mode data, is plotted in red over the photo as y versus time. Prominent features in the vertical position are used to scale the streak photo. The vertical dashed red line shows the trigger time of the camera, and the solid blue lines indicate the beginning and end of the quiescent period. The photo shown was made during a 5 kV hydrogen plasma pulse,

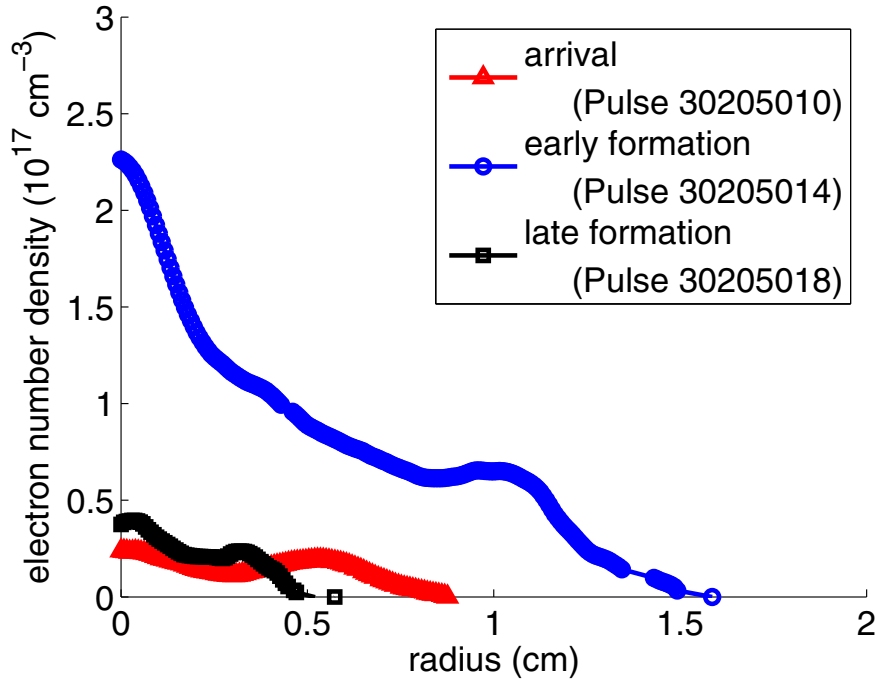


Figure 2.40: Radial electron density profiles for helium Z-pinches during formation of the Z-pinch (Pulses 30205010, 30205014, and 30205018).

with an f-stop setting of 3.5 and no filter. The arrival of the current sheet and eventual formation of a discrete Z-pinch near the beginning of the quiescent period can be seen in the photo. A discrete Z-pinch is visible until the end of the quiescent period, after which the plasma emission is suddenly reduced. During the time period between the arrival of the plasma and formation of the Z-pinch, the plasma emission is typically low and diffuse, although at times what appears to be a wildly oscillating plasma column can be seen.

Figures 2.43(a)–2.43(h) are a series of framed images taken 200 ns apart during the arrival of the current sheet at $z = 0$. The current sheet moves past the 5 cm diameter hole in the outer electrode in four frames, allowing its velocity to be estimated at 60 km/s. The associated normalized $m = 1$ mode, total plasma current, and trigger times for the first and last images are shown in Fig. 2.44.

Figures 1.5(a)–1.5(h) in Chapter 1 are examples of images made during the quiescent

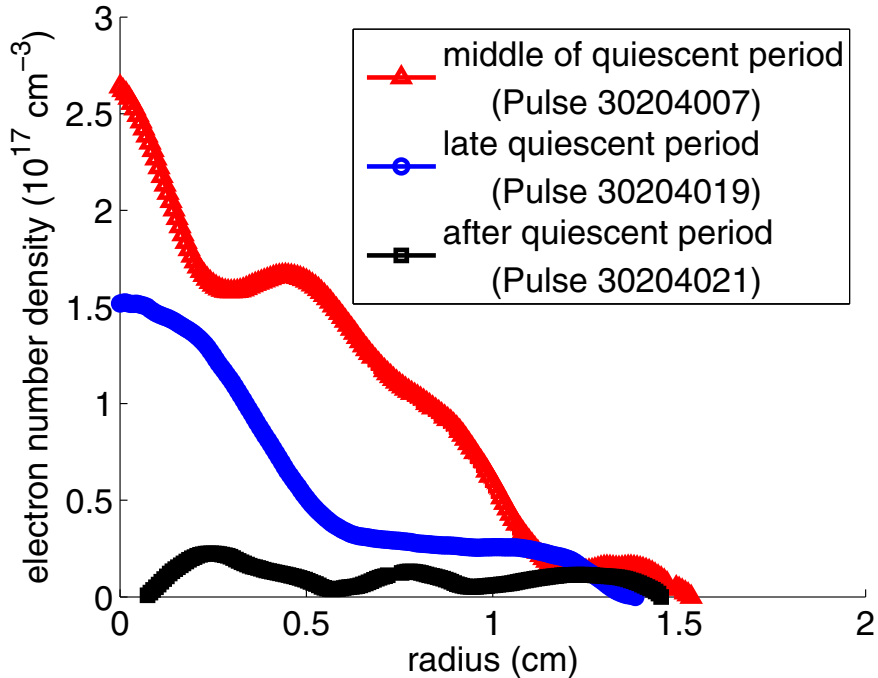


Figure 2.41: Radial electron density profiles for helium Z-pinches during and after the quiescent period (Pulses 30204007, 30204019, 30204021).

period showing the Z-pinch. Figures 2.45(a)–2.45(h) and Figs. 2.47(a)–2.47(h) were made near the end of the quiescent period. They show what looks very much like classical MHD kink and sausage instabilities developing as the mode activity grows near the end of the quiescent period. The plasma current, normalized $m = 1$ mode, and camera trigger times associated with these two sets of images are included in Figs. 2.46 and 2.48.

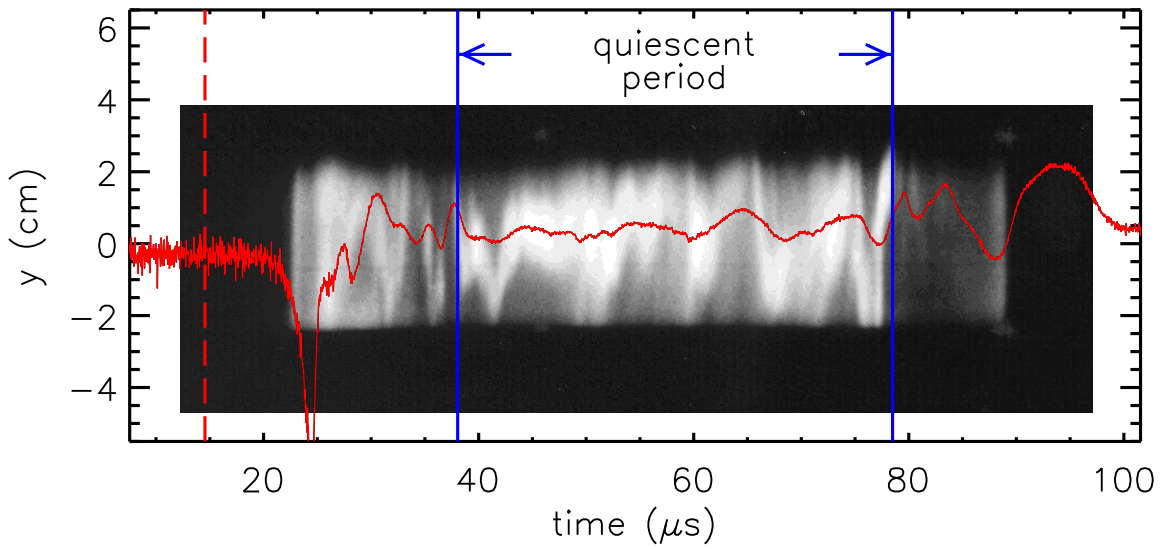


Figure 2.42: Streak photo of the Z-pinch at $z = 0$ made through a 25 micron slit at a scan rate of 1000 ns/mm. The vertical position of the Z-pinch, calculated from the magnetic mode data, is plotted in red over the photo as y versus time. Prominent features in the vertical position are used to scale the streak photo. The trigger time of the camera is indicated by the vertical dashed red line, and the solid blue lines indicate the beginning and end of the quiescent period (Pulse 40219011).

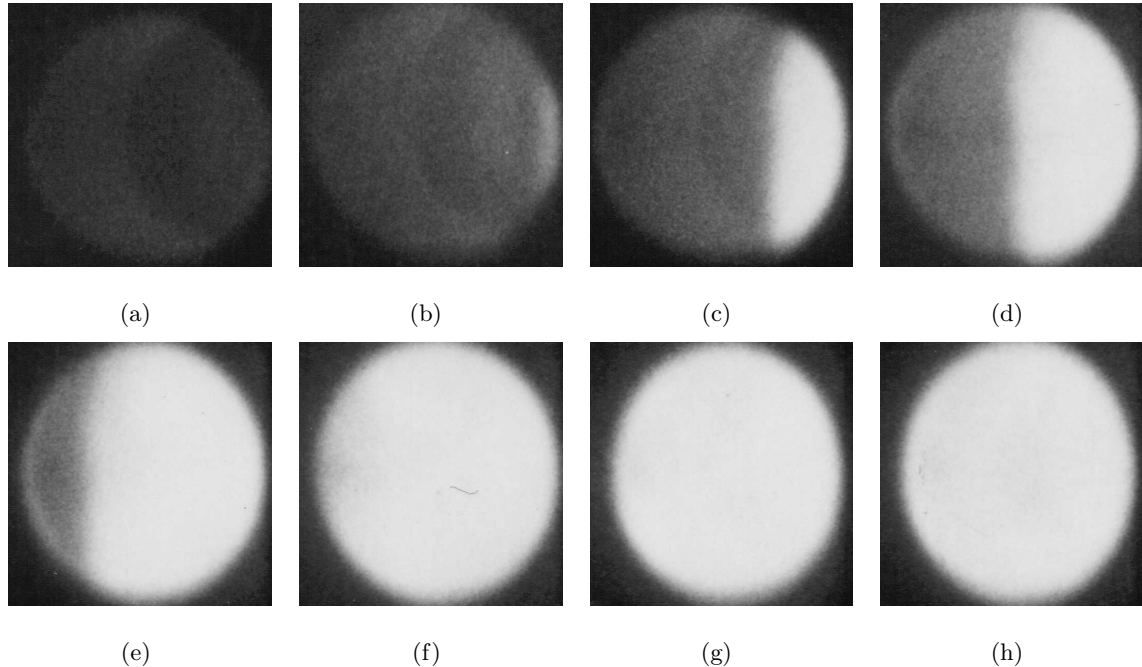


Figure 2.43: Photos of Z-pinch emission showing the arrival of the current sheet at $z = 0$. The photos represent unfiltered visible light emitted by the plasma and are made approximately 200 ns apart through the vacuum tank viewport and 2 in diameter hole in the outer electrode at $z = 0$ (Pulse 40108045). (a) 22.5 μ s. (b) 22.7 μ s. (c) 22.9 μ s. (d) 23.1 μ s. (e) 23.4 μ s. (f) 23.6 μ s. (g) 23.8 μ s. (h) 24.0 μ s.

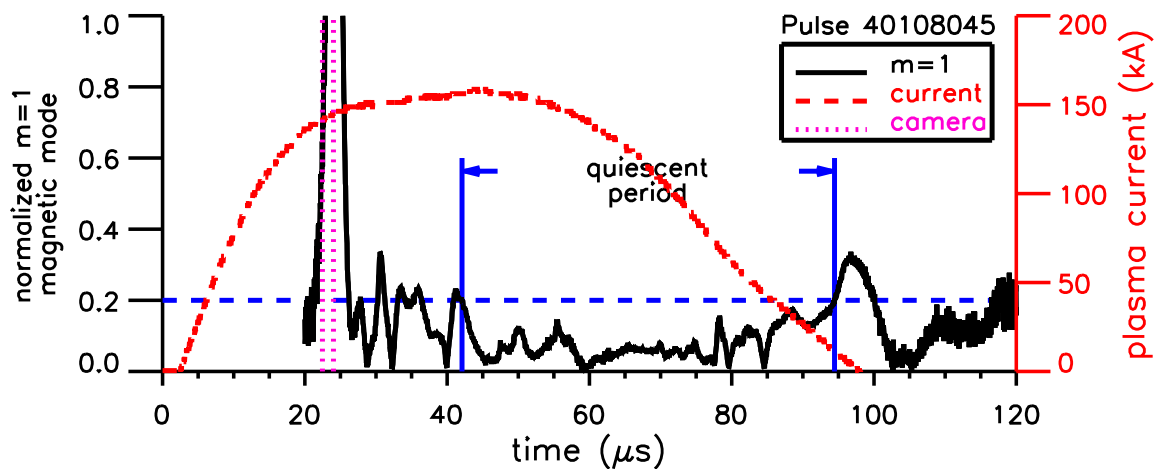


Figure 2.44: Plasma current and normalized $m=1$ mode associated with the images capturing the arrival of the current sheet. Vertical lines indicate the times at which the first and last images were made (Pulse 40108045).

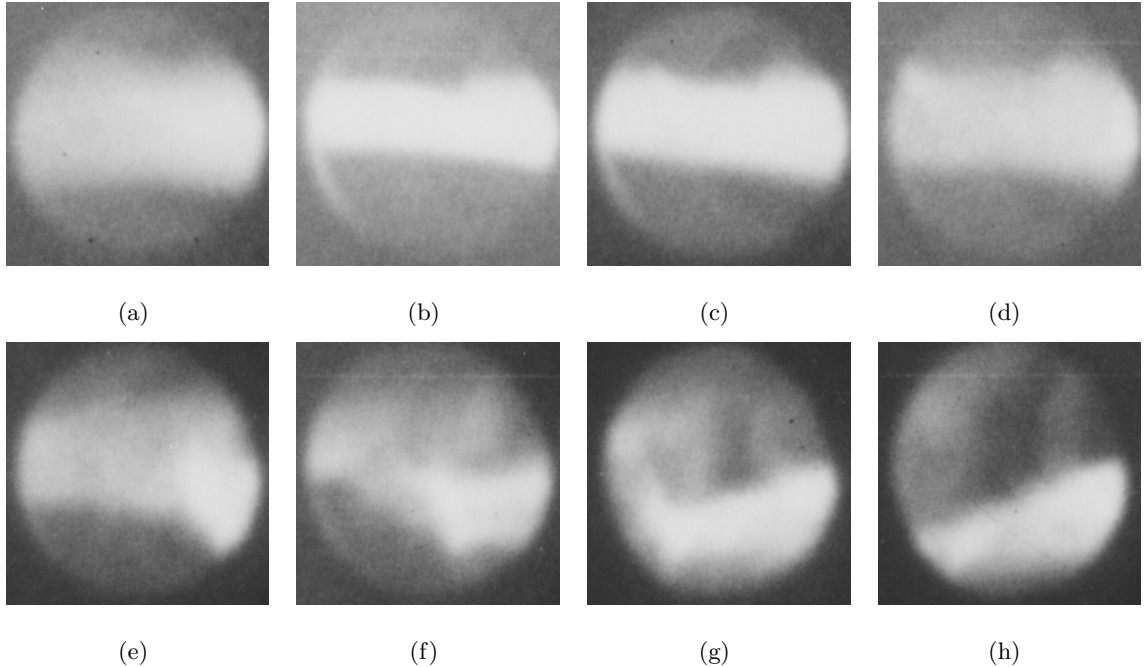


Figure 2.45: Photos of Z-pinch emission showing the development of a possible kink instability near the end of the quiescent period. The photos represent unfiltered visible light emitted by the plasma and are made approximately 200 ns apart through the vacuum tank viewport and 2 in diameter hole in the outer electrode at $z = 0$ (Pulse 40127038). (a) 74.1 μ s. (b) 74.3 μ s. (c) 74.5 μ s. (d) 74.7 μ s. (e) 75.0 μ s. (f) 75.2 μ s. (g) 75.4 μ s. (h) 75.6 μ s.

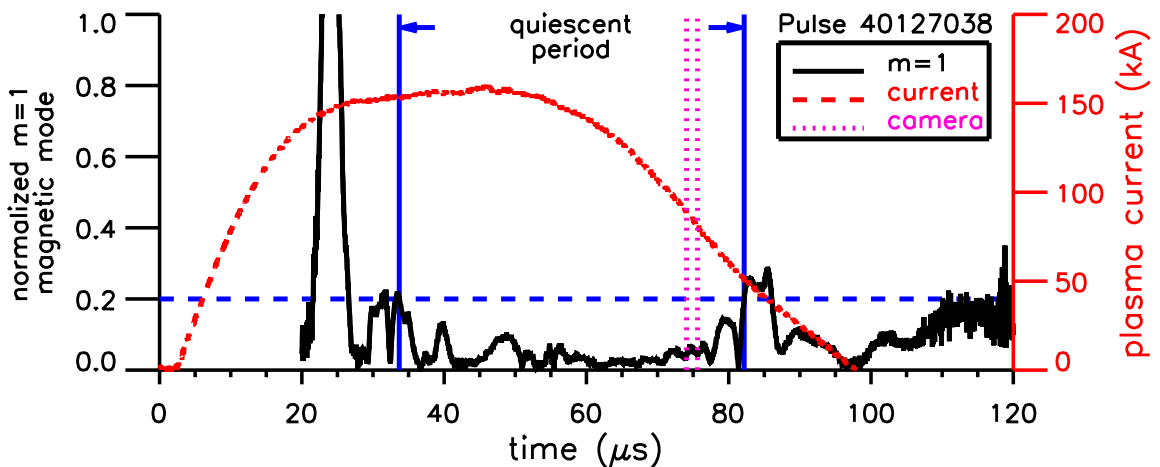


Figure 2.46: Plasma current and normalized $m=1$ mode associated with the images showing the development of a possible kink instability near the end of the quiescent period. Vertical lines indicate the times at which the first and last images were made (Pulse 40127038).

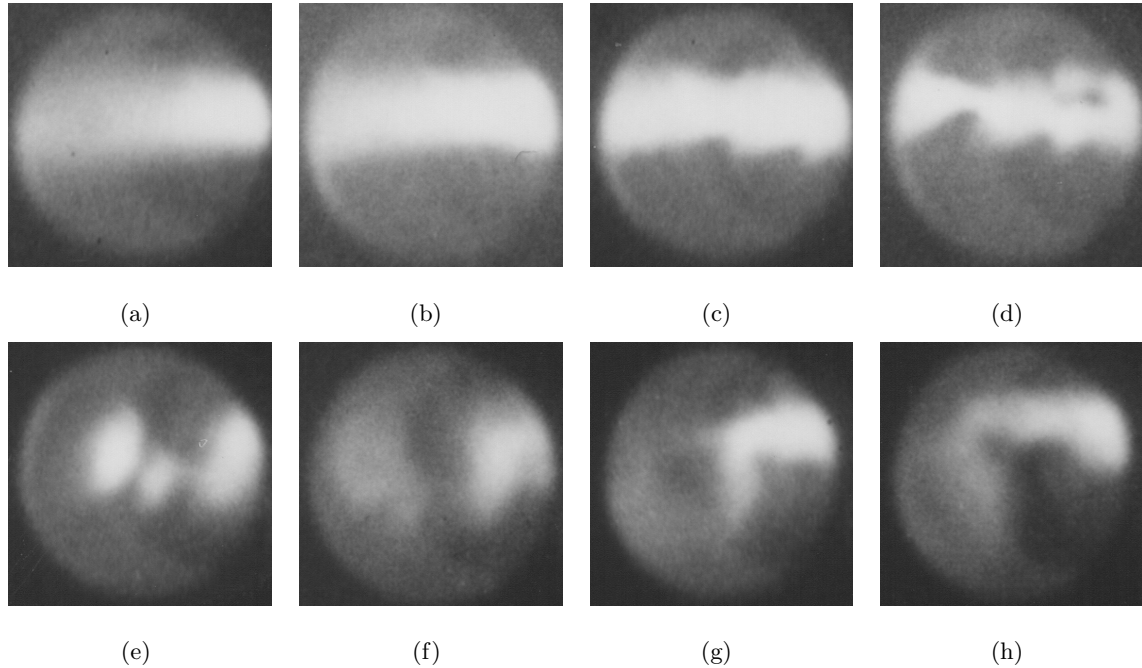


Figure 2.47: Photos of Z-pinch emission showing the development of a possible sausage instability near the end of the quiescent period. The photos represent unfiltered visible light emitted by the plasma and are made approximately 200 ns apart through the vacuum tank viewport and 2 in diameter hole in the outer electrode at $z = 0$ (Pulse 40127040). (a) 74.2 μ s. (b) 74.4 μ s. (c) 74.6 μ s. (d) 74.8 μ s. (e) 75.0 μ s. (f) 75.2 μ s. (g) 75.4 μ s. (h) 75.6 μ s.

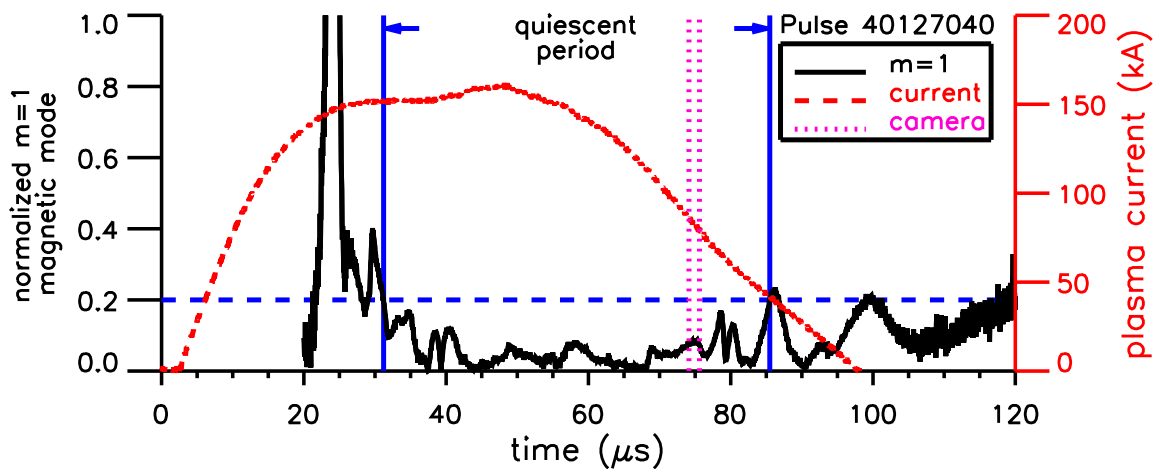


Figure 2.48: Plasma current and normalized $m=1$ mode associated with the images showing the development of a possible sausage instability near the end of the quiescent period. Vertical lines indicate the times at which the first and last images were made (Pulse 40127040).

Chapter 3

EQUILIBRIUM PROFILE CALCULATION

The density and temperature profiles together characterize the equilibrium of the Z-pinch. Quantities such as the pressure, magnetic field, and current density profiles can be determined if the density and temperature profiles are known. Conversely, the temperature and density profiles can be determined if two of the other quantities are known. The density profile of the sheared-flow Z-pinch has been measured using holographic interferometry, but the temperature must be calculated, based on reasonable assumptions, to yield an equilibrium pressure profile that can be compared to theoretical profiles such as the Kadomtsev pressure profile of Sec. 1.4. The pressure profile that results from the measured density profile will also serve as a prediction for future measurements of the equilibrium pressure profile using a Thomson scattering diagnostic currently under development.

Four models were used to calculate the equilibrium profiles from the measured density profile. The Matlab functions used to implement the models are included in Appendix F. These models are described in the following sections, from the simplest model to the most complex. The first model assumes a constant current density across the Z-pinch, and the second assumes the current density is proportional to the electron number density. Uniform heating across the Z-pinch balanced by limited perpendicular thermal conduction out of the Z-pinch is used to solve for the Z-pinch equilibrium in the third model. Because thermal conduction within the Z-pinch is found to be high, the fourth model assumes a constant temperature profile. The fourth model yields physically believable results for all of the density profiles studied and is therefore used to calculate the time evolution of the equilibrium profiles during the quiescent period. These results are then compared to the Kadomtsev pressure profile.

3.1 Constant Current Density

One of the simpler assumptions that can be made in determining the equilibrium profile of the sheared-flow Z-pinch is the assumption that the current density is constant across the Z-pinch. The average magnetic field measured by the probes of the azimuthal magnetic probe array, B_{wall} , can be used along with Ampere's law to calculate the current in the Z-pinch, assuming all current past that point is contained in the Z-pinch,

$$\int \vec{B} \cdot d\vec{l} = \mu_0 I \quad (3.1)$$

$$I = \frac{2\pi r_{wall} B_{wall}}{\mu_0}, \quad (3.2)$$

where $r_{wall} = 0.0936$ m is the radius of the outer electrode wall and the distance from the probes embedded in it to the axis of the experiment. The permeability of free space is given by $\mu_0 = 4\pi \times 10^{-7}$ H/m. The total current can then be divided by the area of the Z-pinch to yield the current density,

$$j = \frac{I}{\pi a^2}, \quad (3.3)$$

where a is the radius of the Z-pinch, determined from the density profile.

This current density can be substituted into Ampere's law to obtain the magnetic field profile,

$$B(r) = \frac{\mu_0 r j}{2}. \quad (3.4)$$

Pressure is related to magnetic field in a Z-pinch by

$$\frac{dp}{dr} = -\frac{B_\theta(r)}{\mu_0 r} \frac{d}{dr} [r B_\theta(r)]. \quad (3.5)$$

The ideal gas law can be used to determine the temperature from the density and pressure,

$$T(r) = \frac{p}{(1 + 1/Z) nk}, \quad (3.6)$$

where the pressure is assumed to be zero outside the Z-pinch, and the electron and ion densities are assumed to be $n = n_e = Z n_i$ and the electron and ion temperatures are assumed to be equal, $T = T_e = T_i$. Z is the ionization state of the ions. $Z = 1$ is assumed here for hydrogen, and $Z = 2$ is assumed for helium.

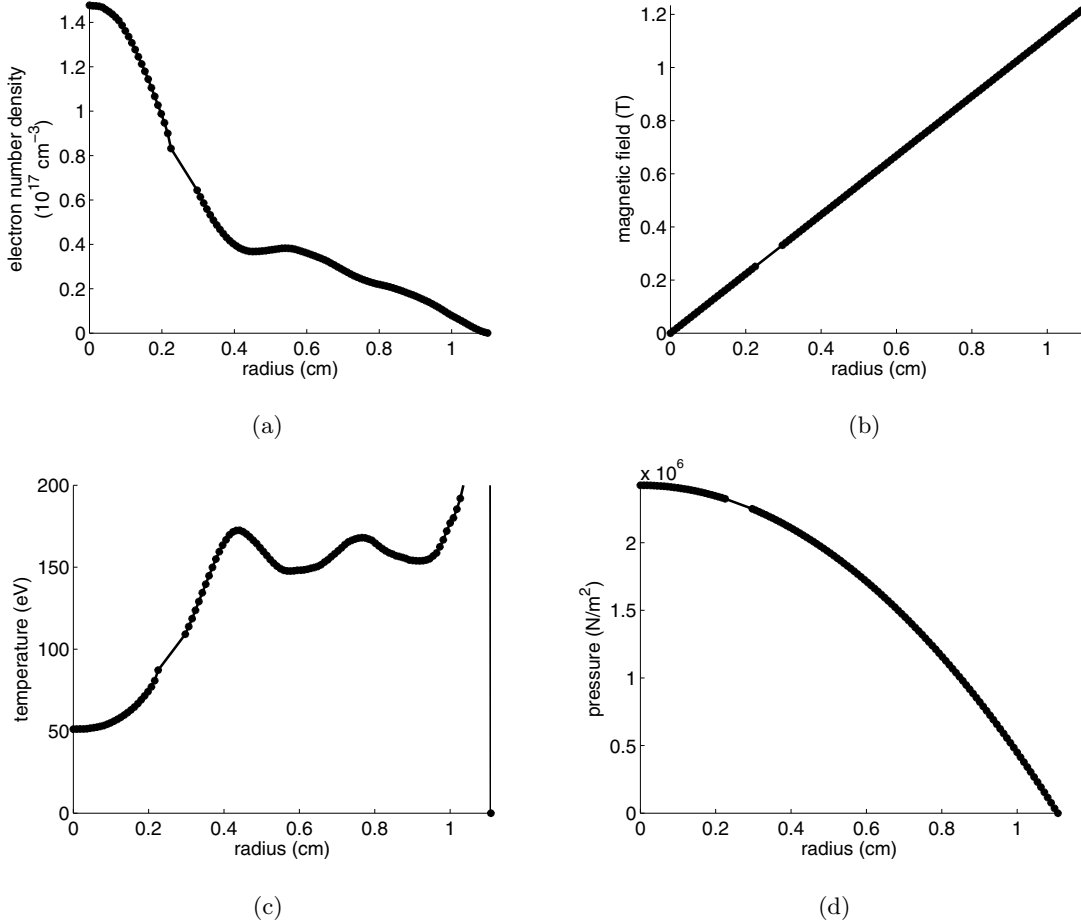


Figure 3.1: Z-pinch equilibrium profiles obtained for a hydrogen Z-pinch with the assumption that the current density is constant. (a) Number density profile input into model. (b) Magnetic field profile. (c) Temperature profile. (d) Pressure profile.

Figures 3.1(a)–3.1(d) show the radial number density profile for a hydrogen Z-pinch and the associated magnetic field, temperature, and pressure profiles that result when the current density across the Z-pinch is assumed to be constant. The number density from the left half ($r < 0$) of Fig. 2.37(b) was used in this case. The resulting temperature profile is less than satisfying, since it is lowest on the axis of the Z-pinch where it should be highest. The temperature also goes to infinity at the edge of the plasma column. This occurs because the constant current density leads to an increasing magnetic field which, according to Eq. 3.5, must be balanced by a decreasing pressure gradient. Equation 3.6 can be rearranged and

differentiated to show the contributions made by the density and temperature and their derivatives to the pressure gradient,

$$\frac{dp}{dr} = (1 + 1/Z) k \left(n \frac{dT}{dr} + T \frac{dn}{dr} \right). \quad (3.7)$$

The density gradient at the edge contributes little to the pressure gradient, so this balance is achieved by the large increase in the temperature.

3.2 Current Density Proportional to Number Density

The current density profile could also be assumed to have the same shape as the electron density profile,

$$j = Cn, \quad (3.8)$$

so that the magnetic field profile in Eq. 3.4 would be calculated from the current density profile,

$$B(r) = \frac{\mu_0}{r} \int_0^r j(r') r' dr'. \quad (3.9)$$

The constant C is obtained using the number density and the Z-pinch current described by Eq. 3.2,

$$C = \frac{I}{\int_0^{2\pi} \int_0^a n(r) r dr d\theta}. \quad (3.10)$$

The Z-pinch radius a in this case is taken to be the radius where the density vanishes. Equations 3.5 and 3.6 are then used to determine the pressure and temperature profiles.

Figures 3.2(a)–3.2(d) show the profiles that result if the current density profile is assumed to be the same as the number density profile. This is equivalent to assuming the quantity j/n is constant across the Z-pinch. The magnetic field profile rises steeply near the axis of the Z-pinch before settling to a relatively constant value of 1.2 to 1.4 T. The temperature profile is hollow, with an on-axis value of 140 eV. It reaches a maximum value of 225 eV near $r = 0.4$ cm before dropping off in the lower-density region outside the core of the Z-pinch.

Several important plasma parameters are apparent from the constant j/n model. These parameters can be compared to those observed in other laboratory plasmas to determine if the results of the model are reasonable. The quantity $C = j/n$ is often referred to as the drift parameter. Its value in this case is $j/n = 6.4 \times 10^{-15}$ A-m, which is close to the

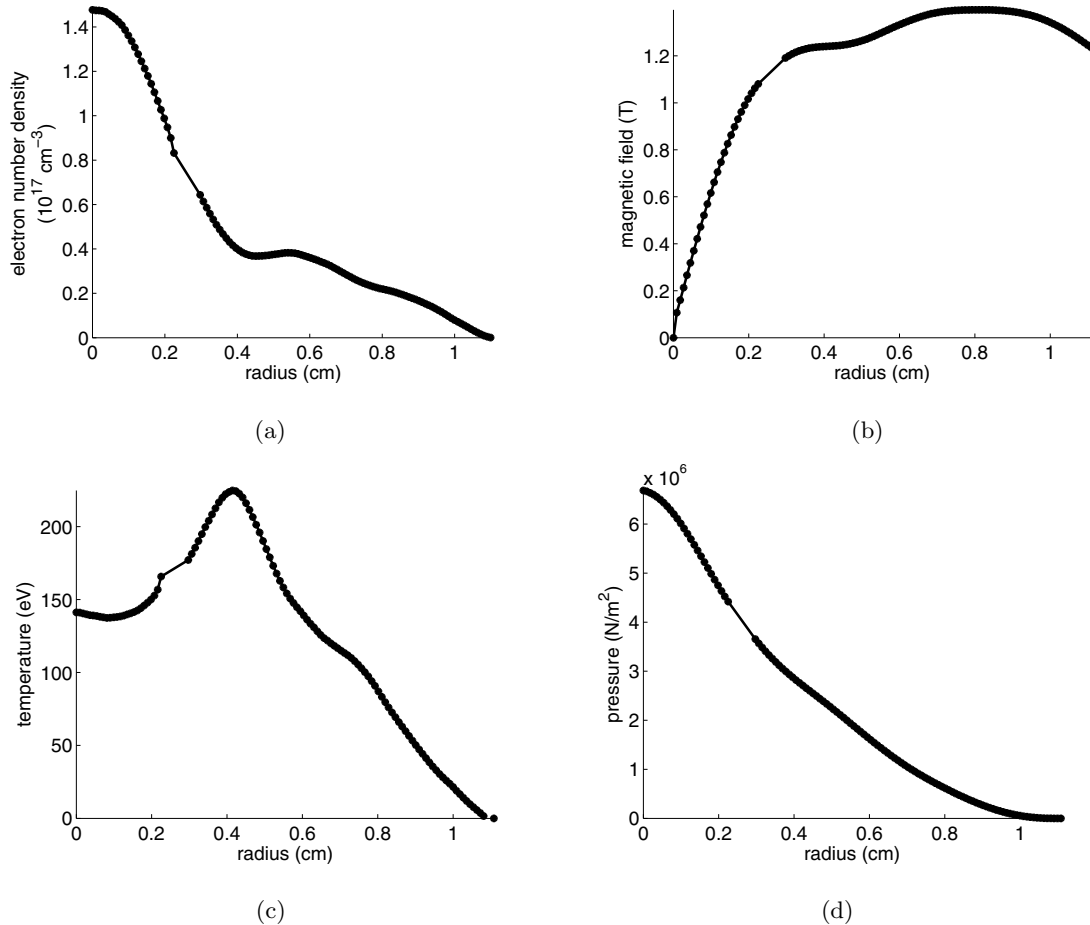


Figure 3.2: Z-pinch equilibrium profiles obtained for a hydrogen Z-pinch with the assumption that the current density is proportional to the number density. (a) Number density profile input into model. (b) Magnetic field profile. (c) Temperature profile. (d) Pressure profile.

typical value of 2×10^{-14} A-m observed to coincide with optimum heating and confinement in many laboratory plasma experiments [2, 29, 41]. The ratio of the electron drift speed to the ion thermal speed is used in the Chodura model to determine the threshold at which anomalous resistivity due to microinstabilities in the plasma becomes significant [9, 10]. The effect of these instabilities is to maintain the ratio of the two speeds to less than or equal to a value of approximately three. The drift parameter can be used to calculate the electron drift speed in the plasma from the relationship

$$v_d = j / (ne), \quad (3.11)$$

where $e = 1.6022 \times 10^{-19}$ C is the elementary charge, which in this case yields a drift speed of approximately 40 km/s. The ion thermal speed in the plasma is

$$v_{i,th} = \left(\frac{kT}{m_i} \right)^{1/2}, \quad (3.12)$$

where $k = 1.6022 \times 10^{-19}$ J/eV is the conversion factor from temperature in electron-Volts to energy in Joules and m_i is the ion mass. For hydrogen, the ion mass is $m_i = 1.6726 \times 10^{-27}$ kg. The ion thermal speed at an average temperature of 100 eV is about 100 km/s. A ratio $v_d/v_{i,th} = 0.4$ is obtained for the hydrogen Z-pinch discussed here. This is below the threshold value of three used in the Chodura model and is therefore reasonable.

The profiles obtained with the constant j/n model are more physically realistic than the profiles obtained with constant current density, since the current density, number density, and temperature all disappear at the edge of the Z-pinch. Several important plasma parameters involved in the model are in line with those for other laboratory plasmas. It is likely, however, that the temperature gradient in the Z-pinch would be reduced by the effects of thermal conduction, causing the profile to be less hollow and reducing the maximum temperature. For that reason, the effects of thermal conduction are investigated by the model described in the next section.

3.3 Limited Perpendicular Thermal Conduction with Uniform Heating

A more refined model of the Z-pinch equilibrium can be obtained by assuming that the conduction of heat out of the Z-pinch determines the temperature profile. This model

is based on a numerical model used by Scudder to calculate Z-pinch equilibrium profiles, including the number density profile [33]. It assumes a steady-state Z-pinch equilibrium where the Z-pinch is embedded in a low-temperature, low-density background plasma that conducts heat away.

The thermal conduction time in the Z-pinch can be compared to the particle flow-through time to assess the importance of thermal conduction and the validity of the model. The cross-field (radial) ion thermal conduction time is given by Haines in terms of the much slower cross-field electron thermal conduction time as

$$\tau_{\kappa_{i\perp}} = \left(\frac{m_e}{m_i} \right)^{1/2} \tau_{\kappa_{e\perp}}, \quad (3.13)$$

where $m_e = 9.1094 \times 10^{-31}$ kg is the electron mass. The cross-field electron thermal conduction time is

$$\tau_{\kappa_{e\perp}} = \frac{3}{2} \frac{nka^2}{\gamma_1^2 \kappa_{e\perp}}, \quad (3.14)$$

where $\gamma_1 = 3.83$ and the cross-field electron thermal conduction coefficient is

$$\kappa_{e\perp} = 0.126 \frac{T^{5/2}}{(\omega_{ce} \tau_{ei})^2} \quad (3.15)$$

for $T = T_e$ in units of electron-Volts. The electron gyrofrequency is

$$\omega_{ce} = \frac{eB}{m_e}, \quad (3.16)$$

and the electron-ion collision time is

$$\tau_{ei} = \frac{12\pi^{3/2}\epsilon_0^2 m_e^{1/2} (kT)^{3/2}}{2^{1/2} \ln \Lambda e^4 Z n}, \quad (3.17)$$

with $n = n_e = Z n_i$. The permittivity of free space is $\epsilon_0 = 8.8542 \times 10^{-12}$ F/m. The appropriate value for the Coulomb logarithm in this case is $\ln \Lambda = 11$. For a typical hydrogen Z-pinch, approximate average values of the density, temperature, magnetic field, and radius are $n = 5 \times 10^{22}$ m⁻³, $T = 100$ eV, $B = 1$ T, and $a = 0.01$ m. Plugging these values into the above equations gives a cross-field ion thermal conduction time of 0.16 μ s. The flow-through time for a 50 cm-long Z-pinch with an axial velocity of 100 km/s is 5 μ s. The density measurements are made half-way down the length of the Z-pinch, so the plasma has 2.5 μ s

to equilibrate by thermal conduction. Since $2.5 \mu\text{s}$ represents sixteen thermal conduction times, thermal conduction is fast enough to significantly affect the Z-pinch equilibrium.

For the thermal conduction model, the total power deposited into the plasma must be balanced by the power conducted out of the Z-pinch,

$$\int_V \dot{q}_{in} dV = \int_S \vec{q} \cdot d\vec{S}. \quad (3.18)$$

The power into the Z-pinch is calculated using the voltage between the inner and outer electrodes (V_{gap}) and the total plasma current (I_p),

$$P_{in} = V_{gap} I_p. \quad (3.19)$$

This quantity is an upper limit on the power deposited into the plasma. It includes ohmic heating in the acceleration region, heating by adiabatic compression as the plasma leaves the assembly region and collapses on axis, and ohmic heating in the Z-pinch. The ohmic heating time for the Z-pinch can be compared to the particle flow-through time to assess the importance of ohmic heating in the Z-pinch relative to the other sources of heat. The ohmic heating time is given by

$$\tau_{OH} = \frac{1}{8} \alpha \mu_0 a^2 k T^{3/2} \quad (3.20)$$

$$= 2.69 \times 10^{-29} a^2 T^{3/2}, \quad (3.21)$$

where $\alpha = 1.1 \times 10^3$ and the temperature is again in units of electron-Volts [15, 16]. For a typical ZaP experiment Z-pinch of radius $a = 0.01 \text{ m}$ and temperature $T = 100 \text{ eV}$, the ohmic heating time is $20 \mu\text{s}$. Since the flow-through time of $5 \mu\text{s}$ is so much shorter than the ohmic heating time required, the bulk of the heat necessary to reach a temperature of approximately 100 eV must be added to the plasma through ohmic heating in the accelerator and adiabatic compression.

The heat deposited into the plasma per unit volume is assumed to be constant across the Z-pinch and given by

$$\dot{q}_{in} = \frac{P_{in}}{\pi a^2 l}, \quad (3.22)$$

where a is the radius of the Z-pinch and $l = 0.5 \text{ m}$ is the length of the Z-pinch. The quantity a is set to the value of the radial coordinate where the density drops to $1 \times 10^{22} \text{ m}^{-3}$, which

is the approximate resolution of the holographic interferometer. The density outside this radius is assumed to be a constant background of $1 \times 10^{22} \text{ m}^{-3}$.

Eq. 3.18, expressed in differential form, is

$$\dot{q}_{in} = \nabla \cdot \vec{q} \quad (3.23)$$

$$= \frac{1}{r} \frac{d}{dr} (rq). \quad (3.24)$$

According to this equation, the heat deposited per unit volume must be balanced by the divergence of the heat conducted radially out of the Z-pinch per unit surface area. This equation can be integrated to obtain

$$\int_0^r r \dot{q}_{in} dr = rq \quad (3.25)$$

$$\frac{r}{2} \dot{q}_{in} = q. \quad (3.26)$$

The heat flux, q , is given by Fourier's Law of Heat Conduction,

$$q = -\kappa_{\perp} \frac{dT}{dr}, \quad (3.27)$$

where κ_{\perp} is the thermal conduction coefficient perpendicular to the magnetic field (in the radial direction). The cross-field ion thermal conduction coefficient is used as the thermal conduction coefficient, since the cross-field electron thermal conduction coefficient is smaller by the square root of the ion-electron mass ratio.

The cross-field ion thermal conduction coefficient must be calculated for the case where the product of the ion cyclotron frequency and the ion-ion collision time, $\omega_{ci}\tau_i$, is not always large and thus finite Larmor radius effects cannot be neglected [33, 5]. The ion gyrofrequency, ω_{ci} , is given by

$$\omega_{ci} = \frac{ZeB}{m_i}. \quad (3.28)$$

The ion collision frequency, τ_i , is given by

$$\tau_i = \frac{12\pi^{3/2}e_0^2 m_i^{1/2} (kT)^{3/2}}{\ln \Lambda e^4 Z^3 n}, \quad (3.29)$$

where $\ln \Lambda = 11$ is the appropriate value of the Coulomb logarithm, the ion number density is assumed to be given by $n_i = n_e/Z = n/Z$, and the ion and electron temperatures are assumed to be equal, so that $T = T_i = T_e$.

The product $\omega_{ci}\tau_i$ is much larger than one across most of the sheared flow Z-pinches produced by the ZaP experiment using hydrogen. Near the axis of the Z-pinch, however, where the magnetic field becomes small, the ion cyclotron frequency also becomes small, and the product $\omega_{ci}\tau_i$ becomes less than one. A similar situation could occur near the edge of the Z-pinch, where the temperature and collision frequency become small. The product $\omega_{ci}\tau_i$ is also less than one across much of the helium Z-pinches because of the factor Z^3 in the denominator of the collision time and the lower temperatures that result from the higher measured electron densities.

Following the method of Braginskii [5], the thermal conduction coefficient is given by

$$\kappa_{\perp} = \frac{nk^2T\tau_i}{Zm_i} \left(\frac{2x_i^2 + 2.645}{\Delta_i} \right) \quad (3.30)$$

$$= a_1 T^{5/2} \left(\frac{2x_i^2 + 2.645}{\Delta_i} \right) \left[\frac{\text{W}}{m \text{ eV}} \right], \quad (3.31)$$

where the quantities x_i and Δ_i are

$$x_i = \omega_{ci}\tau_i \quad (3.32)$$

$$\Delta_i = x_i^4 + 2.70x_i^2 + 0.677, \quad (3.33)$$

and the coefficient a_1 is

$$a_1 = \frac{12\pi^{3/2}\epsilon_0^2 k^{7/2}}{\lambda e^4 Z^4 m_i^{1/2}} \quad (3.34)$$

$$= 1.19 \times 10^{-12} / \left(Z^4 m_i^{1/2} \right) \left[\frac{\text{W}}{m \text{ eV}^{7/2}} \right]. \quad (3.35)$$

Using Eqs. 3.26–3.35, the temperature gradient can be written as

$$\frac{dT}{dr} = -\frac{r\dot{q}_{in}}{2a_1 T^{5/2}} \left(\frac{\Delta_i}{2x_i^2 + 2.645} \right). \quad (3.36)$$

The gradient in the magnetic field can be accounted for by combining Eqs. 3.5 and 3.7 and rewriting the expression to yield

$$\frac{d}{dr}(rB) = -\frac{\mu_0 k(1 + 1/Z) r^2}{rB} \left(n \frac{dT}{dr} + T \frac{dn}{dr} \right). \quad (3.37)$$

Equations 3.36 and 3.37 are the model equations.

The equations are normalized, and a fourth-order Runge-Kutta method written in Matlab is used to solve the system of equations for (rB) and T at each radial location, starting near the axis and moving outward [14]. The radius is normalized by the wall radius, and the number density is normalized by its maximum. The quantity (rB) is normalized by $(r_{wall}B_{wall})$, obtained using the wall radius and the magnetic field at the wall described in Sec. 3.1. The temperature is normalized by the temperature at the axis, which is chosen arbitrarily at first. The initial value of the normalized temperature is one, and the normalized (rB) is set to a very small initial value. The equations are solved across the entire density profile, starting at a point a very small distance from the axis and moving outward. The slight shift in the initial values of r and (rB) avoids problems in Matlab resulting from division by zero at the axis. The on-axis temperature is adjusted and a Newton's Method routine is used to iterate the Runge-Kutta solver until the magnetic field at the edge of the density profile matches the wall field scaled to that radius,

$$B(r_{edge}) = B_{wall}r_{wall}/r_{edge}. \quad (3.38)$$

The Runge-Kutta solver used to find the values of the temperature and (rB) has the form

$$\hat{T}_{i+1} = \hat{T}_i + \frac{\Delta\hat{r}}{6} (F_1 + 2F_2 + 2F_3 + F_4) \quad (3.39)$$

$$F_1 = f \left[\dot{q}_{in,i}, \hat{r}_i, \hat{n}_i, \hat{T}_i, (\hat{r}B)_i \right] \quad (3.40)$$

$$F_2 = f \left[\frac{\dot{q}_{in,i} + \dot{q}_{in,i+1}}{2}, \hat{r}_i + \frac{\Delta\hat{r}}{2}, \frac{\hat{n}_i + \hat{n}_{i+1}}{2}, \hat{T}_i + \frac{\Delta\hat{r}}{2}F_1, (\hat{r}B)_i + \frac{\Delta\hat{r}}{2}G_1 \right] \quad (3.41)$$

$$F_3 = f \left[\frac{\dot{q}_{in,i} + \dot{q}_{in,i+1}}{2}, \hat{r}_i + \frac{\Delta\hat{r}}{2}, \frac{\hat{n}_i + \hat{n}_{i+1}}{2}, \hat{T}_i + \frac{\Delta\hat{r}}{2}F_2, (\hat{r}B)_i + \frac{\Delta\hat{r}}{2}G_2 \right] \quad (3.42)$$

$$F_4 = f \left[\dot{q}_{in,i+1}, \hat{r}_{i+1}, \hat{n}_{i+1}, \hat{T}_i + \Delta\hat{r}F_3, (\hat{r}B)_i + \Delta\hat{r}G_3 \right] \quad (3.43)$$

$$(r\hat{B})_{i+1} = (r\hat{B})_i + \frac{\Delta\hat{r}}{6} (G_1 + 2G_2 + 2G_3 + G_4) \quad (3.44)$$

$$G_1 = g \left[\dot{q}_{in,i}, \hat{r}_i, \Delta\hat{r}_i, \hat{n}_i, \Delta\hat{n}_i, \hat{T}_i, (r\hat{B})_i \right] \quad (3.45)$$

$$G_2 = g \left[\frac{\dot{q}_{in,i} + \dot{q}_{in,i+1}}{2}, \hat{r}_i + \frac{\Delta\hat{r}}{2}, \Delta\hat{r}_i, \frac{\hat{n}_i + \hat{n}_{i+1}}{2}, \Delta\hat{n}_i, \hat{T}_i + \frac{\Delta\hat{r}}{2} F_1, (r\hat{B})_i + \frac{\Delta\hat{r}}{2} G_1 \right] \quad (3.46)$$

$$G_3 = g \left[\frac{\dot{q}_{in,i} + \dot{q}_{in,i+1}}{2}, \hat{r}_i + \frac{\Delta\hat{r}}{2}, \Delta\hat{r}_i, \frac{\hat{n}_i + \hat{n}_{i+1}}{2}, \Delta\hat{n}_i, \hat{T}_i + \frac{\Delta\hat{r}}{2} F_2, (r\hat{B})_i + \frac{\Delta\hat{r}}{2} G_2 \right] \quad (3.47)$$

$$G_4 = g \left[\dot{q}_{in,i+1}, \hat{r}_{i+1}, \Delta\hat{r}_i, \hat{n}_{i+1}, \Delta\hat{n}_i, \hat{T}_i + \Delta\hat{r} F_3, (r\hat{B})_i + \Delta\hat{r} G_3 \right]. \quad (3.48)$$

The functions f and g are Eqs. 3.36 and 3.37, rewritten in terms of the normalized variables, $\hat{r} = r/r_{wall}$, $\hat{n} = n/n_0$, $\hat{T} = T/T_0$, and $(r\hat{B}) = (rB)/(r_{wall}B_{wall})$,

$$f \left[\dot{q}_{in,i}, \hat{r}_i, \hat{n}_i, \hat{T}_i, (r\hat{B})_i \right] = -\frac{\hat{r}\dot{q}_{in}}{2a_1\hat{T}_i^{5/2}} \left(\frac{\Delta_i}{2x_i^2 + 2.645} \right) \frac{r_{wall}^2}{T_0^{7/2}} \quad (3.49)$$

$$g \left[\dot{q}_{in,i}, \hat{r}_i, \Delta\hat{r}_i, \hat{n}_i, \Delta\hat{n}_i, \hat{T}_i, (r\hat{B})_i \right] = -\frac{\mu_0 k (1 + 1/Z) \hat{r}_i^2}{(r\hat{B})_i} \left\{ \hat{n}_i f \left[\dot{q}_{in,i}, \hat{r}_i, \hat{n}_i, \hat{T}_i, (r\hat{B})_i \right] + \hat{T}_i \frac{\Delta\hat{n}_i}{\Delta\hat{r}_i} \right\} \frac{r_{wall}^2 n_0 T_0}{(r_{wall} B_{wall})^2}, \quad (3.50)$$

where $\Delta\hat{r}_i = \hat{r}_{i+1} - \hat{r}_i$ and $\Delta\hat{n}_i = \hat{n}_{i+1} - \hat{n}_i$. These functions describe the gradients of T and (rB) at each point, i , for which the values of r and n are known.

Figures 3.3(a)–3.3(e) show the input density profile and the magnetic field, temperature, pressure, and current density profiles that result for a hydrogen Z-pinch with the thermal conduction model. In general, the behavior of the profiles obtained is physically realistic, but in many ways unlike the behavior of the models described earlier. The temperature is highest at the axis and gradually drops as it approaches the radius, a , beyond which no heat is applied. Outside this radius, the temperature remains constant. In this case, $a = 0.98$ cm, the peak temperature is 95 eV, and the temperature falls to 71 eV at the edge. The current density is highest in the core of the Z-pinch, where the electron number density is highest. Its magnitude is approximately 1.2×10^9 W/m² across much of the Z-pinch. The current density fluctuates near the axis due to the slight offset applied to avoid the singularity at $r = 0$ and is affected near $r = 0.24$ cm by a few missing points in the density

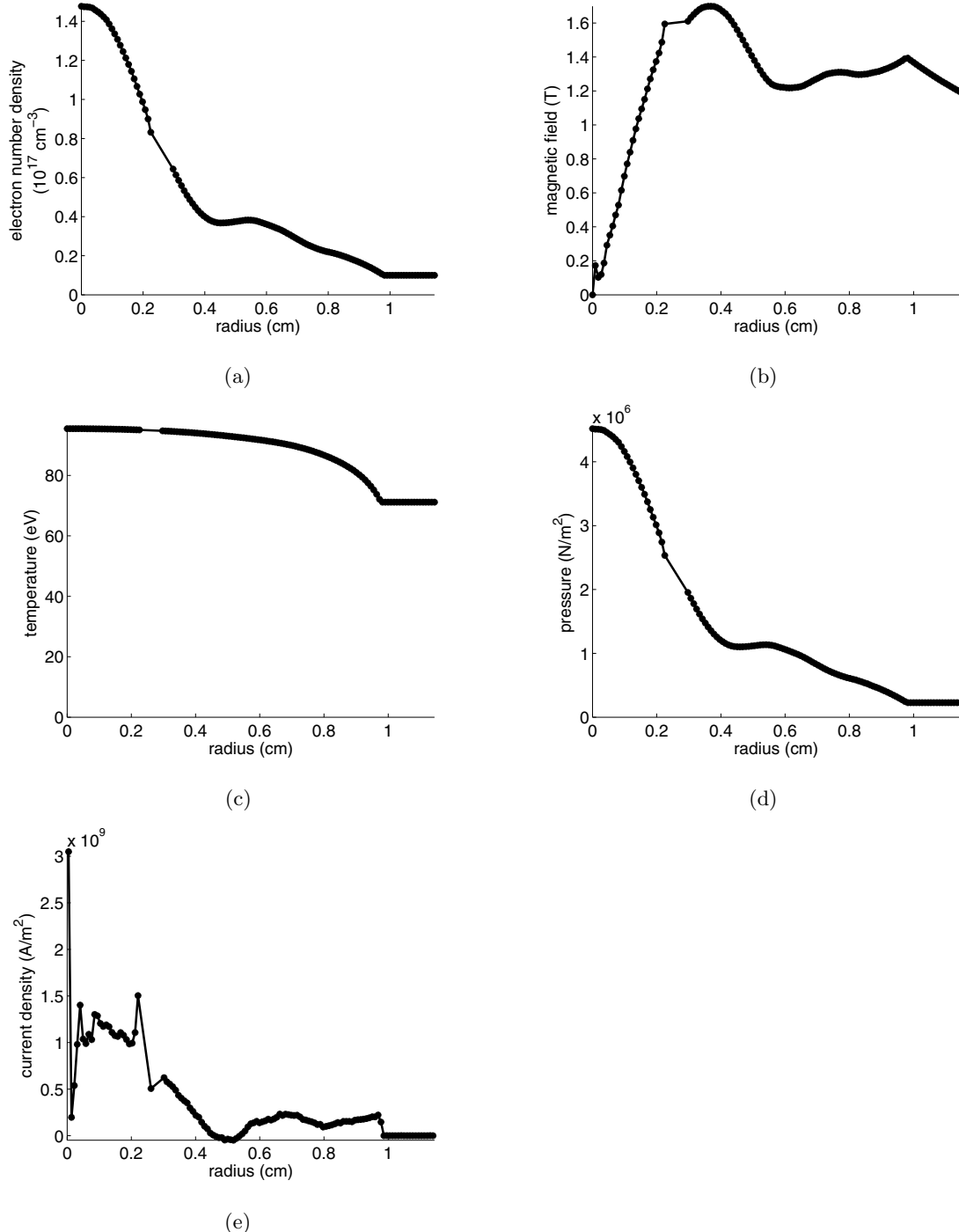


Figure 3.3: Z-pinch equilibrium profiles obtained for a hydrogen Z-pinch obtained using the thermal conduction model. (a) Number density profile input into model. (b) Magnetic field profile. (c) Temperature profile. (d) Pressure profile. (e) Current density profile.

profile. It also becomes briefly negative near $r = 0.5$ cm as a consequence of the inflection in the number density profile near that point. The magnetic field increases steeply to a maximum value of 1.7 T over the region where the number density and current density are highest. As these two quantities decrease, the magnetic field also decreases to a value of 1.2 T and then remains relatively constant over much of the Z-pinch. At the edge of the region where the heat is applied, the magnetic field increases slightly before dropping off as $1/r$. This slight increase is an artifact of the constant background density applied.

Although the model performed well when used with density profiles obtained from hydrogen Z-pinches, it failed to converge or produced physically unrealistic results when helium Z-pinches were studied. This is due primarily to the thermal conduction coefficient values obtained for helium, which were too low to conduct the applied heat out of the Z-pinch. The next section describes a constant temperature model that approximates the flattening effect that thermal conduction has on the temperature profile.

3.4 Constant Temperature

Cross-field thermal conduction is high enough to limit the temperature gradient across the Z-pinch. Equilibrium profiles can be constructed by assuming the temperature profile is uniform and determining its magnitude using the wall magnetic field. No assumption is made about the heat deposited into or conducted out of the Z-pinch, only that thermal conduction within the Z-pinch is high enough to flatten the temperature gradient in the time it takes for the plasma to arrive at the axial location where density measurements are made with the holographic interferometer. This is a reasonable assumption, since the particle flow-through time is much longer than the thermal conduction time computed in the previous section. Any conduction of heat out of the Z-pinch that may occur in the experiment would tend to increase the on-axis temperature and the thermal gradient across the Z-pinch. The temperature calculated here, therefore, represents both a lower limit on and a reasonable estimate of the Z-pinch temperature, and the profiles obtained represent reasonable estimates of the Z-pinch equilibrium profiles.

For a Z-pinch where the temperature profile is constant, the right-hand side of Eq. 3.36

reduces to zero, making it unnecessary. Equation 3.37 becomes

$$\frac{d}{dr}(rB) = -\frac{\mu_0 k(1+1/Z)Tr^2}{rB} \frac{dn}{dr}, \quad (3.51)$$

which is the model equation used.

The equations are normalized, and a fourth-order Runge-Kutta method is combined with a Newton's method to solve for the magnetic field profile and the on-axis temperature in the same way as before. The Runge-Kutta solver used to find (rB) has the form

$$(\hat{rB})_{i+1} = (\hat{rB})_i + \frac{\Delta\hat{r}}{6} (G_1 + 2G_2 + 2G_3 + G_4) \quad (3.52)$$

$$G_1 = g \left[\hat{r}_i, \Delta\hat{r}_i, \hat{n}_i, \Delta\hat{n}_i, \hat{T}, (\hat{rB})_i \right] \quad (3.53)$$

$$G_2 = g \left[\hat{r}_i + \frac{\Delta\hat{r}}{2}, \Delta\hat{r}_i, \frac{\hat{n}_i + \hat{n}_{i+1}}{2}, \Delta\hat{n}_i, \hat{T}, (\hat{rB})_i + \frac{\Delta\hat{r}}{2} G_1 \right] \quad (3.54)$$

$$G_3 = g \left[\hat{r}_i + \frac{\Delta\hat{r}}{2}, \Delta\hat{r}_i, \frac{\hat{n}_i + \hat{n}_{i+1}}{2}, \Delta\hat{n}_i, \hat{T}, (\hat{rB})_i + \frac{\Delta\hat{r}}{2} G_2 \right] \quad (3.55)$$

$$G_4 = g \left[\hat{r}_{i+1}, \Delta\hat{r}_i, \hat{n}_{i+1}, \Delta\hat{n}_i, \hat{T}, (\hat{rB})_i + \Delta\hat{r} G_3 \right], \quad (3.56)$$

where the function g is Eq. 3.51, rewritten in terms of the normalized quantities, $\hat{r} = r/r_{wall}$, $\hat{n} = n/n_0$, $\hat{T} = T/T_0$, and $(\hat{rB}) = (rB)/(r_{wall}B_{wall})$,

$$g \left[\hat{r}_i, \Delta\hat{r}_i, \hat{n}_i, \Delta\hat{n}_i, \hat{T}, (\hat{rB})_i \right] = -\frac{\mu_0 k (1+1/Z) Tr_i^2}{(rB)_i} \frac{\Delta\hat{n}_i}{\Delta\hat{r}_i} \frac{r_{wall}^2 n_0 T_0}{(r_{wall} B_{wall})^2}, \quad (3.57)$$

where $\Delta\hat{r}_i = \hat{r}_{i+1} - \hat{r}_i$ and $\Delta\hat{n}_i = \hat{n}_{i+1} - \hat{n}_i$.

Figures 3.4(a)–3.4(d) show the input density profile and the magnetic field, pressure, and current density profiles that result for a hydrogen Z-pinch with the constant temperature model. The profiles obtained are the most physically realistic and consistent of the four equilibrium profile models used. The magnitude of the temperature is 68 eV. The current density is highest in the core of the Z-pinch, where the electron number density is highest. Its magnitude is approximately 1.0×10^9 W/m² across much of the Z-pinch. The current density fluctuates near the axis due to the slight offset applied to avoid the singularity at $r = 0$ and is affected near $r = 0.24$ cm by a few missing points in the density profile. It also becomes briefly negative near $r = 0.5$ cm as a consequence of the inflection in the number density profile near that point. The magnetic field increases steeply to a maximum value of 1.4 T over the region where the number density and current density are highest. As these

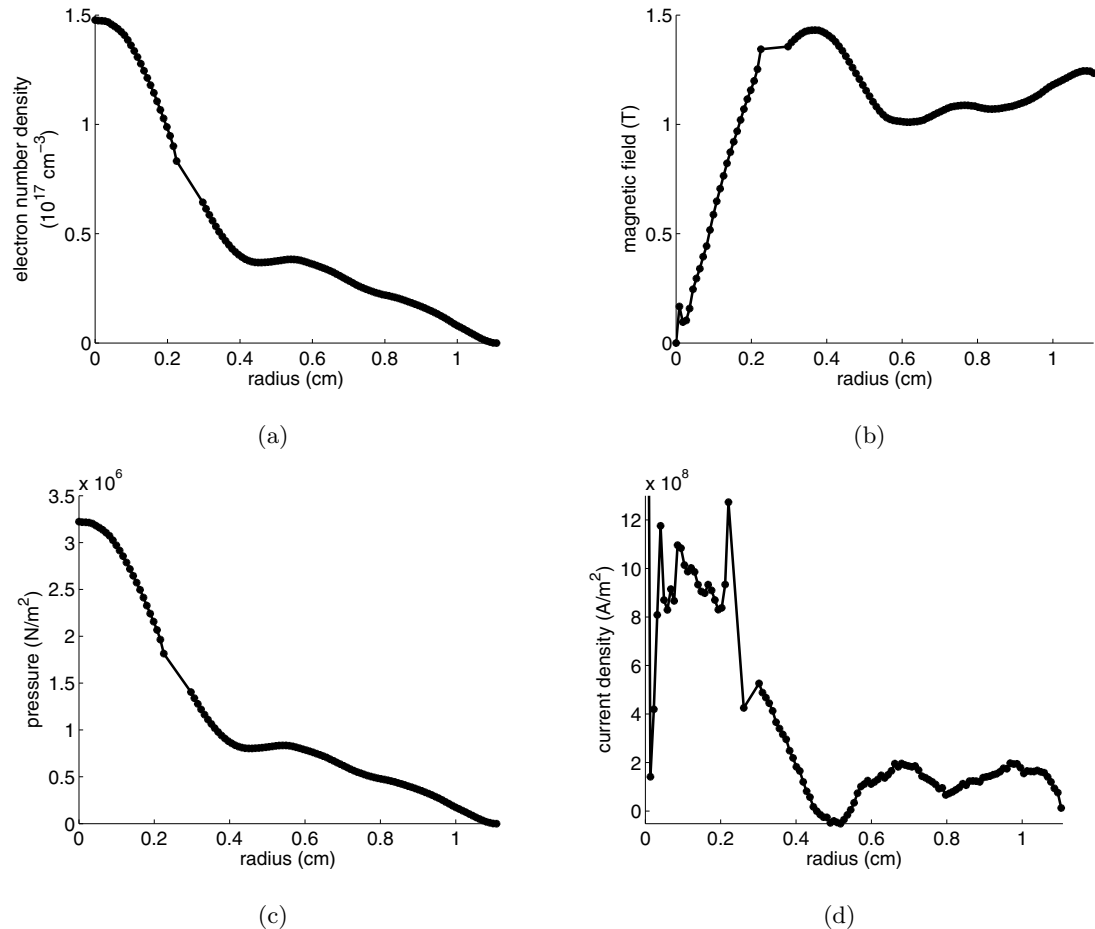


Figure 3.4: Z-pinch equilibrium profiles obtained for a hydrogen Z-pinch obtained using the constant temperature model. (a) Number density profile input into model. (b) Magnetic field profile. (c) Pressure profile. (d) Current density profile.

two quantities decrease, the magnetic field also decreases to a value of 1.0 T. It slowly rises across the rest of the Z-pinch to a value of 1.2 T before dropping off roughly as $1/r$ where the density becomes very low near the edge of the number density profile.

The temperature and magnetic field that result from the model are sensitive to the gradient in the plasma density near the edge of the density profile. If a constant background density of $1 \times 10^{22} \text{ m}^{-3}$ is assumed instead of allowing the density to go to zero at the edge, the results of the constant temperature model become essentially the same as the results of the thermal conduction model, with the exception that the temperature is constant at 99 eV. This occurs because, where the constant density is assumed, the gradient in (rB) becomes zero with the density gradient. From that point, the magnetic field begins to fall off as $1/r$, instead of continuing to increase according to the negative gradient in the density. Since the temperature is set by matching the magnetic field at the edge of the density profile to the wall field scaled to that radius, the temperature in the model is increased to increase the gradient in (rB) . This makes the magnetic field higher at smaller radius, so it can fall off as $1/r$ to the edge and still match the scaled wall field.

Because it produced physically realistic, consistent results for both the hydrogen and helium density profiles studied, the constant temperature model was used to calculate the time evolution of the Z-pinch equilibrium profiles presented in the following sections.

3.5 Time Evolution of Equilibrium Profiles

Figure 3.5 shows magnetic field profiles for helium Z-pinches during the middle of the quiescent period and late in the quiescent period. The model of Sec. 3.4, which assumes a constant temperature across the Z-pinch, was used to calculate these profiles based on the measured density profiles of Fig. 2.41 (Pulses 30204007 and 30204019). A magnetic field profile was not calculated for the density profile obtained after the quiescent period.

The magnetic field profiles that accompany the measured density profiles during the quiescent period show a magnetic field that increases mostly linearly to a maximum value of approximately 1.2 to 1.3 T at a radius of 0.5 to 1.2 cm. Beyond that, the magnetic field drops off and fluctuates around a value of about 1 T to the edge of the density profile. Near $r = 0.5 \text{ cm}$, the magnetic field profile during the middle of the quiescent period decreases

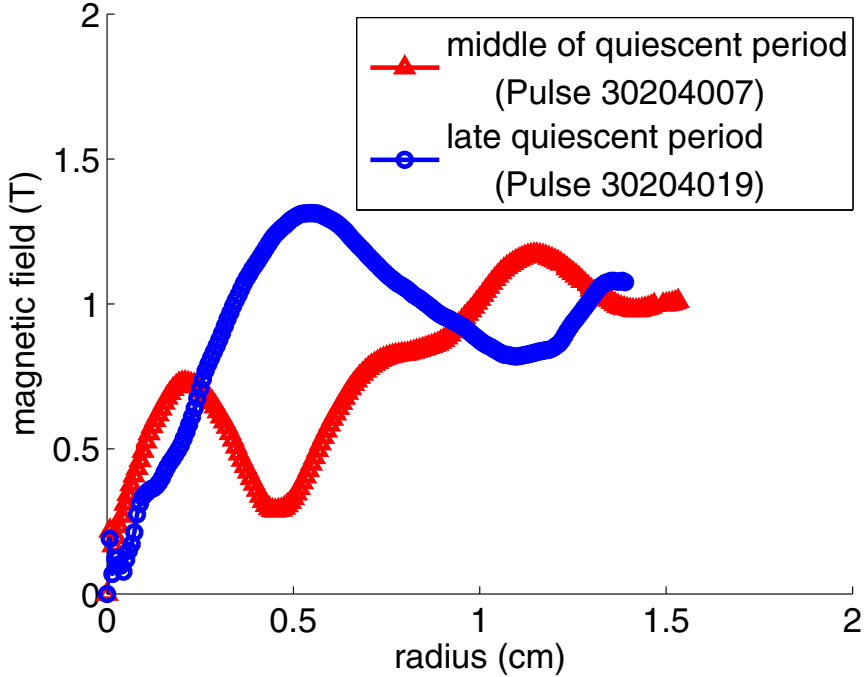


Figure 3.5: Magnetic field profiles for helium Z-pinches during the middle of the quiescent period and near the end of the quiescent period. These profiles were calculated using the measured density profiles of Fig. 2.41 and the constant temperature model described in Sec. 3.4. A temperature of 27 eV was obtained during the middle of the quiescent period with the model, and a temperature of 60 eV was obtained near the end of the quiescent period (Pulses 30204007 and 30204019).

sharply and then increases again due to a dip in the number density profile.

The temperature associated with the high-density helium Z-pinch observed during the middle of the quiescent period is approximately 27 eV. The lower and wider density profile near the end of the quiescent period results in a higher temperature of 60 eV.

3.6 Comparison with Kadomtsev Pressure Profile

As mentioned in Sec. 1.4, a Z-pinch with a pressure profile that falls off less steeply than the Kadomtsev pressure profile will be stable to $m = 0$ perturbations. The Kadomtsev pressure profile is plotted in Figure 3.6 along with two pressure profiles from the experiment. Each of these experimental pressure profiles was obtained using the ideal gas law, Eq. 1.4, a

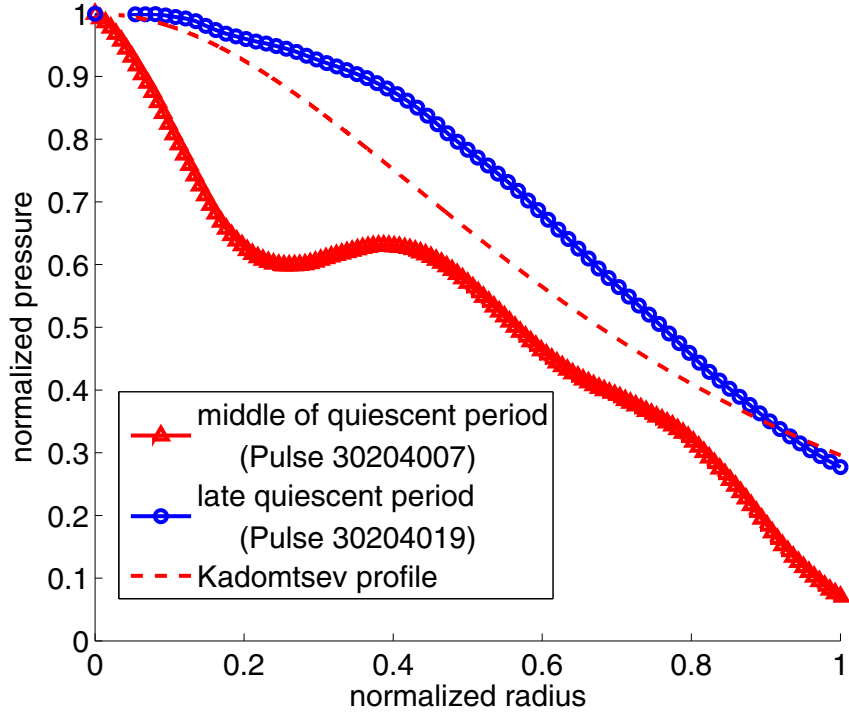


Figure 3.6: Comparison between the Kadomtsev pressure profile and the normalized pressure profiles obtained from the experiment using the constant temperature model described in Sec. 3.4. The pressure profiles obtained during the middle of the quiescent period and near the end of the quiescent period fall off too quickly to stabilize the $m = 0$ “sausage” instability.

density profile measured using the holographic interferometer, and the temperature obtained using the constant temperature model described in Sec. 3.4. Because the temperature is constant, the shapes of the pressure profiles are identical to those of the density profiles used. The pressure profiles are normalized by the on-axis pressure, and the radial coordinate is normalized by the radius where the magnetic field reaches a maximum. Most of the Z-pinch current flows within this radius, so it can be considered the characteristic radius of the Z-pinch. Both pressure profiles fall off more rapidly than the Kadomtsev pressure profile at most points and therefore do not stabilize the Z-pinch against the $m = 0$ “sausage” instability.

Chapter 4

SIMULATION OF DENSITY PROFILE EVOLUTION

A computational study of the density profile evolution was conducted using MACH2. The purpose of the computational study was to model effects not captured by the equilibrium profile calculations described in Chapter 3, such as the geometry of the acceleration region.

MACH2 is a $2\frac{1}{2}$ -dimensional resistive MHD solver [30]. All three components of the simulation quantities are modeled, but may only vary in the \hat{r} and \hat{z} directions.

MACH2 accepts user input in the form of an input file that is divided into “namelists”—lists of input variables divided by category. The contents of the input file are loaded into the appropriate MACH2 variables, and the resistive MHD solver is used to advance the simulation variables at each point in the simulation grid through time, applying additional user-specified physics models such as thermal conduction, radiation, or material ablation, if desired. The contents of the MACH2 input file used for one of the simulations is included in Appendix B.

4.1 *Simulation Geometry*

The simulation geometry is shown in Fig. 4.1. The simulation grid is composed of seven blocks. In the figure, the portion of the grid cells in each block is plotted in a different color so that the boundaries of the blocks are apparent. The locations of the corners of the blocks were specified in the MACH2 input file, in namelist “\$ezgeom.”

4.2 *Boundary Conditions*

Two boundary conditions were set at most external boundaries of the blocks shown in Fig. 4.1. Boundary conditions were not necessary at the border between two blocks, but the number of grid points between the blocks was required to be the same. These boundary

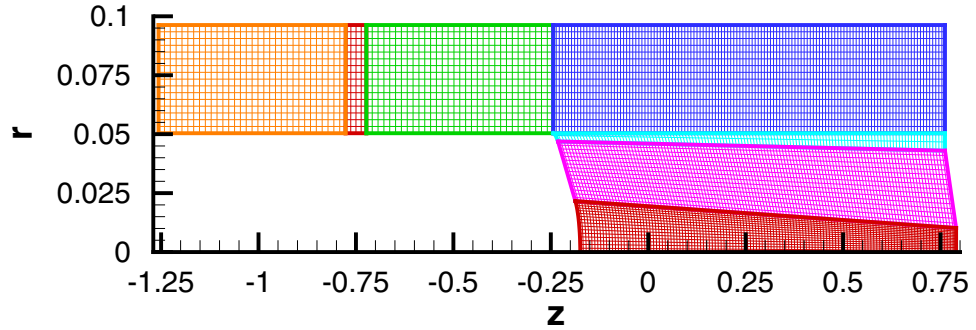


Figure 4.1: Geometry used for the MACH2 simulation, with the radial coordinate axis scaled to show details of the simulation grid. A high-density gas is initialized in the block at $z = -0.75$ m, and the nose cone and end wall hole are included. The simulation geometry can be compared to the experimental geometry shown in Fig. 1.2.

conditions set the values of the various simulation quantities in the layer of ghost cells created just outside the boundaries by MACH2. The first was a hydrodynamic boundary condition, which was set to “wall,” to prevent mass flux across the boundary while placing no constraint on the tangential velocity. Pressure and density are extrapolated from the simulation block with the square of the cell radii to ghost cells. The second was a magnetic boundary condition, which was set to “conductr,” causing rB_θ to be linearly extrapolated from the simulation block into each ghost cell.

More complicated boundary conditions were applied on the blocks along the axis (at $r = 0$ in the figure), along the insulator at the far left of the simulation region ($z = -1.2564$ m in the figure), and at the hole in the end wall ($z = 0.7899$ m). Along the axis, the hydromagnetic boundary condition was set to “axis,” which is the same as the “wall” condition, except that the radial and azimuthal components of the velocity are set to zero. The magnetic boundary condition was also set to “axis,” making B_θ and B_r zero on the axis by setting the ghost cell values equal to the negative of the values in the adjacent real boundary cell. B_z is copied from the real cell to the ghost cell.

Along the insulator, a “flowthru” hydrodynamic boundary condition was used, allowing the temperature and density in the ghost cell to be specified as 1 eV and the 1×10^{-7} kg/m³, the same as the background density. This boundary condition puts no constraint on the

velocity. An “insulatr” magnetic boundary condition is placed on B_θ , setting rB_θ to the value of the current applied at the boundary by the external circuit described in Sec. 4.3. A “symmetric” boundary condition was set for the resistivity on this boundary, causing the resistivity values to be copied from the real cells to the adjacent ghost cells.

At the hole in the end wall, a “flowthru” hydrodynamic boundary condition was also used, with the same ghost cell temperature and density as along the insulator. This effectively allows a vacuum to exist beyond the hole. “Symmetry” magnetic boundary conditions were applied to B_θ and the resistivity, causing rB_θ to be linearly extrapolated and the resistivity to be copied into ghost cells.

4.3 Current Characteristics

A current is applied at $z = -1.2564$ m in Fig. 4.1, across the insulator boundary. The circuit consists of an external 1.36×10^{-3} F capacitor, an external 0.49184×10^{-6} H inductor, and the internal inductance calculated by MACH2 at each time step in the simulation region. The value of the external capacitance matches the eight $170 \mu\text{F}$ capacitors connected in parallel to the experiment. The capacitor’s initial voltage is initialized at 2 to 9 kV to duplicate the charge applied to the capacitor banks in the actual experiment. Originally a value of 1.106×10^{-6} H was calculated for the inductance of the circuit, but the current and voltage waveforms associated with this inductance value did not match the experimental current and voltage waveforms. The external inductance finally used in the simulations was chosen empirically by comparing the current and voltage waveforms that would result from a particular inductance value with the experimental current and voltage waveforms. MACH2 solves for the circuit current and voltage across the insulator boundary at each time step. It is possible, instead, to specify a current waveform for the MACH2 simulation. The decision was made to let MACH2 calculate the current so the current and voltage calculated in the simulation could be compared to the current and voltage measured in the experiment.

Figs. 4.2(a) and 4.2(b) show the current and voltage across the insulator between the inner and outer electrodes in the simulation, plotted along with the experimental current and voltage between the inner and outer electrodes. The initial capacitor charge in both cases is 9 kV. The rise time of the simulation current is similar to that of the experiment.

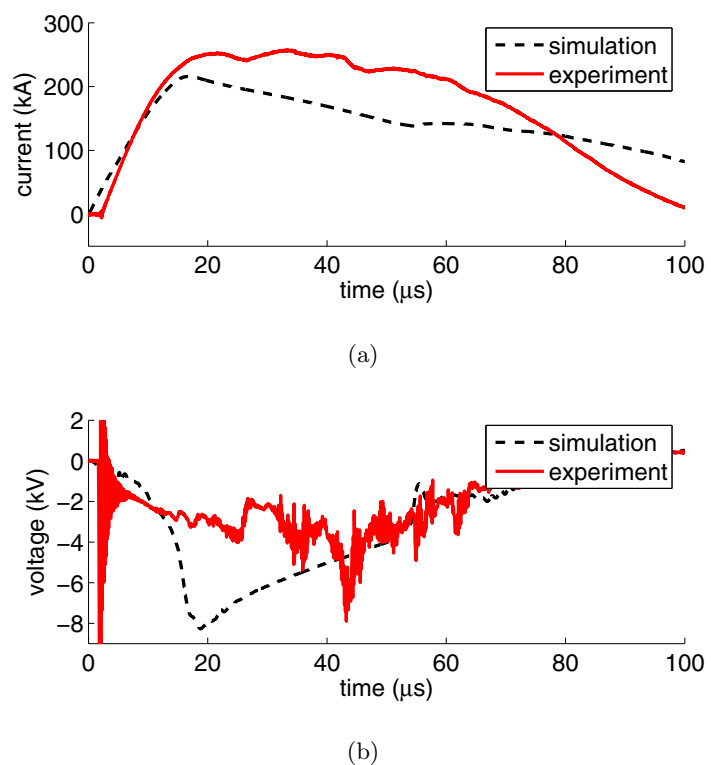


Figure 4.2: Current and voltage across the insulator between the inner and outer electrodes for the simulation and for a plasma pulse (Pulse 40914027). (a) Current. (b) Voltage.

This rise time is largely set by the external inductance and capacitance. After about $15\ \mu\text{s}$, however, the current waveforms diverge, with the simulation current peaking at a lower value.

The voltage waveforms do not match as well as the current waveforms, although their behavior after the voltage spikes at $55\ \mu\text{s}$ are similar. The voltage and current waveforms differ from their experimental counterparts during the first $2\ \mu\text{s}$ of the simulation because MACH2 does not model ionization.

4.4 Initial Conditions

The simulation was generally initialized with an initial mass density of $4.72 \times 10^{-4}\ \text{kg/m}^3$ in the block at $z = -0.75\ \text{m}$, the region that contains the location that corresponds to the gas injection plane in the experiment. This density was assumed to be uniform over the block and corresponds to the mass typically injected into the experiment. The density over the rest of the simulation grid was set to the background density, $1 \times 10^{-7}\ \text{kg/m}^3$. The initial temperature was set to $1\ \text{eV}$ and limited to $200\ \text{eV}$ or less throughout the simulation run. Thermal diffusion was turned off in the simulation, as well. The other initial condition is the capacitor bank voltage, which, as mentioned before, was set to $2\text{--}9\ \text{kV}$ to duplicate the experiment.

4.5 Simulation Results

Contour plots of number density, temperature, rB_θ , and velocity at several times are shown in Figs. 4.3–4.12 for a simulation initialized with a mass density of $4.72 \times 10^{-4}\ \text{kg/m}^3$ and a capacitor bank voltage of $9\ \text{kV}$.

As the simulation begins, magnetic flux diffuses into the simulation region from the insulating boundary at the back of the acceleration region towards the plasma as the plasma expands. $10\ \mu\text{s}$ into the simulation (Fig. 4.3), plasma is pushed along the electrodes in the acceleration region towards the assembly region by Lorentz forces in the accelerator, sweeping up mass along the way. A snowplow effect or blow-by instability develops as the current sheet is accelerated, pushing the majority of the plasma against the outer electrode [8]. A pocket of dense plasma begins to form against the outer electrode, eventually

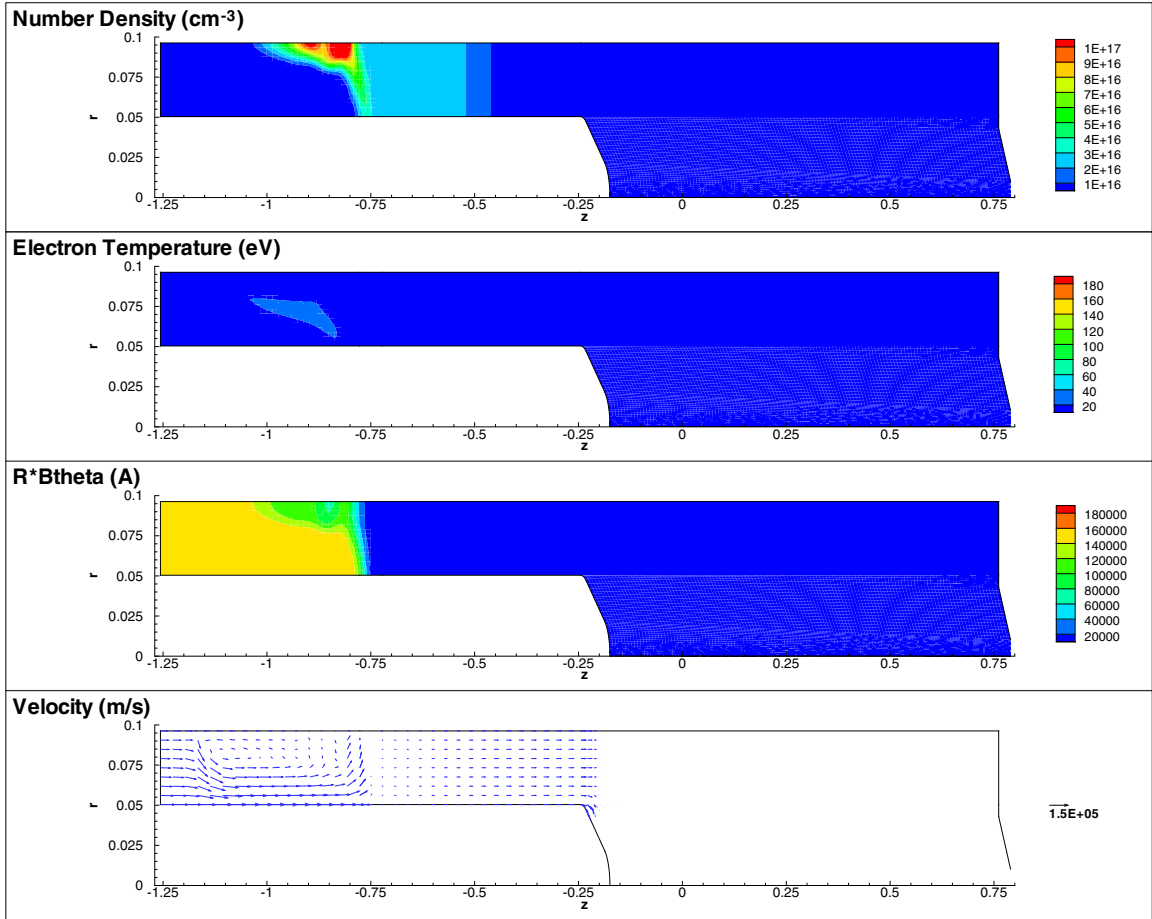


Figure 4.3: Contour plots at $10 \mu\text{s}$ for the simulation with an initial mass density of $4.72 \times 10^{-4} \text{ kg/m}^3$ and a capacitor bank voltage of 9 kV. Magnetic flux diffuses into the simulation region from the insulating boundary at the back of the acceleration region towards the plasma as the plasma expands. Plasma is pushed along the electrodes in the acceleration region towards the assembly region by Lorentz forces in the accelerator, sweeping up mass along the way. A snowplow effect or blow-by instability develops as the current sheet is accelerated, pushing the majority of the plasma against the outer electrode. A pocket of dense plasma begins to form against the outer electrode, eventually extending from $z = -1.25 \text{ m}$ to $z = -0.75 \text{ cm}$.

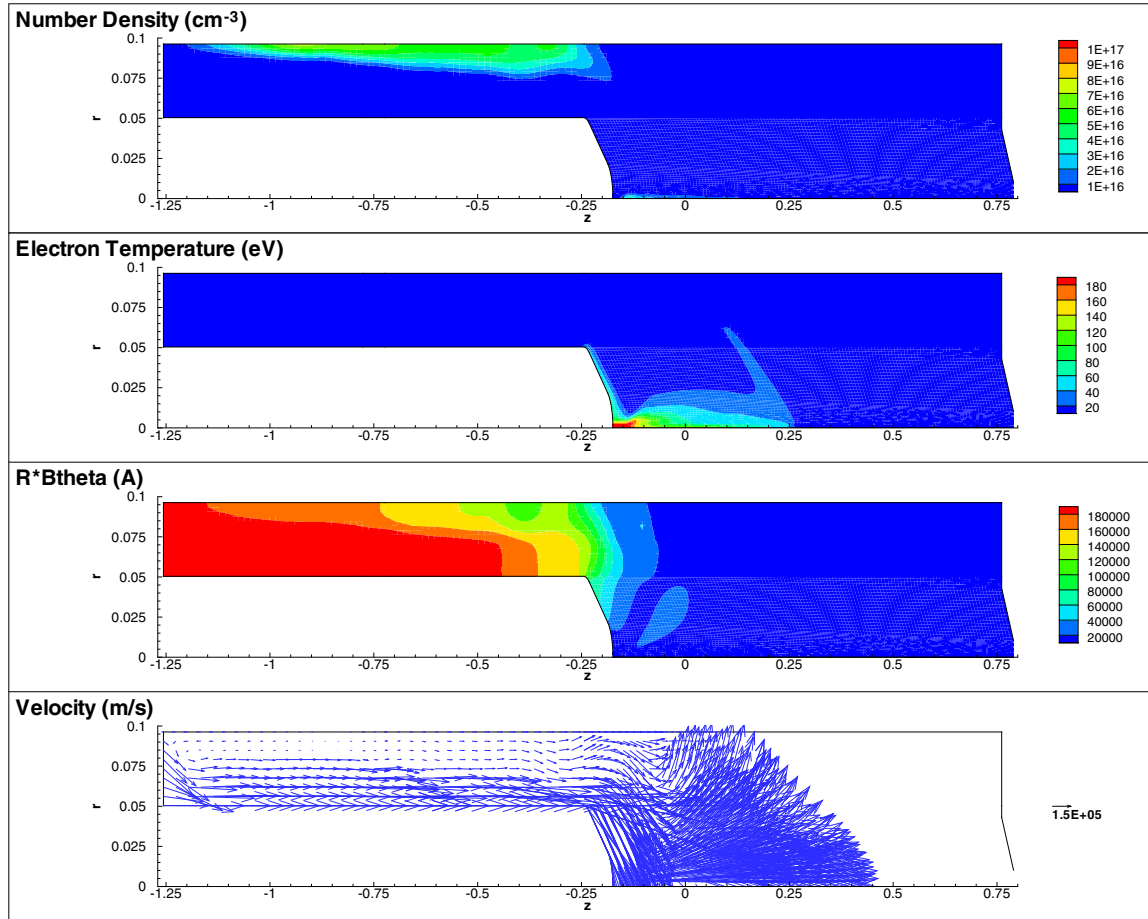


Figure 4.4: Contour plots at $16 \mu\text{s}$ for the simulation with an initial mass density of $4.72 \times 10^{-4} \text{ kg/m}^3$ and a capacitor bank voltage of 9 kV. The plasma reaches the end of the acceleration region and begins to collapse on axis, producing a hot spot at the tip of the inner electrode nose cone. The plasma expands away from this hot spot, radially outward towards the outer electrode and axially towards the outer electrode end wall.

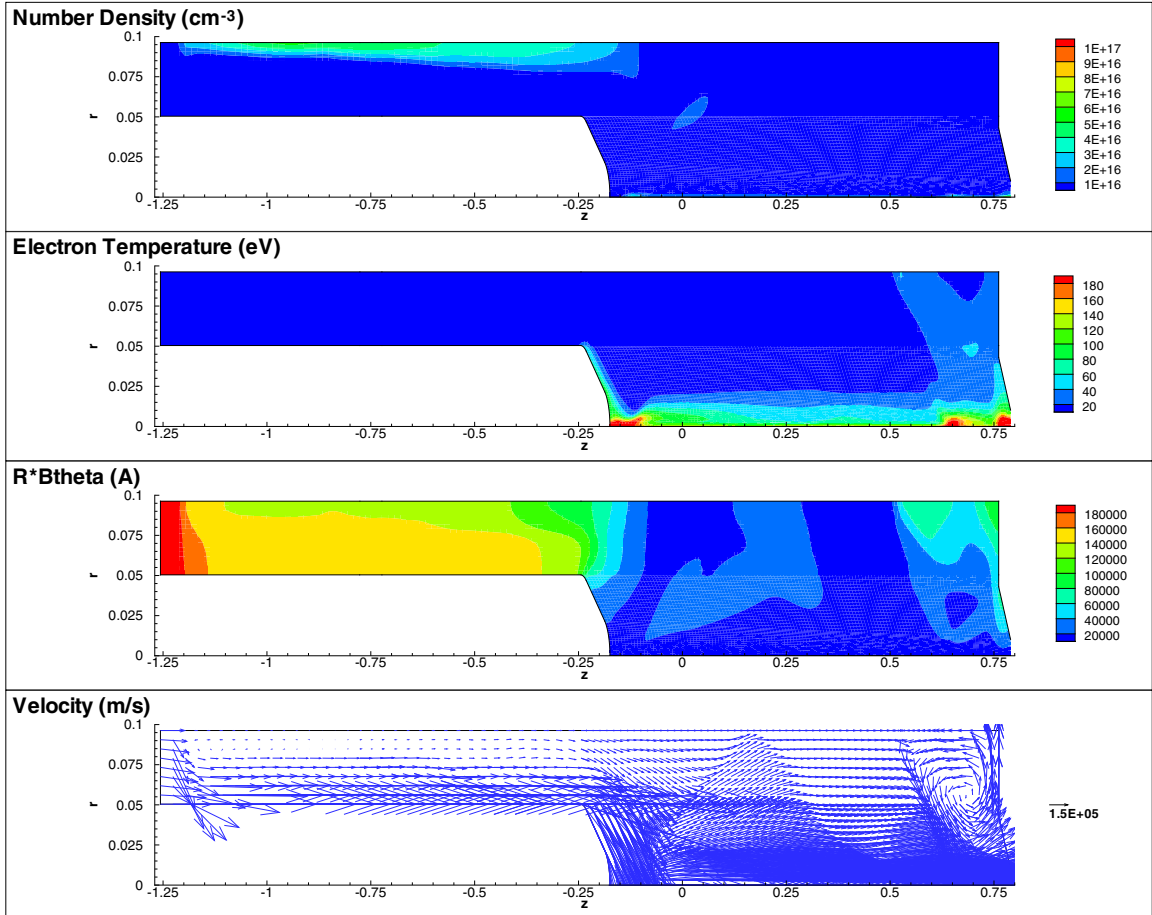


Figure 4.5: Contour plots at $20 \mu\text{s}$ for the simulation with an initial mass density of $4.72 \times 10^{-4} \text{ kg/m}^3$ and a capacitor bank voltage of 9 kV. Plasma fills the assembly region, reaches the end wall, and begins to circulate against the outer electrode. A high-density, high-temperature region forms at the end wall and begins to propagate upstream as the plasma bounces back off the end wall.

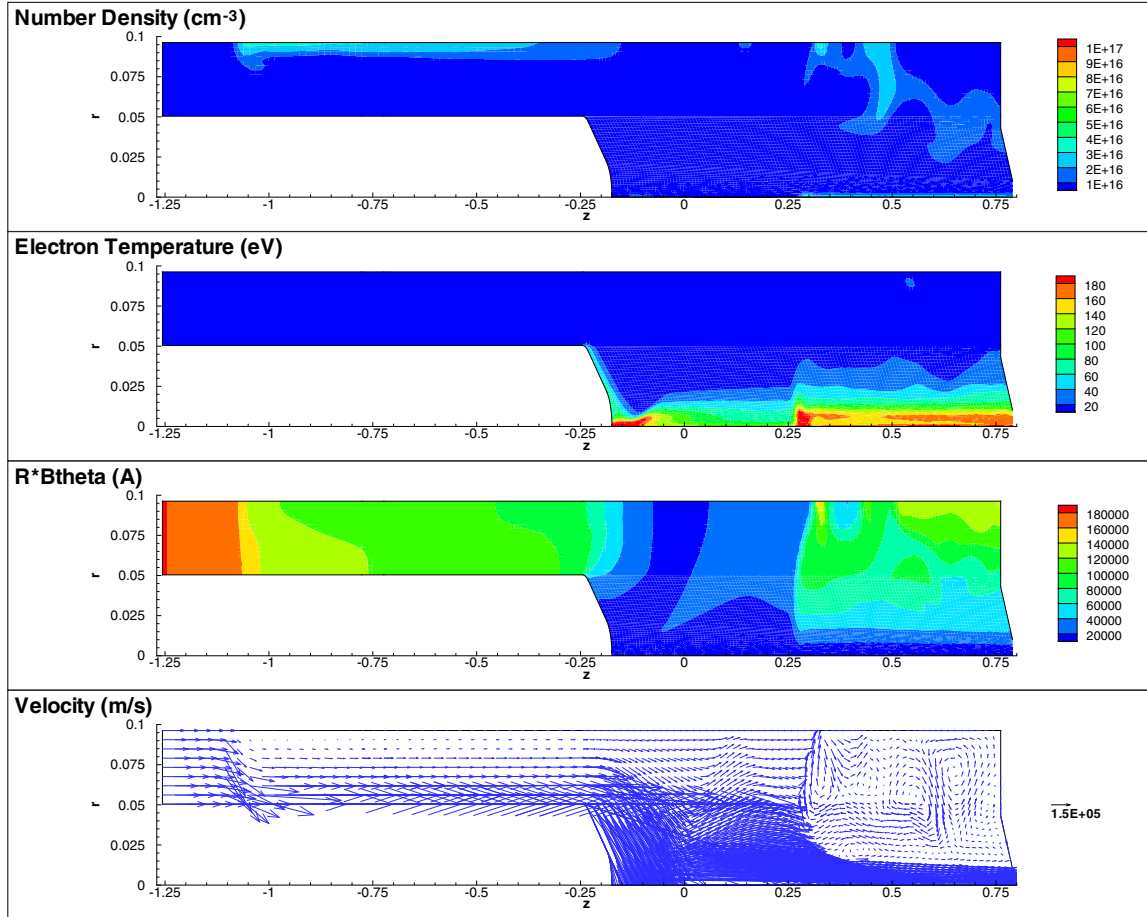


Figure 4.6: Contour plots at $30 \mu\text{s}$ for the simulation with an initial mass density of $4.72 \times 10^{-4} \text{ kg/m}^3$ and a capacitor bank voltage of 9 kV. The high-density, high-temperature region continues to propagate upstream as the plasma bounces back off the end wall. The position of the propagating wave is apparent from the discontinuities in all of the profiles near $z = 25 \text{ cm}$.

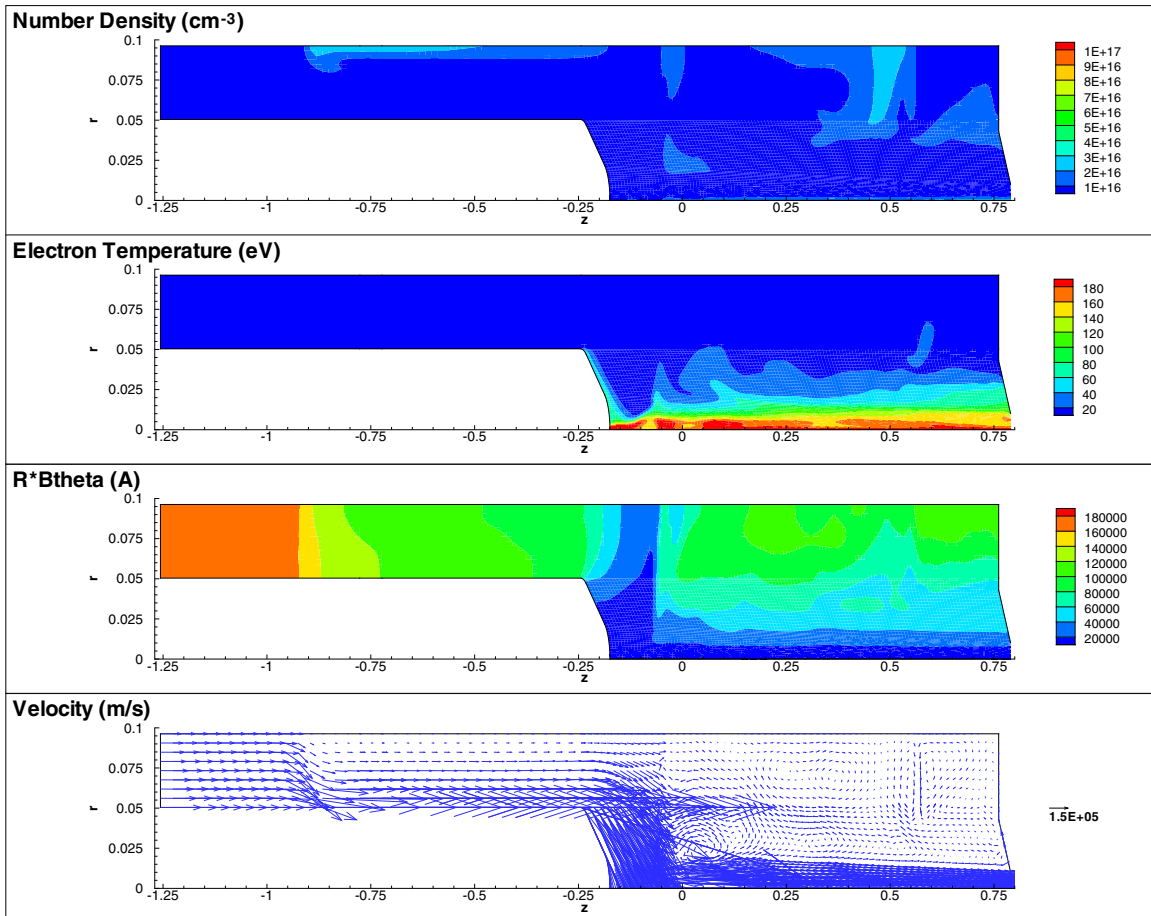


Figure 4.7: Contour plots at $37 \mu\text{s}$ for the simulation with an initial mass density of $4.72 \times 10^{-4} \text{ kg/m}^3$ and a capacitor bank voltage of 9 kV. The wave from the end wall passes $z = 0 \text{ cm}$ and a hot, dense, 100 cm-long Z-pinch is formed along the axis.

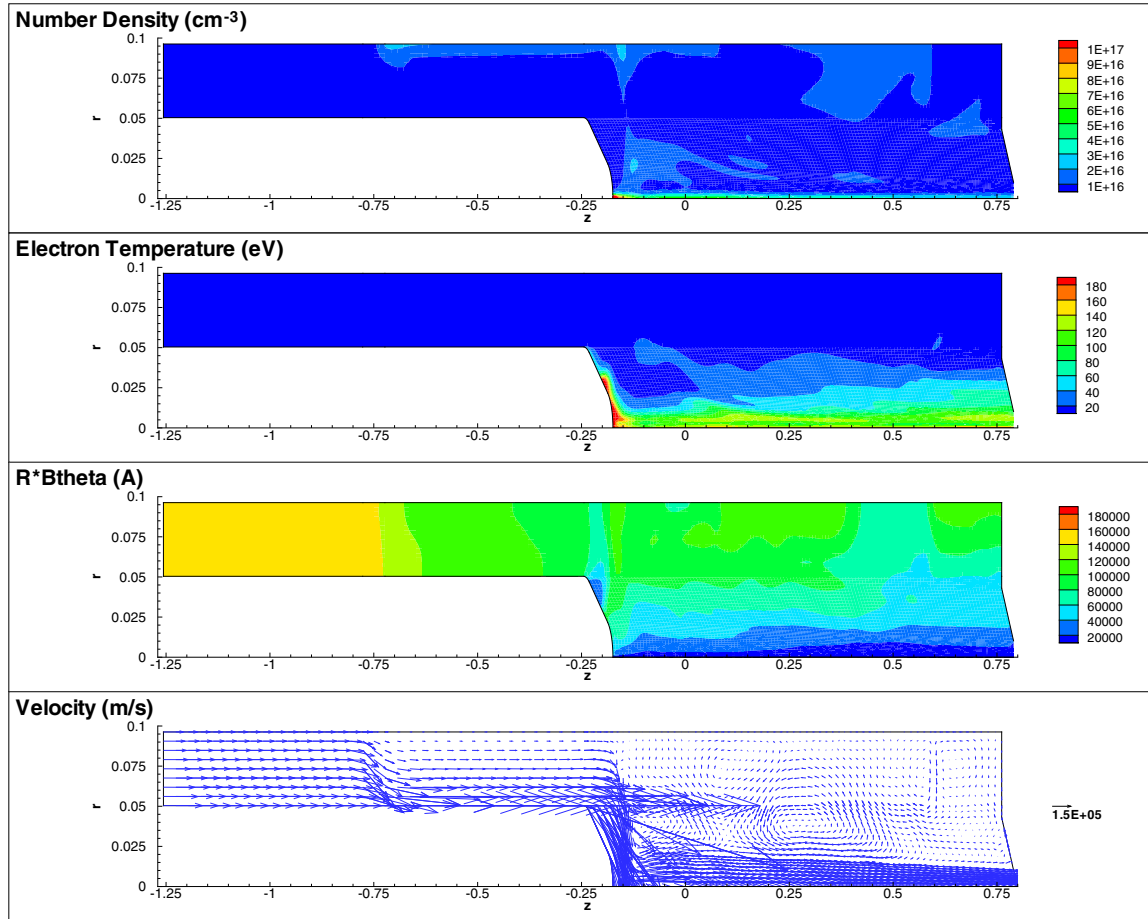


Figure 4.8: Contour plots at $42 \mu\text{s}$ for the simulation with an initial mass density of $4.72 \times 10^{-4} \text{ kg/m}^3$ and a capacitor bank voltage of 9 kV. The wave from the end wall stalls at the nose cone as it hits plasma that continues to be accelerated and leave the acceleration region. The dense Z-pinch persists along the axis as it is fueled by plasma from the accelerator. The Z-pinch also begins to cool.

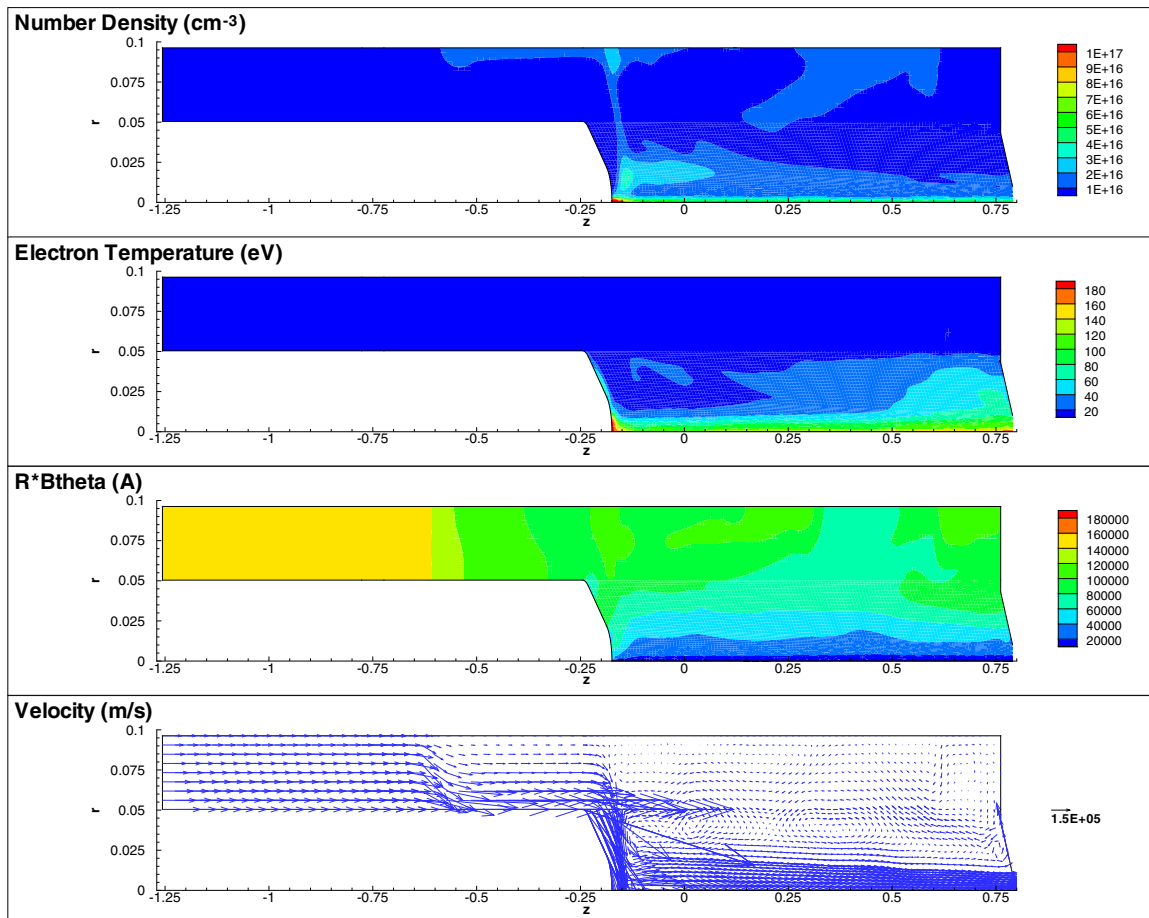


Figure 4.9: Contour plots at $46 \mu\text{s}$ for the simulation with an initial mass density of $4.72 \times 10^{-4} \text{ kg/m}^3$ and a capacitor bank voltage of 9 kV. A dense shoulder develops outside the Z-pinch.

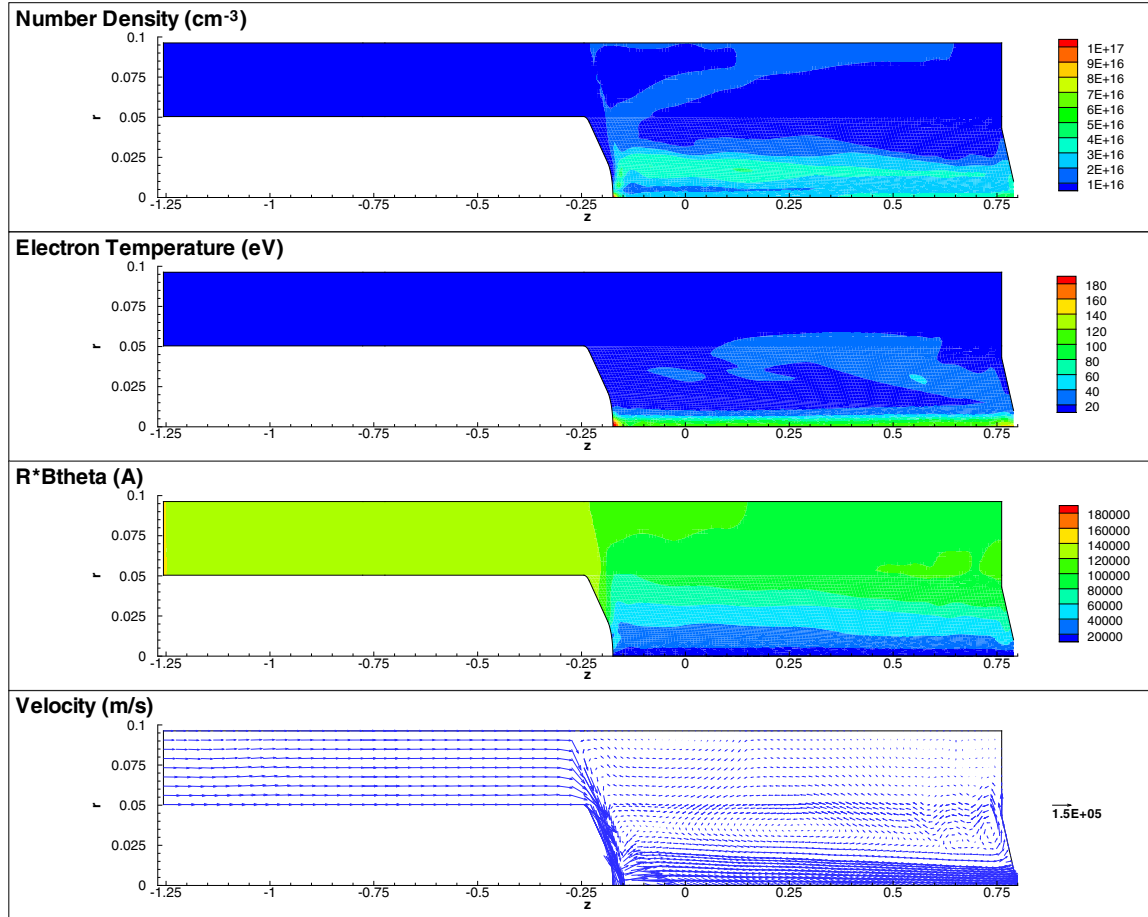


Figure 4.10: Contour plots at $57 \mu\text{s}$ for the simulation with an initial mass density of $4.72 \times 10^{-4} \text{ kg/m}^3$ and a capacitor bank voltage of 9 kV. The plasma in the acceleration region is exhausted and the density of the Z-pinch drops as it is destroyed. The density of the shoulder rises to a value comparable to that along the axis.

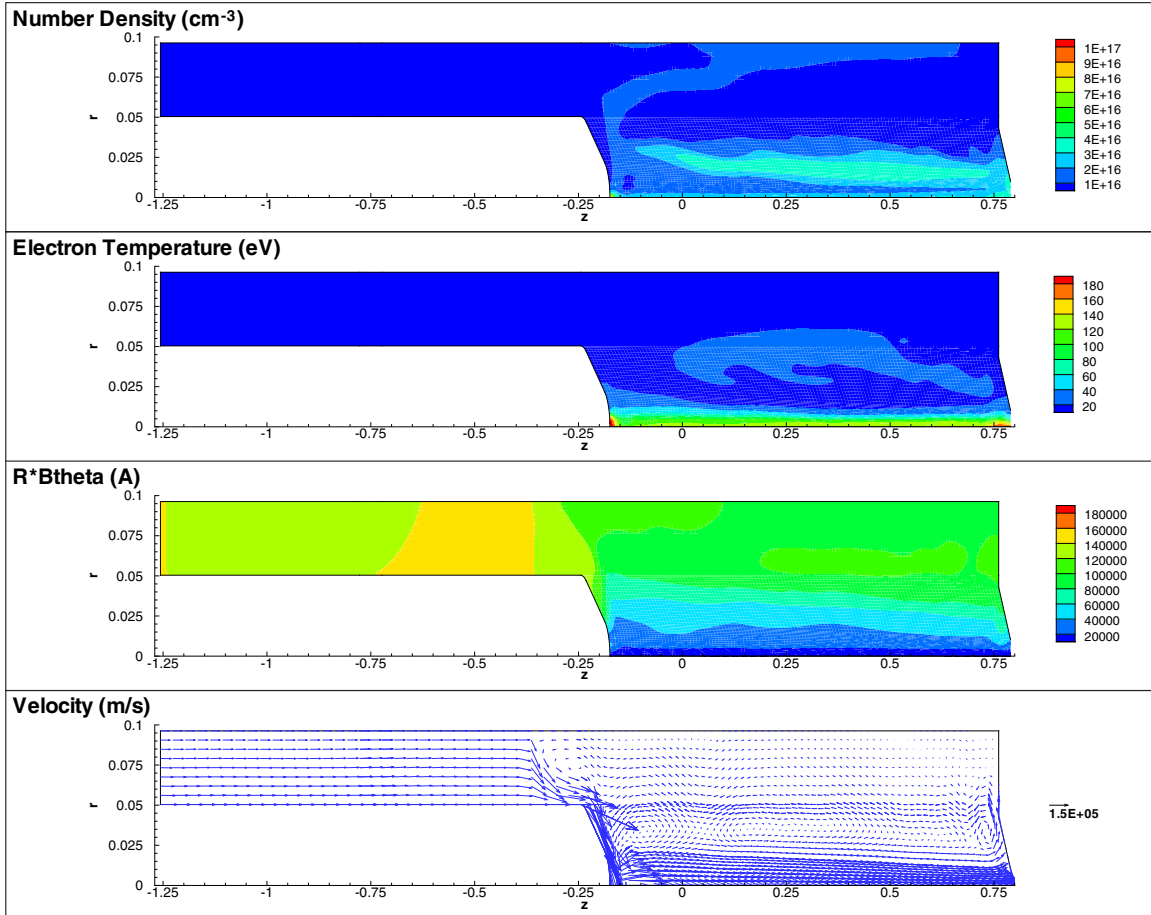


Figure 4.11: Contour plots at $60 \mu\text{s}$ for the simulation with an initial mass density of $4.72 \times 10^{-4} \text{ kg/m}^3$ and a capacitor bank voltage of 9 kV. The wave from the end wall begins to propagate into the exhausted acceleration region, reversing the direction of the velocity vectors in the accelerator. The density along the axis continues to drop.

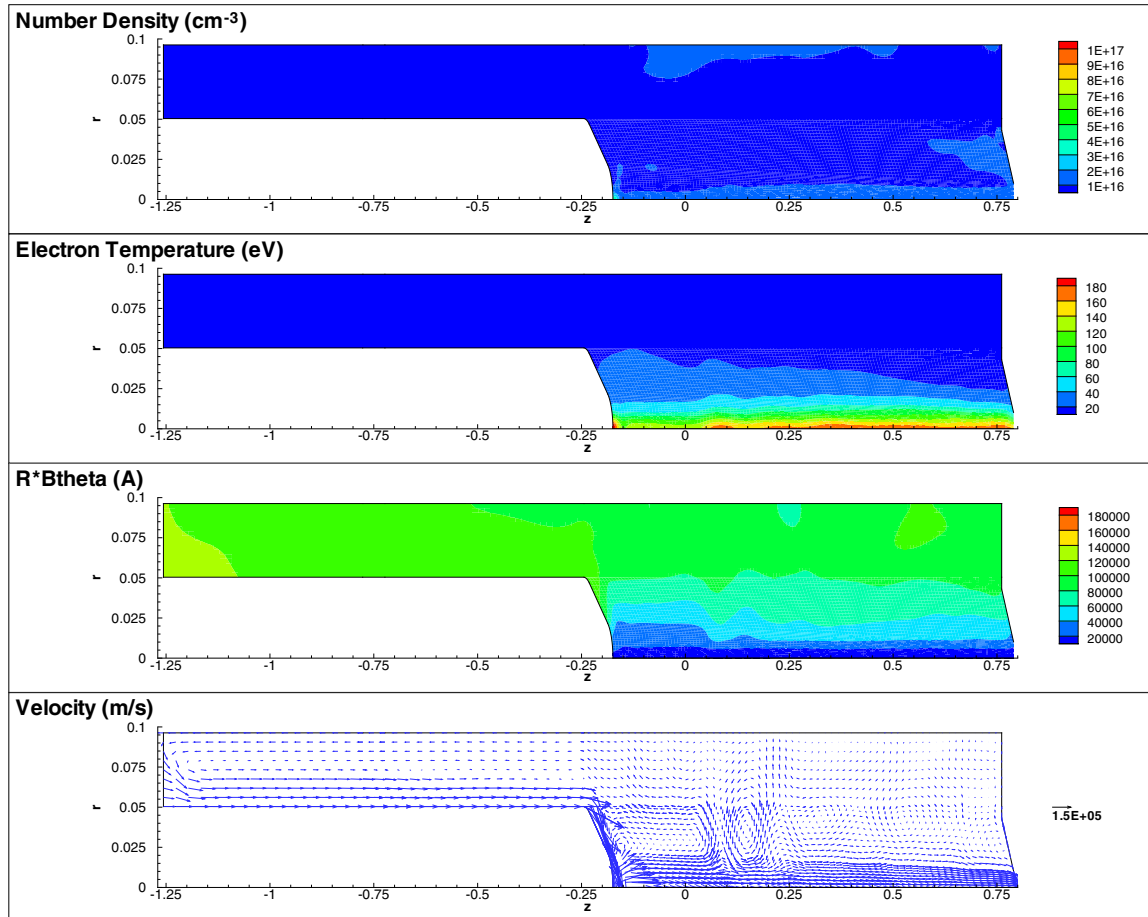


Figure 4.12: Contour plots at $80 \mu\text{s}$ for the simulation with an initial mass density of $4.72 \times 10^{-4} \text{ kg/m}^3$ and a capacitor bank voltage of 9 kV. The wave from the end wall reaches the insulator and the density along the axis continues to drop to the level of the background density.

extending from $z = -1.25$ m to $z = -0.75$ cm.

After $16 \mu\text{s}$ (Fig. 4.4), the plasma reaches the end of the acceleration region and begins to collapse on axis, producing a hot spot at the tip of the inner electrode nose cone. The plasma expands away from this hot spot, radially outward towards the outer electrode and axially towards the outer electrode end wall.

At $20 \mu\text{s}$ (Fig. 4.5), plasma fills the assembly region, reaches the end wall, and begins to circulate against the outer electrode. A high-density, high-temperature region forms at the end wall and begins to propagate upstream as the plasma bounces back off the end wall. The high-density, high-temperature region continues to propagate upstream at $30 \mu\text{s}$ (Fig. 4.6) as the plasma bounces back off the end wall. The position of the propagating wave is apparent from the discontinuities in all of the profiles near $z = 25$ cm. The wave from the end wall passes $z = 0$ cm and a hot, dense, 100 cm-long Z-pinch is formed along the axis at $37 \mu\text{s}$ (Fig. 4.7).

At $42 \mu\text{s}$ (Fig. 4.8), the wave from the end wall stalls at the nose cone as it hits plasma that continues to be accelerated and leave the acceleration region. This sets up a standing wave at the exit of the acceleration region, which helps to deflect plasma towards the axis. The dense Z-pinch persists along the axis as it is fueled by plasma from the accelerator. The Z-pinch also begins to cool. A dense shoulder develops outside the Z-pinch at $46 \mu\text{s}$ (Fig. 4.9). $57 \mu\text{s}$ into the simulation (Fig. 4.10), the plasma in the acceleration region is exhausted and the density of the Z-pinch drops as it is destroyed. The density of the shoulder rises to a value comparable to that along the axis. At $60 \mu\text{s}$ (Fig. 4.11), the plasma in the acceleration region is exhausted, and there is no longer a significant force opposing the upstream propagation of the wave from the end wall into the acceleration region. The wave begins to propagate into the exhausted acceleration region, reversing the direction of the velocity vectors in the accelerator. The density along the axis continues to drop. After $80 \mu\text{s}$ (Fig. 4.12), the wave from the end wall reaches the insulator and the density along the axis continues to drop to the level of the background density.

The simulation was benchmarked by comparing the chord-integrated density and magnetic probe measurements at various locations in the simulation to those measured in the experiment. Figs. 4.13(a)–4.13(c) show the chord-integrated number density from the sim-

ulation at $z = -65$ cm and -25 cm, $z = 0$ cm, and $z = 61$ cm, respectively. The simulated chord-integrated density was calculated using the electron number density at each cell across the simulation region and the Abel integral equation,

$$N_e(y) = 2 \int_y^{\infty} \frac{n_e(r) r dr}{(y^2 - r^2)^{1/2}}, \quad (4.1)$$

where y is the impact parameter of the chord and r is the distance of a point on the chord from the center of the Z-pinch [1, 19]. The closest cell to the desired axial location on each row of the mesh was used, since the axial locations of the cells vary from row to row moving outward from the axis. Figure 4.13(a) shows the simulated chord-integrated density along a chord at $z = -65$ cm and another at $z = -25$ cm. The simulated chord-integrated density rises sharply as the current sheet passes first $z = -65$ cm and then $z = -25$ cm. The large rise in the simulated density well before the current sheet arrives at $z = -65$ cm occurs because ionization is not modeled in the simulation. The particles in the simulation are initialized as a plasma, instead of the neutral gas that is injected into the experiment. The interferometer used on the experiment cannot measure neutral gas density and does not detect the initial expansion of the neutral gas before the current sheet arrives. The arrival of the current sheet at $z = -25$ cm in the simulation may also appear less sharp because of the expansion of what would be neutral gas in the experiment.

Figure 4.13(b) shows the density along two chords at $z = 0$. The arrival of the plasma at this location occurs around $20 \mu\text{s}$. The drop in density along both chords after the current sheet passes is followed by the separation of the measurements along the two chords, indicating the presence of a dense Z-pinch at the axis of the simulation. After the voltage spike at $55 \mu\text{s}$, the density in the simulation slowly decreases, although the overall magnitude of the simulation density remains high. The rise in the chord-integrated density at $z = 61$ cm over time is shown in Fig. 4.13(c).

Simulations were also run with initial capacitor bank voltages lower than 9 kV. The simulated chord-integrated density at the same axial locations is shown in Figs. 4.14(a)–4.14(c) for a 6 kV simulation with the same initial mass density.

Figures 4.15(a) and 4.15(b) show the azimuthal magnetic fields in the 9 kV and 6 kV simulations at the locations of the magnetic probes in the acceleration region. The fields

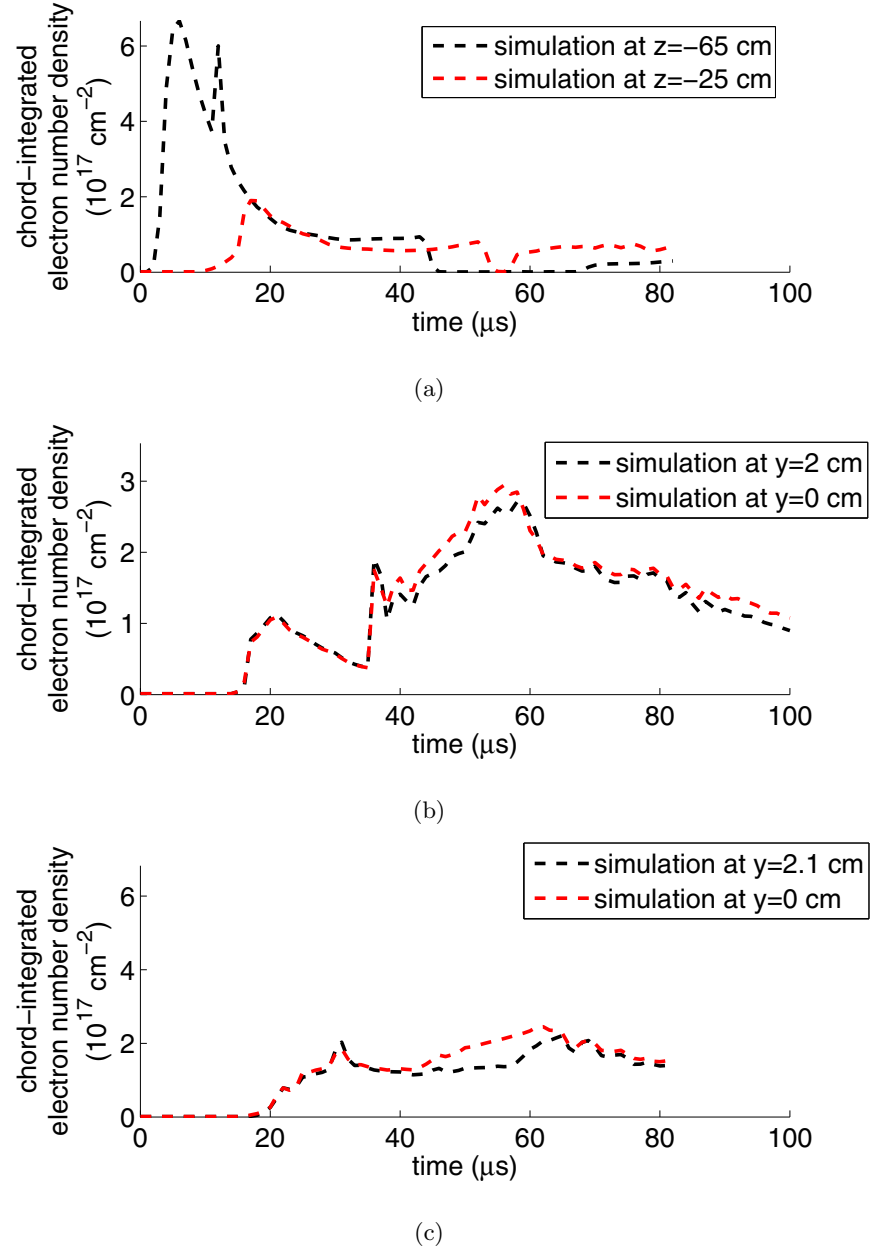


Figure 4.13: Chord-integrated number density at various axial locations from the simulation with an initial mass density of $4.72 \times 10^{-4} \text{ kg/m}^3$ and a capacitor bank voltage of 9 kV. (a) Simulated chord-integrated ion number density in the acceleration region along chords at $z = -65 \text{ cm}$ and $z = -25 \text{ cm}$. (b) Simulated chord-integrated ion number density in the assembly region along chords at axial location $z = 0 \text{ cm}$ and impact parameters $y = 0 \text{ cm}$ and $y = 2 \text{ cm}$. (c) Simulated chord-integrated ion number density in the assembly region near the end wall along chords at axial location $z = 61 \text{ cm}$ and impact parameters $y = 0 \text{ cm}$ and $y = 2.1 \text{ cm}$.

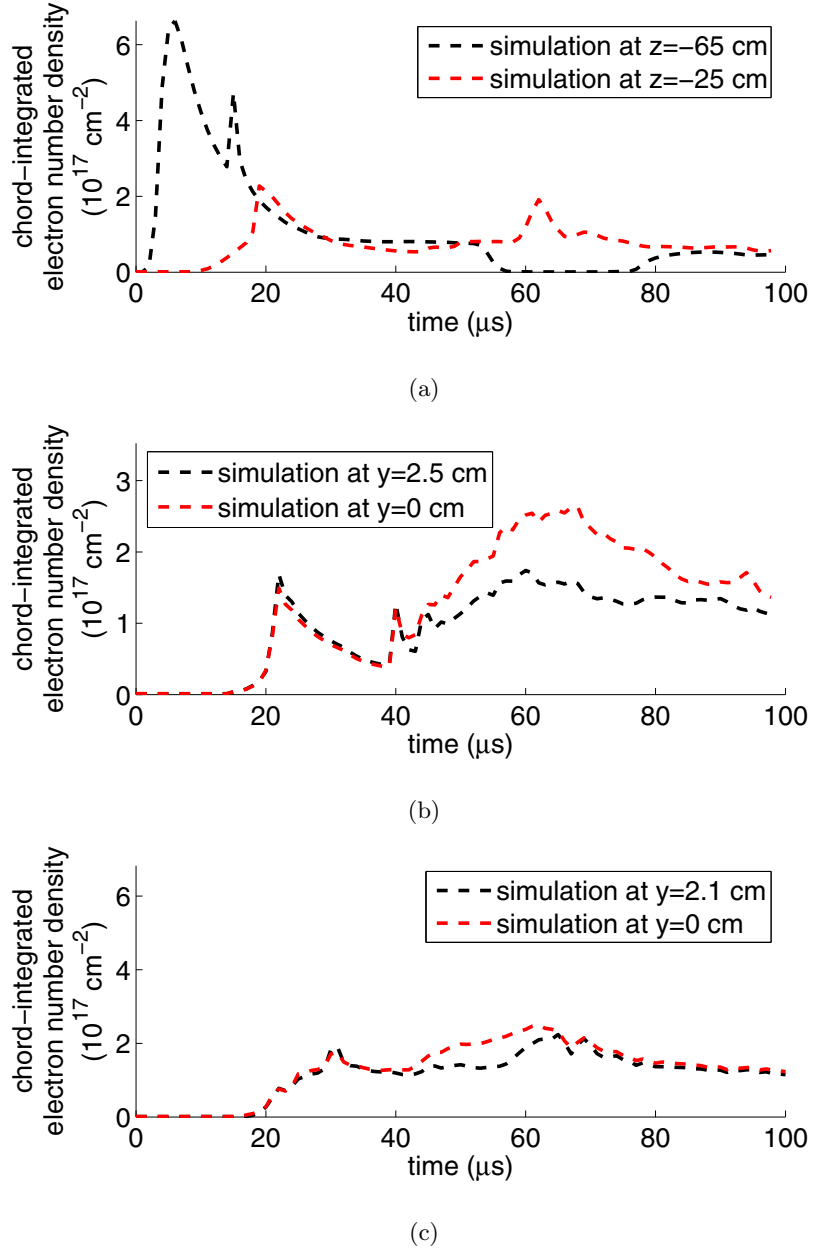


Figure 4.14: Chord-integrated number density at various axial locations from the simulation with an initial mass density of $4.72 \times 10^{-4} \text{ kg/m}^3$ and a capacitor bank voltage of 6 kV. (a) Simulated chord-integrated ion number density in the acceleration region along chords at $z = -65 \text{ cm}$ and $z = -25 \text{ cm}$. (b) Simulated chord-integrated ion number density in the assembly region along chords at axial location $z = 0 \text{ cm}$ and impact parameters $y = 0 \text{ cm}$ and $y = 2 \text{ cm}$. (c) Simulated chord-integrated ion number density in the assembly region near the end wall along chords at axial location $z = 61 \text{ cm}$ and impact parameters $y = 0 \text{ cm}$ and $y = 2.1 \text{ cm}$.

rise sharply at the beginning of the simulation as they soak into the expanding plasma upstream of the gas injection plane at $z = -75$ cm. More insight into modeling of the acceleration region can be gained from the contour plots of the current distribution over time shown in Figs. 4.16(a) and 4.16(b). In the figures, the current past each magnetic probe location in the simulation is normalized by the total current. The result shows what percentage of the total current passes a given magnetic probe along the outer electrode and then attaches downstream through the plasma to return along the inner electrode and produce the magnetic field at the probe, as shown in Fig. 2.8. The locations of the 90, 80, 70, 60, and 50 % lines are plotted as contours versus time, showing the dynamics of the simulated current distribution in the acceleration region. Most of the current flows initially near the gas injection plane, but is quickly swept out of the acceleration region in the current sheet. As the Z-pinch forms, current spreads back into the accelerator and remains there until it is swept out again as the Z-pinch is destroyed. During most of the simulation, half of the total current through the plasma flows in the acceleration region.

4.6 Time Evolution of Equilibrium Profile

Density, magnetic field, and temperature profiles were obtained at various times during the simulation with an initial mass density of 4.72×10^{-4} kg/m³ and a capacitor bank voltage of 9 kV. The time evolution of the density profile in the simulation at $z = 0$ during arrival and formation of the Z-pinch is plotted in Fig. 4.17 at 16, 30, and 37 μ s. The times shown match the times for the contours in Figs. 4.4, 4.6, and 4.7 and can be compared to the experimentally-measured density profiles in Fig. 2.40 during arrival and formation of the Z-pinch. The time evolution of the density, magnetic field, and temperature profiles in the simulation at $z = 0$ is plotted in Figs. 4.18–4.20 at 42, 57, and 60 μ s, corresponding to the time when a dense Z-pinch is present on the axis of the simulation, near the end of that time, and after the dense Z-pinch has begun to fade. The times shown match the times for the contours in Figs. 4.8, 4.10, and 4.11. They can be compared to the profiles based on the experimentally-measured density during the middle of the quiescent period, at the end of the quiescent period, and after the quiescent period shown in Figs. 2.41 and 3.5 and the temperatures calculated in Sec. 3.5. The density values in the cells closest to the

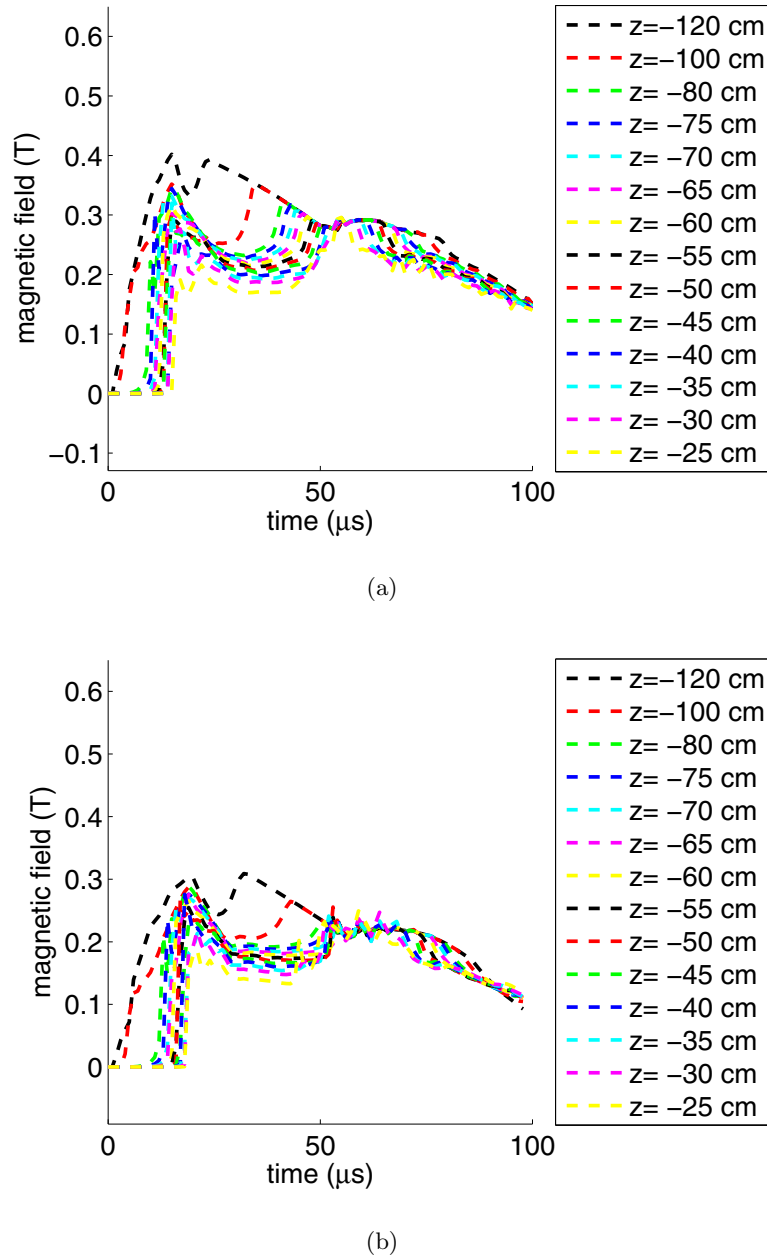


Figure 4.15: Azimuthal magnetic fields at various axial locations in the acceleration region for the 9 kV and 6 kV simulations. (a) Magnetic fields in the 9 kV simulation at $z = -120 \text{ cm}$, $z = -100 \text{ cm}$, etc. (b) Magnetic fields in the 6 kV simulation at $z = -120 \text{ cm}$, $z = -100 \text{ cm}$, etc.

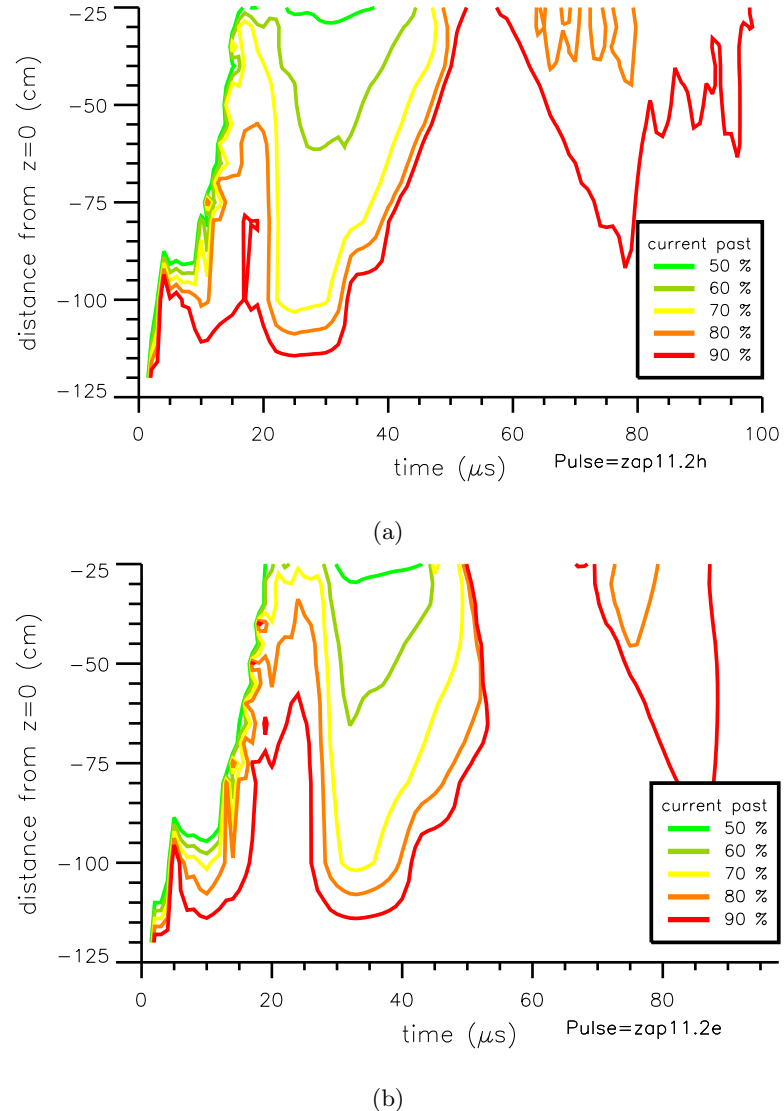


Figure 4.16: Current distribution in the acceleration region for the 9 kV and 6 kV simulations, expressed as percentage of total current passing an axial location along the outer electrode, attaching downstream through the plasma to the inner electrode, and returning through the inner electrode. (a) Current distribution in the 9 kV simulation. (b) Current distribution in the 6 kV simulation.

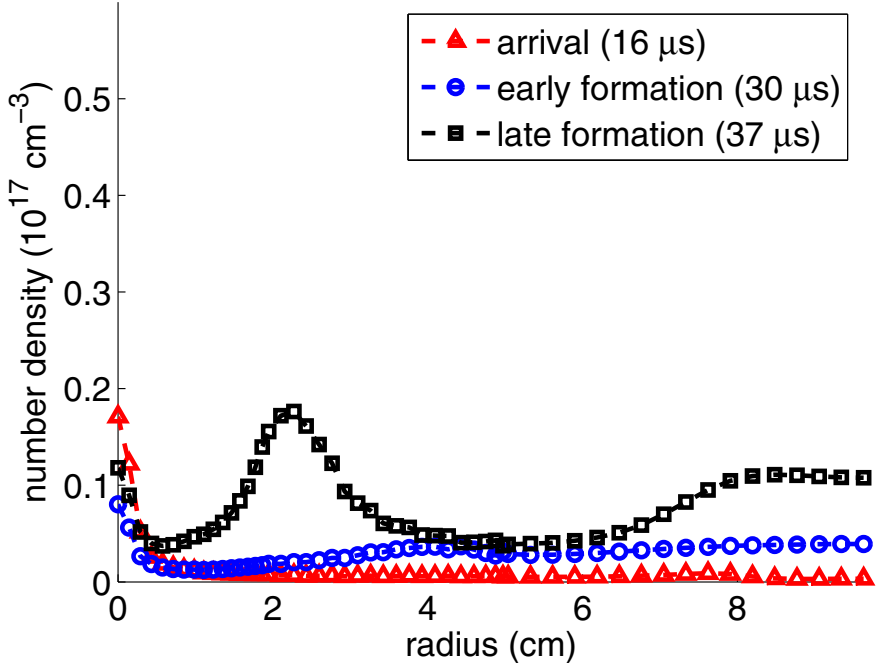


Figure 4.17: Number density evolution from the simulation at 16, 30, and 37 μs , corresponding to arrival and formation of the Z-pinch. The times shown match the times for the number density contours in Figs. 4.4, 4.6, and 4.7 and can be compared to the experimentally-measured density profiles in Fig. 2.40 during arrival and formation of the Z-pinch.

desired axial location on each row of the mesh were again used, as in the earlier case of the chord-integrated density, since the axial locations of the cells vary from row to row moving outward from the axis.

The density is low during early formation of the Z-pinch (25 μs), and rises as the Z-pinch is formed. The density is peaked along the axis, but also develops a shoulder during early formation (39 μs), which is low compared to the on-axis density during the dense Z-pinch period (42 μs), when the peak density is $0.567 \times 10^{17} \text{ cm}^{-3}$. At the end of the dense Z-pinch period, after the voltage spikes around 55 μs , the on-axis density drops as the density in the off-axis shoulder rises (57 μs) and the Z-pinch gradually fades (60 μs).

The narrow magnetic field profile shows that most of the Z-pinch current flows near

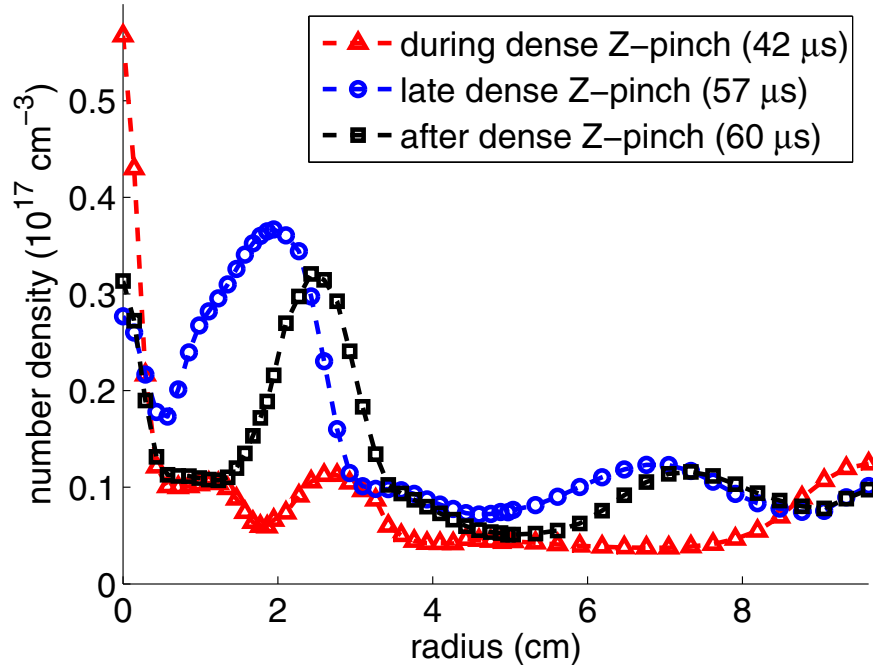


Figure 4.18: Number density evolution from the simulation at $42\ \mu\text{s}$, $57\ \mu\text{s}$, and $60\ \mu\text{s}$, corresponding to during the dense Z-pinch, late dense Z-pinch, and after the dense Z-pinch. The times shown match the times for the number density contours in Figs. 4.8, 4.10, and 4.11 and can be compared to the experimentally-measured density profiles in Fig. 2.41 during the middle of the quiescent period, at the end of the quiescent period, and after the quiescent period. The peak density at $42\ \mu\text{s}$ is $0.567 \times 10^{17}\ \text{cm}^{-3}$.

the axis. The peak magnetic field at $42\ \mu\text{s}$ is $1.8\ \text{T}$, and drops as the dense Z-pinch fades. The temperature profile is peaked and drops only slightly over time, with some small-scale structure apparent at $42\ \mu\text{s}$. The peak temperature at $42\ \mu\text{s}$ is $145\ \text{eV}$.

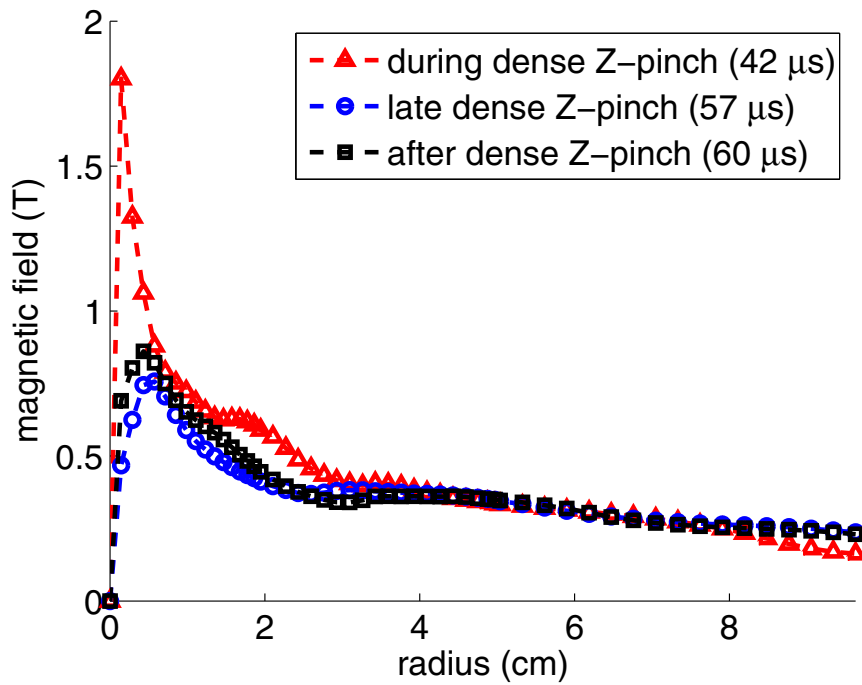


Figure 4.19: Magnetic field profile evolution from the simulation at 42, 57, and 60 μ s, corresponding to during the dense Z-pinch, late dense Z-pinch, and after the dense Z-pinch. The times shown match the times for the rB_θ contours in Figs. 4.8, 4.10, and 4.11 and can be compared to the magnetic field profiles in Fig. 3.5 calculated from the measured density during the middle of the quiescent period and at the end of the quiescent period. The peak magnetic field at 42 μ s is 1.8 T.

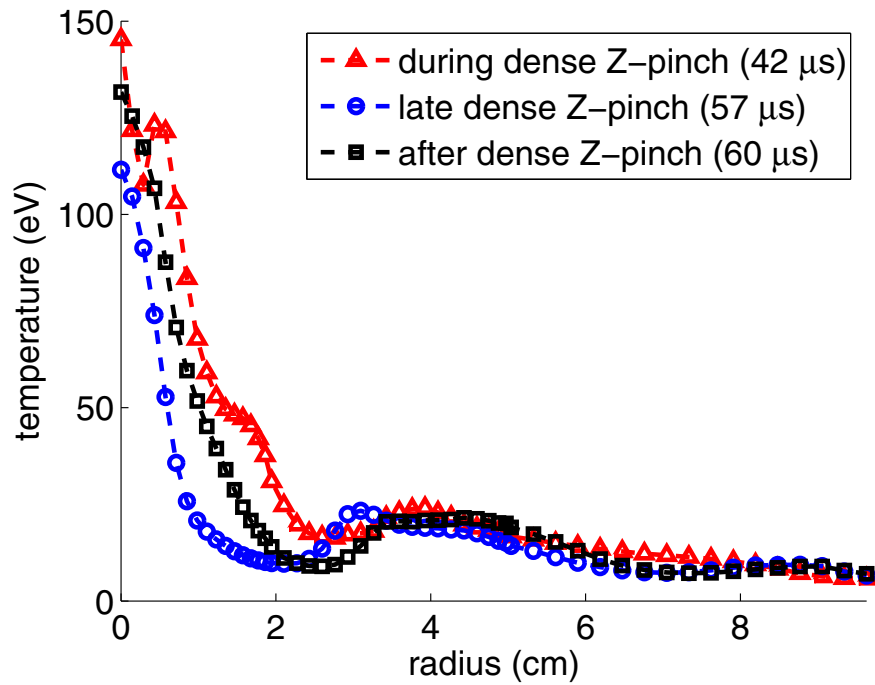


Figure 4.20: Temperature profile evolution from the simulation at 42 , 57 , and 60 μs , corresponding to during the dense Z-pinch, late dense Z-pinch, and after the dense Z-pinch. The times shown match the times for the temperature contours in Figs. 4.8, 4.10, and 4.11 and can be compared to the temperatures in Sec. 3.5 calculated from the measured density during the middle of the quiescent period and at the end of the quiescent period. The peak temperature at 42 μs is 145 eV.

Chapter 5

INFLUENCE OF EXPERIMENTAL PARAMETERS

The influence of the capacitor bank voltage and the amount of neutral gas injected on the behavior of the sheared-flow Z-pinch was studied in an effort to understand the processes involved in its sustainment and destruction. The normalized $m = 1$ mode and density measurements of Figs. 2.25(a) and 2.25(b) show that the end of the quiescent period is correlated with the exhaustion of plasma in the accelerator. The amount of gas injected initially into the experiment was used to test the theory that the depletion of gas in the accelerator leads to the end of the quiescent period [20]. The capacitor bank voltage was also changed to determine its effect on the length of the quiescent period and the density of the Z-pinch.

The depletion of gas in the acceleration region is a gradual process. Some, but not all, of the gas is picked up and entrained in the initial current sheet as it passes by on its way along the space between the electrodes towards the assembly region. The rest of the gas is left behind to be ionized over time and then accelerated out of the acceleration region and into the Z-pinch. When more gas is injected into the acceleration region, it should take longer for all of that gas to be ionized and pushed out of the acceleration region. The amount of gas injected was controlled by changing the gas line pressure. As shown in Fig. 5.1, the total number of particles injected increases with the gas line pressure. These values were obtained experimentally by using each of five gas puff circuits individually to puff gas into the experiment after closing a gate valve to shut off the experiment from the vacuum pumps. The four outer gas puff circuits control two valves each that puff gas radially inward through the outer electrode into the acceleration region. The inner gas puff circuit controls one valve that puffs gas radially outward through the inner electrode into the acceleration region. The ideal gas law and the volume of the experiment were then used to calculate the total number of particles injected. Ten measurements were made for each gas puff circuit,

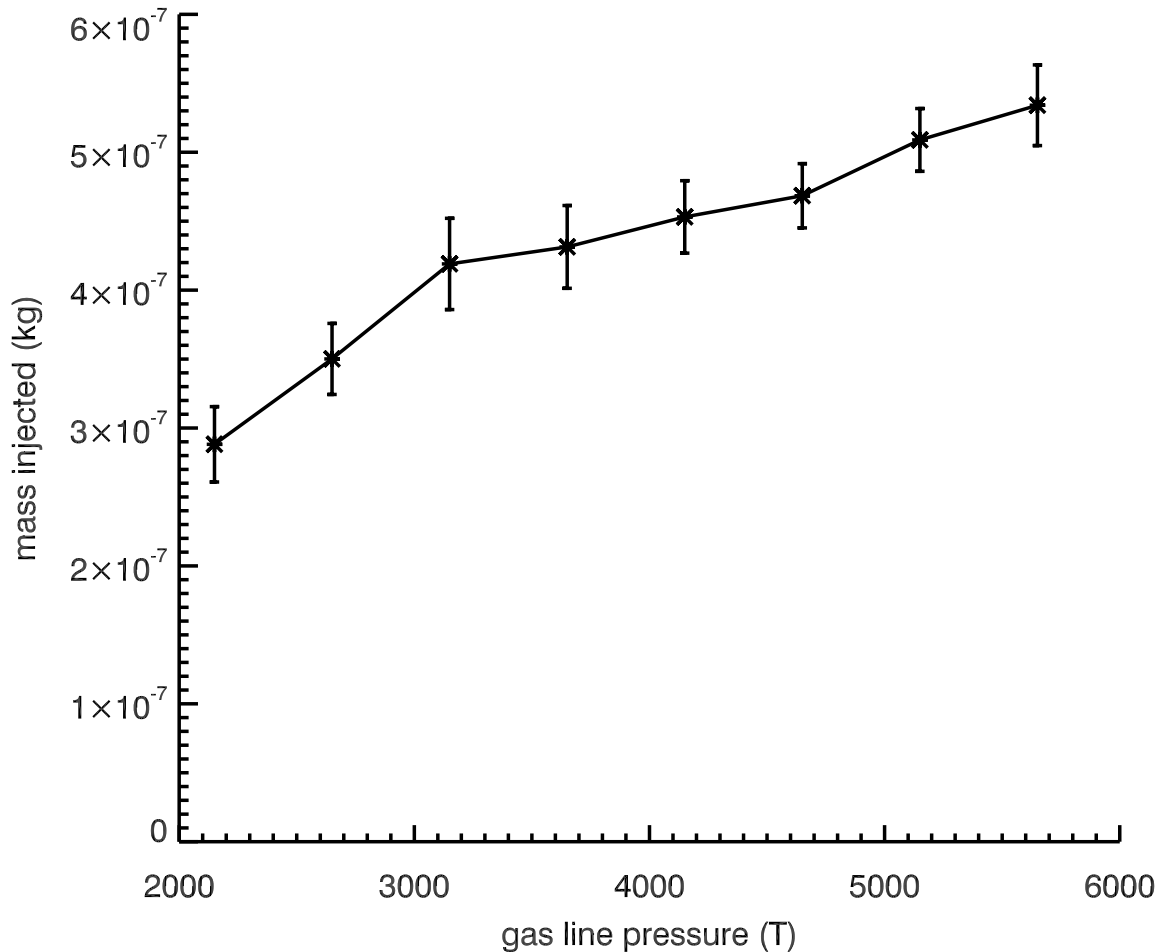


Figure 5.1: Mass injected into the experiment for the gas line pressures used in the experimental investigation of accelerator exhaustion. The mass injected increases with increasing gas line pressure.

and the five averages were added together to yield the values plotted versus line pressure in the figure. The standard deviations for the five valves were added together to obtain the error bar values shown.

Figure 5.2 shows the average quiescent period lengths, based on the normalized $m = 1$ magnetic mode, for at least ten plasma pulses taken at each gas line pressure. Measurements were made while changing the pressure for sets of plasma pulses with bank voltages from 5 to 9 kV. Measurements were not made at several combinations of low pressure and high voltage to avoid large voltage spikes and damage to the experiment. The error bars show the standard deviation of the quiescent period lengths for each set of ten pulses. The length of the quiescent period generally increases with gas line pressure, or total number of particles injected. It decreases with increasing capacitor bank voltage.

Wall conditioning, however, also seems to play a part in the accelerator exhaustion and the length of the quiescent period. Figure 5.3 shows the average quiescent period lengths for ten plasma pulses taken at each gas line pressure with a capacitor bank voltage of 7 kV. The gas line pressure was decreased between each set of ten pulses. The length of time during which a dense Z-pinch is observed in the experiment using the two-chord He-Ne interferometer is also plotted in the figure. Both the quiescent period and the dense Z-pinch period grow longer as the gas line pressure is increased. A similar survey of gas line pressures was conducted by increasing the gas line pressure between each set of plasma pulses. Measurements at a gas line pressure of 2150 T were not taken in the second study. The resulting quiescent period and dense Z-pinch period lengths are shown in Fig. 5.4. The length of the quiescent period and the dense Z-pinch period no longer increase with increasing gas line pressure, but instead remain relatively constant.

Although the length of the quiescent period decreases with increasing capacitor bank voltage, the trend in the chord-integrated density of the Z-pinch is not clear. The time-averaged chord-integrated density during the quiescent period measured by the on-axis chord at $z = 0$ is shown in Fig. 5.5 for capacitor bank voltages between 5 kV and 9 kV. Several lines are plotted—one for each gas line pressure used in the accelerator exhaustion study described in the next section. The chord-integrated density does not exhibit a consistent trend with changing voltage, although it is generally higher at higher gas line pressures.

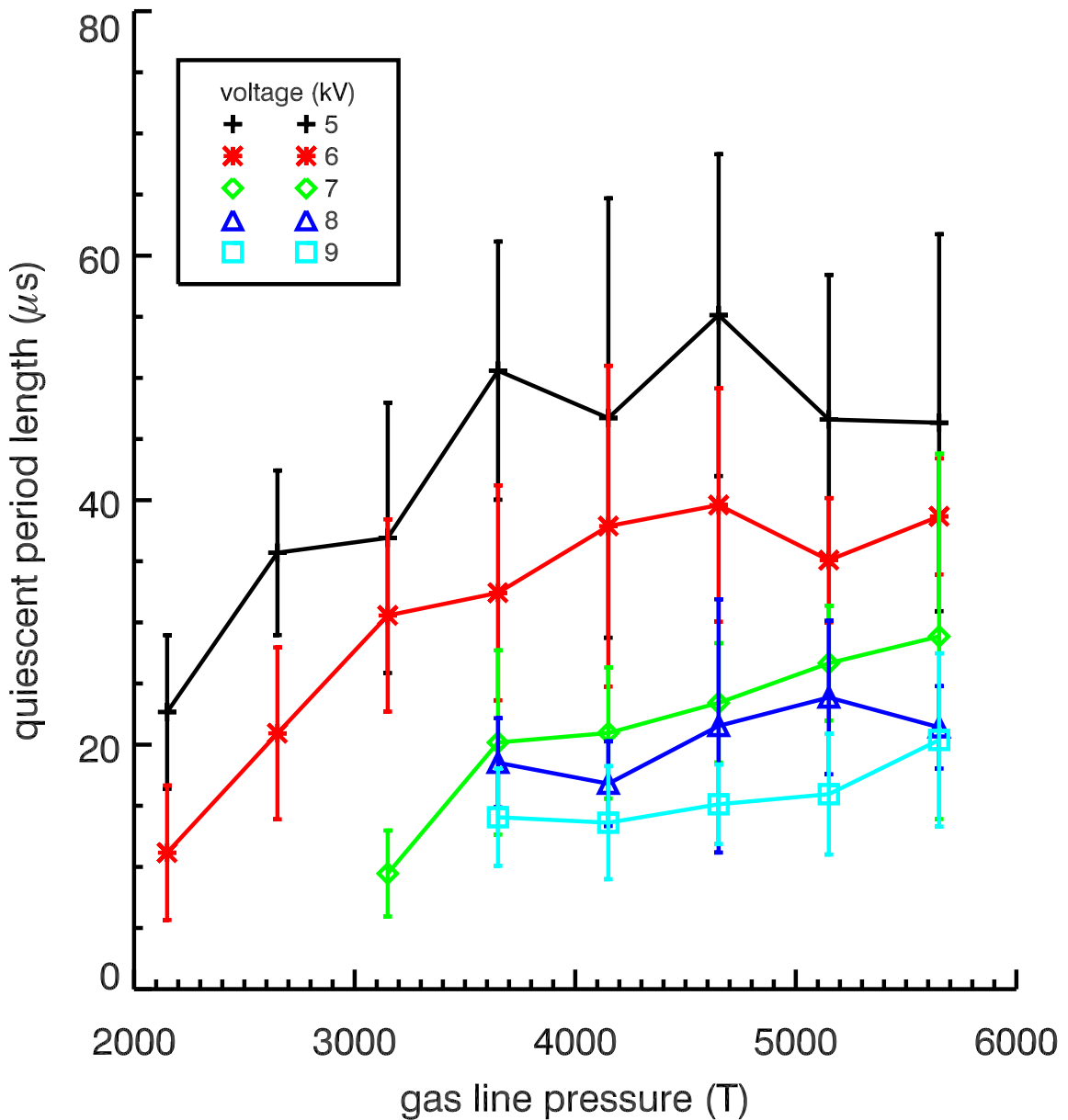


Figure 5.2: Quiescent period length at voltages from 5 to 9 kV for the gas line pressures used in the experimental investigation of accelerator exhaustion. The quiescent period generally becomes longer with decreasing voltage and increasing gas line pressure.

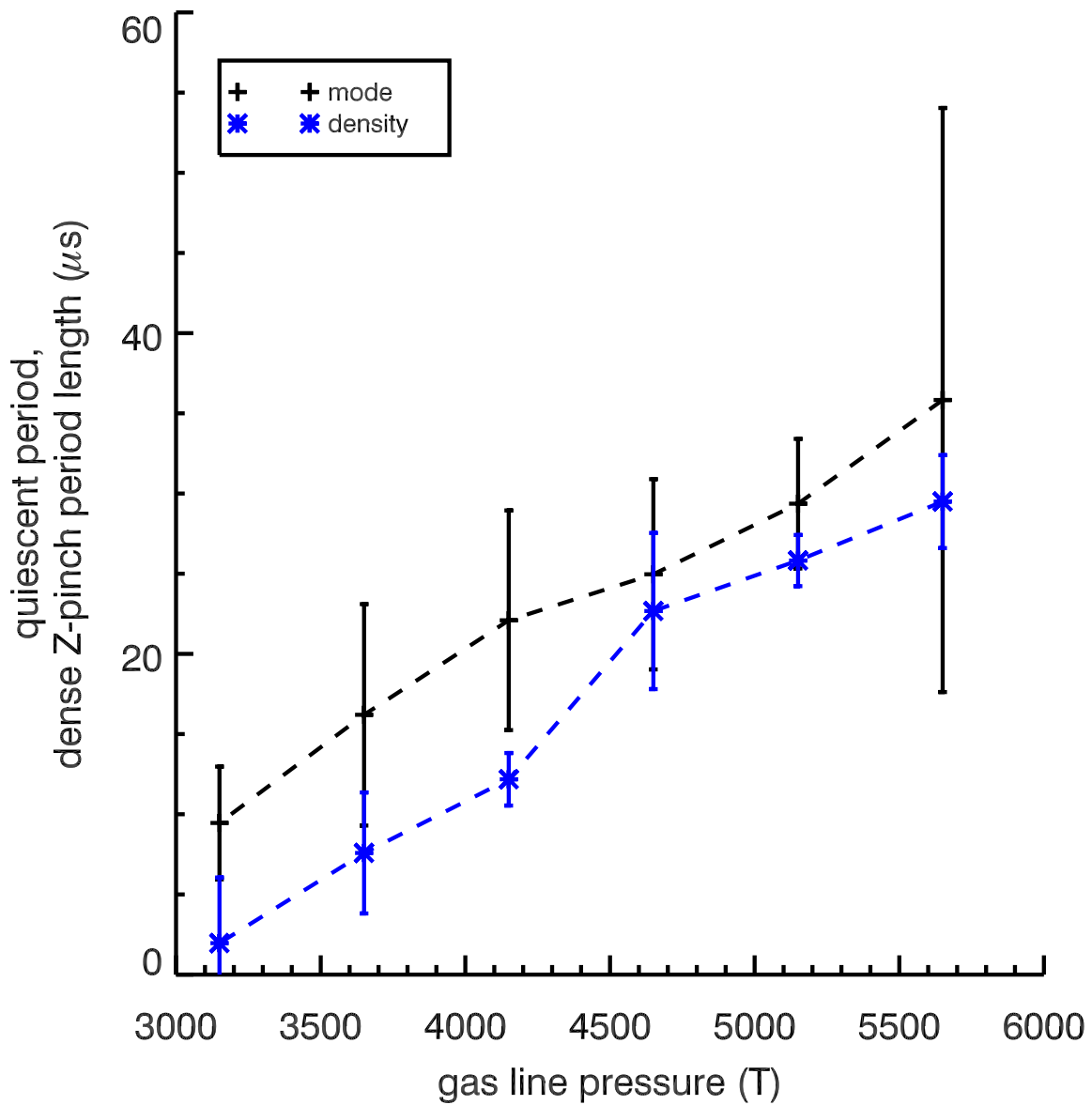


Figure 5.3: Quiescent period length and dense Z-pinch period length while decreasing gas line pressure with a capacitor bank voltage of 7 kV. The quiescent period length is based on the normalized $m = 1$ magnetic mode at $z = 0$. The dense Z-pinch period length is based on measurements made with the two-chord He-Ne interferometer at $z = 0$ cm. The quiescent period and dense Z-pinch period become longer with increasing gas line pressure.

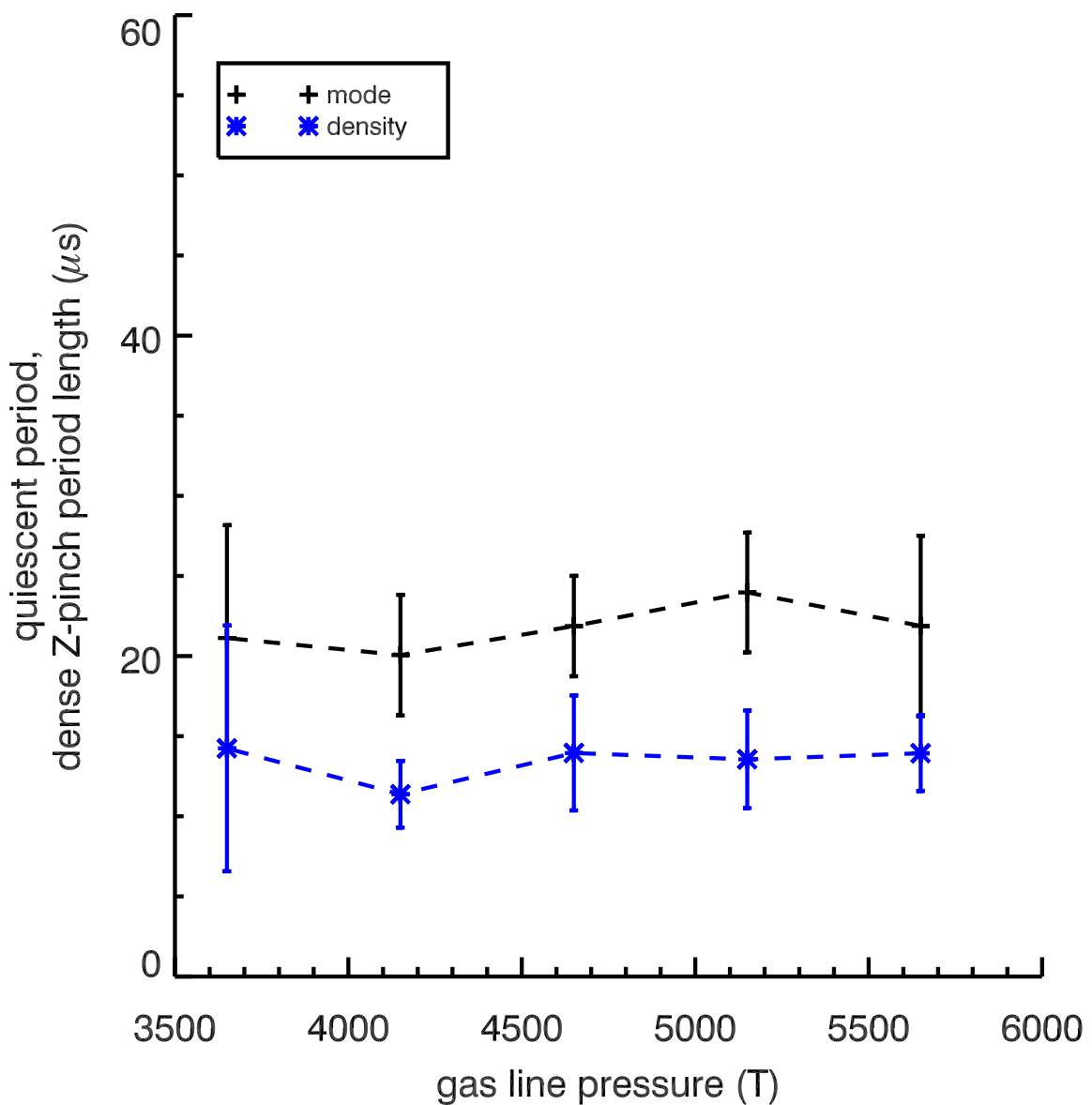


Figure 5.4: The effects of wall conditioning are evident when the gas pressure is increased, rather than decreased, between sets of pulses. The quiescent period and dense Z-pinch period no longer increase with increasing gas line pressure, but instead remain relatively constant. The dense Z-pinch period is also much shorter here than the quiescent period.

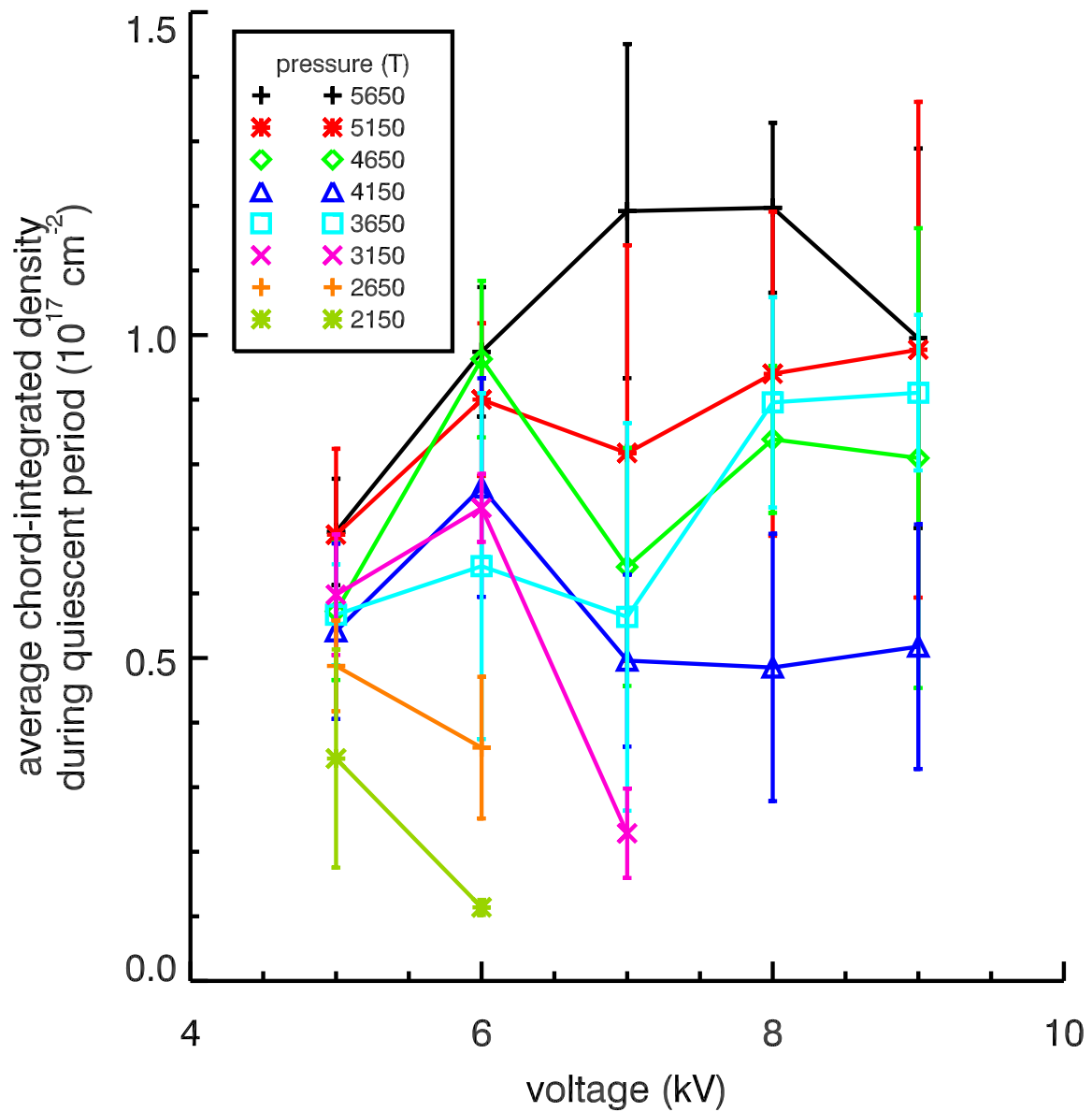


Figure 5.5: The time-averaged chord-integrated density during the quiescent period does not show a clear trend with changing capacitor bank voltage. The chord-integrated density does exhibit an overall tendency to increase with increasing gas line pressure.

Chapter 6

DISCUSSION AND CONCLUSIONS

Combining the experimental and computational results presented in the previous chapters leads to a more thorough understanding of the behavior of the sheared-flow Z-pinches studied. The simulation results shown in Figs. 4.13(a), 4.14(a), 4.15(a), 4.15(b), 4.16(a), and 4.16(b) are for the most part consistent with the density and magnetic field measurements in the accelerator shown in Figs. 2.26(b), 2.25(b), 2.6(b), 2.6(a), 2.7(b), and 2.7(a). The timing of the current sheet's passage and the magnitude of the chord-integrated density are roughly the same. As mentioned earlier, the large rise in the simulated density shown in Figs. 4.13(a) and 4.14(a) well before the current sheet arrives at $z = -65$ cm occurs because ionization is not modeled in the simulation. The particles in the simulation are initialized as a plasma, instead of the neutral gas that is injected into the experiment. The interferometer used on the experiment cannot measure neutral gas density and does not detect the initial expansion of the neutral gas before the current sheet arrives. Plasma is left in the acceleration region after the passage of the current sheet to be accelerated into the Z-pinch over time.

Figures 2.6(b) and 2.6(a) show the azimuthal magnetic fields measured by the magnetic probes in the acceleration region. The sharp rise in the measured fields near $z = -75$ cm is matched by the rise of the magnetic fields for the simulations, shown in Figs. 4.15(a) and 4.15(b). The behavior of the two sets of fields overall is similar, with the few differences likely caused by the presence of an initial plasma and the simplification of the insulator geometry in the simulation. More insight into modeling of the acceleration region can be gained from the contour plots of the current distribution over time shown in Figs. 2.7(b), 2.7(a), 4.16(a), and 4.16(b). Most of the current flows initially near the gas injection plane, but is quickly swept out of the acceleration region in the current sheet. As the quiescent period begins, current spreads back into the accelerator and remains there until it is swept

out again at the end of the quiescent period. During the quiescent period, half of the total current through the plasma flows in the acceleration region. Oscillations in the accelerator current density distribution that occur in the experiment during the quiescent period are not matched by the simulation.

As the plasma leaves the acceleration region in the simulation, it collapses onto the axis, forming a hot spot at the inner electrode nose cone that pushes plasma downstream and radially outward. After an initial rise, the on-axis density downstream of the nose cone near $z = 0$ drops. High-density plasma appears again later at this location when the Z-pinch is formed. Although this bouncing of the density is an unexpected phenomenon, its behavior is consistent with both the He-Ne interferometer measurements and the time evolution of the density profile obtained with the holographic interferometer. Both of these measurements show a high-density plasma on the axis of the experiment shortly after the arrival of the current sheet that quickly drops in magnitude or disappears before forming a more recognizable Z-pinch. The streak and fast-framing camera photos shown in Figs. 2.42–2.43(h) are also consistent with the simulation results.

The time evolution of the chord-integrated electron density at $z = 0$ in the simulation, shown in Figs. 4.13(b) and 4.14(b), appears to match the behavior of lower-voltage hydrogen Z-pinches and the higher-voltage helium Z-pinches used in the density profile investigation (Figs. 2.20(b) and 2.27(a)–2.32(b)). Formation of the Z-pinch occurs much more slowly in the simulation than in higher-voltage (7 to 9 kV) hydrogen Z-pinches such as that shown in Fig. 2.21(b). The high-voltage hydrogen Z-pinches often do not show a drop in density between the arrival of the plasma and the formation of the Z-pinch and are very quickly destroyed, often before the time in the simulation when the Z-pinch is formed. As shown in Fig. 2.22, higher voltage leads to a shorter quiescent period, but it is likely that gas starvation also plays a factor in the performance loss.

The correlation between the low magnetic mode activity during the quiescent period and the presence of a dense plasma along the axis of the experiment shown in Fig. 2.22 supports the notion that a dense, stable Z-pinch is formed and persists throughout the quiescent period. Especially at lower voltages, this Z-pinch is free of the violent instabilities that would be expected to characterize and quickly destroy an otherwise similar, non-flowing

Z-pinch. The sudden end of the quiescent period and concurrent drop in density, however, are not well-captured in the MACH2 simulation, where the Z-pinch slowly fades over time. This may indicate that nonaxisymmetric instabilities not modeled by the simulation play a part in this process. The fast-framing camera photos shown in Figs. 2.45(a)–2.47(h) support the idea that instabilities are involved in the end of the quiescent period.

The simulation results support the idea that exhaustion of the gas in the accelerator leads to the end of the quiescent period. This idea is also supported by the experimental result that injecting more gas into the acceleration region leads to a longer quiescent period, although wall conditioning appears to play a role in this behavior (see Chapter 5). The simulation adds the additional insight that a wave created by plasma bouncing back from the end wall may play a part in the processes leading to the end of the quiescent period.

The density profiles obtained during the middle of the quiescent period using the holographic interferometer at $z = 0$ bear some resemblance to the density profiles in the MACH2 simulation. Both are peaked on-axis with a shoulder at larger radius. The peak value of the MACH2 number density profile is about one-fifth the value of the helium peak. Some discrepancy is to be expected, however, since a fully ionized helium plasma will have twice as many electrons as the hydrogen plasma simulated. A better comparison for the simulation is with the magnitude of the hydrogen profile, which is only about a factor of two greater. Free electrons from multiply-ionized impurity ions will also cause the magnitude of the experimental electron number density to be higher than the simulated number density.

The electron density becomes less peaked in the experiment near the end of the quiescent period, before dropping off completely after the quiescent period. As the Z-pinch in the simulation is destroyed, the on-axis density drops while the density in the shoulder rises. This behavior seems inconsistent with that of the experiment, but may not necessarily be so, since the edge of the shoulder is beyond the view of the holographic interferometer. If the low-density region outside the Z-pinch is not detected, the holographic interferometer will interpret the high density at the edge of its view as zero density, which will be reflected in the magnitude of the inverted profile. The He-Ne interferometer, however, measures a very low chord-integrated density following the quiescent period. This result can be used to assert that the density near the axis is zero or very nearly so.

The magnetic field profiles that accompany the measured hydrogen and helium density profiles during the quiescent period show a magnetic field that increases mostly linearly to a maximum value of approximately 1.2 to 1.4 T at a radius of 0.5 to 1.2 cm. The magnitude of the magnetic field is roughly the same during the middle of the quiescent period as it is near the end. The associated temperatures range from 27 eV for a helium Z-pinch to 68 eV for a hydrogen Z-pinch during the middle of the quiescent period. The lower and wider helium density profile near the end of the quiescent period results in a temperature of 60 eV. These values are reasonable estimates of the Z-pinch temperature calculated using the constant temperature model of Chapter 3. They represent the lower limit on the temperature. The temperatures calculated with the other models presented in the chapter for a hydrogen Z-pinch are higher, 95–225 eV, and represent an upper bound on the temperature.

The magnetic field profiles in the simulation show a similar overall shape to those based on the density measurements, although they tend to be more narrow. Their maximum values are consistent with those in the experiment—0.8 to 1.8 T. Their time evolution, however, is different, as the magnetic field is much higher during the middle of the quiescent period and drops as the Z-pinch is destroyed. The temperature profiles in the simulation are peaked, although some fine-scale structure is observed in the highest-temperature profile near the axis. In contrast, a constant temperature profile was assumed in calculating equilibrium profiles from the experimental density measurements. This assumption was made because thermal conduction within the Z-pinch was determined to be high enough to limit the temperature gradient. The magnitudes of the simulation profiles—100 to 150 eV—are somewhat higher than the 27 to 68 eV temperatures calculated from the experimental helium and hydrogen Z-pinches. The differences in the temperature profiles and their magnitudes may be due to the fact that thermal conduction was turned off in the simulation. A limit of 200 eV was set on the simulation temperature, limiting the temperature reached by the plasma as it is compressed at the nosecone.

The pressure profiles obtained from the experimental density profiles and calculated temperatures fall off more rapidly than the Kadomtsev pressure profile. This indicates that the pressure profile of the Z-pinch does not stabilize it against $m = 0$ perturbations. Another mechanism must be responsible for the stability of the Z-pinch against this mode,

most likely the flow shear.

One of the most striking features of the MACH2 simulation results is the formation of a region of recirculating current by the plasma that reaches the end wall. The plasma in this region then expands, creating a wave that propagates back towards the acceleration region as the Z-pinch is formed. This behavior may help explain the reversal in the flow shear observed in previous work that occurs over the course of the quiescent period [13].

Whether or not this wave is formed in the experiment is difficult to verify, because diagnostic access is limited and more appropriate for viewing dynamic behavior that occurs near the axis of the experiment. Also, the effect may be less pronounced in the experiment, since the low-temperature plasma involved may recombine to form neutral gas. A comparison of the average magnetic fields (the $m = 0$ mode amplitudes) at the three azimuthal arrays located in the assembly region provides experimental evidence of this region of recirculating current. Figure 2.3 shows the average magnetic fields measured by the azimuthal magnetic probe arrays located at $z = 0$, $z = 35$, and $z = 70$ cm. Initially, the field at $z = 0$ is equal to or slightly higher than the fields at the two downstream locations. This situation is not surprising, since most of the current flowing in the assembly region will flow through the Z-pinch to the end wall. A slightly higher field at $z = 0$ might indicate that some current is attaching along the outer electrode before reaching the end wall, which is similar to what occurs in the acceleration region. After some time, however, the magnetic field at $z = 70$ cm rises above the $z = 0$ and $z = 35$ cm fields, opening up the possibility that a higher current is flowing past that magnetic probe array due to a region of recirculating plasma against the end wall. Some time later, the field at $z = 35$ cm also rises above the field at the upstream array, finally followed by a rise in the magnetic field at $z = 0$ cm. This behavior is consistent with the expansion of the recirculating region and upstream propagation of the wave observed in the simulation. The existence of downstream fields at $z = 35$ and $z = 70$ cm that are at times larger than the field at $z = 0$ is evidence that supports the idea that a region of recirculating current is formed by the plasma that reaches the end wall.

Chapter 7

FUTURE WORK

The investigation described in the preceding chapters focused on understanding the character and evolution of a sheared-flow Z-pinch. Future work on the ZaP experiment will continue to increase that understanding. Helium Z-pinches were used here to describe the time evolution of the density profile because their high electron density provided ample phase shift for determining the density profile. The phase shift for hydrogen Z-pinches with the single-pass holographic interferometer was often too small to be reliably measured. A double-pass holographic interferometer should be used to determine the time evolution of the density profile for a hydrogen Z-pinch, since isotopes of hydrogen are of primary fusion interest. The scene beam passes twice through the Z-pinch in the double-pass system, increasing the phase shift to a more easily measured level. It may also be possible to measure density profiles from pulses at lower capacitor bank voltages with the double-pass system.

The two-chord He-Ne interferometer is capable of giving time-resolved, chord-integrated density information on a single plasma pulse. It has been used to supplement the investigation of the time evolution of the radial profile performed with the holographic interferometer. The He-Ne interferometer is being expanded to four chords, allowing an Abel inversion to be used to determine a time-dependent density profile. This density profile will be less accurate than the profile obtained from the holographic interferometer, because only four chord-integrated measurements can be used in the inversion.

In addition, the chords of the He-Ne interferometer could be positioned to make measurements at different axial locations in the assembly region. Positioning four chords at $z = 0$ could allow short-wavelength axial density variations to be investigated. This would allow measurement of the wavelengths of axial density gradients in the Z-pinch and indicate the flow shear required for stabilization.

Continued research will be conducted into how changes in experimental parameters affect the behavior of the Z-pinch. The dependence of the density and length of the quiescent period on the capacitor bank voltage and the amount of gas injected into the experiment will be studied at higher gas line pressures. The limit on the gas line pressure is currently set by the damage threshold of the turbopump. The turbopump inlet will be throttled to eliminate this constraint. The total power input into the experiment will be increased by adding additional capacitors and ignitrons to the capacitor banks. Injecting more gas into the experiment while providing a longer, higher current waveform should extend the quiescent period length and show if it is possible to maintain the Z-pinch indefinitely.

The inner electrode diameter will be increased to increase compression of the plasma as it collapses on axis. This will increase the temperature of the Z-pinch and change its equilibrium profile. Additional gas puff valves will be installed inside the new inner electrode to allow better control of the neutral gas injected. Planned expansion of the outer electrode will double the length of the Z-pinch and provide greater downstream diagnostic access. Downstream density measurements can be used to characterize the Z-pinch density far from the acceleration region.

Agreement between the simulation and the experiment could be improved by making a few changes to the simulation. An experimental current waveform could be applied to the MACH2 simulations, instead of allowing MACH2 to calculate the current using an external inductance, capacitance, and voltage and its own internally-computed inductance. This would better model the effects of the pulse-forming network used to create a constant-current waveform throughout much of the plasma pulse. The voltage across the insulator output by MACH2 could still be used as a basis for comparing the electrical characteristics of the simulation with those of the experiment. Ionization could also be added to the MACH2 model. The dynamics of the current sheet and fluctuations in the accelerator current distribution in the simulation may be brought more in line with experimental observations with ionization included. The behavior of the wave that bounces back from the end wall in the simulation may also change when ionization and recombination are modeled in the simulation. Thermal diffusion could also be turned on to capture the effects of thermal conduction on the Z-pinch density, temperature, and magnetic field profiles.

Chapter 8

SUMMARY

The ZaP Flow Z-Pinch is a basic plasma physics experiment designed to investigate the effects of sheared flow on gross plasma stability. It produces sheared-flow Z-pinches that exhibit characteristics of stability for over one thousand times the theoretical instability growth time for a Z-pinch without sheared flow. The experiment consists of a coaxial acceleration region attached to an assembly region where the Z-pinch is formed. MACH2 simulations show acceleration of the current sheet from the acceleration region into the assembly region. As it leaves the acceleration region, the plasma collapses on axis and a dense, hot Z-pinch is formed along the axis of the assembly region.

The Z-pinch persists throughout a 20 to 40 μ s quiescent period, characterized by low magnetic mode activity and high density on axis. Measurements made using a multi-chord He-Ne interferometer during this period corroborate the existence of the high-density plasma. The chord-integrated density is measured by a holographic interferometer and inverted to yield the radial electron density profile. The density profile for a hydrogen Z-pinch is peaked at a number density on the order of 1×10^{17} cm⁻³ on the axis. An equilibrium profile model is used to construct magnetic field profiles and determine the temperature based on the density profile. The magnetic field for a hydrogen Z-pinch is approximately 1.4 T, and the average temperature is about 68 eV. Measurements are made with the holographic interferometer on successive helium plasma pulses to track the evolution of the Z-pinch equilibrium profile over time.

Simulation results, He-Ne interferometer measurements, and an experimental investigation of neutral gas injection indicate that the Z-pinch is fueled during the quiescent period by plasma from the accelerator. Depletion of plasma in the accelerator is associated with the end of the quiescent period and the destruction of the Z-pinch.

BIBLIOGRAPHY

- [1] N. H. Abel. Resolution d'un probleme de mecanique. *J. Reine u. Angew. Math.*, 1:153–157, 1826.
- [2] V. Antoni, M. Bagatin, A. Buffa, C. Bunting, S. Costa, L. Guidicotti, G. F. Nalessi, S. Ortolani, M. E. Puiatti, P. Scarin, and G. Malesani. Studies on high-density RFP plasmas in the Eta-Beta II Experiment. In *Proceedings of the 9th International Conference on Plasma Physics and Controlled Nuclear Fusion Research*, volume 1, page 619, Baltimore, 1982. International Atomic Energy Association.
- [3] T. D. Arber and D. F. Howell. The effect of sheared axial flow on the linear stability of the z-pinch. *Physics of Plasmas*, 3(2):554–560, 1996.
- [4] J. Bailey, Y. Ettinger, A. Fisher, and N. Rostoker. Gas-puff z pinches with D₂ and D₂-Ar mixtures. *Applied Physics Letters*, 40(6):460–462, 1982.
- [5] S. I. Braginskii. *Reviews of Plasma Physics*, volume 2, chapter Transport Processes in a Plasma, pages 205–311. Consultants Bureau, New York, 1965.
- [6] J. E. Bright. Magnetic mode analysis in the zap flow-stabilized z-pinch experiment. Master's thesis, University of Washington, 2002.
- [7] C. J. Buchenauer and A. R. Jacobson. Quadrature interferometer for plasma density measurements. *Review of Scientific Instruments*, 48(7):769–774, 1977.
- [8] T. D. Butler, I. Henins, F. C. Jahoda, J. Marshall, and R. L. Morse. Coaxial snowplow discharge. *Physics of Fluids*, 12(9):1904–1916, 1969.
- [9] R. Chodura. A hybrid fluid-particle model of ion heating in high-Mach-number shock waves. *Nuclear Fusion*, 16:55, 1975.
- [10] C. T. Dum, R. Chodura, and D. Biskamp. Turbulent heating and quenching of the ion sound instability. *Physical Review Letters*, 32(22):1231, 1974.
- [11] J. P. Freidberg. Ideal magnetohydrodynamic theory of magnetic fusion systems. *Reviews of Modern Physics*, 54(3):801–902, 1982.
- [12] R. P. Golingo. *Formation of a sheared-flow Z-pinch*. PhD thesis, University of Washington, 2003.

- [13] R. P. Golingo, U. Shumlak, and B. A. Nelson. Formation of a sheared flow Z pinch. *Physics of Plasmas*, 12(6):062505, 2005.
- [14] G. H. Golob and J. M. Ortega. *Scientific Computing and Differential Equations: An Introduction to Numerical Methods*. Academic Press, Inc., San Diego, 1992.
- [15] M. G. Haines. The joule heating of a stable pinched plasma. *Proceedings of the Physical Society of London*, 76:205–260, 1960.
- [16] M. G. Haines. Particle orbits, diamagnetism, and energy balance in a Z-pinch satisfying the Lawson criterion. *Journal of Physics D: Applied Physics*, 11:1709–1720, 1978.
- [17] M. G. Haines, S. V. Lebedev, J. P. Chittenden, F. N. Beg, S. N. Bland, and A. E. Dangor. The past, present, and future of Z pinches. *Physics of Plasmas*, 7(5):1672–1673, 2000.
- [18] I. H. Hutchinson. *Principles of Plasma Diagnostics*. Cambridge University Press, 2nd edition, 2002.
- [19] S. L. Jackson. Holographic interferometry on the ZaP Flow Z-Pinch. Master’s thesis, University of Washington, 2003.
- [20] S. L. Jackson, U. Shumlak, B. A. Nelson, R. P. Golingo, R. C. Lilly, and T. L. Shreve. Effects of initial gas injection on the behavior of a sheared-flow Z-pinch. AIAA 2005-3853. *41st AIAA/ASME/SAE/ASEE Joint Propulsion Conference and Exhibit, Tucson, Arizona*, July 10-13, 2005.
- [21] A. R. Jacobson. Heterodyne quadrature interferometer for simultaneous measurements of plasma density along several chords. *Review of Scientific Instruments*, 49(5):673–674, 1978.
- [22] F. C. Jahoda and R. E. Siemon. Holographic interferometry cookbook. Technical Report LA-5058-MS, Los Alamos Scientific Laboratory, Los Alamos, NM 87544, October 1972.
- [23] B. B. Kadomtsev. *Reviews of Plasma Physics*, volume 2, chapter Hydromagnetic Stability of a Plasma, pages 153–199. Consultants Bureau, New York, 1966.
- [24] Korad Laser Systems, a division of Hadron, Inc. *Operation & maintenance manual: model K1 laser head (ruby, ND/GL, or NC/YAG versions)*, 1975.
- [25] Korad Laser Systems, a division of Hadron, Inc. *Operation & maintenance manual: K-QS2 Pockels cell*, ca. 1975.

- [26] M. Kruskal and M. Schwarzschild. Some instabilities of a completely ionized plasma. *Proceedings of the Royal Society of London. Series A, Mathematical and Physical Sciences*, 223(1154):348–360, May 1954.
- [27] J. Marshall. Performance of a hydromagnetic plasma gun. *Physics of Fluids*, 3(1):134–135, 1960.
- [28] H. Meuth. *Radio-Frequency Wave Excitation and Damping on a High Beta Plasma Column*. PhD thesis, University of Washington, 1984.
- [29] M. Murakami, J. D. Callen, and L. A. Berry. Some observations on minimum densities in tokamak experiments. *Nuclear Fusion*, 16:347, 1976.
- [30] R. E. Peterkin, Jr., A. J. Giancola, and J. E. Sturtevant. MACH2: A reference manual—fifth edition. Technical Report MRC/ABQ-R-1490, Mission Research Corporation, July 1992.
- [31] N. Qi, S.F. Fulghum, R.R. Prasad, and M. Krishnan. Space and time resolved electron density and current measurements in a dense plasma focus z-pinch. *IEEE Transactions on Plasma Science*, 26(4):1127 – 37, August 1998.
- [32] N. Qi, J. Schein, J. Thompson, P. Coleman, M. McFarland, R. R. Prasad, M. Krishnan, B. V. Weber, B. G. Moosman, J. W. Schumer, D. Mosher, R. J. Comisso, and D. Bell. Z pinch imploding plasma density profile measurements using a two-frame laser shearing interferometer. *IEEE Transactions on Plasma Science*, 30(1):227–238, February 2002.
- [33] D. W. Scudder. Steady-state radial heat conduction in a z pinch. *Physics of Fluids*, 26(5):1330–1334, 1983.
- [34] E. Sevillano. *Magnetic Reconnection in Field-Reversed Configurations*. PhD thesis, University of Washington, 1983.
- [35] V. D. Shafranov. The stability of a cylindrical gaseous conductor in a magnetic field. *Soviet Journal of Atomic Energy*, 1(5):709, 1956. Translated from Atomnaya Energiya, 1(5):38.
- [36] J. Shiloh, A. Fisher, and E. Bar-Avraham. Interferometry of a gas-puff z-pinch plasma. *Applied Physics Letters*, 35(5):390–392, 1979.
- [37] U. Shumlak and C. W. Hartman. Sheared flow stabilization of the $m=1$ kink mode in Z pinches. *Physical Review Letters*, 75(18):3285–3288, 1995.

- [38] U. Shumlak, B. A. Nelson, R. P. Golingo, S. L. Jackson, E. A. Crawford, and D. J. Den Hartog. Sheared flow stabilization experiments in the ZaP flow Z pinch. *Physics of Plasmas*, 10(5):1683–1690, 2003.
- [39] U. Shumlak, B. A. Nelson, R. P. Golingo, S. L. Jackson, P. C. Norgaard, T. L. Shreve, and K. T. Yirak. A flow-stabilized Z-pinch fusion space thruster. AIAA 2003-4826. *39th AIAA/ASME/SAE/ASEE Joint Propulsion Conference and Exhibit, Huntsville, Alabama*, July 21-23, 2003.
- [40] C. M. Vest. *Holographic Interferometry*. John Wiley & Sons, 1979.
- [41] Zhehui Wang, G. A. Wurden, Cris W. Barnes, C. J. Buchenauer, H. S. McLean, D. N. Hill, E. B. Hooper, R. D. Wood, and S. Woodruff. Density and H_{α} diagnostics and results for the sustained spheromak physics experiment. *Review of Scientific Instruments*, 72(1):1059–1062, 2001.
- [42] Xiaobing Zou, Xinxin Wang, Chengmu Luo, Zhen Liu, and Min Han. Measuring the evolution of electron density profile in a small gas-puff z-pinch. *Transactions of the Institute of Electrical Engineers of Japan, Part A*, 124-A(6):515 – 18, June 2004.

Appendix A

HOLOGRAPHIC INTERFEROMETRY USER'S GUIDE

This appendix serves as a guide to the practical aspects of making density measurements on the ZaP Flow Z-Pinch using the holographic interferometer. Further information is available in Ref. [19] and a journal article that, at the time of publication of this document, is under review for publication in *Review of Scientific Instruments*.

A.1 Safety

The laser used to make interferograms with the holographic interferometer is a high-power, pulsed ruby laser and must only be operated or maintained by trained personnel. Two people must be present when operating the laser—it must not be operated alone. Light is emitted from this laser at a visible wavelength detectable by the human eye, and it is bright enough that even scattered light can cause permanent eye damage. Eye protection in the form of goggles designed for ruby laser use must be worn when operating the laser inside the lab, or the laser may be operated outside the lab without goggles if the laser light is contained within the lab by the black cloth and the walls of the laboratory. The integrity of the black cloth must always be checked before firing the laser, since it must be moved to access the cable tray on top of the screen room or to look through the window outside the screen room into the laboratory. Warning signs must be placed over the doorknobs on the doors at both ends of the lab when the laser is in operation. The laser is interlocked to the laboratory doors and the panic buttons through the ZaP interlock system and the Thomson/holography remote control. Schematics of the ZaP interlocks, Thomson/holography remote control, and holography laser power supply are located in the folder M:\ZaP Electronic Schematics. The power supply contains high-voltage capacitors and electronics and must be treated with care during operation and maintenance. The capacitors must be grounded and the power supply must be unplugged prior to performing maintenance on the power supply or on the

laser head or Pockels cell assembly.

A.2 Optical Configuration of the Holographic Interferometer

The holographic interferometer can be operated in single-pass or double-pass configurations. The single-pass configuration provides sufficient phase shift when used to make density measurements on helium Z-pinches, and it leaves enough room for the multichord He-Ne interferometer to be used to make simultaneous density measurements at the holography port. The double-pass configuration should be used when making density measurements of hydrogen or 50 % hydrogen/50 % methane Z-pinches, which have lower electron densities than helium Z-pinches. It provides twice the phase shift of the single-pass system, increasing the signal-to-noise ratio in the fringe shift. On such low electron density plasmas, with the single-pass system it is often difficult to differentiate between the phase shift due to the plasma electron density and aberrations in the interferogram. The He-Ne interferometer cannot be used with the double-pass system because it is blocked by the mirror that reflects the scene beam back for its second pass through the plasma.

A.2.1 Single-Pass Holographic Interferometer

The single-pass holographic interferometer setup is shown in Fig. A.1. The length of each section of the scene and reference beam paths in millimeters is included in the diagram. The path lengths of the scene and reference beams are equal to within less than a centimeter. The scene beam lens is positioned to image the Z-pinch onto the holographic film with a 1:2 image-to-object magnification ratio. The 305 mm focal length lens is located 915 mm from the center of the 152.4 mm (12 in) diameter vacuum tank and 457.5 mm from the holographic film. The reference beam lens is also positioned 457.5 mm from the holographic film. Figure A.2 is a photograph of the single-pass holographic interferometer, with the scene and reference beam paths indicated.

Max-R mirrors are used in the beam paths whenever possible. These mirrors are designed to reflect as much of the ruby laser light as possible from their coated first surface when positioned at the correct angle to the beam path. Net reflections from other surfaces are minimized. The max-R mirrors only work properly at their design angle, usually 45°, so a

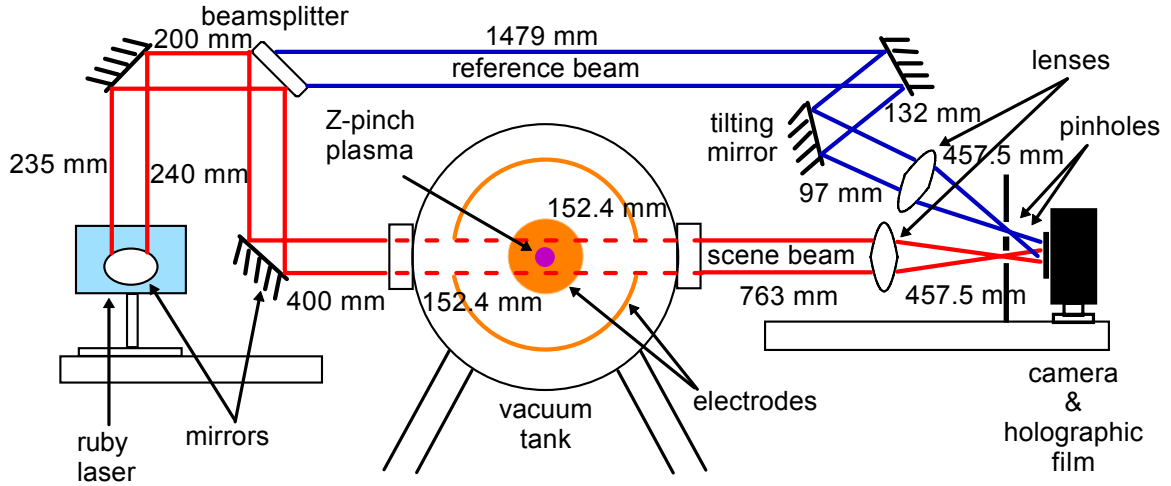


Figure A.1: Optical configuration of the single-pass holographic interferometer with the lengths of each section of the scene and reference beam paths indicated.

metal mirror is used in the tilting mirror location, where the angle of incidence of the laser light is not 45° .

The expanded laser beam is brought above the height of the vacuum tank before being split by the 50 % beamsplitter into the scene and reference beams. On the far side of the vacuum tank, the reference beam is brought down to the level of the scene beam where they interfere at the holographic film. This arrangement is similar to the scheme used with the He-Ne interferometer and makes it easier to match the scene and reference beam path lengths. Incidentally, turning the beam upward from the laser rail and then towards the vacuum tank changes the polarization direction of the laser light from horizontal to vertical. It should also be noted that the reference beam is reflected the same number of times as the scene beam on its way to the holographic film, insuring that light from the same region of the original, split beam hits the film in the same place for both beams. If one beam were reflected an odd number of times and the other were reflected an even number of times, then one of the beams at the film would be reversed with respect to the other, and light from opposite sides of the original beam would be brought together at the film. Neither the change in polarization nor matching the number of reflections was observed to affect the interferograms produced.

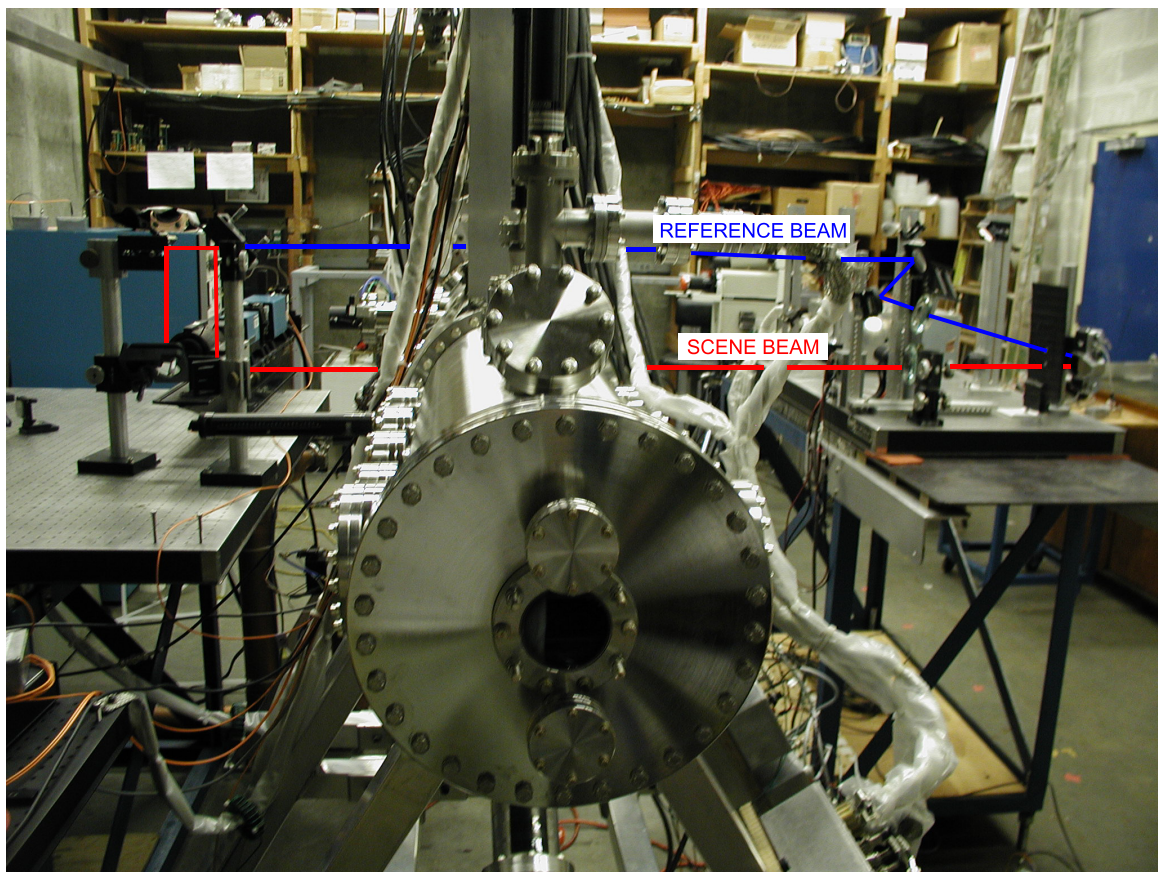


Figure A.2: Photograph of the optical configuration of the single-pass holographic interferometer with the scene and reference beam paths indicated.

One important aspect of the optical setup does not appear in the diagram. The mirrors and beamsplitter on the ruby laser rail side of the vacuum tank are positioned slightly downstream of the center of the $z = 0$ viewports, and the optical components on the film side of the vacuum tank are positioned slightly upstream. This causes the path of the scene beam through the experiment to be slightly skewed, preventing normal reflections as the laser passes through the viewport windows. The reflections that do result are not parallel to the path of the laser through the vacuum tank, and diverge quickly enough to miss both the laser cavity, in the case of back reflections, and the holographic film, for forward reflections.

A.2.2 Double-Pass Holographic Interferometer

The double-pass holographic interferometer setup is shown in Fig. A.3. The length of each section of the scene and reference beam paths in millimeters is again included in the diagram. The difference between path lengths in this case is 60 mm. Interferograms were also made using a simpler double-pass system with a path length difference of 1750 mm, but their quality was much lower than those made with the path lengths nearly equal. Figure A.4 is a photograph of the double-pass holographic interferometer, with the scene and reference beam paths indicated.

In the double-pass arrangement, the scene beam passes through the plasma, bounces off a mirror, and passes through the plasma a second time before traveling through the beamsplitter and hitting the holographic film. The double pass through the plasma (as opposed to a single pass) is needed to increase the phase shift of the scene beam to a more easily measurable level for a hydrogen or methane plasma. As in the single-pass setup, a lens is used to image the plasma onto the film, but only the scene beam's second pass through the Z-pinch is imaged. The reference beam also has a lens in its beam path.

The mirrors and 50 % beamsplitter in the double-pass holographic interferometer act on the ruby laser beams in the horizontal plane. The laser light remains horizontally polarized, unlike in the single-pass system, where the beams are steered from the horizontal to the vertical plane and the polarization direction of the light is shifted. As in the single-pass system, the reference beam and the scene beam are both reflected an even number of times,

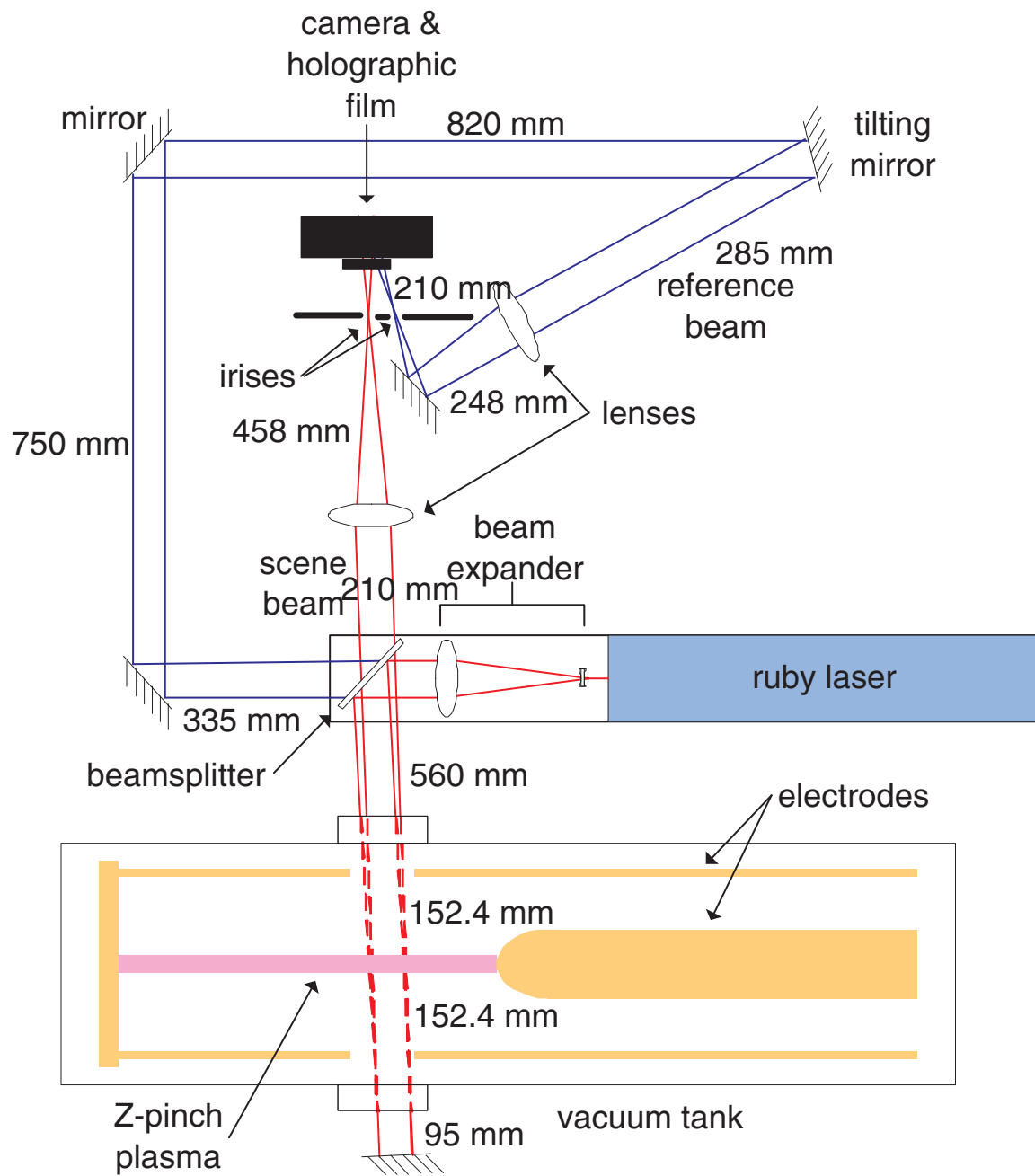


Figure A.3: Optical configuration of the double-pass holographic interferometer with the lengths of each section of the scene and reference beam paths indicated.

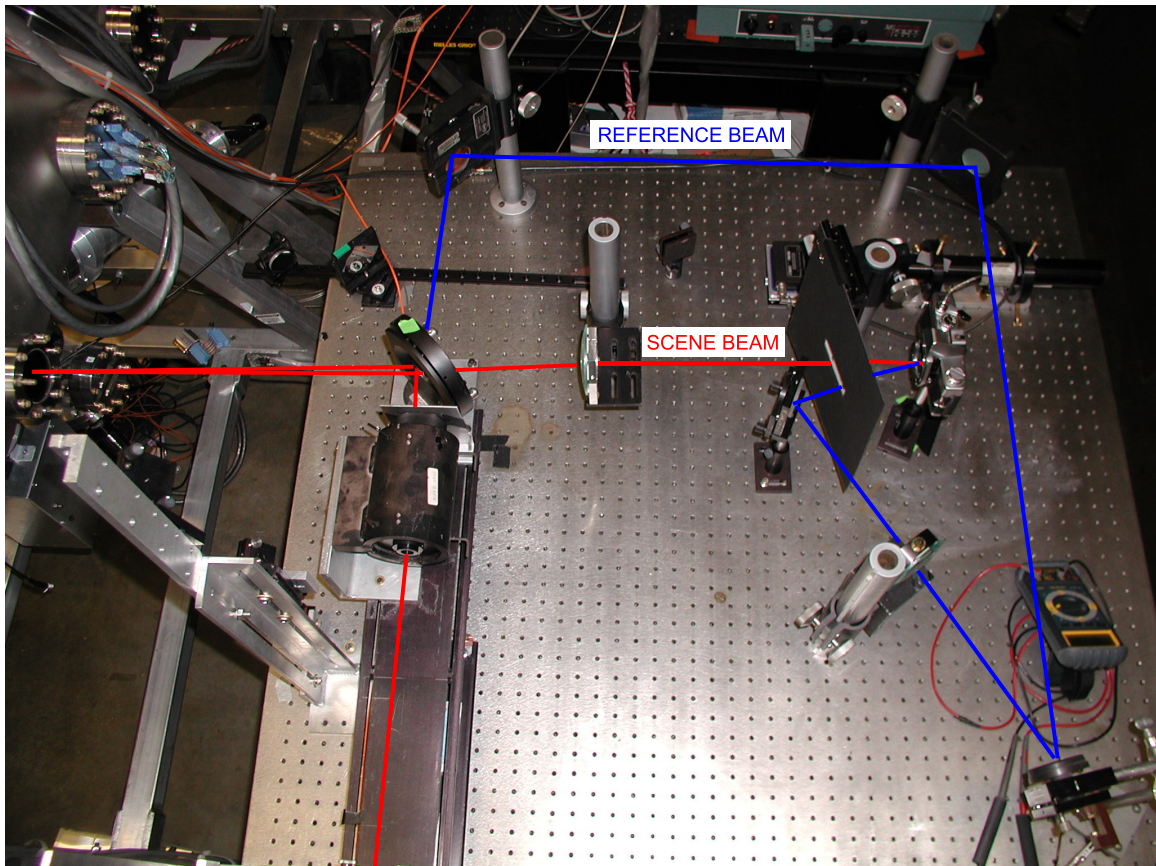


Figure A.4: Photograph of the optical configuration of the double-pass holographic interferometer with the scene and reference beam paths indicated. An alignment guide consisting of a wire cross mounted over a hole in a piece of sheet metal can be seen between the beam expander and the beamsplitter. This guide would not be in the beam path during operation of the holographic interferometer.

so the same parts of the original, unsplit beam are matched at the film. The reference beam, however, is reflected four times, while the scene beam is reflected only twice.

An extremely important detail shown in the diagram of the double-pass setup is the slight misalignment of the scene beam's first and second passes through the film. This misalignment prevents laser light from being reflected off the beamsplitter and into the laser cavity after the scene beam's second pass through the plasma. Without it, reflection of the energetic laser pulse back into the cavity could damage the laser rod. Damage did occur on one occasion, necessitating replacement of the laser rod. To make this misalignment easier, a three-inch diameter visible light beamsplitter was used as the beamsplitter. Only a slight misalignment is necessary, however, and the visible light beamsplitter was replaced by a two-inch diameter beamsplitter designed for use with ruby laser light. Interferograms made with the ruby beamsplitter were of slightly higher quality than those made with the beamsplitter designed for the wider range of wavelengths. When properly misaligned, the reflection of the returning scene beam from the beamsplitter back through the beam expander can be seen with the alignment laser as a focused spot that is blocked by the edge of the etalon mount.

Reflections from the vacuum tank windows must also be prevented from reflecting into the laser cavity or from interfering with the scene and reference beams at the holographic film. The beamsplitter used to reflect the scene beam through the plasma is positioned slightly downstream (towards the outer electrode end wall) of the $z = 0$ viewport. As a result, the scene beam passes through the glass of the $z = 0$ viewports at a slight angle and the stray reflection from the laser-side window hits the beamsplitter mount. The stray reflection from the far-side window passes between the beamsplitter and the beam expander and hits the lab wall.

Max-R mirrors are used whenever possible in the beam paths. The tilting mirror and the scene beam mirror on the far side of the vacuum tank are both metal mirrors, since the angle of incidence between the laser light and these mirrors is not 45° . One additional metal mirror is used in the reference beam path because of a shortage of unblemished max-R mirrors. It is important to use a max-R mirror as the last reference beam mirror, because the beam is more focused at that point, resulting in a higher power per unit area that could

damage the mirror.

A.2.3 Optical Alignment

The first step in setting up the holographic interferometer is to align the ruby laser. This is achieved by using an autocollimator to line up the reflections from the etalon and rear reflector with the front face of the ruby laser rod. It may be necessary to open up the iris in the laser cavity during alignment. The manuals for the laser oscillator head and the Pockels cell may be helpful, especially if the Pockels cell needs alignment [24, 25]. The front and rear faces of the ruby rod, rear reflector, and etalon are not perfectly parallel, so six spots will be visible in the autocollimator, as well as a constellation of reflections from the polarizer stack in the Pockels cell. An index card can be used to block some of the components to determine which reflections correspond to each optical component. After using the autocollimator and removing it from the laser rail, the laser may be fired at Zap-It paper a few times to fine-tune its alignment. Before firing the laser, check that the laser cooler is on and providing adequate water flow, without bubbles, to the laser head. Bubbles may be an indication that the cooler water level is low. Use the conductivity meter to check that the resistivity of the water is greater than 10^5 $\Omega\text{-cm}$. An oscilloscope can be used to observe the laser pulse waveform recorded by the holography laser monitor photodiode during the fine-tuning. After the laser is aligned, it is fired twice more—once at a piece of Zap-It paper mounted at the end of the laser rail and once across the room at a piece of Zap-It paper mounted on the drawers against the screen room wall. The alignment laser pointer mounted behind the rear reflector is then adjusted to hit the centers of both the ruby laser spot on the Zap-It paper and the one against the screen room wall. To avoid damaging the alignment laser, it is always covered with either the laser monitor photodiode or an index card when the ruby laser is fired. The ruby laser is then fired several times at Zap-It paper, and the diameter and position of the iris in the laser cavity is adjusted based on the resulting spots and the beam of the alignment laser to select the best part of the beam. An iris diameter of 4 mm is typically used when making interferograms.

Once the ruby and alignment lasers have been correctly adjusted, the beam expander is

mounted on the laser rail so that the beam of the alignment laser passes through the center of the beam expander and hits the same Zap-It paper spot by the screen room as before. In addition, the beam expander should be adjusted so that the diameter of the laser pointer beam remains constant after it leaves the beam expander. It is correctly adjusted when the lenses are 144 mm apart, placing the foci of the small $f = 16$ mm diverging lens and large $f = 160$ mm converging lens at the same spot on the etalon side of the beam expander. The various mounts available can then be used to position the optical components for either the single or double-pass holographic interferometer shown in Figs. A.1 and A.3. Crosshairs made of wire and mounted across a hole in a piece of sheet metal are placed at the exit of the beam expander as an alignment guide.

For the double-pass holographic interferometer, the two-inch diameter 50 % ruby laser beamsplitter is positioned on the end of the laser rail, slightly off of the rail's axis using the three-inch mirror mount, two-inch Delrin adapter, and aluminum platform with pontoons. For the single-pass setup, a series of towers are used to mount the beamsplitter and mirrors on the ruby laser side of the vacuum tank.

The scene beam is reflected through the vacuum tank along a slightly skewed path to prevent normal reflections from the viewports from feeding back into the laser cavity or reaching the holographic film. Wires are mounted horizontally one centimeter apart near the centers of the viewports on either side of the vacuum tank. A Delrin mount is used to mount the wires on the far side of the vacuum tank from the ruby laser, which will remain in place after alignment to serve as reference wires in the interferograms. The shadow of these wires in the laser beam on a circular piece of paper mounted over the next optical component is used to ensure that the beam is level through the vacuum tank. If the vacuum tank is level, corresponding wire shadows should overlap. If not, either the laser beam or the vacuum tank is not level, and the beam should be adjusted until it is level and passes through the center of the vacuum tank.

For the double-pass holographic interferometer, the mirror on the opposite side of the vacuum tank is cantilevered off the He-Ne interferometer table and positioned to reflect the scene beam back through the experiment. A circular piece of paper with a small hole near its center is put over the mirror, and the mirror is positioned so that the hole is at the center

of the shadow made by the alignment crosshairs in the beam. The return reflection from the mirror on the other side of the vacuum tank will appear as a small square around the crosshairs, and is easily distinguishable from other beams or window reflections. This return reflection is misaligned so that it hits the beamsplitter a centimeter or two closer to the beam expander than the original beam from the laser cavity. When properly misaligned, the return beam will still be reflected into the beam expander, but a focused spot will appear on the etalon mount, which prevents it from reaching the laser cavity and causing damage to the ruby rod.

The scene beam is steered onto an index card held in the back of the camera at the plane of the film. The reference beam path is aligned so that the reference beam hits the card at about a 15° angle to the scene beam. The mirrors in the reference beam are aligned by placing a circular piece of paper on one mirror, and a second circular piece of paper with a hole cut in it on the previous mirror. The two mirrors are adjusted until the crosshairs at the center of the square produced by the hole are centered on the paper over the second mirror. This procedure is repeated until the entire beam path has been aligned. The tilting mirror is particularly difficult to align because it is only capable of fine adjustment in one plane, and must be coarsely adjusted in the other. A magnetic mount is often used with the tilting mirror in the double-pass setup, so that the mount itself can be nudged or turned slightly to make small adjustments.

During initial alignment of both the single-pass and the double-pass configurations, the lenses and the irises that prevent light emitted by the plasma from hitting the film are removed from the beam paths. The scene and reference beams are adjusted until the shadows of the crosshairs in the two beams overlap on the index card at the film plane. A second index card can be used to block a portion of either beam to check alignment. Once the two beams are aligned, the lens for one of the beam paths is moved into place and positioned so that it is normal to and centered in the beam. Its position is adjusted so that the crosshairs in the imaged beam is still aligned with the crosshairs of the other, unimaged beam at the film plane. The lens for the other beam path is positioned in the same way, making sure it the crosshairs of the second beam is still aligned with the imaged beam of the first.

After the beams have been aligned, the alignment crosshairs and reference wires on the side of the vacuum tank near the ruby laser are removed, along with other alignment aids such as the index card at the film plane. The irises are positioned and re-cut from an index card mounted over a larger hole in a piece of cardboard, if necessary. To protect the film from stray light from the laser cavity, a second piece of cardboard is mounted perpendicular to the irises on the laser-cavity side of the camera or the laser cavity is covered by cloth, making sure not to bump any of the aligned optical components. The holography laser monitor photodiode is mounted in front of the alignment laser and the tilting mirror electronics are connected to the two ends of the hot wire on the tilting mirror mount. A multimeter is connected in series with the wire and set up to read a current of approximately 0.35 A. An extension cord is run from the tilting mirror electronics to a switchable power strip outside the lab near the screen room. The black cloth covering the windows and separating the laboratory from the screen room is checked for holes that might leak laser light outside the laboratory and potentially result in eye damage.

A.3 Loading the Film

PFG-01 holographic film is used to make the interferograms. It is a red-sensitive emulsion primarily intended for use with He-Ne lasers. It is made by the Slavich company outside Moscow, Russia and distributed locally by Laser Reflections in Seabeck, Washington. The film is reasonably priced—a 20 meter-long roll of 35 mm film costs \$115, or thirty sheets of approximately 35 mm square film cost \$30. It is stored in a refrigerator to prolong its life. A cool, dry storage environment is best for extending the shelf life of the film.

All handling of the film must be in complete darkness without a safelight, so the film is loaded into the back of the camera in the holography darkroom located in the TIP lab next door to the ZaP lab. Practically speaking, however, film leaders exposed to low light levels in the laboratory become only slightly exposed. For roll film, approximately 1.5 in of space is needed per interferogram on the film, so 12 in of roll film is cut to make 5 interferograms and to provide space for leaders at the beginning and end of the film. The rest of the film roll is immediately put away minimize the possibility that it might be accidentally exposed to light. The end of the 12 in film section is taped to the spool of a 35 mm film canister,

and the rest of the film is wound around the spool, emulsion side in. The emulsion side can be determined by slightly moistening a finger and touching it to both sides of the film in a spot near an end where no interferograms will be made. The slightly sticky side is the emulsion side. After the spool is put into the canister and capped, the light may be turned on.

A corner of the film leader is cut off, so the now trapezoidal leader can be tucked into a clip on the film take-up reel of the camera. The camera is loaded and advanced in the same manner as any other 35 mm camera. When loading the film, check that it does not slip when the advance lever is turned. A remote shutter cable is used to open the shutter and hold it open with one click. A second click will close the shutter. It is a good idea to advance the film after loading it, turn off the lights, open and close the shutter, and advance it again to ensure that an unexposed portion of the film is in position for the first interferogram to be made.

When film squares are used, loading the film is more complicated. In the darkroom, the film squares are removed from their box, and the box is wrapped up and put away to prevent accidental exposure of the rest of the film to light. A paper cutter is used to cut 2 mm or so from the top edge of each square of film, which is actually a little more than 35 mm square and would not otherwise fit in the camera. Each square of film is labeled, in order, with a number on a small sticker that can be used later for identification. The label is placed in the upper right-hand corner of the emulsion side of the film, from the film's perspective. The first piece of film is taped to the camera body over the back of the shutter opening where the film would normally sit. The camera back is closed. The other pieces of film are placed, in order, into a dry developing tank. Once the developing tank lid is closed, the light is turned on and both the tank and the camera are brought into the lab.

A.4 Making the Holographic Interferogram

Most steps involved in making holographic interferograms are included in Ref. [19]. A few of the details, however, are related here.

Before making interferograms, the laser beam path is checked for obstructions, and proper positioning of the irises is verified using the alignment laser pointer. The tilting

mirror electronics are turned on and tested to see that a current of approximately 0.33–0.36 A flows through the hotwire. The alignment laser is covered, and the ruby laser is fired at a piece of Zap-It paper to verify its alignment and beam quality. When making interferograms, the laser is usually set to a power supply voltage of 3.60–3.75 kV, a Pockels cell voltage of 8.3 kV, a Pockels cell delay of 0.90 ms, and an iris size of 4 mm. The holography laser remote control, part of the Thomson/holography laser remote control, is typically used when firing the ruby laser and making interferograms. When making plasma pulse interferograms, however, the fire plug in the back of the laser power supply must be switched to allow the laser to be triggered by the 45 V trigger box on top of the laser. This causes the laser to be triggered by the digital delay generators used to control the experiment, rather than by the button on the remote panel. A trigger box with a 0.90 ms or so delay can also be connected to the Pockels cell, or the internal trigger delay can be used.

The laser keys are disconnected from the hazard lights in the lab and used to turn on the laser power supply. The overhead lights, ionization gauge, and any other large lights in the lab are turned off and the camera shutter is opened. The laboratory door is closed, and the interlock system is energized. The laser is fired once to make the reference, non-plasma holographic exposure. The power strip controlling the hotwire is turned on to move the tilting mirror, and the second holographic exposure is made during the plasma pulse. Typically for a 9 kV pulse, the charge button for the laser must be pushed as the capacitor bank voltage on the experiment passes through 8.75 kV. When the laser is charged and the capacitor bank voltage drops to 9 kV, the experiment is triggered and the holography laser fires automatically according to the time set in the digital delay generator. After the laser is fired and the capacitor banks on the experiment have been dumped, the camera shutter is closed and the lights can be turned on or a flashlight can be used to record the hotwire voltage. If sheet film is being used, the lights are turned off while the exposed film is transferred to a dry developing tank and an unexposed square from the other developing tank is taped into the camera. Regardless of the film type used, the film advance lever is pushed, and the shutter is opened with the room lights off again. The film advance lever advances roll film, but also winds the shutter. The hotwire is turned off, and the next

interferogram can be made.

A.5 Developing the Holographic Interferogram

The holographic interferogram is developed in a developing tank in the darkroom, with the lights on for all steps except loading the film into the developing tank. Loading the film roll onto the wire holder used with the developing tank can be tricky, and should be practiced with an old piece of film, with light, beforehand. The sheets are easier to load, and use a larger, black plastic developing tank. Once the developing tank is closed, the lights can be turned on. The film is developed according to the steps in Table A.1. Many

Table A.1: Darkroom processing of holographic film.

Processing Solution	Solution Used	Processing Time
Developer	Kodak Developer D-19	5 minutes
Stop Bath	Kodak X-Ray Indicator Stop Bath	10 seconds
Fixer	Kodak Rapid Fixer	5 minutes
Rinse	water	5 minutes
Bleach	potassium dichromate	until barely visible
Rinse	water	10 minutes

other developing schemes are also possible, and it would be worthwhile to switch to a more environmentally safe bleach than potassium dichromate. None of the chemicals used, except water, are allowed to be released to the sewer at the University of Washington. All can be used again many times before they are exhausted. The shelf life of the concentrates and powders used to make the darkroom chemicals is several years, up to ten in some cases. The potassium dichromate solution has a long shelf life, as well, but the other working strength solutions have a shelf life of only around three months.

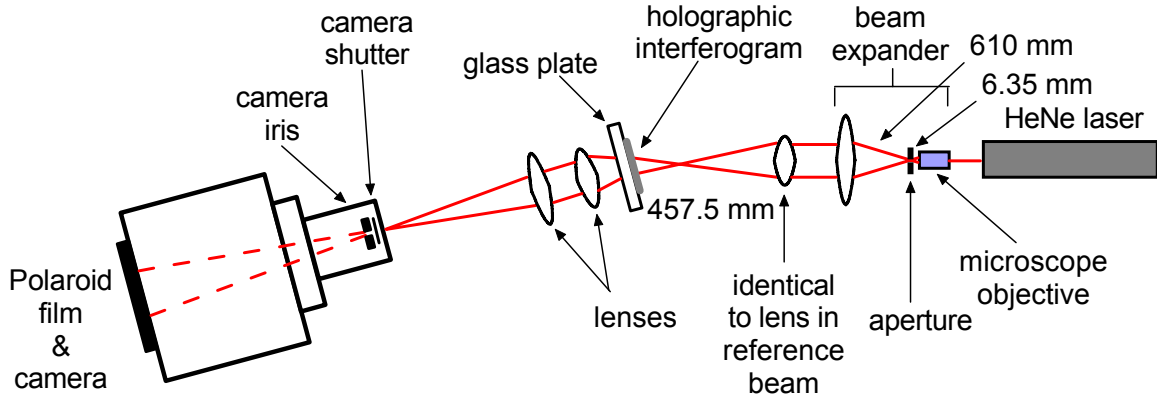


Figure A.5: Optical configuration used to reconstruct holographic interferograms, including important dimensions.

A.6 Reconstructing the Holographic Interferogram

After they are developed, the holographic interferograms are reconstructed and recorded on instant black-and-white film, as described in Ref. [19]. The reconstruction setup is shown in Fig. A.5. A few important dimensions are included in the diagram. The focal lengths of the two lenses that make up the beam expander are shown. The pinhole used to spatially filter the reconstruction beam is located at their mutual focal point, and the sum of their focal lengths is the total length of the beam expander. The distance between the 305 mm focal length lens and the holographic film in the reconstruction setup is the same as the distance between the lens and the film in the holographic interferometer. Since the lenses used to make the interferogram reversed the image of the scene beam at the film, in the reconstruction setup, the interferogram is mounted in the same orientation as when it was made. After the imaging optics, the resulting image is no longer reversed, and the black-and-white photograph represents what would have been “seen” by an observer looking through the back of the camera at the plasma in the experiment.

Figure A.6 is a photograph of the optical configuration used to reconstruct holographic interferograms. A He-Ne laser is used to mimic the reference beam used to make the interferogram. This beam is diffracted by the holographic film, producing the reconstructed scene beam. Figure A.7 shows the reconstructed images that result when the reconstruction

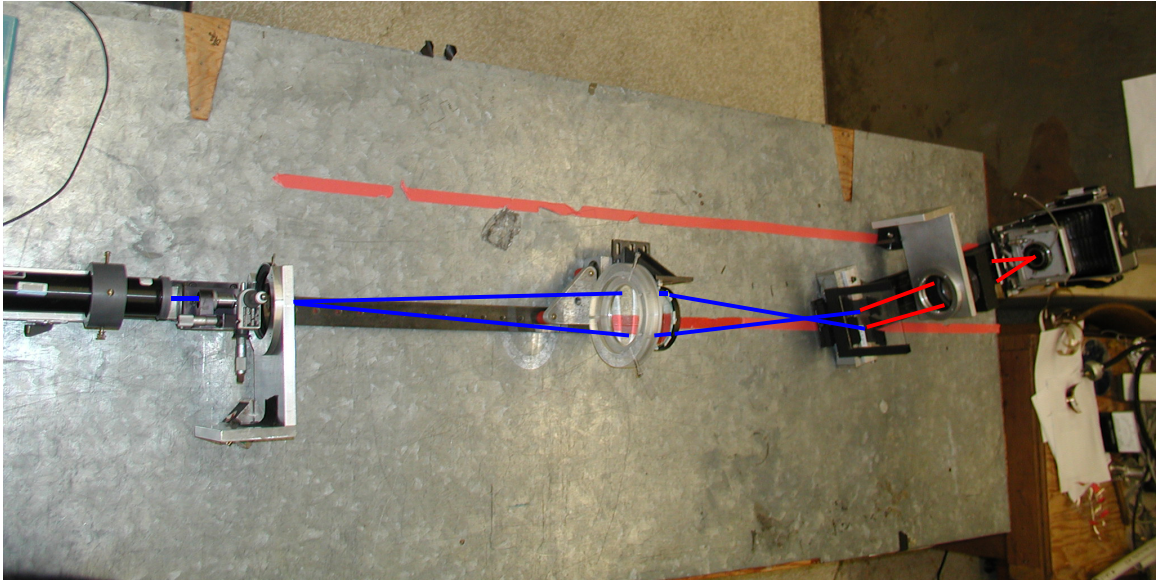


Figure A.6: Photograph of the optical configuration used to reconstruct holographic interferograms. A He-Ne laser is used to mimic the reference beam used to make the interferogram. This beam is diffracted by the holographic film, producing the reconstructed scene beam.

laser beam is diffracted by the holographic film. The second image from the left, which propagates normal to the film, is the virtual image of the reconstructed scene beam that is recorded and used to determine the plasma density.

A.7 Density Determination and Data Storage

The methods used to measure the fringe shift and calculate the chord-integrated electron density and the radial electron density profile are discussed at great length in Ref. [19], and a more concise, up-to-date discussion is included in the RSI paper that is awaiting publication. The IDL routines *analyze_interferogram.pro* and *invert_interferogram.pro*, included in Appendices D and E are used in that order to isolate the fringes in the scanned tagged image format (TIF) of the reconstructed interferogram and to obtain the density. Although a reduction in the error bars was anticipated when higher resolution was used to scan the interferogram, this effect was not observed in practice. In addition, the higher resolution resulted in more problems with missed points during fringe localization. The end result of

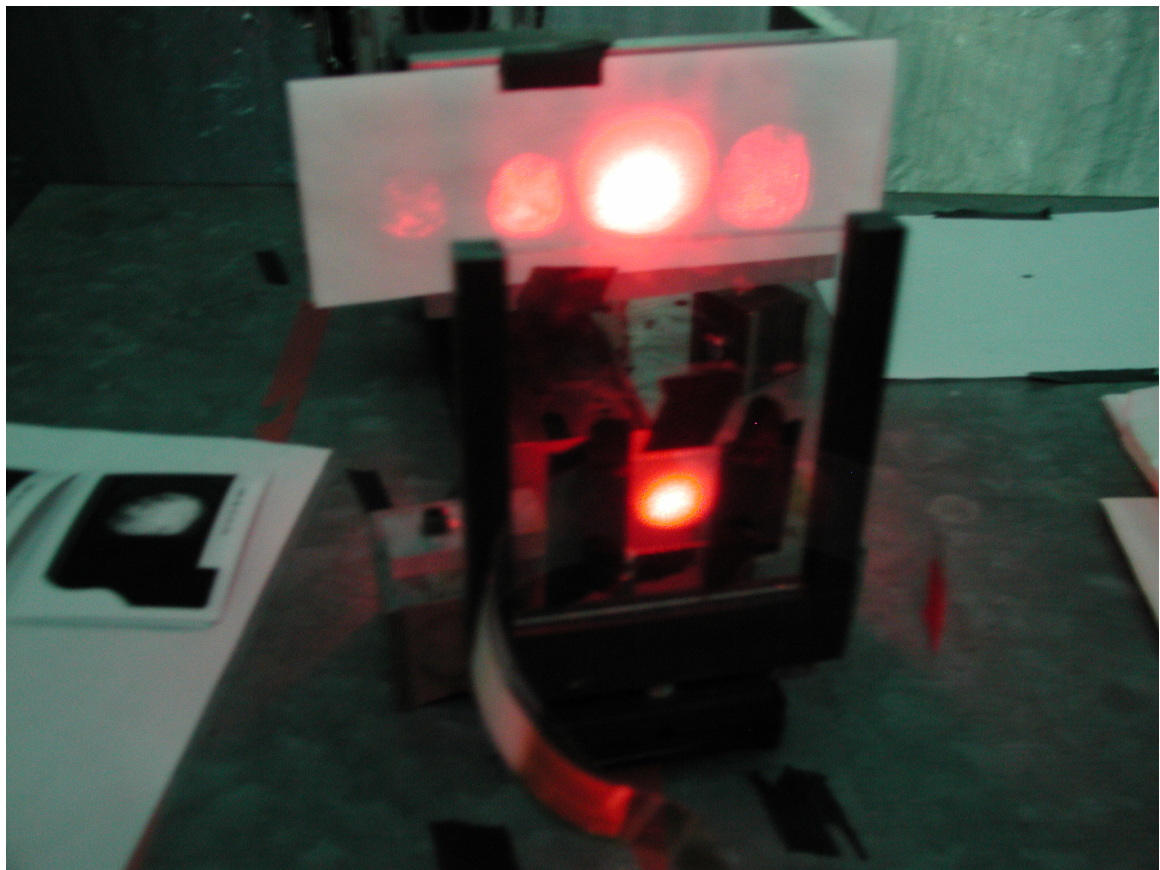


Figure A.7: Reconstructed images that result when the reconstruction laser beam is diffracted by the holographic film. The second image from the left, which propagates normal to the film, is the virtual image of the reconstructed scene beam that is recorded and used to determine the plasma density.

the analysis are two data files containing the fringe coordinates, chord-integrated density, and radial density profile, among other quantities, as IDL variables. The radial coordinate, chord-integrated density, and density profile can be written to a text file by the IDL procedure *write_holography_ascii.pro*. Another IDL procedure, *write_holography_tree.pro* is currently under development to write these and other relevant quantities to the Zapmain MDSPlus tree database. The raw interferograms and the associated data files are stored in the folder

M:\Users\Archived_Users\Stuart_Jackson\ZaP\Holograms,

which contains an Excel spreadsheet called *Catalog of Holograms.xls* describing many of the interferograms. The IDL procedures are stored in the folder

M:\Users\Archived_Users\Stuart_Jackson\ZaP\IDL\holography.

The black-and-white instant photos of the reconstructed interferograms can be found in two red binders, labeled “Holograms I” and “Holograms II,” while the interferograms themselves can be found in several labeled, small boxes in the holography reconstruction area. The naming convention for plasma pulse interferograms is “YYYY MM DD NNN-H1”, where “YYYY” is the four-digit year, “MM” is the two-digit month, “DD” is the two-digit day, and “NNN” is the three-digit pulse number on the day. The interferogram named “2003 02 04 007-H1” was made on Pulse 30204007, for example. Baseline interferograms are not made during a plasma pulse, so the “NNN” is dropped, and the “H1” is incremented as baseline interferograms are made over the course of the day. The fourth baseline made on February 4, 2003 is named “2003 02 04-H4”, for example. The reconstructed interferograms are named by adding “-P1”, “-P2”, and so on to the name of the interferogram to indicate if they were the first, second, or later photo taken of the reconstruction. The second photo made of interferogram “2003 02 04 007-H1”, for example, is named “2003 02 04 007-H1-P2.” Often several photos are made of a single reconstruction as the exposure is adjusted, and different exposure levels may make different features apparent in the interferogram.

Appendix B

INPUT FILE FOR MACH2 ZAP SIMULATION

```
ZaP Experiment Simulation zap11.2h
zap11.2h
!
! filename izap11.2h
! 06/01/31 11.2h: volt=9.e3
! 06/01/31 11.2g: volt=8.e3
! 06/01/31 11.2f: volt=7.e3
! 06/01/31 11.2e: volt=6.e3
! 06/01/31 11.2d: volt=5.e3
! 06/01/31 11.2c: volt=4.e3
! 06/01/31 11.2b: volt=3.e3
! 06/01/31 11.2a: volt=2.e3
! 06/01/26 11.1b: volt=2.e3->3.e3
! 06/01/26 11.1a: volt=9.e3->2.e3
! 06/01/24 11.0b: volratm=0.8->0.1, courmax=0.8->5.
! 06/01/02 11.0a: roi(1)=1.879e-4->4.72e-4
! corrected initial density caused by using incorrect
! radius to calculate total mass injected
! to run, type: /usr/bin/nohup m2 -i input_file > output_file &
!
$contrl
! begin at t = 0
t = 0.,
```

```
! initial and maximum timesteps
dt = 1.e-9,
!x  dtmax = 2.e-7,
! run to 50 microseconds
twfn = 100.e-6, ! 10.1b 1e-9,
!  ncycwfn = 40,
! cylindrical symmetry
cyl = 1.,
! physics simulation switches:
eoson = .true.,
! assume electron-ion equilibrium
tsplit = 0,
! multi material model
!      con2on = .true.,
! no radiation
radiate = .false.,
radmodl = 'none',
! external circuit
ciron = .true.,
! no thermal diffusion
thmldif = .false.,
anisot = .false.,
mgmodet = 'vcycle ',
nthrmax = 200,
flxlmt = 0.4,
tdtol = 1.e-4,
tdrelax = 0.5,
! magnetic diffusion
bdiff = .true.,
! vcycle the magnetic diffusion solver
```

```

mgmode = 'vcycle',
ncorplv = 100, ! 6.0i 40
itmaxrd = 500, ! 6.0c 50
rdtol = 1.e-6,
rdrelax = 0.5,
aresfdg = 0.05,
jouhmlt = 1.,
aresvac = 1.e0, ! 6.3f-i 2e8 6.2c 5e7; 6.01 1e7; 6.0j 1e8; 5.6q 1e4
! rofanom = 1.e-7,
hallon = .false.,
magon = .true.,
! B-theta only
brbzon = .false.,
! itpot > 0 means the potential solver is used to cleanup the magnetic field
! by reducing the divergence while maintaining the current density
itpot = 0,
potrelx = 0.1,
hydron = .true.,
! Lagrangian problem requires fully time-advanced differencing
theb = 1.,
vldenf = 1.e-5,
volratm = 0.1, ! 11.0b 0.8,
! large courant multiplier to keep the vacuum from constraining dt
courmax = 5., ! 11.0b 0.8,
rmvolrm = 0.9,
! artificial viscosity multiplier
mu = 0.0,
eps = 1e-5, ! 9.0r 1.e-6,
! no shear material strength
strength = .false.,

```

```
! construct an ideal mesh each cycle
  meshon = .false.,
  nsmooth = 4,
  wrelax = 0.25,
  nigen = 0,
  niter = 5,
  eqvol = 0.,
! use multi-grid for solving the diffusion equation
  multgrd = .false.,
$end
$output
! output control -- need cgslib from LANL to make pictures
! terminal edits
  intty = 'edits,10',
!  ncyc tty = 1,
! write restart: outrestart
  dtrst = 10.e-6, ! 9.5a 31.e-6,
!  ncycrst = 1.e-6,
! tecplot output
  poston = .false.,
  tecon = .true.,
  dtplot = 1.e-6, ! generates plot file every 1000 nanoseconds
    tplot(9) = 'rbtheta', ! 8.0e 'ni',
    tplot(10) = 'ni', ! 8.0f 'ti',
    tplot(11) = 'te', ! 8.0e 'pressure',
    tplot(12) = 'pressure', ! 8.0e 'magp',
! history plot of current versus time
  ncychist = 1.e-6,
  histnum = 6,
  histpic = .true.,
```

```
!      hstnumfc = 0,
probtype(1) = 'rbzdot',
histx(1) = 0.0900d0, ! 9.5a 0.0508d0,
histy(1) = -0.6500d0, ! 9.5a 0.d0,
probtype(2) = 'elecdens',
histx(2) = 0.0900d0,
histy(2) = -0.6500d0,
probtype(3) = 'rbzdot',
histx(3) = 0.0900d0,
histy(3) = -0.2500d0,
probtype(4) = 'elecdens',
histx(4) = 0.0900d0,
histy(4) = -0.2500d0,
probtype(5) = 'rbzdot',
histx(5) = 0.0900d0,
histy(5) = -0.0000d0,
probtype(6) = 'elecdens',
histx(6) = 0.0000d0,
histy(6) = -0.0000d0,
! 2-D picture file: cpm2
! print 14 pictures every microsecond
!      dtp = 0.5e-6,
!      ncycp = 10,
!      ncycpost = 10,
!      fichfram = 14,
!      plot(0) = 'pfs      ',
!      plot(14) = 'ni',
!      kcon(1) = 5,
! print slice plots
!      dtslic = 0.5e-6,
```

```

!    ncycslic = 2,
!    ibdyslic = 4,
!    lblkslic = 4,
!    ijslic = 16,
!        slice(1) = 'ni',
!        slice(4) = 'current',
!    sliccomp(4) = 'vectorx',
!        slice(5) = 'current',
!    sliccomp(5) = 'vectory',
!        slice(10) = 'density',
! don't draw internal block boundaries
!    intbound = .false.,
!    pltscal = 'none',
! print letter labels on the contours
!    clabpict = .false.,
! color-code vectors according the magnitude of the out-of-plane component
!    mvecclr = -1,
!        vsclmlt = 0.05,
! don't show both sides of the axis
!    pflip = .false.,
!    frccl = .true.,
$end
$curnt
! external circuit model
! 8/9/01 6.3b changed circuit type from rlc
!            so vars added are currvalu and currtime
!            current and time values obtained from shot 10705008
!    circtype(1) = 'linear',
!    currvalu(1,1) = 0,
! currtime(1,1) = 0.e-6,

```

```

! currvalu(2,1) = 1.5e4,
! currtime(2,1) = 1.e-6,
! currvalu(3,1) = 4e4,
! currtime(3,1) = 2.e-6,
! currvalu(4,1) = 7e4,
! currtime(4,1) = 4.e-6,
! currvalu(5,1) = 1e5,
! currtime(5,1) = 7.e-6,
! currvalu(6,1) = 1.7e5,
! currtime(6,1) = 10.e-6,
! currvalu(7,1) = 2.15e5,
! currtime(7,1) = 12.e-6,
! currvalu(8,1) = 2.5e5,
! currtime(8,1) = 14.e-6,
! currvalu(9,1) = 2.6e5,
! currtime(9,1) = 17.e-6,
! currvalu(10,1) = 3.e5,
! currtime(10,1) = 27.e-6,
    circtype(1) = 'rlc',
    volt = 9.e3, ! 11.2h 8.e3, ! 11.2g 7.e3, ! 11.2f 6.e3, ! 11.2e 5.e3,
! 11.2d 4.e3, ! 11.2c 3.e3, ! 11.2b 2.e3,
    capac = 1.36e-3,
    exind = .49184e-6,
$end
$ezgeom
! specify the geometry -- 7 logical blocks
! 05/02/17 added nosecone and adjusted other coordinates
! 05/06/16 10.1a: added end wall hole geometry
! 05/06/21 10.1e: got rid of block 8
    nblk = 7, ! 10.1e 8,

```

```
npnts = 18, ! 10.1e 20,
numarcs = 2, ! 10.01 0,
pointx(1) = 0.0504, pointy(1) = -0.77675, ! 8.0a 0.0504,
pointx(2) = 0.0963, pointy(2) = -0.77625, ! 8.0a 0.0932,
pointx(3) = 0.0504, pointy(3) = -0.72325, ! 8.0a 0.0508,
pointx(4) = 0.0963, pointy(4) = -0.72325, ! 8.0a 0.0932,
pointx(5) = 0.0469, pointy(5) = -0.2315, ! 10.0g -0.2310
pointx(6) = 0.0504, pointy(6) = -0.2440, ! 8.0a 0.0508, -0.25,
pointx(7) = 0.0963, pointy(7) = -0.2440, ! 8.0a 0.0932, -0.25,
pointx(8) = 0.0430, pointy(8) = 0.7613, ! 10.1e 0.0469,
pointx(9) = 0.0504, pointy(9) = 0.7613, ! 9.0a 0.76,
pointx(10) = 0.0963, pointy(10) = 0.7613, ! 9.0a 0.76,
pointx(11) = 0.0504, pointy(11) = -1.2564, ! 9.0a -1.25,
pointx(12) = 0.0963, pointy(12) = -1.2564, ! 9.0a -1.25,
pointx(13) = 0.0216, pointy(13) = -0.1869, ! 10.0a -0.2440,
pointx(14) = 0.0102, pointy(14) = 0.7899, ! 10.1e 0.0216, 0.7613,
pointx(15) = 0.0000, pointy(15) = -0.1744, ! 10.0g -0.1764,
pointx(16) = 0.0000, pointy(16) = 0.7899, ! 10.0e 0.7613,
pointx(17) = 0.0494, pointy(17) = -0.2375,
pointx(18) = 0.0125, pointy(18) = -0.1778,
corners(1,1) = 3, 4, 2, 1,
corners(1,2) = 6, 7, 4, 3,
corners(1,3) = 9, 10, 7, 6,
corners(1,4) = 8, 9, 6, 5,
corners(1,5) = 1, 2, 12, 11,
corners(1,6) = 14, 8, 5, 13,
corners(1,7) = 16, 14, 13, 15,
arcs(1,1) = 6, 5, 17, ! 10.0g 0.75, ! 10.0e -0.5, ! 10.0d 0.0,
arcs(1,2) = 13, 15, 18, ! 10.0g 0.6667, ! 10.0f 1.3333,
arctype(1) = '3point', ! 10.0g '2pt_dir',
```

```
arctype(2) = '3point', ! 10.0g '2pt_dir',
$end
$ezphys
! specify the global physics models
! moderate-density hydrogen
eosmodlg = 'idealgas',
ang = 1,
awg = 1,
roig = 1.e-7, ! 10.1j 9.e-7,
tempig = 1., ! 6.4g 10 tempig = tflow(3,5)
icellsg = 16,
jcellsg = 16,
! initial fields are set to small values
bxig = 0.,
byig = 0.,
bzig = 0.,
! classical spitzer electrical resistivity
resmodlg = 'spitzer',
etaming = 0.5,
etamaxg = 1.e8,
! vacuum anomalous resistivity
arsmodlg = 'vacuum ',
! classical spitzer thermal conductivity
tcnmodlg = 'spitzer ',
! allow negative energies because we have solid aluminum
siecoldg = -1.e99,
dirintpg = 'intp3t1 ',
! use much of the ideal mesh
gdvlg = 0.,
! adapt on the density gradient
```

```

!      psdlagrg = .false.,
      rofg = 1.e-10,
! turn hydro off in low-density cells
!      rofrad = 1.e-2,
!      rofanomg = 1.e-4,
      rofvacg = 1.e-8,
! keep temperature below 0.2 keV
      tecapg = 2.e2,
$end
$matmdl
      matnam(1) = 'vacuum',
      sesanam(1) = 'h',
      an(1) = 1,
      aw(1) = 1, ! 9.5a 2,
      rofanom(1) = 1.e-8,
      rofjoule(1) = 1.e-8,
      rofsiecp(1) = 1.e99,
      matnam(2) = 'plasma',
      sesanam(2) = 'h',
      an(2) = 1,
      aw(2) = 1, ! 9.5a 2,
      rofsiecp(2) = 1.e99,
$end
$inmesh
! specify block-specific initial data and boundary conditions

      matnami(1) = 'plasma',
      jcells(1) = 4,

```

```

roi(1) = 4.72e-4, ! 11.0a 1.879e-3,
hydbc(2,1) = 'wall',
hydbc(4,1) = 'wall',
magbc(2,1) = 'conductr',
magbc(4,1) = 'conductr',

matnami(5) = 'vacuum',
jcells(5) = 32, !6.4a 16, 6.3e 4; 5.6r 8
hydbc(2,5) = 'wall',
hydbc(4,5) = 'wall',
magbc(2,5) = 'conductr',
magbc(4,5) = 'conductr',
! attach capacitor here
hydbc(3,5) = 'flowthru', ! 10.1h 'wall',
roflow(3,5) = 1.e-7, ! 10.1j 9.e-7, keeping equal to roig
tfflow(3,5) = 1., ! 6.4g 10 tfflow =tempig
magzbc(3,5) = 'insulatr',
currcir(3,5) = 1,
rstbc(3,5) = 'symmetry'

matnami(2) = 'vacuum',
jcells(2) = 32,
hydbc(2,2) = 'wall',
hydbc(4,2) = 'wall',
magbc(2,2) = 'conductr',
magbc(4,2) = 'conductr',

matnami(3) = 'vacuum',
jcells(3) = 128, ! zap10.0z 64, ! zap9.0m 32,
hydbc(1,3) = 'wall',

```

```

hydbc(2,3) = 'wall',
magbc(1,3) = 'conductr',
magbc(2,3) = 'conductr',

! boundary conditions for regions bordering nosecone

matnami(4) = 'vacuum',
jcells(4) = 128, ! zap10.0z 64, ! zap9.2e 128,
icells(4) = 4, ! 10.01 2,
hydbc(1,4) = 'wall',
hydbc(3,4) = 'wall',
magbc(1,4) = 'conductr',
magbc(3,4) = 'conductr',

matnami(6) = 'vacuum',
jcells(6) = 128, ! zap10.0z 64, ! zap9.0m 32
icells(6) = 16, ! 10.0i 32,
hydbc(1,6) = 'wall',
hydbc(3,6) = 'wall',
magbc(1,6) = 'conductr',
magbc(3,6) = 'conductr',

matnami(7) = 'vacuum',
jcells(7) = 128, ! zap10.0z 64, ! zap9.0m 32
icells(7) = 16, ! 10.0i 32,
hydbc(1,7) = 'flowthru', ! 10.1e
roflow(1,7) = 1.e-7, ! 10.1m 9e-7, ! 10.1e keeping equal to roig
tflow(1,7) = 1., ! 10.1e keeping equal to tempig
! 10.1m probc(1,7) = 'contnutv', ! 10.1f
hydbc(3,7) = 'wall',

```

```
hydbc(4,7) = 'axis',
magzbc(1,7) = 'symmetry', ! 10.1e
rstbc(1,7) = 'symmetry', ! 10.1e
magbc(3,7) = 'conductr',
magbc(4,7) = 'axis',
$end
! $modtim
! modify simulation parameters when it reaches 32 us
!      tmod = 31.0e-6, ! 9.4d 1.8e-6,
! $end
! $output
! write graphics output every 10 ns
!      dtpost = 1.e-8,
! $end
```

Appendix C

IDL PROCEDURE *DENSE_FIN.PRO*

This appendix contains the source code for the IDL procedure *dense_fin.pro*, written by Raymond Golingo and Ted Shreve to obtain the chord-integrated electron number density of the plasma from the digitized sine and cosine of the phase shift measured by the interferometer.

```
pro dense_fin
;
;getting shot
;
shot = mdsvalue('$shot')
;
; Conversion using 632.8nm for laser wavelength,
;eq 4.2 in Hermann Thesis
;
convert=5.61
;
;chord length of each view
;
l=dblarr(4)
l(0)=0.0938
l(1)=0.124
l(2)=0.145
l(3)=19.261
;
```

```

;Setting initial noise end to I_P = 50000
;
Ip=mdsvalue('I_P')
Tip=mdsvalue('dim_of(I_P)')
ip=abs(dsmooth(ip,5,7))

Kip=min(where(ip gt 2e4))
If (kip eq -1) then kip=0
Noise_end = tip(kip)*1e6

Kip=max(where(ip gt 2e4))
If (kip eq -1) then kip=max(where(Tip gt 200e-6))
Plasma_end = tip(kip)*1e6 + 200
;
; Digital filter parameters
;
Flow=0
Fmid=.2
Fhigh=1
a=50
N_terms=13
Coeff_low = DIGITAL_FILTER(Flow, Fmid, A, N_terms)
Coeff_high= DIGITAL_FILTER(Fmid, Fhigh, A, N_terms)
;
; Magnitude of phi change to account for fringe jumps
;
jump=!pi
;
;Do loop for 2 chords
;

```

```
for chord=1,2 do begin
;
;Getting time base, location, sin and cos values
;
if (chord eq 1) then begin

cos1=mdsvalue('\digitizers::cos1')
sin1=mdsvalue('\digitizers::sin1')
to=mdsvalue('dim_of(\digitizers::cos1)')
loc=mdsvalue('\NE_1:HOLE_LOC')
baseline=mdsvalue('\ne_1:baseline')
z=mdsvalue('\ne_1:z_loc')
endif else begin

cos1=mdsvalue('\digitizers::cos2')
sin1=mdsvalue('\digitizers::sin2')
to=mdsvalue('dim_of(\digitizers::cos2)')
loc=mdsvalue('\NE_2:HOLE_LOC')
baseline=mdsvalue('\ne_2:baseline')
z=mdsvalue('\ne_2:z_loc')
endelse
;
;added 21 April 2004 to fix minus sin introduced by new IF setup
;removed 23 June 2004 to remove minus sin with new IF setup
;
sin1=sin1
;
; Adjusting time base
;
to=to*1e6
```

```

;

;Get the array size

;

ndata=n_elements(cos1)

;

;Offset method

;

if ( shot ne baseline) then begin

  mdsopen,'zapmain',stremo(baseline)

  if (chord eq 1) then begin

    xpo=mdsvalue('\ne_1:sin_offset')

    ypo=mdsvalue('\ne_1:cos_offset')

    del_xpo=mdsvalue('\ne_1:sin_offset:error')

    del_ypo=mdsvalue('\ne_1:cos_offset:error')

  endif else begin

    xpo=mdsvalue('\ne_2:sin_offset')

    ypo=mdsvalue('\ne_2:cos_offset')

    del_xpo=mdsvalue('\ne_2:sin_offset:error')

    del_ypo=mdsvalue('\ne_2:cos_offset:error')

  endelse

  mdsopen,'zapmain',stremo(shot)

endif else begin

  xpo=total(sin1)/ndata

  ypo=total(cos1)/ndata

  del_xpo=sqrt(total((sin1-xpo)^2)/(ndata-1))

  del_ypo=sqrt(total((cos1-ypo)^2)/(ndata-1))

  sin1=sin1+1.

  cos1=cos1+1.

endelse

```

```
;  
; Adjustment for center offset  
;  
xo=sin1-xpo  
yo=cos1-ypo  
;  
; Rotating the coordinate system  
;  
theda_0=atan(total(xo(0:10))/11,total(yo(0:10))/11)  
xo_t=xo  
yo_t=yo  
xo=xo_t*cos(theda_0)-yo_t*sin(theda_0)  
yo=yo_t*cos(theda_0)+xo_t*sin(theda_0)  
;  
; Calculate the phase shift  
;  
y=atan(xo,yo)  
;  
; Calculate the phase shift with applying the digital filter  
;  
x_low=CONVOL(xo, Coeff_low)  
y_low=CONVOL(yo, Coeff_low)  
x_high=CONVOL(xo, Coeff_high)  
y_high=CONVOL(yo, Coeff_high)  
  
y_sm=atan(x_low,y_low)  
to_sm=to  
ndata_sm=n_elements(to_sm)  
;  
;Correction for VAX atan(0,0)
```

```

n_xy_zero=where(((x_low eq 0) and (y_low eq 0)) and (to le 0))
y_sm(n_xy_zero)=y_sm(max(n_xy_zero)+2)
n_xy_zero=where(((x_low eq 0) and (y_low eq 0)) and (to ge 0))
y_sm(n_xy_zero)=y_sm(min(n_xy_zero)-2)

;

;getting the amplitude of the noise
;

x_high1=dsmooth(abs(x_high))+sqrt((del_xpo*cos(theda_0))^2 $
+(del_ypo*sin(theda_0))^2)
y_high1=dsmooth(abs(y_high))+sqrt((del_ypo*cos(theda_0))^2 $
+(del_xpo*sin(theda_0))^2)
;

;finding errors in psi
;

r_2=(x_low^2+y_low^2)>(del_xpo^2+del_ypo^2)
del_y=sqrt(((yo*x_high1)^2+(xo*y_high1)^2)/((r_2)^2))
del_y=del_y<(2*dpi)
;

;Finding earliest vibration fringe jump
;

ave1=total(y_sm(1:50))/50.
n_time_m1=min(where(to_sm ge -1e-6))
ave2=total(y_sm(n_time_m1-50:n_time_m1-1))/50.
ave_slope=(ave2-ave1)/(to_sm(n_time_m1-25)-to_sm(25))
t_end_slope=to(25)+(2.5-abs(ave1))/abs(ave_slope)
;

; Finding region for vibration fits
;

k=min(where(to ge noise_end))

```

```

pk=min(where(to ge plasma_end<t_end_slope))
;
; Accounting for fringe jumps after the plasma pulse
;
a=dblarr(ndata-pk)
b=dblarr(ndata-pk)
d=dblarr(ndata-pk)
a=(y(pk:ndata-2)-y((pk+1):ndata-1)) gt jump
b=(y(pk:ndata-2)-y((pk+1):ndata-1)) lt -jump
d=1.0*a-1.0*b
sum=dblarr(ndata-pk)
for I=long(1),ndata-1-pk do $
  sum(I)=sum(I-1)+d(I-1)
y(pk+1:ndata-1)=y(pk+1:ndata-1)+2.0*!pi*sum(1:ndata-pk-1)
a=dblarr(ndata_sm-pk)
b=dblarr(ndata_sm-pk)
d=dblarr(ndata_sm-pk)
a=(y_sm(pk:ndata_sm-2)-y_sm(pk+1:ndata_sm-1)) gt jump
b=(y_sm(pk:ndata_sm-2)-y_sm(pk+1:ndata_sm-1)) lt -jump
d=1.0*a-1.0*b
sum=dblarr(ndata_sm-pk)
for I=long(1),ndata_sm-1-pk do $
  sum(I)=sum(I-1) + d(I-1)
y_sm(pk+1:ndata_sm-1)=y_sm(pk+1:ndata_sm-1) $
  +2.0*!pi*sum(1:ndata_sm-pk-1)
;
pk=min(where(to ge plasma_end))
;
;finding time for baseline
;

```

```

nset=[where(to_sm le 2e-6),where(to_sm ge plasma_end)]
;
; Finding baseline and error
;
diag=INDGEN(5)*(5 + 1)
pder=[[replicate(1., n_elements(nset))],[to(nset)],[to(nset)^2], $
[to(nset)^3],[to(nset)^4]]
weight=1/(del_y(nset)^2)
alpha = transpose(pder) # (weight# (fltarr(5)+1.)*pder)
alpha_inv=invert(alpha)
drift_coeff=invert(transpose(pder) # pder) # (transpose(pder) $
# y_sm(nset))
sigma = sqrt( alpha_inv[diag] )

del_phi_vib=sigma(0)+to*sigma(1)+(to^2)*sigma(2)+(to^3)*sigma(3) $
+(to^4)*sigma(4)

del_phi_p=sqrt(del_y^2+del_phi_vib^2)
del_phi_p(0:20)=0
del_phi_p(ndata-21:ndata-1)=0
drift=drift_coeff(0)+to*drift_coeff(1)+(to^2)*drift_coeff(2) $
+(to^3)*drift_coeff(3)+(to^4)*drift_coeff(4)
y=y-drift
y_sm=y_sm-drift
;
; Modified Milroy code using Uri's idea for accounting for fringe
;jumps (Jul 03)
;
nstart=min(where(to ge 0))
a1=fltarr(ndata)

```

```

b1=fltarr(ndata)
a1(1:ndata-1)=(y(0:ndata-2)-y(1:ndata-1)) ge jump
b1(1:ndata-1)=(y(0:ndata-2)-y(1:ndata-1)) le -jump
d1=1.0*a1-1.0*b1
d1(0:nstart+100)=0
sumf=fltarr(ndata)
for i=long(1),ndata-1 do $
  sumf(i)=sumf(i-1)+d1(i)
sumb=fltarr(ndata)
for i=long(ndata-2),0,-1 do $
  sumb(i)=sumb(i+1)+d1(i+1)
phi_f=y+2*!pi*sumf
phi_b=y-2*!pi*sumb

phi_b_new= -phi_b+ phi_f(0)+phi_b(0)
a_new=phi_f - phi_b_new

cross= 1.*(phi_b(ndata-100) gt phi_f(ndata-100)) $
  - 1.*(phi_b(ndata-100) lt phi_f(ndata-100))
count=long(0)
if cross gt 0 then begin
  phi_b_new= -phi_b+ phi_f(0)+phi_b(0)
a_new=phi_f - phi_b_new
while (cross ne 0) and (count le 15) do begin
fringe=max(where(a_new(0:ndata-200)*cross gt -1*!pi))
new_sum=fltarr(ndata)
new_sum(fringe:ndata-1)=2*!pi*cross
phi_f=phi_f+new_sum
phi_b=phi_b-2*!pi*cross +new_sum
phi_b_new= -phi_b+ phi_f(0)+phi_b(0)

```

```

a_new=phi_f - phi_b_new
cross= 1.*(phi_b(ndata-100) gt phi_f(ndata-100)) $
        - 1.*(phi_b(ndata-100) lt phi_f(ndata-100))
count=count+1
endwhile
endif else begin
  phi_b_new= -phi_b
  a_new=phi_f - phi_b_new
  while (cross ne 0) and (count le 15) do begin
    fringe=max(where(a_new(0:ndata-200)*cross gt 1.*!pi))+1
    new_sum=fltarr(ndata)
    new_sum(fringe:ndata-1)=2*!pi*cross
    phi_f=phi_f+new_sum
    phi_b=phi_b-2*!pi*cross +new_sum
    phi_b_new= -phi_b
    a_new=phi_f - phi_b_new
    cross=- 1.*((phi_f(0)-phi_b(0)) gt .001)
    count=count+1
  endwhile
endelse

y=-phi_b_new
;
;Modified Milroy code using Uri's idea for accounting for fringe
;jumps w/filtered data (Jul 03)
;
a1=fltarr(ndata_sm)
b1=fltarr(ndata_sm)
a1(1:ndata_sm-1)=(y_sm(0:ndata_sm-2)-y_sm(1:ndata_sm-1)) gt jump
b1(1:ndata_sm-1)=(y_sm(0:ndata_sm-2)-y_sm(1:ndata_sm-1)) lt -jump

```

```

d1=1.0*a1-1.0*b1
d1(0:nstart+100)=0
sumf=fltarr(ndata_sm)
for i=long(1),ndata_sm-1 do $
  sumf(i)=sumf(i-1)+d1(i)
sumb=fltarr(ndata_sm)
for i=long(ndata_sm-2),0,-1 do $
  sumb(i)=sumb(i+1)+d1(i+1)
phi_f=y_sm+2*!pi*sumf
phi_b=y_sm-2*!pi*sumb

phi_b_new= -phi_b+ phi_f(0)+phi_b(0)
a_new=phi_f - phi_b_new

cross= 1.*(phi_b(ndata_sm-100) gt phi_f(ndata_sm-100)) $
       - 1.*(phi_b(ndata_sm-100) lt phi_f(ndata_sm-100))
count=long(0)
if cross gt 0 then begin
  phi_b_new= -phi_b+ phi_f(0)+phi_b(0)
  a_new=phi_f - phi_b_new
  while (cross ne 0) and (count le 10) do begin
    fringe=max(where(a_new(0:ndata_sm-200)*cross gt -1*!pi))
    new_sum=fltarr(ndata_sm)
    new_sum(fringe:ndata_sm-1)=2*!pi*cross
    phi_f=phi_f+new_sum
    phi_b=phi_b-2*!pi*cross +new_sum
    phi_b_new= -phi_b+ phi_f(0)+phi_b(0)
    a_new=phi_f - phi_b_new
    cross= 1.*(phi_b(ndata_sm-100) gt phi_f(ndata_sm-100)) $
           - 1.*(phi_b(ndata_sm-100) lt phi_f(ndata_sm-100))
  end
end

```

```

        count=count+1
    endwhile
    endif else begin
        phi_b_new= -phi_b
        a_new=phi_f - phi_b_new
        while (cross ne 0) and (count le 10) do begin
            fringe=max(where(a_new(0:ndata_sm-200)*cross gt 1.*!pi))+1
            new_sum=fltarr(ndata_sm)
            new_sum(fringe:ndata_sm-1)=2*!pi*cross
            phi_f=phi_f+new_sum
            phi_b=phi_b-2*!pi*cross +new_sum
            phi_b_new= -phi_b
            a_new=phi_f - phi_b_new
            cross=- 1.*((phi_f(0)-phi_b(0)) gt .001)
            count=count+1
        endwhile
        endelse

        y_sm=-phi_b_new
        ;
        ; forcing all densities to be positive
        ;
        y(where(y le -.5)>0)=y(where(y le -.5)>0)+2*!pi
        y_sm(where(y_sm le -.5)>0)=y_sm(where(y_sm le -.5)>0)+2*!pi
        ;
        ;forcing last point to be a fringe jump
        ;
        y(ndata-1)=2*!pi
        y_sm(ndata_sm-1)=2*!pi
        ;

```

```

; Converting to density
;
y=y*convert
y_sm=y_sm*convert
del_phi_p=del_phi_p*convert
;stop
;
; Putting data unto the tree
;
build_string = 'build_signal(build_with_units($1*1e20,"m^(-2)") , ' + $
'*,(build_with_units($2*1e-6,"s")))',

build_string_sm = 'build_signal(build_with_units($1*1e20/' + $
stremo(l(loc-1))+',"m^(-2)") , ' + $
'*,(build_with_units($2*1e-6,"s")))',

build_string_with_err = 'build_signal(build_with_errors $
(build_with_units($1*1e20,"m^(-2)") , $3)' + $
'*, (build_with_units($2*1e-6,"s")))',

mdsopen,'zapmain',stremo(shot)

if (chord eq 1) then begin
  mdsput, '\ne_1', build_string, y, to
  mdsput, '\ne_1:ne_1_sm', build_string, y_sm, to
  mdsput, '\ne_1:ne_1_ave', build_string_sm, y, to
  mdsput, '\ne_1:ne_1_sm_ave', build_string_sm, y_sm, to
  mdsput, '\ne_1:fmid', '$', Fmid
  mdsput, '\ne_1:jump', '$', jump
  mdsput, '\ne_1:sin_offset', '$', xpo
  mdsput, '\ne_1:sin_offset:error', '$', del_xpo
  mdsput, '\ne_1:cos_offset', '$', ypo

```

```

mdsput, '\ne_1:cos_offset:error', '$', del_ypo
mdsput, '\ne_1:error', build_string, del_phi_p, to
endif else begin
  mdsput, '\ne_2', build_string, y, to
  mdsput, '\ne_2:ne_2_sm', build_string, y_sm, to
  mdsput, '\ne_2:ne_2_ave', build_string_sm, y, to
  mdsput, '\ne_2:ne_2_sm_ave', build_string_sm, y_sm, to
  mdsput, '\ne_2:fmid', '$', Fmid
  mdsput, '\ne_2:jump', '$', jump
  mdsput, '\ne_2:sin_offset', '$', xpo
  mdsput, '\ne_2:sin_offset:error', '$', del_xpo
  mdsput, '\ne_2:cos_offset', '$', ypo
  mdsput, '\ne_2:cos_offset:error', '$', del_ypo
  mdsput, '\ne_2:error', build_string, del_phi_p, to
endelse
endfor
end

;

; Past comments and code

;

;

;--Made major changes for higher volage on 7 Feb 00
;--added double smooth 7 feb 00
; changed 24 apr 01 by RPG smo1 3->5 smo2 5->7
;--jump changed 24 apr 01 by RPG 4->!pi.;(changed 3 to 5,7 feb 00)
;--end of noise region in microseconds (deleted 7 Feb 99)
;[;noise_end=5]
;--Finding the center of the DC offsets (No longer used 7 Feb 99)

```

```

; [;xpo=total(sin1(0:ndata-1))/ndata]
; [;ypo=total(cos1(0:ndata-1))/ndata]
; [;xp=sin1-xpo]
; [;yp=cos1-ypo]
; [;xpp=(total(xp^3+xp*yp^2)*total(yp^2) $
;           -(total(yp^3+yp*xp^2)*total(xp*yp))$]
; [;      /(2*(total(xp^2)*total(yp^2)-(total(xp*yp))^2)) ]
; [;ypp=(total(yp^3+yp*xp^2)*total(xp^2) -(total(xp^3+xp*yp^2)) $
;           *total(xp*yp))$]
; [;      /(2*(total(xp^2)*total(yp^2)-(total(xp*yp))^2)) ]
;

;--rotating the coordinate system, added 4jun02
;--Who knows?
; [;l=dblarr(4)]
; [;l(0)=0.0938]
; [;l(1)=0.124]
; [;l(2)=0.145]
; [;l(3)=19.261]
;--added to offset method 4jun02:
;[;sin1=fltarr(ndata)+1.;cos1=fltarr(ndata)+1. ]
;--removed from adjustement of offset: [;xpp=0;ypp=0]
;--changed 02 july 02 to use time before zero for vibration for
;setting phase shift to zero
; [;average=total(y(1:25))/25.0]
;---removed 4jun02 from setting phase shift to zero
; [;if ((ave1(0)-ave2(0)) gt 2) $]
;     [;then ave2(0)=ave2(0)+(2*!pi)]
; [;if ((ave1(0)-ave2(0)) lt -2) $]
;     [;then ave2(0)=ave2(0)-(2*!pi)]
;-- Removed jul 03:

```

```

; -Accounting for fringe jumps (Thanks Richard Milroy)
; [;a=dblarr(ndata)]
; [;b=dblarr(ndata)]
; [;d=dblarr(ndata)]
; [;a=(y(0:ndata-2)-y(1:ndata-1)) gt jump]
; [;b=(y(0:ndata-2)-y(1:ndata-1)) lt -jump]
; [;d=1.0*a-1.0*b]
; [;d(0:K)=0]
; [;sum=dblarr(ndata)]
; -routine for moving backward in time
; [;for i=ndata-5,0,-1 do begin]
;      [;sum(i)=sum(i+1)-d(i)]
; [;endfor]
; [;for I=1,ndata-1 do $]
;      [;sum(I)=sum(I-1)+d(I-1)]
; -setting fringe jumps for noise regions to zero jumps
; [;sum(0:k)=0.0]
; [;y(1:ndata-1)=y(1:ndata-1)+2.0*!pi*sum(1:ndata-1)]
; -Accounting for fringe jumps in smoothed data
; [;a=(y_sm(0:ndata-2)-y_sm(1:ndata-1)) gt jump]
; [;b=(y_sm(0:ndata-2)-y_sm(1:ndata-1)) lt -jump]
; [;d=1.0*a-1.0*b]
; [;d(0:k)=0.0]
; [;sum=dblarr(ndata)]
; [;for i=ndata-5,0,-1 do begin]
;      [;sum(i)=sum(i+1)-d(i)]
; [;endfor]
; [;for I=1,ndata-2 do $]
;      [;sum(I)=sum(I-1) + d(I-1)]
; -setting fringe jumps for noise regions to zero jumps

```

```
; [;sum(0:k)=0.0]
; [;y_sm(1:ndata-1)=y_sm(1:ndata-1)+2.0*pi*sum(1:ndata-1)]
;
```

Appendix D

IDL PROCEDURE *ANALYZE_INTERFEROGRAM.PRO*

```
;Program to find fringes in holographic interferogram
;Input file is grayscale TIF image of interferogram, for example,
; 2003 01 23 009-H1-P2_cropped.tif
;Output file is interferogram data file, for example,
; 2003 01 23 009-H1-P2_cropped.dat, and contains IDL variables
; associated with the fringes in the holographic interferogram:
; top.....location of top reference wire in interferogram
; bottom.....location of bottom reference wire in interferogram
; peaks_x.....array with horizontal device coordinates of bright
; fringes in columns (remember that the element
; located at column 1, row 3 in IDL is called by
; peaks_x[1,3])
; peaks_y.....array with vertical device coordinates of bright
; fringes in columns
; n_pk.....array containing number of points in each bright
; fringe
; straight_peaks_x.....array with horizontal device coordinates of
; straight lines associated
; with bright fringes in columns
; troughs_x.....array with horizontal device coordinates of dark
; fringes in columns
; troughs_y.....array with horizontal device coordinates of dark
; fringes in columns
```

```
; n_trghs.....array containing number of points in each dark
; fringe
; straight_troughs_x....array with horizontal device coordinates of
; straight lines associated with dark fringes in
; columns
; hologram_raw.....array containing brightness of each point in
; interferogram

;Stuart Jackson
;November 25, 2003

pro analyze_interferogram

;Open TIF image of holographic interferogram
hologram_raw=open_hologram(hologram_file=hologram_file)

;Crop interferogram
hologram_raw=crop_hologram(hologram_raw, n_columns=n_columns, $
n_rows=n_rows, noise=noise)

hologram=hologram_raw

window,1,xsize=(size(hologram))[1],ysize=(size(hologram))[2]
tv,hologram

window,10
num_row=(size(hologram))[2]/2
plot,hologram[*,num_row],title='row '+stremo(num_row),charsize=2, $
charthick=2,thick=2,xthick=2,ythick=2
```

```
;Find y coordinates of reference wires
dummy=ref_wires(hologram,top,bottom)

;Make the sinusoidal fringe pattern into a square wave fringe pattern
hologram=dsmooth(hologram,3,5)
hologram=make_square(hologram,top,bottom)

window,11
plot,hologram[*,num_row],title='row '+stremo(num_row),charsize=2, $
charthick=2,thick=2,xthick=2,ythick=2

;Find "peaks" and "troughs"--centers of bright and dark fringes--in
;each row
hologram=digitize_hologram(hologram, n_columns, n_rows, noise, $
num_row=num_row)

wset,12
oplot,hologram_raw[*,num_row],thick=2

;Assign peaks to bright fringes, and assign troughs to dark fringes
peaks=make_fringes(hologram,n_columns,n_rows,fringe_x=peaks_x, $
fringe_y=peaks_y,200),middle=210)
troughs=make_fringes(hologram,n_columns,n_rows,fringe_x=troughs_x, $
fringe_y=troughs_y,100),middle=210)

;Count number of points in each fringe
fringes=count_fringes(peaks_x,peaks_y,n_pk)
fringes=count_fringes(troughs_x,troughs_y,n_trghs)

;Fit straight lines to fringes
```

```

;straight_peaks_x=straight_one_side(peaks_x,peaks_y,n_pk)
;straight_troughs_x=straight_one_side(troughs_x,troughs_y,n_trg)
straight_peaks_x=straight(peaks_x,peaks_y,n_pk)
straight_troughs_x=straight(troughs_x,troughs_y,n_trg)

;Count number of bright and dark fringes
n_peaks=(size(peaks_x))[1]
n_troughs=(size(troughs_x))[1]

;Plot bright fringes and associated straight lines over raw hologram
window,3,xsize=(size(hologram))[1],ysize=(size(hologram))[2]
tv,hologram_raw

wset,3
for m=0,n_peaks-1 do begin
  plots,peaks_x[m,0:n_pk[m]-1],peaks_y[m,0:n_pk[m]-1],color=2, $
thick=2,psym=3,/device
  ;xyouts,peaks_x[m,n_pk[m]-1],peaks_y[m,n_pk[m]-1],stremo(m), $
  ; color=2,charthick=2,/device
endfor

wset,3
for m=0,n_peaks-1 do begin
  plots,straight_peaks_x[m,0:n_pk[m]-1],peaks_y[m,0:n_pk[m]-1], $
color=2,thick=2,/device
endfor

;Plot dark fringes and associated straight lines over raw hologram
window,4,xsize=(size(hologram))[1],ysize=(size(hologram))[2]
tv,hologram_raw

```

```

wset,4
for m=0,n_troughs-1 do begin
  plots,troughs_x[m,0:n_trghs[m]-1],troughs_y[m,0:n_trghs[m]-1], $
color=7,thick=2,psym=3,/device
  ;xyouts,troughs_x[m,n_trghs[m]-1],troughs_y[m,n_trghs[m]-1], $
  ; stremo(m),color=2,charthick=2,/device
endfor

wset,4
for m=0,n_troughs-1 do begin
  plots,straight_troughs_x[m,0:n_trghs[m]-1], $
troughs_y[m,0:n_trghs[m]-1],color=2,thick=2,/device
endfor

;Store variables in a file to be read by deconvolve_hologram
folder_index=strpos(hologram_file,'\',/reverse_search)
extension_index=strpos(hologram_file,'.',/reverse_search)
length=extension_index-folder_index
data_filename=strmid(hologram_file, folder_index+1, length-1)+'.dat'

print,'data_filename: ',data_filename

save,top,bottom,peaks_x,peaks_y,n_pkts,straight_peaks_x,troughs_x, $
troughs_y,n_trghs,straight_troughs_x,hologram_raw, $
filename=data_filename

end

```



```

top_edge=0

;Figure out where the edges of the uncropped hologram are
for y=0,n_rows-1 do begin
    left_edge=0
    right_edge=0
    smoothed_row=hologram(*,y)
    noise=max(smoothed_row(0:20))
    left_edge=min(where(smoothed_row gt 2*noise))
    right_edge=max(where(smoothed_row gt 2*noise))
    if right_edge gt left_edge then begin
        if bottom_edge eq 0 then bottom_edge=y
        if farthest_left_edge gt left_edge then $
            farthest_left_edge=left_edge
        if farthest_right_edge lt right_edge then $
            farthest_right_edge=right_edge
        top_edge=y
    endif
endfor

;Crop the hologram
hologram=hologram(farthest_left_edge:farthest_right_edge, $
bottom_edge:top_edge)

;Figure out how many columns and rows are in the hologram_smoothed
hologram_size=(size(hologram))
n_columns=hologram_size(1)
n_rows=hologram_size(2)

return, hologram

```

```

end

function lowpass_filter, hologram, n_rows, noise, plot_row=plot_row
;*****Not used*****
;>>>>>>>>Filters hologram using lowpass filter<<<<<<<<

hologram_size=size(hologram)
hologram_lowpass=make_array(hologram_size[1],hologram_size[2],value=0)

for y=0,n_rows-1 do begin
  row_raw=hologram[*,y]
  left_edge=min(where(row_raw gt 2*noise))
  right_edge=max(where(row_raw gt 2*noise))
  if right_edge gt left_edge then begin
    row_x=where(row_raw)
    row=row_raw[left_edge:right_edge]
    nl_row=n_elements(row)
    if float(nl_row)/2 gt fix(nl_row/2) then begin
      row=row[0:n_elements(row)-2]
      nl_row=n_elements(row)
    endif
    row_x=row_x[left_edge:left_edge+nl_row-1]
    row_fourier=fft(row)

    x=[FINDGEN(nl_row/2),FINDGEN(nl_row/2)-nl_row/2]
    x[nl_row/2:nl_row-1]=reverse(x[0:nl_row/2-1])
    filter=1.0/(1+(x/40)^10)
    row_lowpass=FFT(FFT(row,1)*filter,-1)
  endif
end

```

```

if defined(plot_row) then begin
  if y eq plot_row then begin
    window,12
    plot,row_raw
    oplot,row_x,row_lowpass,color=2
    window,13
    plot,row_fourier
    window,14
    plot,filter
  endif
  endif
  hologram_lowpass[left_edge:left_edge+nl_row-1,y]=row_lowpass
endif
endfor

return,hologram_lowpass

end

function make_square, hologram, top, bottom
;>>>>>>>>Makes square wave fringes out of sinusoidal fringes<<<<<<
middle_fraction=0.95
outside_fraction=0.75
fs=4
max_value=float(max(hologram))
print,'maximum value',max_value
min_value=float(min(hologram))
print,'minimum value',min_value
;Center of hologram is better exposed, so
; brightness in center must be higher to be set to max

```

```

width=(size(hologram))[1]
height=(size(hologram))[2]
hologram_middle=hologram[width/fs:width-(width/fs),height/fs:height $ 
-(height/fs)]
hologram[width/fs:width-(width/fs),height/fs:height-(height/fs)]=0
hologram_middle[where(hologram_middle ge middle_fraction*max_value)] $ 
=255
;Top and bottom are dimmer, so
; brightness of top and bottom is set to max at a lower value
hologram[where(hologram ge outside_fraction*max_value)]=255
hologram[width/fs:width-(width/fs),height/fs:height-(height/fs)] $ 
=hologram_middle
;Values below brightness threshold are made zero
hologram[where(hologram ne 255)]=0
return,hologram

end

function ref_wires, hologram, top, bottom

;Asks user to select the location of the top and bottom wires in the
;hologram
wset,1
tv,hologram
print,'Click on location of top wire. '

cursor,x,top,/down,/device
plots,[0,250],[top,top],color=3,/device
print,'Click on location of bottom wire. '
cursor,x,bottom,/down,/device

```



```

; negative slope-->value=-1
; zero slope-->value=0
; positive slope-->value=1
y_sl_sign=make_array(n_elements(y_slope),value=3)
y_sl_sign[where(y_slope gt 0)]=1
y_sl_sign[where(y_slope lt 0)]=-1
y_sl_sign[where(y_slope eq 0)]=0

zeros=where(y_slope eq 0)
pos_slope=where(y_slope gt 0)
neg_slope=where(y_slope lt 0)

;*****Finds peaks*****
;Finds pixels where the slope (y_sl_sign) changes from 1 to 0 or from
;0 to -1
peaks=where(y_sl_sign[1:n_elements(y_sl_sign)-1] lt $
y_sl_sign[0:n_elements(y_sl_sign)-2])+1
;Each element in peaks where the slope changes from 1 to 0 will be
; followed by an element where the slope changes from 0 to -1. To
; resolve this conflict in the peak location, the peak is placed at
; the pixel where the slope changes from 1 to 0 that is closest to
; halfway between the two conflicting elements of peaks.
; This is done in the next few lines by taking 1/2 the difference
; between the conflicting elements (one where the slope changes
; from 1 to 0 and one where the slope changes from 0 to -1),
; rounding down, adding that to the element where the slope changes
; from 1 to 0, and setting the element where the slope changes from
; 0 to -1 to this value.
; The element where the slope changes from 1 to 0 is then
; eliminated from peaks.

```

```

;max k is set to original number of elements in peaks - 1
for k=0,n_elements(peaks)-1 do begin
    ;for loop exits when k is too big for reduced peaks array
    if k lt n_elements(peaks)-1 then begin
        if y_sl_sign[peaks[k]] eq 0 then begin
            ;takes 1/2 the difference of the two conflicting elements
            avg=fix((peaks[k+1]-peaks[k])/2)
            ;sets the element where the slope changes from -1 to 0
            ;to this value
            peaks[k+1]=peaks[k]+avg
            ;eliminates the point where the slope changed from 1 to 0
            peaks=peaks[where(where(peaks) ne k)]
        endif
    endif else GOTO, EXIT_FOR
endfor
EXIT_FOR:

;*****Finds troughs*****
troughs=where(y_sl_sign[1:n_elements(y_sl_sign)-1] gt $
y_sl_sign[0:n_elements(y_sl_sign)-2])+1
for k=0,n_elements(troughs)-1 do begin
    if k lt n_elements(troughs)-1 then begin
        if y_sl_sign[troughs[k]] eq 0 then begin
            avg=fix((troughs[k+1]-troughs[k])/2)
            troughs[k+1]=troughs[k]+avg
            troughs=troughs[where(where(troughs) ne k)]
        endif
    endif else GOTO, EXIT_FOR_2
endfor
EXIT_FOR_2:

```



```

value))

;Prevent subscripts from causing errors on rows with fewer than
;4 fringes

if n_fringes[n] ge 4 then begin
    fringe_row=where(hologram[*,middle-n_pts/2+n] eq value)
    fringe_width[n]=mean(fringe_row[1:n_fringes[n]-2] $
    -fringe_row[0:n_fringes[n]-1])
endif

endfor

;Limit fringe width and number of fringes to rows with 4 or more
;fringes

fringe_width=fringe_width[where(n_fringes ge 4)]
n_fringes=n_fringes[where(n_fringes ge 4)]

;Find the mean number of fringes and the mean fringe width
n_fringes=round(mean(n_fringes))
fringe_width=round(mean(fringe_width))

;If the mean number of fringes equals the number of fringes in
; the middle row, put those x-values in the fringe storage matrix
; if not, move the middle up 10 rows and find the mean number of
; fringes again

;initialize the fringe storage matrix
fringes=intarr(n_fringes,n_rows)
current_fringes=intarr(n_fringes)
last_good_fringes=intarr(n_fringes)
fringes_middle=where(hologram[*,middle] eq value,ct)
if n_fringes eq ct then begin
    fringes[*,middle]=fringes_middle
endif else begin
    middle=middle+1

```

```

GOTO,LINE_1

endelse

n_fringes=n_elements(where(hologram[*,middle] eq value))

;Use an array called current_fringes to store the last set of
; good fringe values (initially the fringes in the middle row are used)
for m=0,n_fringes-1 do current_fringes[m]=fringes[m,middle]
;Store the x-coordinates of the fringes, starting from the middle row
; and going up.
;An array named current_fringes is used to store the last good x-values
; for each fringe in case a fringe is missed on a row.

for n=middle+1,n_rows-1 do begin
    ;Count the number of fringes in the active row
    n_fringes_row=n_elements(where(hologram[*,n] eq value))
    ;Initialize arrays to store the distance between
    ; each of the fringes in the active row
    ; and the last good value of each of the fringes
    ; and the index of the minimums of these distances for each active
    ;fringe
    fringe_diff=intarr(n_fringes_row,n_fringes)
    fringe=intarr(n_fringes_row)
    ;Find the fringes in the active row
    fringes_row=where(hologram[*,n] eq value)
    ;Find the distance between
    ; each of the fringes in the active row
    ; and the last good value of each of the fringes
    ; (which were stored in current_fringes)
    for m=0,n_fringes_row-1 do begin
        ;Find the distances between the active fringe
        ; and the last good value of each of the fringes

```

```

; (which were stored in current_fringes)
for k=0,n_fringes-1 do begin
    fringe_diff[m,k]=abs(fringes_row[m]-current_fringes[k])
endfor
;Find the minimum of the distances
change=abs(min(fringe_diff[m,*],index))
;If this minimum value is reasonable, store its index (which is
; the fringe number that the active fringe should be assigned
; to) as fringe[m]
if change lt fringe_width/4 then begin
    fringe[m]=index
    ;If a value has already been assigned to the desired fringe
    ; number (fringe[m]) for the active fringe,
    ; the active value is stored anyway
    fringes[fringe[m],n]=fringes_row[m]
endif
endfor

;The x-values of the active fringes are stored as the last good
; values in current_fringes
; If a fringe was missed, its value is not stored in
;current_fringes
for m=0,n_fringes-1 do begin
    if fringes[m,n] ne 0 then begin
        current_fringes[m]=fringes[m,n]
    endif
endfor
endfor

for m=0,n_fringes-1 do current_fringes[m]=fringes[m,middle]

```

```

;Store the x-coordinates of the fringes, starting from the middle row
; and going down.

for n=middle,0,-1 do begin
  n_fringes_row=n_elements(where(hologram[*,n] eq value))
  fringe_diff=intarr(n_fringes_row,n_fringes)
  fringe=intarr(n_fringes_row)
  fringes_row=where(hologram[*,n] eq value)
  for m=0,n_fringes_row-1 do begin
    for k=0,n_fringes-1 do begin
      fringe_diff[m,k]=abs(fringes_row[m]-current_fringes[k])
    endfor
    change=min(fringe_diff[m,*],index)
    if change lt fringe_width/4 then begin
      fringe[m]=index
      fringes[fringe[m],n]=fringes_row[m]
    endif
  endfor

  for m=0,n_fringes-1 do begin
    if fringes[m,n] ne 0 then begin
      current_fringes[m]=fringes[m,n]
    endif
  endfor
endfor

;Store the x and y values of the fringes in arrays
y=make_array(n_rows,/index)
fringe_y=intarr(n_fringes,n_rows)
fringe_x=intarr(n_fringes,n_rows)

```



```

;When both edges of Z-pinch are within field of view
;Two points used to fit straight line are
; mean of 10 points in upper half of fringe with least fringe shift
; and mean of 10 points in lower half of fringe with least
; fringe shift

if not defined( vacuum ) then vacuum=fix(0.75*max(n_vals))
n_fringes=(size(fringe_y))[1]
mins_array_y=intarr(n_fringes,11)
mins_array_x=intarr(n_fringes,11)
straight_x_vals=intarr(n_fringes)
straight_y_vals=intarr(n_fringes)
straight_fringes_x=fringe_y

lower=make_array(n_fringes,value=0)
upper=n_vals/2
for half=0,1 do begin
  for m=0,n_fringes-1 do begin
    fringe_y_act=fringe_y[m,lower[m]:upper[m]]
    fringe_x_act=fringe_x[m,lower[m]:upper[m]]
    ord=sort(fringe_x_act)
    straight_x_vals[m] =
=mean(fringe_x_act[ord[0:fix(n_elements(ord)/10)]])
    straight_y_vals[m] =
=mean(fringe_y_act[ord[0:fix(n_elements(ord)/10)]])
  endfor
  if half eq 0 then begin
    straight_x_lower=straight_x_vals
    straight_y_lower=straight_y_vals
    lower=upper
  end
end

```

```
    upper=n_vals-1
  endif else begin
    straight_x_upper=straight_x_vals
    straight_y_upper=straight_y_vals
  endelse
endfor

for m=0,n_fringes-1 do begin
  slope=(float(straight_y_upper[m])-float(straight_y_lower[m])) $
/(float(straight_x_upper[m])-float(straight_x_lower[m]))
  b=straight_y_upper[m]-slope*straight_x_upper[m]
  straight_fringes_x[m,*]=1/slope*(fringe_y[m,*]-b)
endfor

return,straight_fringes_x

end
```

Appendix E

IDL PROCEDURE *INVERT_INTERFEROGRAM.PRO*

```
pro invert_interferogram

;Inverts chord integrated density data obtained from holographic
; interferogram to obtain radial electron density profile
;Input file is data file containing bright and dark fringes as IDL
; variables made by analyze_interferogram.pro, for example,
; 2003 01 23 009-H1-P2_cropped.dat
;Output file is electron density data file, for example,
; 2003 01 23 009-H1_p2_cropped electron density.dat, and contains
; IDL variables
; associated with electron density:
; integrated_density
; std
; electron_density
; baseline
; peak
; peak_n
; upper
; lower
; center
; top_region
; bottom_region
;
```

```
;Stuart Jackson
;December 14, 2003
;Modified December 12, 2005
;Modified January 11, 2006 to allow for variable shell widths
;    (in the event that points were not found along the fringe)

post=0          ;set post=1 for postscript plotting
peak=1          ;set peak=1 to deconvolve peak (trough otherwise)
peak_n=5        ;set peak_n=number of peak/trough to deconvolve
double_pass=0   ;set double_pass=1 for a double-pass interferogram
center_range=15 ;looks for center +/- center_range points about centroid
margin=0        ;pixel shift considered to be zero for finding edge of
;Z-pinch
iterate=1       ;set iterate=1 to iterate for center
upper=0          ;move top of straight fringe right upper pixels
lower=0          ;move bottom of straight fringe right lower pixels

;Open datafile.
data_filename=open_datafile()
restore,data_filename

;Plot interferogram with either light (peaks) or dark (troughs) fringes
;over it.
set_plot,'win'
window,0;,ysize=450
tv,hologram_raw
if peak eq 1 then begin
dummy=plot_peaks(peaks_x, peaks_y, n_pk, number=0, c=2, peak_n=peak_n, $
single=1, line=1)
```

```

dummy=plot_peaks(straight_peaks_x, peaks_y, n_pk, c=2, peak_n=peak_n, $
single=1, line=1)
endif else begin
dummy=plot_peaks(troughs_x, troughs_y, n_trghs, number=1, c=2, peak_n=peak_n)
dummy=plot_peaks(straight_troughs_x, troughs_y, n_trghs, c=6, peak_n=peak_n)
endelse

;Get x and y values of selected fringe and an initial guess for the x and y
;values of the straight line.
if peak eq 1 then begin
y_values=float(peaks_y[peak_n,0:n_pk[peak_n]-1])
x_values=float(peaks_x[peak_n,0:n_pk[peak_n]-1])
straight_values_guess=float(straight_peaks_x[peak_n,0:n_pk[peak_n]-1])
endif else begin
y_values=float(troughs_y[peak_n,0:n_trghs[peak_n]-1])
x_values=float(troughs_x[peak_n,0:n_trghs[peak_n]-1])
straight_values_guess=float(straight_troughs_x[peak_n,0:n_trghs[peak_n]-1])
endelse

;x_values_orig, etc. variables are unsmoothed variables that will be
;subtracted
;later from the smoothed variables to produce an error estimate for
;error bars.
x_values_orig=x_values
y_values_orig=y_values

;Smooth fringe.
fringe=smooth_fringe(x_values,y_values,double_pass)

;Use the original straight values to estimate the pixel shift before

```

```

;adjusting edges and shifting straight line to intersect fringe at
;edge points
pixel_shift=measure_shift(y_values,x_values,y_values,straight_values_guess)

;Find the edges of the shifted part of the pixel shift
dummy=find_edges(y_values,pixel_shift,top_edge,bot_edge,center=center, $
margin=margin)

;Find the indices of these edges
upper=max(where(y_values le top_edge))
lower=min(where(y_values ge bot_edge))

;Connect a line from the upper and lower edge values that will be
;subtracted from the fringe.
dummy=make_straight(y_values,x_values,y_straight_values,straight_values, $
upper=upper,lower=lower)

;Measure the pixel shift by subtracting the straight line from the fringe.
pixel_shift_orig=measure_shift(y_values_orig,x_values_orig, $
y_straight_values,straight_values)
pixel_shift=measure_shift(y_values,x_values,y_straight_values, $
straight_values)

;Check that the pixel shift is correct by adding it to the straight line
;and plotting it over the interferogram and original fringe.
!P.multi=0
wset,0
theta=atan((x_values(upper)-x_values(lower))/(y_values(upper)- $
y_values(lower)))
theta_orig=atan((x_values_orig(upper)-x_values_orig(lower))/ $

```

```

(y_values_orig(upper)-y_values_orig(lower)))
;plots,straight_values,y_straight_values,color=4,/device
;plots,pixel_shift*cos(theta)+straight_values,-pixel_shift*sin(theta)+ $
; y_straight_values,color=4,/device

;Plot the original and smoothed fringes and straight lines.

window,1
!P.MULTI=0

plot,y_values_orig,x_values_orig,yrange=[min(straight_values), $
max(x_values)],xtitle='impact parameter [pixels]', $
ytitle='horizontal coordinate [pixels]',charsize=2, $
charthick=2,thick=2,xthick=2,ythick=2
oplot,y_values_orig,x_values_orig,color=5,thick=2
oplot,y_values_orig,x_values_orig,psym=3,color=2
oplot,y_values,x_values,thick=2
oplot,y_straight_values,straight_values,thick=2;,color=4

;Crop the fringe
top_region=fix(y_values(upper))
bottom_region=fix(y_values(lower))
print,'top edge',top_region
print,'bottom edge',bottom_region
dummy=crop_fringe(y_values_orig, pixel_shift_orig, top_region,
$bottom_region)
dummy=crop_fringe(y_values, pixel_shift, top_region, bottom_region)
dummy=crop_fringe(y_straight_values, straight_values, top_region,
$bottom_region)

;Show the edges over the interferogram.

wset,0

```

```
dummy=plot_line(top_region,color=2,linestyle=2)
dummy=plot_line(bottom_region,color=2,linestyle=2)

;Calculate the uncertainty in the pixel shift by subtracting the
;unsmoothed values from the smoothed values.
std=abs(pixel_shift-pixel_shift_orig)
print,'max(std in pixels)',max(std)

;Plot the cropped pixel shift over the uncropped pixel shift
;(both smoothed and unsmoothed), show where it
;was cropped, and print out where it was cropped.

wset,1
vline,top_region,linestyle=2,thick=2
vline,bottom_region,linestyle=2,thick=2
print,'pixel_shift at top_edge',pixel_shift[where(y_values eq $top_region)]
print,'pixel_shift at bottom_edge',pixel_shift[where(y_values eq $bottom_region)]
wset,1
;oplot,-pixel_shift_orig*sin(theta)+y_straight_values, $
; pixel_shift_orig*cos(theta)+straight_values,color=2
;oplot,-pixel_shift*sin(theta)+y_straight_values, $
; pixel_shift*cos(theta)+straight_values,color=4

;Find the fringe width (average distance between fringes).
fringe_width=find_width(straight_peaks_x)
;fringe_width=17.5
print,'fringe_width',fringe_width

;Check that the fringe width is right by adding it to the straight
```

```
;line and plotting it over the hologram.  
;(It should roughly line up with the straight line associated with  
;the next fringe.)  
;wset,0  
;plots,straight_values+fringe_width,y_straight_values,color=3,/device  
  
;Calculate the fringe order by using the fringe width to normalize  
;the fringe shift in pixels (pixel shift).  
fringe_order=find_order(pixel_shift,fringe_width)  
std=find_order(std,fringe_width)  
  
;Find the chord-integrated density  
integrated_density=find_integrated(fringe_order)  
std=find_integrated(std)  
print,'max(std in cm!u-2!n)',max(std)  
  
;Find the centroid of the chord-integrated density, which will be the  
;initial guess used in iterating for  
;the best center location for the inversion method shell model.  
centroid=find_centroid(y_values, pixel_shift)  
print,'centroid',centroid  
wset,0  
dummy=plot_line(centroid,color=2,linestyle=2)  
wset,1  
vline,centroid,linestyle=2,thick=2  
center_guess=centroid  
  
;Iterate to find the best center for the shell model, i. e. run the  
;inversion method a bunch of times with different centers.  
center=center_guess
```

```
if iterate eq 1 then center=iterate_center(center_guess,center_range, $  
y_values,top,bottom,pixels_per_cm,pixel_shift, $  
integrated_density,std,double_pass)  
print,'center',center  
  
;Show the center over the interferogram.  
;wset,0  
;dummy=plot_line(center,color=2,linestyle=2)  
  
;Convert the impact parameter (vertical coordinate in the interferogram)  
;to the radial coordinate in cm.  
r_cm=conv_y(y_values,top,bottom,center,pixels_per_cm)  
  
;Show the center over the pixel shift.  
wset,1  
vline,center,linestyle=2,thick=2  
  
;Plot the fringe shift in pixels (pixel shift). Show the center.  
window,2  
plot,y_values,pixel_shift,yrange=[0,max(pixel_shift)], $  
xtitle='impact parameter [pixels]', $  
ytitle='fringe shift [pixels]',charsize=2,charthick=2,thick=2, $  
xthick=2,ythick=2  
vline,center,linestyle=2,thick=2  
  
;Invert the chord-integrated density using the Abel inversion method  
;to obtain the radial electron number density profile.  
electron_density=deconvolve(r_cm, integrated_density,pixels_per_cm, $  
std,double_pass)
```

```

;Plot the fringe order.

window,4

plot,r_cm,fringe_order,yrange=[0,max(fringe_order)], $
    xtitle='impact parameter [cm]', ytitle='fringe order', $
    charsize=2,charthick=2,thick=2,xthick=2,ythick=2

vline,0,linestyle=2,thick=2

;Create part of the name for the postscript and data files where the
;radial electron number density
;profile, etc. will be plotted or saved.

folder_index=strpos(data_filename,'\',/reverse_search)
extension_index=strpos(data_filename,'.',/reverse_search)
length=extension_index-folder_index

data_filename=strmid(data_filename,folder_index+1,length-1)

if post eq 1 then begin
    ;Create filename for postscript plot.

    plot_filename=data_filename

    if peak eq 0 then plot_filename=plot_filename+'_trough_' $
+stremo(peak_n)+'_electron_density_plot.ps'

    if peak eq 1 then plot_filename=plot_filename+'_peak_' $
+stremo(peak_n)+'_electron_density_plot.ps'

    ;Set up for postscript plotting.

    dummy=set_ps(plot_filename,mydevice,post)

endif

;Plot the radial electron number density profile (as a postscript,
;if directed to).

dummy=plot_density(electron_density, data_filename, post)
if post eq 1 then dummy=close_ps(mydevice,post)

```



```

ysize=25,xsize=35,yoffset=1.2,/bold,/color,scale_factor=0.5
  if peak ne 1 then DEVICE, FILENAME=data_filename+' trough ' $
+stremo(peak_n)+' electron density plot.ps', /portrait, $
ysize=25,xsize=35,yoffset=1.2,/bold,/color,scale_factor=0.5
endif

end

function plot_peaks, peaks_x, peaks_y, n_pk, number=number, c=c, $
peak_n=peak_n, single=single, line=line

  if not defined(number) then number=0
  if not defined(c) then c=2
  if not defined(single) then single=0
  if not defined(line) then line=0
  n_pk=(size(peaks_x))[1]

  if line eq 1 then begin
    if single eq 0 then begin
      for m=0,n_pk-1 do begin
        plots,peaks_x[m,0:n_pk[m]-1],peaks_y[m,0:n_pk[m]-1], $
color=c,thick=2,/device
        if number eq 1 then xyouts,peaks_x[m,n_pk[m]-1], $
peaks_y[m,n_pk[m]-1],stremo(m),charsize=.5,/device
      endfor
    endif
    if defined(peak_n) then begin
      plots,peaks_x[peak_n,0:n_pk[peak_n]-1], $
peaks_y[peak_n,0:n_pk[peak_n]-1],color=2,thick=2,/device
      if number eq 1 then xyouts,peaks_x[peak_n,n_pk[peak_n]-1], $

```

```

peaks_y[peak_n,n_pk[peak_n]-1],stremo(peak_n), $
charsize=.5,color=2,/device
endif
endif else begin
if single eq 0 then begin
  for m=0,n_pk-1 do begin
    plots,peaks_x[m,0:n_pk[m]-1],peaks_y[m,0:n_pk[m]-1], $
color=c,thick=2,psym=3,/device
    if number eq 1 then xyouts,peaks_x[m,n_pk[m]-1], $
peaks_y[m,n_pk[m]-1],stremo(m),charsize=.5,/device
  endfor
endif
if defined(peak_n) then begin
  plots,peaks_x[peak_n,0:n_pk[peak_n]-1], $
peaks_y[peak_n,0:n_pk[peak_n]-1],color=2,thick=2, $
psym=3,/device
  if number eq 1 then xyouts,peaks_x[peak_n,n_pk[peak_n]-1], $
peaks_y[peak_n,n_pk[peak_n]-1],stremo(peak_n), $
charsize=.5,color=2,/device
endif
endelse
end

function measure_shift, y_values, x_values, y_straight_values, $
straight_values
;>>>>>>>>>Measures fringe shift in units of pixels<<<<<<<<<
;Get sign of pixel shift
sign=(x_values-straight_values)/abs(x_values-straight_values)
;Set sign to zero where sign is NAN

```



```
end

function find_centroid, y_values, pixel_shift
;>>>>>>>>Find centroid in pixels and center in cm $
of the plasma column<<<<<<<<
centroid=fix(y_values(min(where(y_values ge $
int_tabulated(y_values,float(pixel_shift)*y_values)/ $
int_tabulated(y_values,float(pixel_shift))))))

return, centroid

end

function find_edges, y_values, pixel_shift, top_edge, bot_edge, $
center=center, margin=margin
;>>>>>>>>Finds edges of Z-pinch<<<<<<<<
if not defined(center) then center=find_centroid(y_values,pixel_shift)
if not defined(margin) then margin=0
center_index=(where(y_values eq center))[0]
pos_edge=where(pixel_shift[center_index:n_elements(pixel_shift)-1] $
margin le 0)
if pos_edge[0] eq -1 then top_shift $
=min(pixel_shift[center_index:n_elements(pixel_shift)-1], $
top_edge_index) $
else begin
top_edge_index=min(pos_edge)
top_shift=pixel_shift[center_index+top_edge_index]
endelse
top_edge=y_values[center_index+top_edge_index]
```

```

if top_shift lt 0 then top_edge=top_edge-1

pos_edge=where(pixel_shift[0:center_index]-margin le 0)
if pos_edge[0] eq -1 then bot_shift=min(pixel_shift[0:center_index], $
bot_edge_index) $
else begin
bot_edge_index=max(pos_edge)
bot_shift=pixel_shift[bot_edge_index]
endelse
bot_edge=y_values[bot_edge_index]
if bot_shift lt 0 then bot_edge=bot_edge+1

end

function find_width, straight_fringes
;>>>>>>>>>Calculate fringe width<<<<<<<<
; Determines fringe width by averaging distance between fringes
peaks_size=size(straight_fringes)
n_peaks=peaks_size[1]
avg=fltarr(n_peaks)
dif=make_array(n_peaks,n_peaks,value=0)

for n=0,n_peaks-1 do begin
avg[n]=mean(straight_fringes[n])
endfor

avg=avg[where(avg ne 0)]
peaks_size=size(avg)
n_peaks=peaks_size[1]

```

```
tot=0
cnt=0
for m=0,n_peaks-1 do begin
  for n=m+1,n_peaks-1 do begin
    dif=(avg[n]-avg[m])/(n-m)
    tot=tot+dif
    cnt=cnt+1
  endfor
endfor

avg_width=tot/cnt

return,avg_width

end

function conv_y,y_pixels,top,bottom,centroid,pixels_per_cm
;>>>>>>>>>Converts y coords in pixels to cm<<<<<<<<
pixels_per_cm=float(abs(top-bottom))
centroid_cm=float(centroid)/pixels_per_cm
y_cm=float(y_pixels)/pixels_per_cm
r_cm=y_cm-centroid_cm
return,r_cm

end

function find_order, pixel_shift, fringe_width
;>>>>>>>>>Determines fringe order from pixel shift<<<<<<<<
fringe_order=float(pixel_shift)/fringe_width
```

```
return,fringe_order

end

function find_integrated, fringe_order
;>>>>>>>>Determines chord integrated density
;from fringe order<<<<<<<<
integrated_density=fringe_order*3.212e17
return,integrated_density

end

function std_compute, fcn, data
;>>>>>>>>Calculates standard deviation of data points
;from fit function<<<<<<<<
std=sqrt(1/float(n_elements(data))*total((data-fcn)^2))
return, std

end

function deconvolve, r_cm, integrated_density, pixels_per_cm, $
std,double_pass
;>>>>>>>>Deconvolves chord integrated density
;to yield radial density profile<<<<<<<<
; Divide chord integrated electron_density in half
n_rows=n_elements(integrated_density)
centroid=(where(r_cm eq 0))[0]
n_lower=integrated_density[0:centroid]
n_lower_error=std[0:centroid]
r_lower=abs(r_cm[0:centroid])
```

```

n_upper=integrated_density[centroid:n_rows-1]
n_upper_error=std[centroid:n_rows-1]
r_upper=r_cm[centroid:n_rows-1]

for m=1,2 do begin

  if m eq 1 then begin
    bottom_edge=0
    ;no_shift=where(n_lower le 0)
    ;if no_shift[0] eq -1 then bottom_edge=0
    ;if no_shift[0] gt -1 then bottom_edge=max(no_shift)
    size_a=centroid-bottom_edge+1
    n_lower=n_lower[bottom_edge:centroid]
    n_lower_error=n_lower_error[bottom_edge:centroid]
    r_lower=r_lower[bottom_edge:centroid]
    n_lower_reversed=reverse(n_lower)
    n_lower_reversed_error=reverse(n_lower_error)
    r_lower_reversed=reverse(r_lower)
    ;store number density for lower half of hologram
    f_lower=fltarr(size_a)
    ;store number density errors for lower half of hologram
    f_lower_error=fltarr(size_a)
    r=[r_lower_reversed,max(r_lower_reversed)+1/pixels_per_cm]
  endif

  if m eq 2 then begin
    top_edge=n_elements(n_upper)-1
    ;no_shift=where(n_upper le 0)
    ;if no_shift[0] eq -1 then top_edge=n_elements(n_upper)-1
    ;if no_shift[0] gt -1 then top_edge=min(no_shift)
  endif

```

```

size_a=top_edge+1
n_upper=n_upper[0:top_edge]
n_upper_error=n_upper_error[0:top_edge]
r_upper=r_upper[0:top_edge]
;store number density for upper half of hologram
f_upper=fltarr(size_a)
;store number density errors for upper half of hologram
f_upper_error=fltarr(size_a)
r=[r_upper,max(r_upper)+1/pixels_per_cm]

endif

; Create coefficient matrix (A) and determine density of each shell
A=dblarr(size_a,size_a)
for j=1,size_a do begin
  i=size_a-j
  for k=i,size_a-1 do begin
    A[k,i]=sqrt((r[k+1])^2-(r[i])^2)-sqrt((r[k])^2-(r[i])^2)
    ;A[k,i]=sqrt((k+1)^2-i^2)-sqrt(k^2-i^2)
    ;A[k-1,i-1]=2*(sqrt((k+1)^2-i^2)-sqrt(k^2-i^2))
    ;A[k-1,i-1]=2*((k+i)*sqrt((k+1)^2-i^2)-k*sqrt(k^2-i^2)-i^2 $
    ;      *alog((k+1+sqrt((k+1)^2-i^2))/(k^2+sqrt(k^2-i^2))))
  endfor
endfor
h=2
if double_pass eq 1 then A=2*A

if m eq 1 then begin
  f_lower=invert(A)*1/2##n_lower_reversed
  f_lower_error=sqrt((invert(A))^2*1/2##(n_lower_reversed_error)^2)
endif

```

```

if m eq 2 then begin
  f_upper=invert(A)*1/2##n_upper
  f_upper_error=sqrt((invert(A))^2*1/2##(n_upper_error)^2)
  endif

endfor

electron_density_lower=transpose(f_lower)
f_lower_error=transpose(f_lower_error)
electron_density_upper=transpose(f_upper)
f_upper_error=transpose(f_upper_error)

electron_density={Y_LOWER:reverse(abs(r_cm[bottom_edge:centroid])), $
LOWER:electron_density_lower, ERROR_LOWER:f_lower_error,$
Y_UPPER:r_cm[centroid:centroid+top_edge], $
UPPER:electron_density_upper, ERROR_UPPER:f_upper_error}

return,electron_density

end

function compare_deconvolutions, electron_density,n_pts=n_pts, $
slope=slope,mag=mag
;>>>>>>>>Sees if deconvolutions from bottom & top match
;at the center<<<<<<<
if not(define(n_pts)) then n_pts=4
max_density=max([electron_density.UPPER,electron_density.LOWER])
match1=sqrt(total(((electron_density.UPPER[1:n_pts+1]$-
electron_density.UPPER[0:n_pts])) $
```

```

/(electron_density.Y_UPPER[1:n_pts+1]- $
electron_density.Y_UPPER[0:n_pts]) $
-(electron_density.LOWER[1:n_pts+1]-$
electron_density.LOWER[0:n_pts]) $
/(electron_density.Y_LOWER[1:n_pts+1] $
-electron_density.Y_LOWER[0:n_pts]))/max_density)^2))
match2=sqrt(total(((electron_density.UPPER[0:n_pts] $
-electron_density.LOWER[0:n_pts])/max_density)^2))
;match1=abs(mean((electron_density.UPPER[1:n_pts+1] $
;    -electron_density.UPPER[0:n_pts]) $
;    /(electron_density.Y_UPPER[1:n_pts+1] $
;    -electron_density.Y_UPPER[0:n_pts])) $
;    -mean((electron_density.LOWER[1:n_pts+1] $
;    -electron_density.LOWER[0:n_pts]) $
;    /(electron_density.Y_LOWER[1:n_pts+1] $
;    -electron_density.Y_LOWER[0:n_pts])))
;match2=abs(mean(electron_density.UPPER[0:n_pts]) $
;    -mean(electron_density.LOWER[0:n_pts]))
if defined(slope) then match=match1 else if defined(mag) $
then match=match2 else match=match1*match2

return,match

end

function iterate_center,center_guess,center_range,y_values,top, $
bottom,pixels_per_cm,pixel_shift,integrated_density,std, $
double_pass,plot_it=plot_it
;>>>>>>>>Iterates to find the center of the pinch<<<<<<<<<
; Finds the center of the pinch by moving it +/-center_range

```

```

; about the center guess. The center of the pinch is chosen
; as the row that minimizes the difference between the
; deconvolution from the top and the deconvolution from the bottom
; by comparison of the densities of the innermost shell of each
; deconvolution.

match=make_array(2*center_range+1,value=1e20)

if not defined(plot_it) then plot_it=1

for k=0,2*(center_range) do begin

center_guess_inx=min(where(y_values ge center_guess))
center=fix(y_values(center_guess_inx-center_range+k))

r_cm=conv_y(y_values,top,bottom,center,pixels_per_cm)

electron_density=deconvolve(r_cm, integrated_density,pixels_per_cm, $
std,double_pass)

if plot_it eq 1 then begin
  if fix(k/10) eq float(k)/10.0 then begin
    window,20+fix(k/10),xsize=1000,ysize=900
    !p.multi=[0,4,10]
  endif
  x_range=[0,max(abs(r_cm))]
  y_range=[min(pixel_shift),max(pixel_shift)]
  plot,abs(r_cm[0:(where(r_cm eq 0))[0]]), $
  pixel_shift[0:(where(r_cm eq 0))[0]], $
  title='lower row '+stremo(center), $
  xrange=x_range,yrange=y_range

```

```

    oplot,abs(r_cm[0:(where(r_cm eq 0))[0]]), $
pixel_shift[0:(where(r_cm eq 0))[0]],psym=4

    plot,r_cm[(where(r_cm eq 0))[0]:(where(r_cm eq max(r_cm)))[0]], $
pixel_shift[(where(r_cm eq 0))[0]:(where(r_cm eq max(r_cm)))[0]], $
title='upper row '+stremo(center), $
xrange=x_range,yrange=y_range

    oplot,r_cm[(where(r_cm eq 0))[0]:(where(r_cm eq max(r_cm)))[0]], $
pixel_shift[(where(r_cm eq 0))[0]:(where(r_cm eq max(r_cm)))[0]], $
psym=4

    x_range=[0,min([electron_density.Y_LOWER,electron_density.Y_UPPER])] $
y_range=[min([electron_density.LOWER,electron_density.UPPER]), $
max([electron_density.LOWER,electron_density.UPPER])]

    plot,electron_density.Y_LOWER,electron_density.LOWER,xrange=x_range, $
yrange=y_range

    oplot,electron_density.Y_LOWER,electron_density.LOWER,psym=4

    plot,electron_density.Y_UPPER,electron_density.UPPER,xrange=x_range, $
yrange=y_range

    oplot,electron_density.Y_UPPER,electron_density.UPPER,psym=4
endif

;print,center
match[k]=compare_deconvolutions(electron_density,n_pts=10,slope=1)

endfor

if plot_it eq 1 then !p.multi=0

```

```

dummy=min(match,index)
center=fix(y_values(center_guess_inx-center_range+index))

return,center

end

function plot_density, electron_density, data_filename, post

if post ne 1 then window,3,xsize=1000,ysize=400
!P.MULTI=[0,2,1]
x_range=[0,min([electron_density.Y_LOWER,electron_density.Y_UPPER])]
y_range=[min([electron_density.LOWER,electron_density.UPPER]), $
max([electron_density.LOWER,electron_density.UPPER])]
plot,electron_density.Y_LOWER,electron_density.LOWER, $
xtitle='r [cm]',ytitle='electron density [cm!u-3!n]', $
title=data_filename, $
xrange=x_range,yrange=y_range
plot,electron_density.Y_UPPER,electron_density.UPPER, $
xtitle='r [cm]',ytitle='electron density [cm!u-3!n]', $
xrange=x_range,yrange=y_range
!P.MULTI=0
end

function close_ps, mydevice, post

if post eq 1 then begin
  DEVICE, /CLOSE
  SET_PLOT, mydevice
endif

```

```
end
```

```
function make_straight, y_values, x_values, y_straight_values, $  

straight_values, upper=upper, lower=lower  

;Connects a line from the upper and lower edge values that will  

;be subtracted from the fringe.  

;Points on the line are located so that a perpendicular can be  

;drawn from a point on the fringe to the associated point on the  

;straight line (which could be tilted) with respect to IDL's  

;x and y axes.  

slope=(y_values(upper)-y_values(lower))/(x_values(upper)- $  

x_values(lower))  

if finite(slope) then begin  

  b=y_values(upper)-slope*x_values(upper)  

  slopep=-1/slope  

  bp=y_values-slopep*x_values  

  straight_values=(bp-b)/(slope-slopep)  

  y_straight_values=slope*straight_values+b  

endif else begin  

  ;if the slope is NAN, make a vertical line  

  y_straight_values=y_values  

  straight_values=make_array(n_elements(y_values), $  

value=x_values(upper),/float)  

endelse  

end  

function smooth_fringe,fringe_x,fringe_y,double_pass
```



```

for k=0,n_elements(last_inxs)-1 do begin
    slope=(fringe_x[next_inxs[k]]-fringe_x[last_inxs[k]]) $
        /(fringe_y[next_inxs[k]]-fringe_y[last_inxs[k]]) 
    b=fringe_x[last_inxs[k]]-slope*fringe_y[last_inxs[k]]
    y_values=fringe_y[last_inxs[k]]+1 $
    +make_array(n_filled_pts[k],/index,/float)
    x_values=slope*y_values+b
    fringe_filled_y[last_filled_inxs[k]+1:next_filled_inxs[k]-1] $
    =y_values
    fringe_filled_x[last_filled_inxs[k]+1:next_filled_inxs[k]-1] $
    =x_values
endfor
endif else fringe_filled_x=fringe_x

;Smooth fringe
if double_pass eq 1 then fringe_filled_x $
=smooth(float(fringe_filled_x),7,/edge_truncate) $
else fringe_filled_x=smooth(smooth(float(fringe_filled_x),19, $ 
/edge_truncate),29,/edge_truncate)

if last_inxs[0] ne -1 then begin
    ;Remove filled-in points
    for k=0,n_elements(start_inxs)-1 do begin
        fringe_y[start_inxs[k]:end_inxs[k]] $
        =fringe_filled_y[start_filled_inxs[k]:end_filled_inxs[k]]
        fringe_x[start_inxs[k]:end_inxs[k]] $
        =fringe_filled_x[start_filled_inxs[k]:end_filled_inxs[k]]
    endfor
endif else fringe_x=fringe_filled_x

```

```
fringe=1
return,fringe

end

function set_ps, data_filename, mydevice, post
;>>>>>>>>Set postscript device options<<<<<<<<<<<<<<
if post eq 1 then begin
mydevice = !D.NAME
; Set plotting to PostScript:
SET_PLOT, 'PS'

; Use DEVICE to set some PostScript device options:
DEVICE, FILENAME=data_filename, /portrait,xsize=17,ysize=25, $
yoffset=1.2,/bold,/color
endif

end

function close_ps, mydevice, post

if post eq 1 then begin
DEVICE, /CLOSE
SET_PLOT, mydevice

endif

end
```

Appendix F

MATLAB FUNCTIONS FOR TEMPERATURE PROFILE CALCULATION

F.1 *Constant Current Density*

```
% NAME:
%   temp_calc_const_j
%
% PURPOSE:
%   This Matlab function calculates a temperature
%   profile from the density profile of the Z-pinch.
%   A constant current density is assumed.
%
% CATEGORY:
%   Data analysis code
%
% CALLING SEQUENCE:
%   temp_calc_const_j(datafile,pulse,helium)
%
% INPUTS:
%   datafile: string that contains the name of the file
%             containing the density profile
%   pulse: the pulse number of the plasma pulse whose current
%         and voltage is to be used to calculate the resistive
%         heating into the plasma
%
```

```
% OPTIONAL INPUTS:  
% helium: set to one for a helium Z-pinch  
%  
% OUTPUTS:  
% none  
%  
% EXAMPLE:  
% temp_calc_const_j('20910027_upper_rn.dat',20910027)  
% temp_calc_const_j('30204007_upper_rn.dat',30204007,1)  
%  
% MODIFICATION HISTORY:  
% Written By: Stuart Jackson, 14 Feb 2006  
  
function value=temp_calc_const_j(datafile,pulse,helium)  
filepath='M:\Users\Stuart_Jackson\ZaP\matlab\temp_calc\temp_calc_const_j\'  
filename=[filepath,datafile]  
num=dlmread(filename);  
r=num(:,1);  
n=num(:,2);  
  
%Establish values of constants  
Z=1;  
mp=1.6726e-27; %kg  
mi=mp;  
if nargin > 2  
    Z=2*Z  
    mi=4*mi %kg  
end  
mu0=4e-7*pi; %N/A^2  
k=1.6022e-19; %J/eV
```

```

%Initialize T and B arrays, setting T(r=0)=100 eV
% and B(r=0)=0 T
T=ones(length(r),1);
rB2=zeros(length(r),1);

%Find current through the Z-pinch
% at the time the hologram was made
[a,status] = mdsopen('alfven.aa.washington.edu::zapmain',pulse);
%holography laser monitor
holo=mdsvalue('\holography_raw');
%time base for holography laser monitor
t_holo=mdsvalue('dim_of(\holography_raw)');
%get holography time from holography laser monitor
[dummy,holo_time_inx]=max(holo);
holo_time=t_holo(holo_time_inx);
%get holography time from digitizer
t_digi=1.37e-6+mdsvalue('\digitizers::zap_dg11_b:channel_4');
%use the digitizer time if the monitor time is way off
if abs(t_digi-holo_time) > 0.1*t_digi
    holo_time=t_digi;
end
holo_time
%m=0 mode at P0
m0=mdsvalue('\m_0_p0');
%time base for m=0 mode
tm0= mdsvalue('dim_of(\m_0_p0)');
%outer electrode wall radius
rwall=mdsvalue('\r_wall'); %m
[dummy,m0_time_inx]=min(abs(tm0-holo_time));

```

```

%find magnetic field at the wall
%at the time the hologram was made
Bwall=m0(m0_time_inx) %T
%find the current through the Z-pinch
Iz=2*pi*rwall*Bwall/(mu0) %A

%Z-pinch radius
n_edge_inx=min(find(n<=0));
if n_edge_inx
else
    n_edge_inx=length(r);
end
r=r(1:n_edge_inx);
n=n(1:n_edge_inx);
a=r(n_edge_inx);
%current density
j=Iz./(pi.*a.^2);
%magnetic field
B=mu0.*r*j/2;
%find pressure, moving from P(a)=0 to P(0)
p=zeros(n_edge_inx,1);
for m=n_edge_inx:-1:2
    p(m-1)=p(m)+(B(m)+B(m-1))./(mu0.* (r(m)+r(m-1)))...
        .* (r(m).*B(m)-r(m-1).*B(m-1));
end
%temperature
T=p./(1+(1./Z).*n.*k);

figure(1)
plot(r./a,n./n(1), 'k')

```

```
hold on
plot(r./a,B./B(length(B)), 'r')
hold on
plot(r./a,T./T(1), 'b')
plot(r./a,1./(r./a), 'r--')
axis([min(r./a) max(r./a) ...
min([min(n./n(1)),min(B./B(length(B))),min(T./T(1))]) ...
max([max(n./n(1)),max(B./B(length(B))),5])])

figure(3)
subplot(3,1,1)
plot(r,n, 'k')
axis([min(r) max(r) min(n) max(n)])
subplot(3,1,2)
plot(r,B, 'r')
hold on
plot(r,Bwall.*rwall./r, 'r--')
axis([min(r) max(r) min(B) max(B)])
subplot(3,1,3)
plot(r,T, 'b')
axis([min(r) max(r) min(T) 200])
hold off

%Store r,n,B, and T in that order to an output file
if findstr(filename, '_rn')
    output_filename=strrep(filename, '_rn', '_rnBT')
else
    output_filename=[filepath, 'output.dat']
end
```

```
dlmwrite(output_filename,[r,n,B,T])
```

```
end
```

F.2 Current Density Proportional to Number Density

```
% NAME:
%   temp_calc_jpropn
%
% PURPOSE:
%   This Matlab function calculates a temperature
%   profile from the density profile of the Z-pinch.
%   The shape of the current density profile is
%   is assumed to be the same as the shape of the
%   number density profile.
%
% CATEGORY:
%   Data analysis code
%
% CALLING SEQUENCE:
%   temp_calc_jpropn(datafile,pulse,helium)
%
% INPUTS:
%   datafile: string that contains the name of the file
%             containing the density profile
%   pulse: the pulse number of the plasma pulse whose current
%         and voltage is to be used to calculate the resistive
%         heating into the plasma
%
```

```

% OPTIONAL INPUTS:
%   helium: set to one for a helium Z-pinch
%
% OUTPUTS:
%   none
%
% EXAMPLE:
%   temp_calc_jpropn('20910027_upper_rn.dat',20910027)
%   temp_calc_jpropn('30204007_upper_rn.dat',30204007,1)
%
% MODIFICATION HISTORY:
%   Written By: Stuart Jackson, 14 Feb 2006

function value=temp_calc_jpropn(datafile,pulse,helium)
filepath='M:\Users\Stuart_Jackson\ZaP\matlab\temp_calc\temp_calc_jpropn\' ;
filename=[filepath,datafile]
num=dlmread(filename);
r=num(:,1);
n=num(:,2);

%Establish values of constants
Z=1;
mp=1.6726e-27; %kg
mi=mp;
if nargin > 2
    Z=2*Z
    mi=4*mi %kg
end
mu0=4e-7*pi; %N/A^2
k=1.6022e-19; %J/eV

```

```

%Find current through the Z-pinch
% at the time the hologram was made
[a,status] = mdsopen('alfven.aa.washington.edu::zapmain',pulse);
%holography laser monitor
holo=mdsvalue('\holography_raw');
%time base for holography laser monitor
t_holo=mdsvalue('dim_of(\holography_raw)');
%get holography time from holography laser monitor
[dummy,holo_time_inx]=max(holo);
holo_time=t_holo(holo_time_inx);
%get holography time from digitizer
t_digi=1.37e-6+mdsvalue('\digitizers::zap_dg11_b:channel_4');
%use the digitizer time if the monitor time is way off
if abs(t_digi-holo_time) > 0.1*t_digi
    holo_time=t_digi;
end
holo_time
%m=0 mode at P0
m0=mdsvalue('\m_0_p0');
%time base for m=0 mode
tm0= mdsvalue('dim_of(\m_0_p0)');
%outer electrode wall radius
rwall=mdsvalue('\r_wall'); %m
[dummy,m0_time_inx]=min(abs(tm0-holo_time));
%find magnetic field at the wall
%at the time the hologram was made
Bwall=m0(m0_time_inx) %T
%find the current through the Z-pinch
Iz=2*pi*rwall*Bwall/(mu0) %A

```

```

%Z-pinch radius
n_edge_inx=min(find(n<=0));
if n_edge_inx
else
    n_edge_inx=length(r);
end
r=r(1:n_edge_inx);
n=n(1:n_edge_inx);
a=r(n_edge_inx);
%current density
c=Iz./(2.*pi.*sum(n(1:n_edge_inx-1).*r(1:n_edge_inx-1)...
.*(r(2:n_edge_inx)-r(1:n_edge_inx-1))));
j=c.*n;
%magnetic field
B=[0;mu0./r(2:n_edge_inx).*cumsum(j(2:n_edge_inx)...
.*r(2:n_edge_inx).*(r(2:n_edge_inx)-r(1:n_edge_inx-1))];
%find pressure, moving from P(a)=0 to P(0)
p=zeros(n_edge_inx,1);
for m=n_edge_inx:-1:2
    p(m-1)=p(m)+(B(m)+B(m-1))./(mu0.*((r(m)+r(m-1))...
.*((r(m).*B(m)-r(m-1).*B(m-1));
end
%temperature
T=p./(1+(1./Z).*n.*k);

figure(1)
plot(r./a,n./n(1), 'k')
hold on
plot(r./a,B./B(length(B)), 'r')

```

```
hold on
plot(r./a,T./T(1), 'b')
plot(r./a,1./(r./a), 'r--')
axis([min(r./a) max(r./a) ...
      min([min(n./n(1)),min(B./B(length(B))),min(T./T(1))]) ...
      max([max(n./n(1)),max(B./B(length(B))),max(T./T(1))])])

figure(2)
plot(r,j)
hold on
plot(r,c.*n, 'r')

figure(3)
subplot(3,1,1)
plot(r,n, 'k')
axis([min(r) max(r) min(n) max(n)])
subplot(3,1,2)
plot(r,B, 'r')
hold on
plot(r,Bwall.*rwall./r, 'r--')
axis([min(r) max(r) min(B) max(B)])
subplot(3,1,3)
plot(r,T, 'b')
axis([min(r) max(r) min(T) max(T)])
hold off

%Store r,n,B, and T in that order to an output file
if findstr(filename, '_rn')
    output_filename=strrep(filename, '_rn', '_rnBT')
else
```

```

    output_filename=[filepath,'output.dat']

end

dlmwrite(output_filename,[r,n,B,T])

end

```

F.3 Limited Perpendicular Thermal Conduction with Uniform Heating

```

% NAME:
%   temp_calc_const_heat_wt
%
% PURPOSE:
%   This Matlab function calculates a temperature
%   profile from the density profile of the Z-pinch.
%   Heat deposited into the plasma [W/m^3] is
%   assumed to be constant across the Z-pinch
%   (and not necessarily due just to resistive heating).
%   Radial thermal conduction out of the plasma
%   [W/m^2] must balance the heat put into the plasma.
%   The cross-field thermal conduction coefficient
%   is calculated so that the model is valid for
%   arbitrary gyrofrequencies and collision times.
%
% CATEGORY:
%   Data analysis code
%
% CALLING SEQUENCE:
%   temp_calc_const_heat_wt(datafile,pulse,helium)

```

```
%  
% INPUTS:  
%     datafile: string that contains the name of the file  
%             containing the density profile  
%     pulse: the pulse number of the plasma pulse whose current  
%             and voltage is to be used to calculate the resistive  
%             heating into the plasma  
%  
% OPTIONAL INPUTS:  
%     helium: set to one for a helium Z-pinch  
%  
% OUTPUTS:  
%     none  
%  
% EXAMPLE:  
%     temp_calc_const_heat_wt('20910027_lower_rn.dat',20910027)  
%     temp_calc_const_heat_wt('30204007_upper_rn.dat',30204007,1)  
%  
% MODIFICATION HISTORY:  
%     Written By: Stuart Jackson, 2 Apr 2006  
  
function value=temp_calc_const_heat_wt(datafile,pulse,helium)  
filepath='M:\Users\Stuart_Jackson\ZaP\matlab\temp_calc\...  
temp_calc_const_heat_wt\';  
filename=[filepath,datafile]  
num=dlmread(filename);  
r=num(:,1);  
%Move r=0 to r^0 to avoid the singularity at r=0  
r(1)=0.001.*mean(r(2:length(r))-r(2:length(r)));  
n=num(:,2);
```

```

n_avg=mean(n);
n_bgnd=1e22;
bgnd_inxs=find(n<n_bgnd);
n(bgnd_inxs)=n_bgnd;
%edge_inx=length(r);
edge_inx=min(bgnd_inxs);
%edge_inx=min(find(n<n_avg));

%Establish values of constants
Z=1;
mp=1.6726e-27; %kg
mi=mp;
if nargin > 2
    Z=2*Z;
    mi=4*mi; %kg
end
me=9.1094e-31; %kg
eps0=8.8542e-12; %F/m
mu0=4e-7*pi; %N/A^2
k=1.6022e-19; %J/eV
lnL=11; %the Coulomb logarithm

%Calculate total heat into Z-pinch
[shot,status] = mdsopen('alfven.aa.washington.edu::zapmain',pulse);
%find power/volume into the Z-pinch
% at the time the hologram was made
%plasma current
ip=mdsvalue('\i_p');
%time base for plasma current
tip= mdsvalue('dim_of(\i_p)');

```

```
%gap voltage
vgap=mdsvalue('\v_gap');
%time base for gap voltage
tvgap= mdsvalue('dim_of(\v_gap)');
%holography laser monitor
holo=mdsvalue('\holography_raw');
%time base for holography laser monitor
t_holo=mdsvalue('dim_of(\holography_raw)');
%get holography time from holography laser monitor
[dummy,holo_time_inx]=max(holo);
holo_time=t_holo(holo_time_inx);
%get holography time from digitizer
t_digi=1.37e-6+mdsvalue('\digitizers::zap_dg11_b:channel_4');
%use the digitizer time if the monitor time is way off
if abs(t_digi-holo_time) > 0.1*t_digi
    holo_time=t_digi;
end
holo_time
%get index for plasma current at holography time
[dummy,ip_time_inx]=min(abs(tip-holo_time));
%get index for gap voltage at holography time
[dummy,vgap_time_inx]=min(abs(tvgap-holo_time));
%calculate total power into experiment at holography time
%(vgap and plasma current are both negative, but ip is
% stored as a positive current, so taking the absolute
% value of pgap makes the power positive)
vgap=vgap(vgap_time_inx)
ip=ip(ip_time_inx)
%-----
%A different way of calculating ip
```

```

%find current through the Z-pinch
%at the time the hologram was made
%m=0 mode at P0
m0=mdsvalue('m_0_p0');
%time base for m=0 mode
tm0= mdsvalue('dim_of(m_0_p0)');
%outer electrode wall radius
rwall=mdsvalue('r_wall'); %m
[dummy,m0_time_inx]=min(abs(tm0-holo_time));
Iz=2*pi*rwall*m0(m0_time_inx)/(mu0) %A
%-----
pgap=abs(vgap.*ip)
%Pin=abs(vgap.*Iz)
%Set heat flux to pgap/(volume of a m-diameter,
% 0.5 m-long Z-pinch)
% a is the radius where the density drops
% below the resolution of the holographic
% interferometer
%qin=pgap./(pi.*a.^2.*0.5)

%set heat in per unit volume to one across the Z-pinch
qin=ones(length(r),1);
%set heat in per unit volume to zero where density
% drops to background value and beyond
qin(edge_inx:length(r))=0;
%use total power in to scale heat in per unit volume
c=pgap./(2.*pi.*0.5.*sum((qin(2:length(r))+qin(1:length(r)-1))./2 ...
.*(r(2:length(r))+r(1:length(r)-1))./2 ...
.*(r(2:length(r))-r(1:length(r)-1))))
qin=c.*qin;

```

```

pin=(2.*pi.*0.5.*sum((qin(2:length(r))+qin(1:length(r)-1))./2 ...
.*(r(2:length(r))+r(1:length(r)-1))./2 ...
.*(r(2:length(r))-r(1:length(r)-1))));
qout=cumsum(2.*pi.*0.5.*sum((qin(2:length(r)) ...
+qin(1:length(r)-1))./2 ...
.*(r(2:length(r))+r(1:length(r)-1))./2 ...
.*(r(2:length(r))-r(1:length(r)-1)))) ...
./(2.*pi.*0.5.*r(2:length(r))+r(1:length(r)-1))./2);
figure(6)
plot(r,qin,'o-'), xlabel('radius'), ylabel('heat in per unit volume')

%Initialize arrays to hold Runge-Kutta terms
F=zeros(4,1);
G=zeros(4,1);

%Initialize normalized T and B arrays,
% setting T(r^0)=1 and B(r^0)=0.001
T=ones(length(r),1);
rB=zeros(length(r),1);
rB(1)=0.001;

%Normalize variables
n0=max(n);
n=n./n0;
r0=rwall;%r(edge_inx);%max(r);
r=r./r0;
%find magnetic field at the wall
%at the time the hologram was made
Bwall=m0(m0_time_inx); %T
%rB array is already normalized

```

```

rB0=rwall.*Bwall;

%Iterate for T0 that matches 1/r to Bwall
nits=500;
delta_conv=0.01;
delta_array=zeros(nits,1);
T0_array=zeros(nits,1);
T0=70;
dT=0;
inx=length(r);
for t=1:nits
    %T array is already normalized
    T0=T0-dT
    %terms used to normalize f and g
    %fconst=r0.^2./T0;
    fconst=r0.^2./(T0.^7/2);
    gconst=r0.^2.*n0.*T0./rB0.^2;
    %set a flag to indicate radial location
    % of first imaginary T or rB value
    imag_flag=0;
    F_array=zeros(length(r),4);
    G_array=zeros(length(r),4);

    for m=1:length(r)-1

        %delta r
        dr=r(m+1)-r(m);
        %delta n
        dn=n(m+1)-n(m);
        %n(r(m)+h/2)
    end
end

```

```

ndr2=(n(m)+n(m+1))./2;
%q(r(m)+h/2)
qindr2=(qin(m)+qin(m+1))./2;

F(1)=calc_f(r(m),n(m),T(m),rB(m),qin(m),Z,r0,rB0,T0,n0, ...
mp,mi,me,eps0,mu0,k,lnL,fconst);
G(1)=calc_g(r(m),dr,n(m),dn,T(m),rB(m),qin(m),Z,r0,rB0,T0,n0, ...
mp,mi,me,eps0,mu0,k,lnL,fconst,gconst);
F(2)=calc_f(r(m)+dr./2,ndr2,T(m)+dr./2.*F(1), ...
rB(m)+dr./2.*G(1),qindr2,Z,r0,rB0,T0,n0, ...
mp,mi,me,eps0,mu0,k,lnL,fconst);
G(2)=calc_g(r(m)+dr./2,dr,ndr2,dn,T(m)+dr./2.*F(1), ...
rB(m)+dr./2.*G(1),qindr2,Z,r0,rB0,T0,n0, ...
mp,mi,me,eps0,mu0,k,lnL,fconst,gconst);
F(3)=calc_f(r(m)+dr./2,ndr2,T(m)+dr./2.*F(2), ...
rB(m)+dr./2.*G(2),qindr2,Z,r0,rB0,T0,n0, ...
mp,mi,me,eps0,mu0,k,lnL,fconst);
G(3)=calc_g(r(m)+dr./2,dr,ndr2,dn,T(m)+dr./2.*F(2), ...
rB(m)+dr./2.*G(2),qindr2,Z,r0,rB0,T0,n0, ...
mp,mi,me,eps0,mu0,k,lnL,fconst,gconst);
F(4)=calc_f(r(m+1),n(m+1),T(m)+dr./2.*F(2), ...
rB(m)+dr./2.*G(2),qin(m+1),Z,r0,rB0,T0,n0, ...
mp,mi,me,eps0,mu0,k,lnL,fconst);
G(4)=calc_g(r(m+1),dr,n(m+1),dn,T(m)+dr.*F(3), ...
rB(m)+dr.*G(3),qin(m+1),Z,r0,rB0,T0,n0, ...
mp,mi,me,eps0,mu0,k,lnL,fconst,gconst);
F_array(m,:)=F';
G_array(m,:)=G';
T(m+1)=T(m)+dr./6.*(F(1)+2.*F(2)+2.*F(3)+F(4));
rB(m+1)=rB(m)+dr./6.*(G(1)+2.*G(2)+2.*G(3)+G(4));

```

250

```
end

B=rB./r;
B(1)=0;
figure(1)
plot(r,n,'k')
hold on
plot(r,B./10,'r')
hold on
plot(r,1./r./10,'r--')
hold on
plot(r,T,'b')

%if t==1
%axis([min(r) max(r) min(B) max(B)])
axis([min(r) max(r) -1 2])
%end

hold off
pause(1)

[inx,dummy]=min(find(imag(rB)^=0));
if inx
    inx=inx;
    delta=real(B(inx))-1./r(inx);
    plot([r(inx),r(inx)], [0,10])
else
    inx=length(r);
    delta=real(B(inx))-1./r(inx);
    plot([r(inx),r(inx)], [0,10])
```

```
%delta=1;  
end  
delta_array(t)=delta;  
T0_array(t)=T0;  
if t>1  
    dT=delta./((delta-delta_old)./(T0-T0_old));  
    %dT=1;  
    if abs(delta)<delta_conv  
        disp(['converged to T0=' ,num2str(T0)])  
        disp(['in ' ,num2str(t) , ' iterations'])  
        break  
    end  
    if t==nits  
        disp(['failed to converge'])  
        disp(['in ' ,num2str(t) , ' iterations'])  
    end  
else  
    %dT=50;  
    dT=1;  
end  
T0_old=T0;  
delta_old=delta;  
end  
  
figure(2)  
subplot(2,1,1)  
semilogy([1:t],abs(delta_array(1:t)),'v-')  
xlabel('T iteration'),ylabel('log(abs(delta))')  
subplot(2,1,2)  
plot([1:t],T0_array(1:t),'v-')
```

```
xlabel('T iteration'), ylabel('T_0')

r=r.*r0;
n=n.*n0;
T=T.*T0;
B=rB.*rB0./r;
B(1)=0;

figure(3)
subplot(3,1,1)
plot(r,n,'ko-')
ylabel('n')
axis([min(r) max(r) 0 max(n)])
% hold on
% plot([min(r),max(r)],[n_avg,n_avg],'--')
subplot(3,1,2)
plot(r,B,'ro-')
ylabel('B')
hold on
plot(r,Bwall.*rwall./r,'r--')
axis([min(r) max(r) 0 2])
subplot(3,1,3)
plot(r,T,'bo-')
ylabel('T')
axis([min(r) max(r) 0 max(real(T))])

figure(4)
subplot(3,1,1)
plot(r,n,'ko-')
ylabel('n')
```

```
axis([min(r) max(r) min(n) max(n)])
subplot(3,1,2)
plot(r,real(B),'ro-')
ylabel('real(B)')
hold on
plot(r,Bwall.*rwall./r,'r--')
axis([min(r) max(r) -3 3])
subplot(3,1,3)
plot(r,real(T),'bo-')
ylabel('real(T)')
axis([min(r) max(r) -200 200])

figure(5)
subplot(3,1,1)
plot(r,n,'ko-')
ylabel('n')
axis([min(r) max(r) min(n) max(n)])
subplot(3,1,2)
plot(r,imag(B),'ro-')
ylabel('imag(B)')
hold on
plot(r,Bwall.*rwall./r,'r--')
axis([min(r) max(r) -3 3])
subplot(3,1,3)
plot(r,imag(T),'bo-')
ylabel('imag(T)')
axis([min(r) max(r) -200 200])

%Store r, n, B, and T in that order to an output file
```

```

if findstr(filename,'_rn')
    output_filename=strrep(filename,'_rn','_rnBT')
else
    output_filename=[filepath,'output.dat']
end

dlmwrite(output_filename,[r,n,B,T])

end

function lnL=calc_lnL(r,n,T,rB,qin,Z,r0,rB0,T0,n0,mp,mi,me,eps0,mu0,k)
B_real=rB.*rB0./r0;
T_real=T.*T0;
n_real=n.*n0;
e=k;
LD=real((eps0.*k.*T_real./(n_real.*e.^2.*(1+Z))).^(0.5))
b0=abs(real(Z.*e.^2./(4.*pi.*eps0.*k.*T_real)))
lnL=log(LD./b0);
end

function f=calc_f(r,n,T,rB,qin,Z,r0,rB0,T0,n0,%
    mp,mi,me,eps0,mu0,k,lnL,fconst)
%Calculates dT/dr
%e=k;
%lnL=calc_lnL(r,n,T,rB,qin,Z,r0,rB0,T0,n0,mp,mi,me,eps0,mu0,k)
%a1=12.*pi.^1.5.*eps0.^2.*k.^(7./2)./(lnL.*e.^4);
a1=1.19e-12./(Z.^4.*mi.^0.5); %W/(m eV^(7/2))
ti=calc_ti(r,r0,rB,rB0,T,T0,n,n0,Z,mp,mi,me,eps0,mu0,k,lnL);
xi=calcxi(r,r0,rB,rB0,T,T0,n,n0,Z,mp,mi,me,eps0,mu0,k,lnL);
di=xi.^4+2.70.*xi.^2+0.677;

```

```

%Kp=n.*k.^2.*T.*ti./mi.*(2.*xi.^2+2.645./di);
if (r ~= 0)
    %f=-r.*qin./(2.*Kp).*fconst;
    f=-r.*qin./(2.*a1.*T.^(5/2)).*di./(2.*xi.^2+2.645).*fconst;
    %f=-r.*qin./(2.*a1.*T.^(5/2)).*xi.^2./2.*fconst;
else
    f=0;
end

end

function g=calc_g(r,dr,n,dn,T,rB,qin,Z,r0,rB0,T0,n0,%
    mp,mi,me,eps0,mu0,k,lnL,fconst,gconst)
%Calculates d(rB)/dr
f=calc_f(r,n,T,rB,qin,Z,r0,rB0,T0,n0,mp,mi,me,eps0,mu0,k,lnL,fconst);
if (rB~=0)
    g=-mu0.*k.*((1+1./Z).*r.^2./rB.*((n.*f+T.*dn./dr).*gconst));
else
    g=0;
end

end

function xi=calcxi(r,r0,rB,rB0,T,T0,n,n0,Z,mp,mi,me,eps0,mu0,k,lnL)
B_real=rB.*rB0./r0;
T_real=T.*T0;
n_real=n.*n0;
e=k;
ti=calc_ti(r,r0,rB,rB0,T,T0,n,n0,Z,mp,mi,me,eps0,mu0,k,lnL);
wi=Z.*e.*B_real./mi;

```

256

```
xi=wi.*ti;
end

function ti=calc_ti(r,r0,rB,rB0,T,T0,n,n0,Z,mp,mi,me,eps0,mu0,k,lnL)
B_real=rB.*rB0./r0;
T_real=T.*T0;
n_real=n.*n0;
e=k;
ti=12.*pi.^1.5.*eps0.^2.*mi.^0.5.*(k.*T_real).^1.5 ...
./(lnL.*e.^4.*Z.^3.*n_real);
end
```

F.4 Constant Temperature

```
% NAME:
% temp_calc_const_t
%
% PURPOSE:
% This Matlab function calculates equilibrium
% profiles from the density profile of the Z-pinch
% assuming a constant temperature across the Z-pinch.
% The magnitude of the temperature is adjusted until
% the edge field matches the wall field scaled to
% the edge radius.
%
% CATEGORY:
% Data analysis code
%
% CALLING SEQUENCE:
```

```
% temp_calc_const_t(datafile,pulse,helium)
%
% INPUTS:
%
% datafile: string that contains the name of the file
% containing the density profile
%
% pulse: the pulse number of the plasma pulse whose current
% and voltage is to be used to calculate the resistive
% heating into the plasma
%
%
% OPTIONAL INPUTS:
%
% helium: set to one for a helium Z-pinch
%
%
% OUTPUTS:
%
% none
%
%
% EXAMPLE:
%
% temp_calc_const_t('20910027_lower_rn.dat',20910027)
%
% temp_calc_const_t('30204007_upper_rn.dat',30204007,1)
%
%
% MODIFICATION HISTORY:
%
% Written By: Stuart Jackson, 11 Apr 2006

function value=temp_calc_const_t(datafile,pulse,helium)
filepath='M:\Users\Stuart_Jackson\ZaP\matlab\temp_calc...
    \temp_calc_const_t\';
filename=[filepath,datafile]
num=dlmread(filename);
r=num(:,1);
%Move r=0 to r~0 to avoid the singularity at r=0
r(1)=0.001.*mean(r(2:length(r))-r(2:length(r)));
```

```

n=num(:,2);
% n_bgnd=1e22;
% bgnd_inxs=find(n<n_bgnd);
% n(bgnd_inxs)=n_bgnd;

%Establish values of constants
Z=1;
mp=1.6726e-27; %kg
mi=mp;
if nargin > 2
    Z=2*Z;
    mi=4*mi; %kg
end
me=9.1094e-31; %kg
eps0=8.8542e-12; %F/m
mu0=4e-7*pi; %N/A^2
k=1.6022e-19; %J/eV
lnL=11; %the Coulomb logarithm

%Find magnetic field at the wall
%at the time the hologram was made
[shot,status] = mdsopen('alfven.aa.washington.edu::zapmain',pulse);
holo=mdsvalue('\holography_raw');
%time base for holography laser monitor
t_holo=mdsvalue('dim_of(\holography_raw)');
%get holography time from holography laser monitor
[dummy,holo_time_inx]=max(holo);
holo_time=t_holo(holo_time_inx);
%get holography time from digitizer
t_digi=1.37e-6+mdsvalue('\digitizers::zap_dg11_b:channel_4');

```

```

%use the digitizer time if the monitor time is way off
if abs(t_digi-holo_time) > 0.1*t_digi
    holo_time=t_digi;
end

holo_time

%m=0 mode at P0

m0=mdsvalue('\m_0_p0');

%time base for m=0 mode

tm0= mdsvalue('dim_of(\m_0_p0)');

%get magnetic field at the wall

[dummy,m0_time_inx]=min(abs(tm0-holo_time));

Bwall=m0(m0_time_inx); %T

%outer electrode wall radius

rwall=mdsvalue('\r_wall'); %m

%Initialize arrays to hold Runge-Kutta terms

F=zeros(4,1);

G=zeros(4,1);

%Initialize normalized T and B arrays,
% setting T(r^0)=1 and B(r^0)=0.001

T=ones(length(r),1);

rB=zeros(length(r),1);

rB(1)=0.001;

%Normalize variables

n0=max(n);

n=n./n0;

r0=rwall;%r(edge_inx);%max(r);

r=r./r0;

```

```

%rB array is already normalized
rB0=rwall.*Bwall;

%Iterate for T0 that matches 1/r to Bwall
nits=25;
delta_conv=0.01;
delta_array=zeros(nits,1);
T0_array=zeros(nits,1);
T0=70;
dT=0;
inx=length(r);
for t=1:nits
    %T array is already normalized
    T0=T0-dT
    %terms used to normalize g
    gconst=r0.^2.*n0.*T0./rB0.^2;

    for m=1:length(r)-1

        %delta r
        dr=r(m+1)-r(m);
        %delta n
        dn=n(m+1)-n(m);
        %n(r(m)+h/2)
        ndr2=(n(m)+n(m+1))./2;

        G(1)=calc_g(r(m),dr,n(m),dn,T(m),rB(m),Z,mu0,k,gconst);
        G(2)=calc_g(r(m)+dr./2,dr,ndr2,dn,T(m),rB(m)+dr./2.*G(1),...
                     Z,mu0,k,gconst);
        G(3)=calc_g(r(m)+dr./2,dr,ndr2,dn,T(m),rB(m)+dr./2.*G(2),...

```

```

Z,mu0,k,gconst);
G(4)=calc_g(r(m+1),dr,n(m+1),dn,T(m+1),rB(m)+dr.*G(3),...
Z,mu0,k,gconst);
rB(m+1)=rB(m)+dr./6.* (G(1)+2.*G(2)+2.*G(3)+G(4));
end

B=rB./r;
B(1)=0;
figure(1)
plot(r,n,'k')
hold on
plot(r,B./10,'r')
hold on
plot(r,1./r./10,'r--')
hold on
plot(r,T,'b')

%if t==1
%axis([min(r) max(r) min(B) max(B)])
axis([min(r) max(r) -1 2])
%end

hold off
pause(1)

[inx,dummy]=min(find(imag(rB) ~=0));
if inx
    inx=inx;
    delta=real(B(inx))-1./r(inx);
    plot([r(inx),r(inx)], [0,10])
end

```

```

else
    inx=length(r);
    delta=real(B(inx))-1./r(inx);
    plot([r(inx),r(inx)], [0,10])
    %delta=1;
end
delta_array(t)=delta;
T0_array(t)=T0;
if t>1
    dT=delta./((delta-delta_old)./(T0-T0_old));
    %dT=1;
    if abs(delta)<delta_conv
        disp(['converged to T0=' ,num2str(T0)])
        disp(['in ' ,num2str(t), ' iterations'])
        break
    end
    if t==nits
        disp(['failed to converge'])
        disp(['in ' ,num2str(t), ' iterations'])
    end
else
    %dT=50;
    dT=1;
end
T0_old=T0;
delta_old=delta;
end

figure(2)
subplot(2,1,1)

```

```
semilogy([1:t],abs(delta_array(1:t)),'v-')
xlabel('T iteration'),ylabel('log(abs(delta))')
subplot(2,1,2)
plot([1:t],T0_array(1:t),'v-')
xlabel('T iteration'),ylabel('T_0')

r=r.*r0;
n=n.*n0;
T=T.*T0;
B=rB.*rB0./r;
B(1)=0;

figure(3)
subplot(3,1,1)
plot(r,n,'ko-')
ylabel('n')
axis([min(r) max(r) 0 max(n)])
% hold on
% plot([min(r),max(r)],[n_avg,n_avg],'--')
subplot(3,1,2)
plot(r,B,'ro-')
ylabel('B')
hold on
plot(r,Bwall.*rwall./r,'r--')
axis([min(r) max(r) 0 2])
subplot(3,1,3)
plot(r,T,'bo-')
ylabel('T')
axis([min(r) max(r) 0 max(real(T))])
```

```
figure(4)
subplot(3,1,1)
plot(r,n,'ko-')
ylabel('n')
axis([min(r) max(r) min(n) max(n)])
subplot(3,1,2)
plot(r,real(B),'ro-')
ylabel('real(B)')
hold on
plot(r,Bwall.*rwall./r,'r--')
axis([min(r) max(r) -3 3])
subplot(3,1,3)
plot(r,real(T),'bo-')
ylabel('real(T)')
axis([min(r) max(r) -200 200])
```

```
figure(5)
subplot(3,1,1)
plot(r,n,'ko-')
ylabel('n')
axis([min(r) max(r) min(n) max(n)])
subplot(3,1,2)
plot(r,imag(B),'ro-')
ylabel('imag(B)')
hold on
plot(r,Bwall.*rwall./r,'r--')
axis([min(r) max(r) -3 3])
subplot(3,1,3)
plot(r,imag(T),'bo-')
ylabel('imag(T)')
```

```
axis([min(r) max(r) -200 200])

%Store r, n, B, and T in that order to an output file
if findstr(filename,'_rn')
    output_filename=strrep(filename,'_rn','_rnBT')
else
    output_filename=[filepath,'output.dat']
end

dlmwrite(output_filename,[r,n,B,T])

end

function g=calc_g(r,dr,n,dn,T,rB,Z,mu0,k,gconst)
%Calculates d(rB)/dr
g=-mu0.*k.* (1+1./Z).*T.*r.^2./rB.*dn./dr.*gconst;

end
```

VITA

Stuart Jackson was born in Lynchburg, Virginia in 1978 and is a 1996 graduate of E. C. Glass High School and the Central Virginia Governor's School for Science and Technology. He moved to Boston in 1996 to attend the Massachusetts Institute of Technology in Cambridge, Massachusetts and received a Bachelor of Science in Aeronautics and Astronautics in 2000. Over the summers during college, he worked as an intern at Hughes Space and Communications, Orbital Sciences Corporation, and the MIT Space Systems Laboratory. After college, he moved to Seattle and completed a Master of Science in Aeronautics and Astronautics at the University of Washington in 2003. He received a Doctor of Philosophy from the Department of Aeronautics and Astronautics at the University of Washington in 2006